Université du Québec
Institut National de la Recherche Scientifique
Centre Eau, Terre et Environnement

Improvement, verification, and application of a process-based numerical model of groundwater–surface water interactions

by
MAURO SULIS

Thesis presented
in fulfillment of the thesis requirement for the degree of
Doctor of Philosophy
in
Water Science

Evaluation Committee

President of the committee and internal evaluator	Dr. Miroslav Nastev Geological Survey of Canada Natural Resources Canada
External evaluator	Dr. René Therrien Dept. of Geology and Geological Engineering Université Laval
External evaluator	Dr. Cécile Dagès Lab. d'étude des Interactions Sol - Agrosystème - Hydrosystème Institut National de la Recherche Agronomique
Advisor	Dr. Claudio Paniconi INRS-ETE Université du Québec

September 2010

a Francesca e Caterina

Acknowledgments

I wish to sincerely thank my advisor Claudio Paniconi for his guidance and support throughout this work. The joy and enthusiasm he has for his research was contagious and motivational for me, even during tough times in the Ph.D. pursuit. I am also indebted to Mario Putti, Matteo Camporese, Reed Maxwell, Stefan Kollet, Steven Meyerhoff, Christine Rivard, Diane Chaumont, and Richard Harvey for their constructive contribution to the journal articles included in this thesis. I would like to thank my reading committee members, Miroslav Nastev, René Therrien, and Cécile Dagès, who spent their valuable time to share their opinions and suggestions with me.

I would like to thank Stefano Orlandini who hosted me at the University of Modena and Reggio Emilia, for his valuable advice and friendly help. His extensive discussions around hydrological processes have been very helpful for the progress of my research work. Many thanks also to Giovanni Moretti for his great patience and assistance with terrain analysis problems, and for the nice time spent talking on Skype. I am very grateful to Enrico Piga and Roberto Deidda who kindly hosted me at the Department of Land Engineering of the University of Cagliari where I had the opportunity to finalize my thesis being close to my wife Francesca and to my daughter Caterina.

A thank you also to John Riva for helpful comments on the writing of the synthesis of this dissertation and to Suzanne Dussault for her help with all the administrative details of the thesis. Office mates and friends, Bala, Nicoleta, Thomas, Marie-Éve, Sylvain, Lorenzo, Camille, Daniela, Giuseppe, and Maria Grazia were always there for distraction and support. Thanks also to my parents Gino and Rina, and my brother Giovanni for the moral motivation during these years.

Part of the work described in this thesis is a contribution to the "Châteauguay project" (Grant CRDPJ-319968-04, with funding by the Ouranos Consortium and the Natural Sciences and Engineering Research Council of Canada, and data from Ministère du Développement durable de l'Environnement et des Parcs, Environment Canada, and other sources). I would like to acknowledge this support and also the useful discussions with other participants in this project (in particular Marie Larocque, Alain Rousseau, and Mélanie Trudel).

Finally, a special thanks to Francesca who accepted to move to Quebec City and shared the good and bad moments of this thesis with me. Without her constant support and encouragement I would have never finished this work.

Abstract

Numerical models are modern tools for capturing the spatial and temporal variability in the land-surface hydrologic response to rainfall and for understanding the physical relations between internal watershed processes and observed streamflow. This thesis presents the improvement and application of a distributed hydrologic model distinguished by its path-based description of surface flow across the drainage basin and by its coupling of the surface and subsurface components that contribute to the catchment response. As a research tool for hydrologic forecasting and experimentation, the CATchment HYdrology (CATHY) model fully incorporates spatial heterogeneities in basin topography, surface descriptors, and hydrometeorological forcing to produce dynamic maps of hydrologic states and fluxes. These capabilities allow investigation of theoretical questions and practical problems in hydrologic science and water resources engineering.

Three related themes are developed in this thesis. First, an assessment via a comparative analysis of two different approaches for handling surface–subsurface interactions is conducted. This intercomparison study considers the coupling between the land surface and the subsurface via an explicit exchange term resolved by continuity principles implemented in the ParFlow model (a fully-coupled approach) and via special treatment of atmospheric boundary conditions in CATHY (a sequential approach). Different test cases are used to investigate the models' sensitivity to factors such as vertical mesh resolution, time step size, and slope angle. Second, surface-subsurface interactions are evaluated in a climate change scenario extracted from projections generated by the Canadian Regional Climate Model (CRCM). We assess the sensitivity of the hydrological response (river discharge, aquifer recharge, and soil water storage) to future climate conditions for the des Anglais catchment located in southwestern Quebec (Canada). In this context, we also compare the hydrologic predictions obtained with CATHY with those obtained from the Canadian Land Surface Scheme (CLASS). An examination of the runoff and soil water storage response is used to highlight some of the key differences in these two models. Third, the surface and subsurface runoff response in a complex basin such as the des Anglais catchment is investigated with respect to changes in digital elevation model (DEM) resolution. In particular, we examine the effects of grid size on both the integrated response of the catchment (discharge) and on the distributed response (water table depth, surface saturation, and soil water storage).

The model applications presented in this thesis highlight the advantages of surface–suburface coupled modeling for hydrologic forecasting and process-oriented studies over complex terrain. In particular, the multi-resolution and multi-scale capabilities are encouraging for a range of applied and scientific problems in catchment hydrology.

Résumé

Les modèles numériques sont des instruments modernes permettant de capturer la variabilité spatiale et temporelle des processus hydrologiques résultant d'événements pluviaux. Ils permettent aussi de comprendre les relations physiques entre les processus se produisant à l'intérieur d'un bassin versant et les débits observés. Ainsi, cette thèse présente un modèle hydrologique distribué intégrant les chemins préférentiels empruntés par l'écoulement de surface ainsi que le couplage entre les eaux de surface et souterraines. Le modèle CATchment HYdrology (CATHY) est un puissant outil de prédiction et d'expérimentation hydrologique incorporant l'hétérogénéité spatiale liée à la topographie du bassin, à ses conditions de surface ainsi qu'au forçage atmosphérique, permettant de générer des cartes dynamiques des différents états et débits hydrologiques. Ceci représente un atout majeur du modèle CATHY pour la résolution de problèmes pratiques et théoriques en hydrologie et en ingénierie hydrique.

Trois thèmes connexes sont développés dans cette thèse. D'abord, une analyse comparative basée sur deux différentes approches décrivant les interactions entre les eaux de surface et souterraines, est réalisée. Cette étude considère le couplage entre la composante de surface et de sub-surface via un terme explicite de change, déterminé selon les principes de continuité tels qu'implémentés dans le modèle ParFlow (approche entièrement couplée) et via un traitement particulier des conditions de frontières (approche couplée séquentielle) tel qu'implémenté dans CATHY. Différents cas sont utilisés afin d'analyser la sensibilité des modèles aux facteurs comme la résolution des mailles verticales, le pas de temps et la pente. Ensuite, les interactions entre les eaux de surface et souterraines sont évaluées selon un scénario de changement climatique extrait des projections produites par le modèle canadien du climat regional (MRCC). La sensibilité de la réponse hydrologique (débit de rivière, recharge à l'aquifère et stockage d'eau dans le sol) est évaluée par rapport aux conditions climatiques futures du bassin versant des Anglais situé dans le sud-ouest du Québec (Canada). De plus, dans ce même contexte, les prédictions hydrologiques obtenues avec CATHY et celles obtenues avec CLASS sont comparées. Finalement, la réponse produite par le ruissellement de surface et souterrain, dans un bassin versant complexe comme celui des Anglais, est étudié pour plusieurs résolutions du modèle digital de terrain (MDT). Particulièrement, les effets de la résolution des mailles horizontales sur la réponse intégrée du bassin versant (débit) et sur

la réponse distribuée (profondeur de la nappe, saturation en surface et stockage d'eau sans le sol) sont examinés de près.

Les applications de modélisation présentées dans cette thèse mettent en relief les avantages d'une approche couplée entre les eaux de surface et souterraines pour les prévisions hydrologiques et les études orientées sur la description de processus de terrains complexes. La possibilité d'utiliser différentes résolutions et échelles est particulièrement encourageante pour aborder des problématiques pratiques ou scientifiques dans le domaine de l'hydrologie du bassin versant.

Contents

List of Tables

List of Figures

Chapter 1

Research synthesis

The research described in this dissertation aims to shed light on surface water–subsurface water interactions over different spatial and temporal scales. This first chapter of the dissertation synthesizes the main results of the research work, which are described in detail in Chapters 2, 3, and 4 and which have been submitted, respectively, as the following journal papers:

- "A comparison of two physics-based numerical models for simulating surface water–groundwater interactions", Mauro Sulis, Steven B. Meyerhoff, Claudio Paniconi, Reed M. Maxwell, Mario Putti, and Stefan J. Kollet, *Adv. Water Resour.*, 33(4), 456–467, 2010
- "Assessment of climate change impacts at the catchment scale with a detailed hydrological model of surface/subsurface interactions, and comparison with a land surface model", Mauro Sulis, Claudio Paniconi, Christine Rivard, Richard Harvey, and Diane Chaumont. *Water Resour. Res.*, re-submitted with "minor to moderate revisions", July 2010
- "Impact of grid resolution on the integrated and distributed response of a coupled surface–subsurface hydrological model", Mauro Sulis, Claudio Paniconi, and Matteo Camporese, *Hydrol. Process.*, to be re-submitted with minor revisions, reviews received August 2010

The first section of this synthesis introduces some basic concepts and provides a broad literature review of the main themes and issues that are touched on in the research work. The second section presents the summary of the main results. In the third and final section, auxiliary research conducted during the course of the PhD work is summarized. This additional

material is intended to fill in some gaps, in particular with regards to the pre-processor of the hydrological model on which the dissertation research is based.

1.1 Introduction

1.1.1 Interactions between surface and subsurface waters

Surface and subsurface waters are not isolated components of the hydrologic cycle, but instead interact in response to topographic, soil, geologic, and climatic factors *[Eagleson, 1978]*. The study of these interactions has been addressed at both small (streambed and hillslope) *[Harvey and Bencala, 1993; Tonina and Buffington, 2007]* and large (watershed to global) scales *[Levine and Salvucci, 1999; Syed et al., 2005; Günter et al., 2007; Lemieux et al., 2008]*. The interactions have also been probed in sandbox laboratories and via detailed field plot studies *[Abdul and Gillham, 1984; VanderKwaak and Loague, 2001]*. The various issues involved in the study of these phenomena include the geomorphic role of groundwater sapping *[Howard and McLane, 1998]*, conjunctive water management strategies *[Illangasekare and Morel-Seytoux, 1982]* and water quality evaluation in an integrated framework *[Bencala, 1984; Castro and Hornberger, 1991]*.

Hydrologic interactions between surface and subsurface waters in a landscape occur by subsurface lateral flow through the unsaturated soil and by infiltration into or exfiltration from the saturated zones. Also, in the case of karst or fractured terrain, interactions occur through flow in fracture/solution channels. During any particular storm, different mechanisms can generate runoff from different parts of a catchment. The response of the catchment may be dominated by a single mechanism or by a combination of mechanisms, depending on the magnitude of the rainfall event, the antecedent soil moisture conditions of the catchment, and the heterogeneity in soil hydraulic properties *[Beven, 2000b]*. Surface runoff from infiltration excess (Horton saturation mechanism, Figure 1.1(a)-1.1(b)) occurs when the rainfall intensity exceeds the infiltration capacity of the land surface. This mechanism can be a dominant process in urbanized areas, as well as in zones that typically receive high intensity precipitation and that are characterized by a low permeability layer at the soil surface. Surface runoff from saturation excess (Dunne saturation mechanism) usually occurs on relatively small landscape portions susceptible to becoming completely saturated when the rainfall rate is smaller than the saturated hydraulic conductivity of the soil and the water table reaches up to the ground surface. If the water table and capillary fringe are close to the soil surface, then only small amounts of applied water are needed to saturate the soil profile completely. This excess water might discharge onto the surface as return flow (Figure 1.1(c)) or it can also enter streams

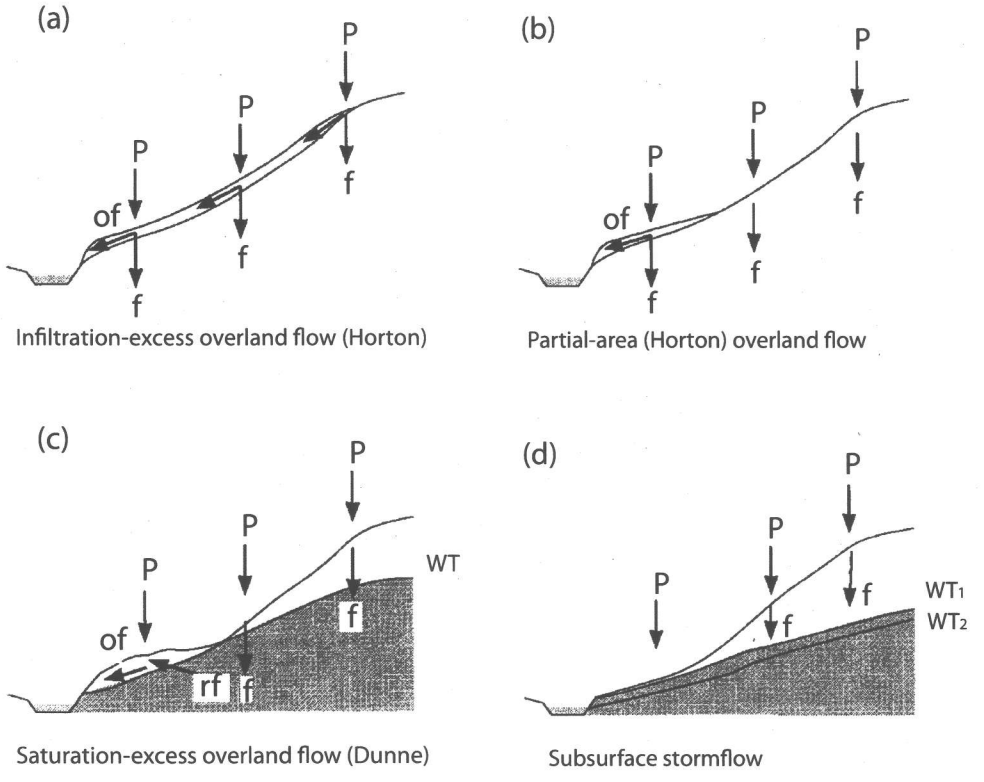

Figure 1.1: Mechanisms of runoff production. "P" is precipitation, "f" is infiltration, "of" is overland flow, "rf" is return flow, and "WT" is the water table. Adapted from *Beven [2000b]*.

quickly enough to contribute directly to the event response (Figure 1.1(d)). An overview of runoff generation mechanisms that may be dominant at the hillslope scale and in different environments is provided in Figure 1.2.

The water exchange between groundwater and surface water in a stream network is controlled by *(i)* the distribution and magnitude of hydraulic conductivities, both within the channel and the associated alluvial–plain sediments; *(ii)* the relation of stream stage to the adjacent groundwater level; and *(iii)* the geometry and position of the stream channel within the alluvial plain *[Woessner, 2000]*. The direction of the exchange processes varies with hydraulic head, whereas flow rate depends on sediment hydraulic conductivity. Precipitation events and seasonal patterns alter the hydraulic head and thereby induce changes in flow direction. Traditionally, it is usual to differentiate the relations that can exist between surface and groundwater flow according to two net directions of water flow: *(i)* the influent condition, where surface water contributes to subsurface flow; and *(ii)* the effluent condition, where groundwater drains into the stream. Following this representation, stream-aquifer relations can be distinguished as perennial, intermittent, or ephemeral. In perennial streams, baseflow

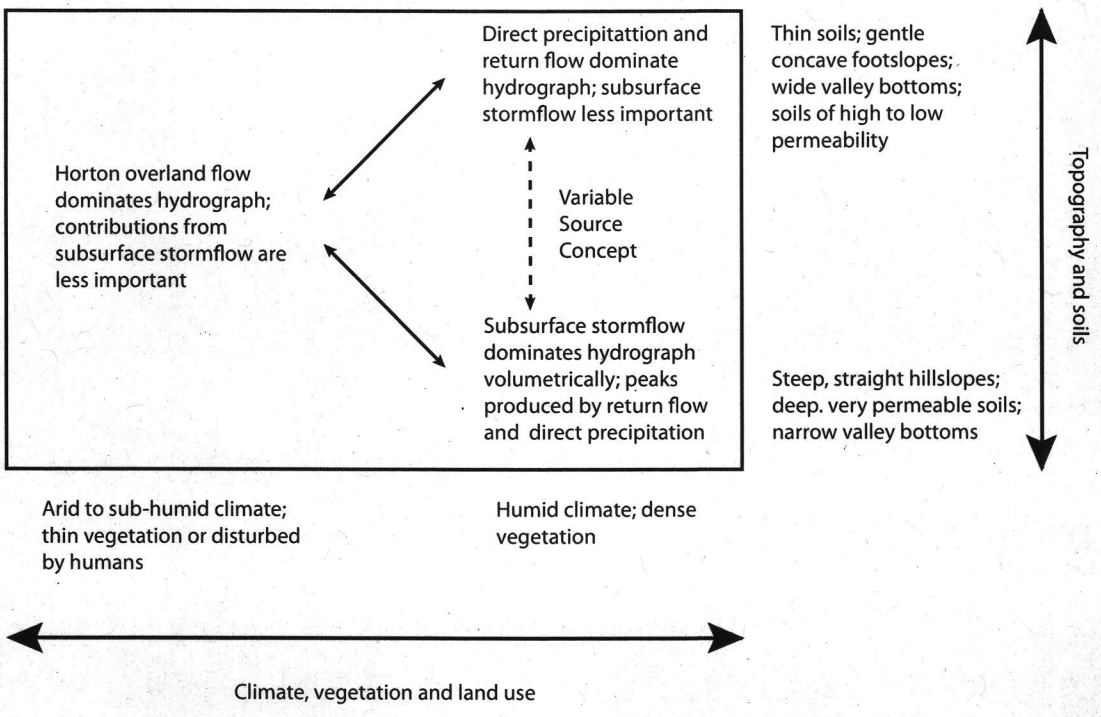

Figure 1.2: Dominant processes of hillslope response from rainfall. Adapted from *Dunne [1978]*.

is more or less continuous, whereby the streams are primarily effluent and flow continuously throughout the year (Figure 1.3(a)), or simultaneously receive and lose groundwater (Figure 1.3(d)). Intermittent streams receive water only at certain times of the year and are either influent (losing) or effluent (gaining), depending on the season (Figure 1.3(a)–1.3(b)). In ephemeral streams the groundwater level is always beneath the channel, so they are exclusively influent when they are flowing (Figure 1.3(c)).

Interactions between surface water and groundwater also play a critical role in the water cycle between the land and the atmosphere *[Liang et al., 2003; Gulden et al., 2007; Maxwell et al., 2007]*. With the exception of deserts, where it can be deep and disconnected from the land surface, groundwater receives the surplus during wet periods and supplies the deficit during dry periods *[Sophocleous, 2002]*. As such, it can influence the near-surface and root-zone soil water content which, in turn, plays a key role in partitioning precipitation into infiltration, surface runoff, and drainage to groundwater. Surface soil water content also controls the partitioning of energy into sensible and latent heat fluxes at the ground surface, affecting the coupling between the land surface and the planetary boundary layer and thereby the mechanisms of soil-atmosphere interaction *[Brubaker and Entekhabi, 1996; Eltahir, 1998]*.

An outline of the complex feedback processes involved in the link between the atmospheric and

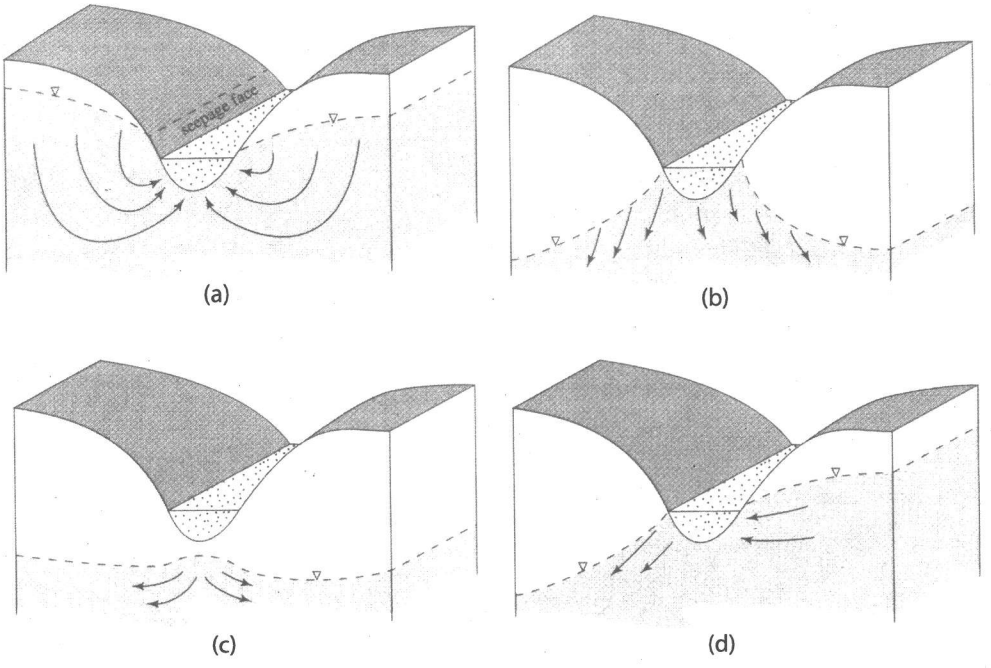

Figure 1.3: Stream-aquifer relations. (a) Gaining stream receiving water from local, intermediate, or regional groundwater flow; (b) losing stream connected to water table; (c) losing stream perched above water table; (d) flow-through stream. Source: *Dingman [2002]*.

the land surface component of the hydrological cycle is shown in the form of a conventional Forrester diagram in Figure 1.4. This diagram shows the direction of some of the feedback mechanisms which arise from a change in the moisture content of the upper soil layers. Thus it can be seen that soil moisture and net radiation are linked by eight pathways, four of them involving overall positive feedback and four involving overall negative feedback. The arrows reported in this diagram are based on the following considerations: *(i)* relationship between soil moisture conditions and two basic properties of the land surface, albedo and Bowen ratio (the ratio between sensible and latent heat fluxes); *(ii)* the surface radiation balance; *(iii)* the energy balance at the land-atmosphere boundary; *(iv)* the energy balance of the atmospheric boundary layer; and *(v)* the thermodynamic and dynamic processes that relate boundary layer conditions and subsequent rainfall. As an example, basic radiation physics suggests that water absorbs significantly more solar radiation than dry soil. Thus, albedo is negatively correlated with average water content in the soil. The negative relation between soil water content and albedo implies that wet soil moisture conditions would tend to enhance net solar radiation at the surface.

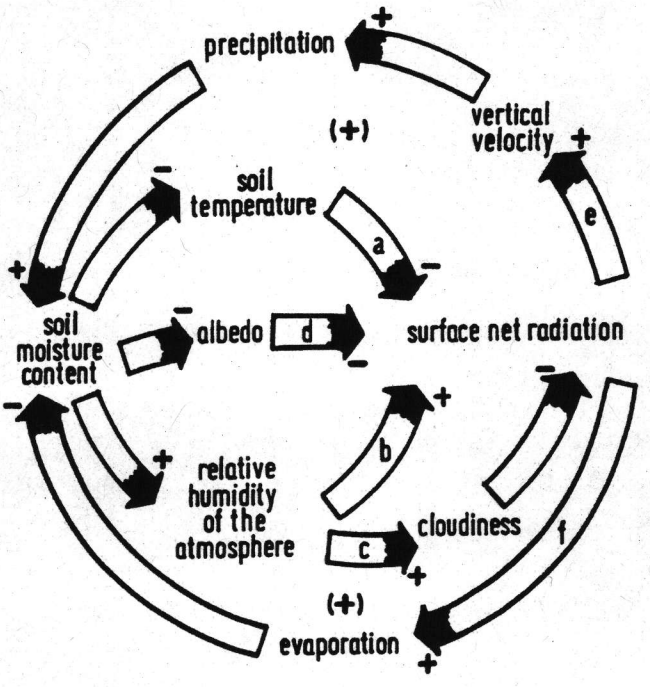

Figure 1.4: Diagram of feedback mechanisms between the land surface and the atmospheric boundary layer. Source: *Dooge [1989].*

1.1.2 Modeling of surface–subsurface interactions

The growing recognition of groundwater–surface–atmosphere interactions as a potentially significant influence on spatial and temporal climate variability has expanded, in recent years, the study of these interactions in hydrology, terrestrial hydrometeorology, and other fields. Increasing attention is being focused on improving the process representations of subsurface hydrology within large-scale land surface models from simple *[Manabe et al., 1965]* to more sophisticated parameterizations *[Lee and Abriola, 1999; Yeh and Eltahir, 2005; Niu et al., 2007].* Altough atmospheric scientists have turned more and more to hydrology to come up with better land–atmosphere parameterizations in order to improve climate models and weather prediction, land surface models are still limited to vertical moisture transport in the soil column and lack an adequate representation of surface and subsurface lateral transport due to topography or moisture gradients. Conversely, hydrologist have focused their attention on modeling tools which vary from conceptual lumped models *[Crawford and Linsley, 1966; Todini, 1996]* to detailed multiprocess models of water flow physics *[Abbott et al., 1986; Refsgaard and Storm, 1995].* A common basis amongst these hydrological models is a simplified upper boundary condition that is externally specified and intended to represent fluxes of water related to processes such as infiltration and evapotranspiration. These fluxes are often simplified, uncoupled, and may be averaged in time and space, possibly missing the

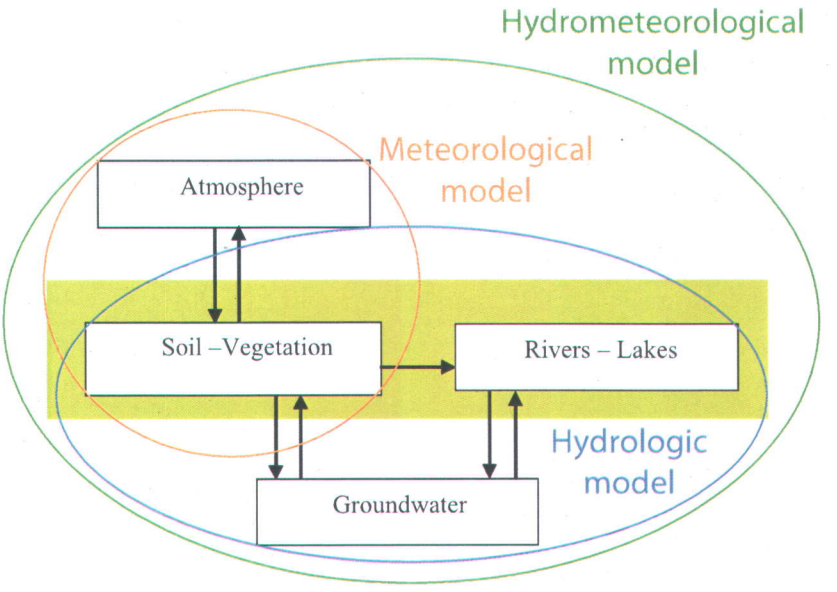

Figure 1.5: Diagram illustrating the different modeling simulation communities involved in the study of surface–subsurface water interactions. Adapted from *Miguez-Macho et al. [2007]*.

key feedback dynamics between the land surface and atmospheric boundary layer previously described.

The increased interest in climate change and the study of its impacts has underlined the need for a convergence towards a unified hydroclimatological simulation paradigm shared by both atmospheric and hydrologic scientists of the Earth Science community, such as represented in Figure 1.5. In this perspective, the ability to incorporate fully-distributed atmospheric inputs, topographic features, the effects of shade and aspect on hydrologic response, and geologic and land cover variability, makes physically-based (or process-based), distributed-parameter models suitable tools to decipher the principal influences and feedbacks when the many state variables and physical processes in water and energy balance are all interconnected in complicated ways.

In the class of physically-based models, the more computationally intensive approaches use shallow water equations to describe surface flow, i.e., one- or two-dimensional approximation of the Saint-Venant equations for overland and/or channel flow, coupled with a groundwater component, treated in three dimensions by an equation for variably saturated subsurface flow, i.e., Richards equation *[e.g., Freeze, 1972; Sudicky et al., 2000; VanderKwaak and Loague, 2001; Morita and Yen, 2002; Panday and Huyakorn, 2004; Therrien et al., 2004; Kollet and Maxwell, 2006]*. Simpler, but still process-based, approaches involve approximations such as

spatial averaging *[e.g., Anderson, 2005; Gunduz and Aral, 2005]* and the use of analytical or linearization techniques *[e.g., Fan and Bras, 1998; Ni and Capart, 2006]*.

Coupled hydrological models require some scheme to account for the interactions between the land surface and subsurface. One solution scheme in integrating the surface and subsurface equations is the fully implicit solution technique with the two governing equations and the interaction fluxes simultaneously solved. This approach was proposed by *Panday and Huyakorn [2004]* and *VanderKwaak and Loague [2001]*, amongst others. A second way of coupling surface and subsurface equations is to separately and iteratively solve the two equations at each time step. The convergence of the scheme is obtained when the exchange term attains a prescribed tolerance. Examples of this approach are found in the works of *Govindaraju and Kavvas [1991]* and *Morita and Yen [2002]*. A third coupled modeling approach was proposed recently by *Kollet and Maxwell [2006]*. In this case, the two governing equations are directly coupled via continuity principles at the ground surface, with the overland flow equation embedded in the subsurface equation as a boundary condition. This results in a fully integrated approach with just one equation to be solved per time step.

Coupled surface–subsurface models also differ in the way overland flow is represented. In most models, surface runoff from a catchment is represented as sheet flow. According to these models, the water available at the surface is considered to be uniformly distributed. Assuming a uniform water distribution over the computational units allows a numerically clean coupling between surface and subsurface flow models. However, in nature overland flow tends to be concentrated along a complex network of rivulets and channels, as illustrated in Figure 1.6. This network forms owing to topographic irregularities or differences in soil erodibility, and deepens and widens during the runoff event as a function of slope, runoff characteristics, and soil erodibility *[Emmett, 1978; Li et al., 1980]*.

The importance of rill formation on erosion processes and flow dynamics is now well recognized in many experimental studies *[e.g., Abrahams et al., 1989; Abrahams and Parsons, 1990; Hairsine and Rose, 1992b; Abrahams et al., 1994]*. Some examples of rilled surface modeling and the relation between rill geometry and hydrologic properties are reported in the works of *Moore and Burch [1986]*, *Govindaraju and Kavvas [1992]*, and *Tayfur and Kavvas [1994]*. However, despite being more realistic, the rill flow conceptualization of surface runoff propagation poses the structural problem of parameter identifiability, i.e., the match between the complexity in model formulation and the real possibility of retrieving the related parameters by field surveys. Indeed, there are currently no sound examples illustrating how to characterize a drainage network at hillslope scale from field inspections. Thus, more experimental and theoretical work needs to be done to fully understand the complex phenomena of rill structure over hillslopes and to express them in a quantifiable manner.

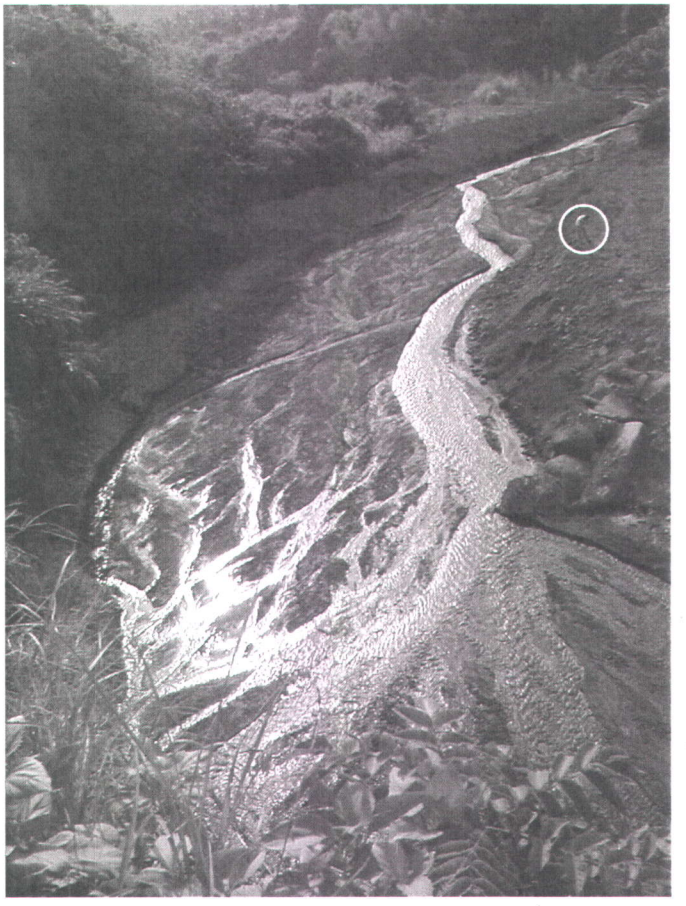

Figure 1.6: Network of channels and rivulets incised into irregular ground. Source: *Ni and Capart [2006].*

1.1.3 Discretization, calibration, and other modeling issues

The increasing availability of spatially distributed rainfall data, data on distributed watershed properties, and inexpensive computational resources is encouraging the use of physically-based hydrological models for a broad range of applications. As a consequence of this increase in activity, there have also been a number of discussions in the literature regarding issues associated with the use of such physically-based hydrological models *[Beven, 1989, 1993, 2000a; Beven and Binley, 1992; Grayson et al., 1992b; Smith et al., 1994; Abbott, 1996; Loague and VanderKwaak, 2004].* The issues pointed out by these discussions can be summarized as follows: *(i)* there is a great danger that the theoretical rigour underlying these models will engender uncritical belief in their predictions *[Beven, 1989]*; *(ii)* parameter values are often selected without taking into account their physical nature and variability, considerations that are essential for physically-based distributed models *[Grayson et al., 1992b]*; *(iii)* the ease with which they are applied often leads to less critical evaluation of their limitations *[Loague*

and VanderKwaak, 2004]. In general, the accurate use of physically-based models requires a particular attention to those aspects (e.g., gridding options) concerning the numerical resolution of the underlying partial differential equations, which describe the surface and subsurface flow, and on the effects of parameter assignment (e.g., uniqueness) on the reliability of model response.

The need when solving the Richards equation for a fine vertical resolution to simulate sharp wetting fronts into initially dry soils has been demonstrated by *Ross [1990]* and *El-Kadi and Ling [1993]. Smirnova et al. [1997]* and *Dam and Feddes [2000]* showed how the number of vertical grid cells and its size affect the calculation of soil moisture and hydrological fluxes. For surface flow, numerical problems arise while solving the full Saint-Venant equations for studying flood wave movement when the magnitudes of different terms of the momentum equation vary widely *[Ferrick, 1985].* By analyzing different wave types, *Ferrick [1985]* suggested the use of appropriate wave type equations for obtaining accurate solutions without facing numerical problems, and argued that the use of more complete equations may not yield more accurate river wave simulations for all wave types. Accuracy and stability issues related to the finite-difference resolution of the diffusion wave equation as well as the definition of criteria for choosing numerical algorithms and approriate space and time steps, were investigated in *Moussa and Bocquillon [1996a,b].*

The aforementioned studies have extensively described the accuracy, robustness, and other performance features of surface and subsurface numerical models, but they do not provide insights on numerical issues arising from the coupling of such surface and subsurface equations at the watershed scale. Compared to field-scale, at the watershed scale the effects of such factors as the vertical and horizontal resolution are complicated by pronounced local topographic features, diverse runoff production mechanisms, groundwater effects on runoff production, runon phenomena, and heterogeneous watershed characteristics. One of the few rigorous investigations in this sense is represented by the work of *Downer and Ogden [2004].* Through a spatial convergence study, *Downer and Ogden [2004]* identified the proper resolution that accurately describes the solution with maximum computational efficiency by using physically realistic parameter values. One of the concluding remarks of this work, however, is that proper discretization and the thickness of the near-surface layer depends on the application and the watershed being studied. Thus, a sound insight has not been reached as to how robust physics-based hydrologic-response models are (or can be) with respect to issues such as spatial and temporal resolution, especially with regard to simulation of distributed hydrologic response. Yet, the question of an adequate discretization is of fundamental importance if physics-based hydrologic simulations are to provide a reliable foundation for investigating physical processes where the distributed hydrologic response is important.

By definition, a fully distributed physically-based model contains only those parameters that

can be assessed from field measurements. This implies that, in principle, when sufficient data are available, calibration is unnecessary. However, these models are frequently applied to a scale different from that from which the model equations were deduced and validated. As a consequence of this discrepancy in scales, lack of data, and measurement errors, these models usually have to be calibrated. The goal of the calibration process for physically-based models is to find an optimal set of physically realistic parameter values that simulate the behavior of the catchment as accurately as possible *[Sooroshian and Gupta, 1995]*. To accomplish this, physically based constraints for parameter values have to be specified on the basis of the information available.

The calibration of a physically-based hydrological model, however, may fail to produce adequate results. *Refsgaard and Storm [1996]* distinguished six different reasons for this failure: *(i)* random and/or systematic errors in the input and calibration data; *(ii)* errors as a result of a non-optimal parameter set; *(iii)* mathematical errors in the model, in relation to the physical and mathematical basis of the computer code; *(iv)* conceptual errors in the model, e.g., incorrect boundary conditions; *(v)* numerical errors inherent in the solution of algorithm, e.g., numerical dispersion as a result of discretization; and *(vi)* interpretation errors of the predicted results. Thus, it is important to distinguish between the various sources of uncertainty so as not to change the values of the parameters outside physically acceptable boundaries when compensating for other error sources.

One of the claimed attractions of physics-based models is that, in theory, the governing equations, boundary conditions, and parameter values calibrated to a brief hydrologic record should apply to most hydrologic conditions, even to conditions beyond the successfully tested range *[e.g., Abbott et al., 1986; Bathurst and O'Connell, 1992]*. The question of whether hydrologic response can also be simulated for a validation period outside of a calibration period addresses the issue of uniqueness. The definition of uniqueness *[Neuman, 1973; Carrera and Neuman, 1986]* requires that only one set of parameter values can be estimated from a given set of observations and that this parameter set must also represent the observed behavior for other hydrologic conditions. When employing a distributed model, the simulated hydrologic response should be compared to distributed observations of state variables in the watershed *[Beven, 1989; Grayson et al., 1992a,b]*. A focus on the distributed response is of particular importance for physics-based simulation because of the many degrees of freedom (e.g., parameters, boundary conditions), which can give rise to equifinality when only the integrated response (i.e., discharge or solute concentrations in discharge) is used for evaluation *[e.g., Beven, 1989, 2006; Ebel and Loague, 2006]*. An additional question is whether uniqueness with regard to simulation of the integrated response indicates if uniqueness for the distributed response will also be achieved.

Despite the importance of employing both integrated (e.g., discharge) and distributed (e.g.,

piezometric, soil water content, or surface water depth) observations when evaluating the simulated hydrologic response during a validation period, there are relatively few studies addressing this issue. *Refsgaard [1997]* reported an application of a physically-based hydrologic model where discharge and piezometric response were shown to be non-unique for a validation period following a calibration period. *Feyen et al. [2000]* found that discharge at the catchment outlet was well simulated during a validation period after calibration, but internal discharges and water table levels were not well simulated during the validation period. *Anderton et al. [2002]* reported physically-based simulation results in which discharge, soil water content, and water table levels were all worse simulated during the validation period following a calibration period. *Downer and Ogden [2003]* investigated the level of sophistication required for a model calibrated to observed outflow to actually approximate processes at the cell level. *Heppner et al. [2008]*, employing a characterization developed from event-based simulations for long-term continuous simulation with a physics-based model, found that water balance components, peak discharge, and sediment discharge were each well simulated while distributed soil water contents were poorly simulated.

The above studies highlight how the practical application of a physically-based distributed-parameter model is not always evident. This is due to the difficulty of retrieving field data to parameterize the model components (subsurface and surface flow) over a large area, which often leads to the use of values provided in literature. A related difficulty is the lack of detailed information to support accurate implementation of internal or lateral outflow boundaries, which often leads to the use of simple model setup, such as a no-flow boundary condition at the lateral boundaries. These issues relate to themes that are much-debated within the scientific community such as the effects of model complexity and parameter assignment on the reliability of model estimates, and represent a constant challenge for hydrological modelers.

To fully realize their potential, physically-based distributed models require widespread measurements of distributed state variables and parameters which, to date, are difficult to measure and costly to collect. This lack-of-data condition has made the application of these models mostly for research purposes as a means of formalizing knowledge about hydrological systems and less as operational tools to address the decision-making process of real hydrological problems. This situation, however, may change over the next years with the increased availability of data from remote and automated ground-based sensors, and by the use of advanced geophysical and environmental tracer-based techniques for the characterization of the hydrogeologic features of a catchment. The use of these techniques will ultimately provide estimation over wider spatial and temporal scales of state variables such as soil moisture *[Leconte et al., 2004; Thoma et al., 2006]*, streamflow discharge *[Koblinsky et al., 1993; Bjerklie et al., 2005]*, snow cover and snow water equivalent *[Romanov et al., 2003; Dong et al., 2007]*, and model parameters such as hydraulic conductivity *[Cook et al., 1996; Dafflon et al., 2009]* and surface roughness *[Järvelä, 2004; Antonarakis et al., 2009]*. An important

role in this effort will also be played by the development of platforms based on distributed high-performance parallel computers linked by fast network connections (e.g., GRID; *[Beven, 2003]*) and by the establishment of consortia to enhance the sharing of hydrologic data (e.g., CUAHSI; *[Consortium of Universities for the Advancement of Hydrological Science]*). This new framework will in turn need to devote more attention to intelligent methods for processing and integrating large amounts of information into hydrological simulation models (e.g., data assimilation techniques; *[McLaughlin, 2002; Camporese et al., 2009]*), and for supporting the sharing of data over different platforms (e.g., NetCDF; *[Rew and Davis, 1990]*).

1.1.4 The CATHY (CATchment HYdrology) model

The research in this dissertation has been carried out using the CATHY (CATchment HYdrology) model, a coupled, physically-based, spatially-distributed model for surface–subsurface simulations *[Bixio et al., 2000; Camporese et al., 2010]*. The model is based on the separate and sequential resolution of the three-dimensional Richards equation for subsurface flow in variably saturated soils *[Paniconi and Wood, 1993; Paniconi and Putti, 1994]* and a diffusion wave approximation of the Saint-Venant equation for overland and channel flow *[Orlandini and Rosso, 1996, 1998]*. The hydrologic interactions between surface and subsurface waters are handled by an automatic boundary condition (BC) switching algorithm acting on the source/sink term of the subsurface flow equation *[Putti and Paniconi, 2004]*. A more detailed description of key features of the model (e.g., mathematical formulation, surface–subsurface coupling approach, and surface routing conceptualization) can be found in Chapter 2, whereas specific aspects dealing with characteristic soil curves (Appendix A), numerical discterization of surface and subsurface equations (Appendices B and C), parameterization of the surface flow equation (Appendix D and E), and the representation of heterogeneity for the des Anglais catchment (Appendix F) are described in the appendices at the end of the thesis. In addition, the data set of the simulation runs has been included in a CD-ROM (Appendix G).

1.2 Summary of main research and results

The investigation of surface–subsurface water interactions was initially undertaken by considering simple test cases aimed in illustrating some of the features of the CATHY model, in particular the behavior of the boundary condition switching algorithm, under a variety of conditions. These test simulations, illustrated in the first paper of this dissertation (Chapter 2), were focused on direct runoff production via saturation excess and infiltration excess

mechanisms, on return flow occurrence during rainfall and evaporation episodes, and on other physical processes which make up the integrated hydrological response of a catchment. Moreover, the simulation of single-events under simple configuration settings allowed to clearly assess the influence of factors such as vertical and horizontal resolution, time step size, and slope angle on both accuracy and computing time of model response. As such, these simple simulation runs were also considered as a preliminary exercise to the application of the CATHY model, as described in the second and third paper of this dissertation (Chapter 3 and 4), to a real catchment with more complex geometry and topography, under long series of rainfall-evaporation episodes, and with expensive computing time.

1.2.1 Comparative analysis of the CATHY and ParFlow models (Chapter 2)

The first part of the research work was dedicated to a comparison between the CATHY model and ParFlow, a coupled model presented by *Kollet and Maxwell [2006]*. The governing equations for ParFlow are the three-dimensional Richards equation for subsurface flow in variably saturated soils and the kinematic wave approximation of the Saint-Venant equation for overland and channel flow. Compared to the sequential coupling and boundary condition switching procedure used in CATHY, ParFlow uses a full coupling approach and continuity of pressures and fluxes across the land surface to resolve the surface–subsurface interactions. In addition to different schemes for coupling and exchange flux resolution, the two models use different conceptualizations of surface routing: sheet flow in ParFlow; rill flow in CATHY (Figure 1.7). Although not directly inherent to coupling issues, these additional differences were also considered worthy of assessment, given the high interest in applying coupled hydrological models at catchment and river basin scales where terrain features (slope, roughness, etc.), and consequently surface flow conditions, can vary greatly.

The comparison of these two very different models represented a first opportunity to critically examine some key features of coupled hydrological models, but also to establish a set of simple cases to be used as benchmark tests in further developments of the CATHY model. These numerical tests, on a sloping plane and a tilted V-catchment, examined saturation excess and infiltration excess runoff production under homogeneous and heterogeneous conditions and the dynamics of the return flow process as described earlier. These tests were intended to investigate the effects of factors such as grid discretization (horizontal and vertical), time step size, and slope angle on the surface–subsurface coupled response of these two models.

Overall, the simulation runs showed a low sensitivity to vertical discretization and time step size for the two models under saturation excess and homogeneous conditions. Larger sensi-

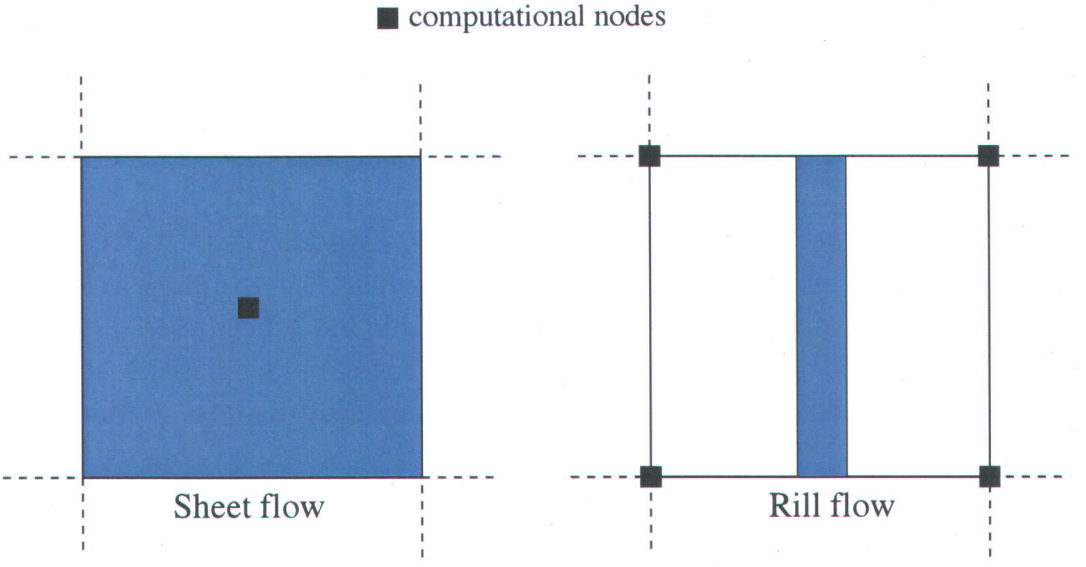

Figure 1.7: Sketch of surface flow conceptualizations implemented in ParFlow (left) and CATHY (right).

tivity and differences in response were observed under infiltration excess and heterogeneous conditions, due to the different coupling approaches and spatial discretization schemes (finite differences in ParFlow and finite elements in CATHY). In particular, for the simulation of saturation and infiltration excess mechanisms under heterogeneous conditions, the simultaneous solution of the surface and subsurface equations in ParFlow produces a sharper, more localized hydrograph that is less influenced by the temporal discretization. In CATHY, on the other hand, the sequential solution procedure implies, for instance, that once the surface becomes saturated at certain localized nodes (and the boundary condition for these nodes is switched from Neumann to Dirichlet), all of this water is routed downslope for the duration of one time step, delaying any possible reinfiltration until the next (subsurface) time step. Thus the CATHY model hydrograph appears a little bit earlier than ParFlow's, and the reinfiltration front more spread out early in the simulation. In return flow behavior, we found the models in general agreement, with the largest discrepancies achieved during the recession phase where the model responses are dominated by surface routing, and thus attributable to the different parameterizations of diffusion in the surface water propagation schemes.

The intercomparison study also examined the differences in the hydrologic response under the rill flow and sheet flow parameterizations implemented in the CATHY and ParFlow model, respectively. The effects of these two conceptualizations were highlighted in terms of flow discharge and ponding heads (surface flow depths). The simulation runs showed that under "equivalent" sheet flow parameterizations, the CATHY and ParFlow models produce very

similar hydrograph responses at the catchment outlet and comparable flow depth profiles. Other simulation runs highlighted the different hydrograph responses and water depth profiles produced by the rill and sheet flow parameterizations in CATHY (steeper in space and faster in time for the rill flow parameterization), underscoring the differences in erosion potential and sediment transport capacity between the two conceptualizations.

A broader goal of this research objective was to encourage additional efforts to assess coupled surface–subsurface models, given the variety of formulations and approaches that have recently been proposed for representing flow interactions and other processes. Further intercomparison studies that clearly expose model differences and similarities under complex physical conditions (including geometry and topography) and for real catchments will be needed to further extend this research work and to create suitable benchmark test cases.

1.2.2 Assessment of climate change impacts at the catchment scale (Chapter 3)

In the second part of the thesis surface–subsurface water interactions were addressed at a larger spatial and temporal scale by implementing the CATHY model over a 30-year period to provide an assessment of climate change impacts for a medium size ($\sim$ 690 km^2) catchment. The study catchment was the des Anglais river basin located in southwestern Quebec which is a subcatchment of the transboundary Chateauguay River watershed (Figure 1.8). The novelty of this research objective was the use of a physically-based surface–subsurface coupled model to underline the role played by important hydrodynamic feedbacks between the land surface, soil, and groundwater zones. The use of a detailed spatially-distributed model such CATHY allowed us also to show how local heterogeneity in topography, soils, and geology can result in significant spatio-temporal variations in a catchment's response to climate change.

A prior step of this research objective was the processing of climate variables (precipitation and min / max temperatures) generated by the Canadian Regional Climate Model (CRCM) for a past (1961-90) and future (2041-70) scenario. This consisted in performing a statistical analysis to verify the null hypothesis of no trend in a time series, and to construct the future climate projection dataset for the hydrological model simulations. The statistical analysis was carried out by using the Mann-Kendall test on annual and mean monthly values. The results of this analysis revealed a significant positive trend in temperature (and hence in potential evapotranspiration) and no significant trend in precipitation. The positive trend in temperature was particularly strong for the winter and early summer months of the future scenario. These findings were found to be consistent with the results of a previous study based on an observation dataset for the entire country. To construct the future climate projection

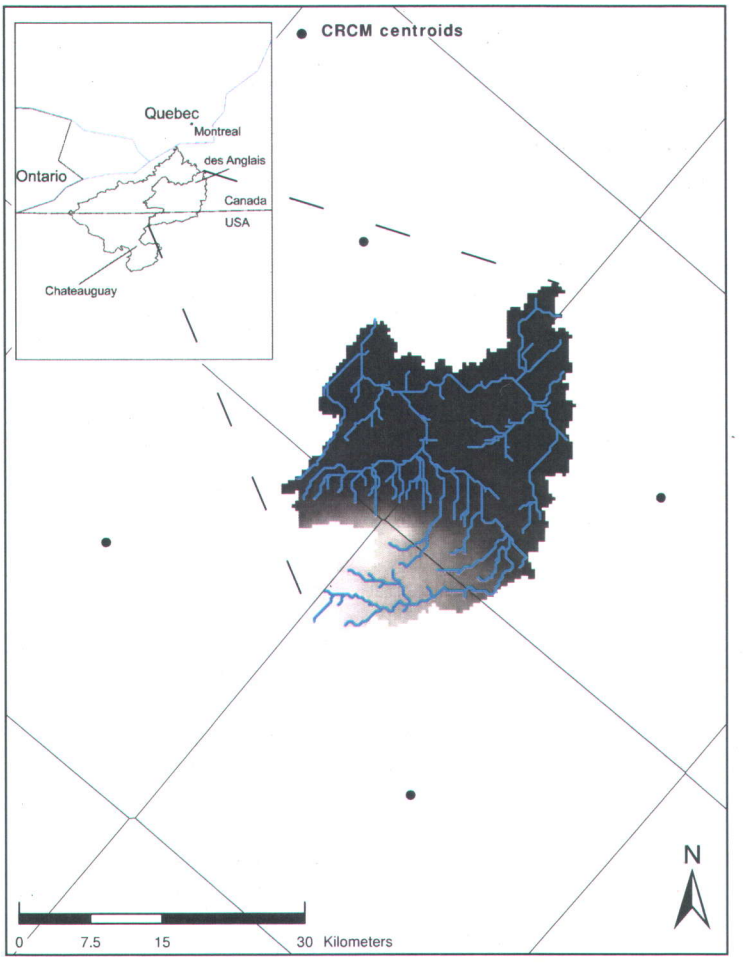

Figure 1.8: Map of the des Anglais river basin showing the location of the centroids of the CRCM grid.

dataset for the hydrological model simulations we applied a transfer scheme, the commonly used delta change method, which consists in perturbing baseline meteorological data with monthly change values. The monthly change values were calculated as the difference in CRCM atmospheric outputs between the past and future 30-year climate periods.

The assessment of climate change impacts was conducted by driving the CATHY hydrological model by the observed 1961-90 dataset (daily precipitation and min and max temperatures) for the past simulation, and by this same baseline dataset perturbed as per the delta change method for the future projection. The assessment examined in particular the impacts on river discharge, aquifer recharge, and near-surface soil water storage. The results of the simulations showed that at the main outlet the climate change impacts are most significant during the peak winter period due to the combination of more precipitation and higher temperature (and hence an increased of rainfall to snowfall ratio) and during summer months

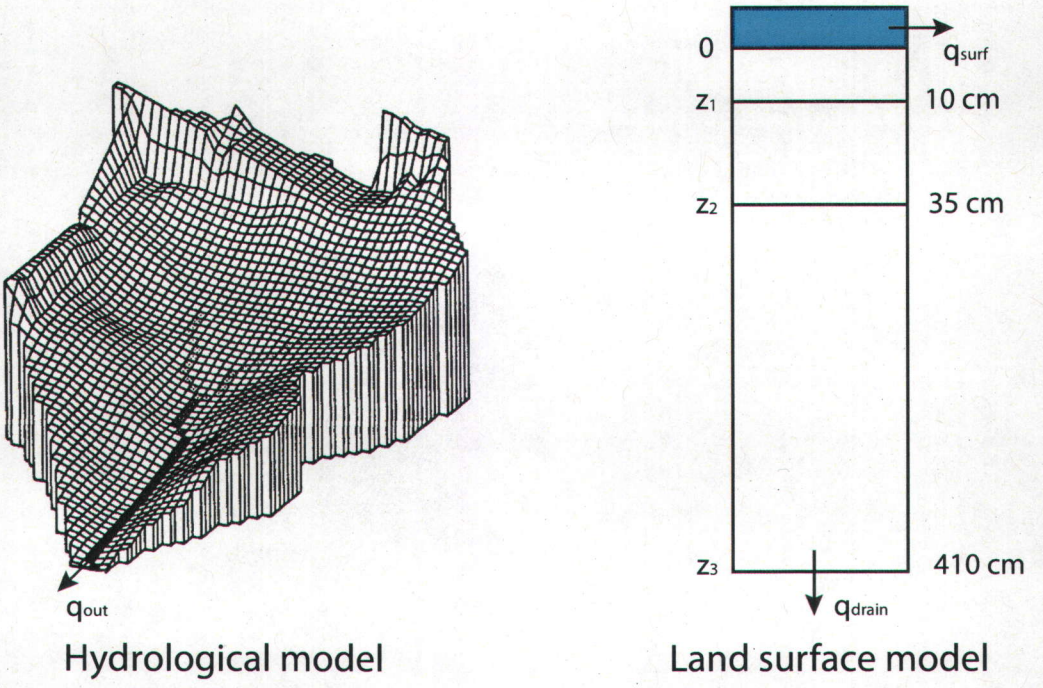

Figure 1.9: DEM-based 3D and 3-layer 1D conceptualizations used in the CATHY and CLASS models, respectively.

due to a marked increase of temperature (and hence evaporation). The results also showed significant spatio-temporal variations in the river discharge response to climate change owing to a different partitioning between the overland runoff and baseflow components of the hydrograph, with the latter alleviating the marked decrease in discharge during the summer period. Recharge to the aquifer increases significantly during the winter season due to a higher rain/snow ratio caused by higher temperatures, whereas it decreases in the spring due to an earlier and less intense snowmelt, and over the summer period due to increased evaporation. A spatial analysis of recharge patterns shows that the greatest variations are expected to occur, throughout the year, in the southern portion of the catchment, where the elevations are highest. This analysis also highlighted a possible reversal, during summer months, in groundwater-river interactions in response to groundwater storage deficits.

Compared to river discharge and aquifer recharge, the water storage volumes are less sensitive to climate changes. Storage variations are most strongly felt nearest to the surface, which is directly exposed to fluctuations in precipitation and evapotranspiration, and are progressively dampened as soil depth increases. From a spatial analysis of soil moisture variations it was possible to observe organizational patterns that follow the topographic and pedologic

characteristics of the catchment. Moreover, through an investigation of the relationship between the tangent curvature of the surface and the soil water variation, performed for a section of the catchment near the outlet, it was found that the hillslope cells located along convergent parts of the catchment tend to experience an increase in soil moisture content in February and March in response to climate change, and less variation in the late summer and early fall (August to October).

An additional objective of this study was to compare the predictions obtained with CLASS, the land surface scheme that is coupled to the CRCM model, to those from the CATHY model for past and future climate change projections. CLASS and CATHY represent two very different classes of hydrological model, and this study was a first and instructive opportunity to highlight some of their key differences. We found that CLASS produces higher estimates than CATHY of surface and subsurface runoff throughout the annual cycle for both past and future scenarios, with the greatest difference occurring at the peak flow during snowmelt. The key factors contributing to these discrepancies were the different degree of physical detail included in the surface and subsurface parameterizations (1D Green-Ampt model vs 3D Richards equation) and the different spatial resolutions of the two models that affect the ability to capture important topographic features and subsurface heterogeneities that strongly influence the response of the catchment (Figure 1.9). For soil water storage, CLASS and CATHY were found to be in general agreement in terms of the intra-annual variability of moisture content in the first two soil layers (0-0.10 m and 0.10-0.35 m), particularly for the top layer in which water variations are most directly affected by rainfall events and by diurnal temperature changes during interstorm periods. The largest differences between the two models occur in the third layer (0.35-4.10 m), with CATHY predicting wetter soil conditions over the entire simulation period and moisture fluctuations of much smaller amplitude. The probable causes of this behavior are underestimation of infiltration in CLASS, together with the absence of an underlying groundwater reservoir that results in faster depletion of the bottom layer.

1.2.3 Investigation of grid impacts on the response of the CATHY model (Chapter 4)

The third part of the research work was dedicated to the investigation of the sensitivity of hydrologic response to digital elevation model (DEM) cell resolution, focusing in particular on the impact of grid discretization on the factors that control partitioning and other interactions between surface water and groundwater. The effects of grid size were investigated on both the integrated (discharge at the main outlet and at two internal points), and distributed (water table depth, surface saturation, and soil water storage) responses of the des Anglair

river basin.

A prior step of the work consisted in performing a terrain analysis based on frequency distributions of local slope, plan curvature, drainage area, and topographic index for DEMs of resolution 180, 360, and 720 m. A comparison of the distributions of these topographic attributes allowed direct assessment of the influence of grid size on landscape representation. The main findings of this analysis are that: *(i)* local slope systematically decreases as the DEM grid size increases; *(ii)* the spectrum of plan curvature decreases as DEM grid size increases; *(iii)* larger grid sizes lead to bias in favor of larger contributing areas; and *(iv)* decreasing grid size shifts the cumulative distribution of topographic index towards lower values.

The simulation results with CATHY showed that discharge volumes increase as the DEM is coarsened, and that coarser DEMs are also wetter overall in terms of water table depth and soil water storage. The reasons for these trends include an increase of the total drainage area of the catchment for larger DEM cell sizes, due to aggregation effects at the boundary cells of the catchment, and a decrease in local slope and plan curvature variations, which in turn limits the capacity of the watershed to transmit water downslope and laterally. An analysis of simulated discharge volumes at different points within the catchment revealed significant spatio-temporal variations in the river discharge sensitivity to DEM resolution owing to a different partitioning between the overland runoff and baseflow components of the hydrograph, with the portion of the catchment characterized by permeable soils and a flat topography being less sensitive to grid resolution effects due to its dominant overland flow character. The analysis of soil moisture at the end of a 10-day rainfall period (in October, 2005) and at the end of a 10-day dry period (August, 2003) showed that the grid resolution effects are less pronounced during dry periods. This is because moisture content differences during wet periods are caused by lateral water transport, and this process is dominated by the plan curvature. During dry periods, on the other hand, evaporation is the main factor in moisture loss and lateral transport is small, thus plan curvature plays a lesser role.

1.3 Auxiliary research

In addition to the research work represented by the 3 chapters summarized above, some effort was also expended to bring changes to the CATHY model in order to improve the model's modularity and to provide the model with state of the art options for drainage network delineation and its characterization. This work was carried out by fully externalizing the DEM-based pre-processor, an improvement that also facilitates exchange of information between the model and geographical information systems (GIS) such as ArcGIS or GRASS.

The investigation, based on numerical experiments and supported by measured data, of implications for hydrological modeling of such model's improvements was deemed beyond the scope of this dissertation. However, a simulation domain similar to that used in the first paper, and the DEM of a portion of the real catchment used in the second and third paper, were considered to briefly illustrate some of the improvements led by this auxiliary research work on the definition of the drainage network. In the practical application of the pre-processor, such as described into the second and third paper of the dissertation, the choice amongst the different options for the delineation and characterization of the drainage network was bounded by the available resolution of the DEM and by the lack of field measurements.

1.3.1 Drainage network delineation for the CATHY model

In the previous version of CATHY the drainage network was automatically extracted from a digital elevation model implementing the D8 (eight drainage directions) method proposed by *O'Callaghan and Mark [1984]* and *Marks et al. [1984]*. Surface flow was propagated downstream from the uppermost DEM cell through a conceptual network of channels defined by an ordering system where two numbers were assigned to each cell (Figure 1.10): the cell order (CO) and the cell link number (LN). The CO is the sum of the neighboring upslope cell orders from which the cell can receive water (source cells are assigned an order of 1). The LN identifies the first cell of each link in the drainage system. It is equal to the cell order for the uppermost cell of the link and to zero for all other link cells. The distinction between hillslope rill and channel network cells was based on the "constant critical support area" concept described by *Montgomery and Foufoula-Georgiou [1993]*. In this method rill flow is assumed to occur for all those catchment cells for which the upstream drainage area A does not exceed a constant threshold value A_t, while channel flow is assumed to occur for all those cells for which A equals or exceeds A_t.

The automatic drainage network extraction procedures cannot handle isolated topographic depressions ("pits"). Thus in the pre-processor a depitting technique is used to modify the elevation values and to regularize the DEM. This technique consists of a recursive procedure to raise the elevations of the cells located in flat or depressed areas so as to ensure a drainage direction with a small positive slope (downward) for all the cells of the catchment.

However, when depressions play an important role in the formation of surface and subsurface fluxes the depitting procedure introduces inconsistent flow directions and do not correctly reproduce the storage and retardation effects of pools and lakes on the catchment response. This typically happens in relatively flat areas where flow patterns are strongly influenced by small slope changes. Once the topographic depressions are localized (this task can be performed by using digitized maps), a "lake boundary-following" procedure *[Mackay and*

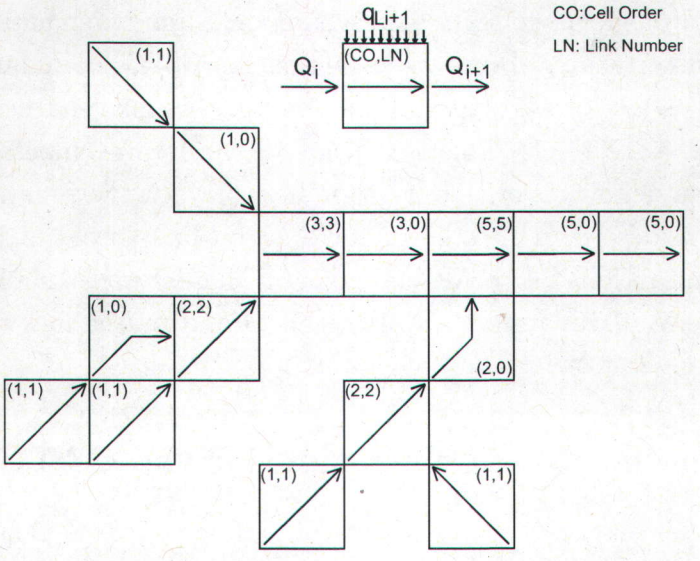

Figure 1.10: Sketch of the DEM-based drainage network ordering system in the previous version of the CATHY model. Source: *Orlandini and Rosso [1998].*

Band, 1998] is employed to isolate and correct for potential breakdown in the subsequent drainage network extraction process. In this procedure, each cell along the boundary of the pit (also called "buffer cells") acts as a depression point for all the catchment cells draining into the pit (Figure 1.11). To ensure correct flow paths in the area, the drainage direction in all the buffer cells is forced to form a circulation path that drains into a single cell (the lake outlet or "reservoir" cell). A flow path algorithm, in combination with a "slope tolerance" based correction procedure to account for the remaining erroneous depressions, is then applied to the modified DEM that excludes the central cells of the depression. The storage and retardation effects of the pit are accounted for by transferring with infinite celerity all the water drained by the buffer cells to the lake outlet cell, which is now treated as a reservoir. In the current version of the pre-processor the topographic depressions are "manually" identified from the analysis of the DEM. An automatic identification procedure is envisaged in further improvements of the pre-processor.

The hydraulic characterization of the drainage network was achieved by applying the "hydraulic geometry" concept *[Leopold and Maddock Jr., 1953].* This term connotes the relationships between the mean stream channel form and discharge both "at-a-station" and in a "downstream" direction along a stream network. The channel form includes the mean cross-section geometry (e.g., width), and the hydraulic variables which include the mean slope, mean friction, and mean velocity for a given influx of water. The term "at-a-station" is used to mean at a given cross section, and the phrase "in a downstream direction" refers to cross

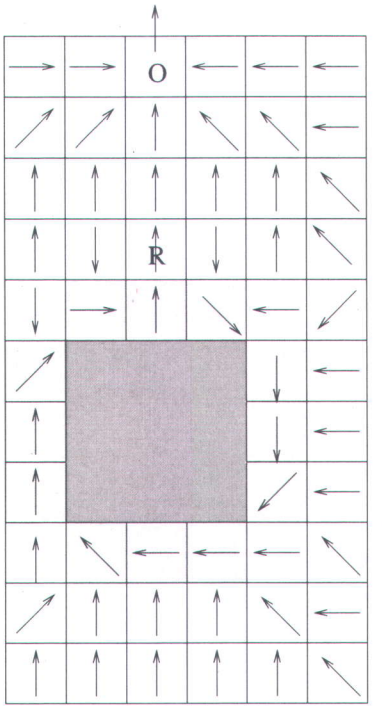

Figure 1.11: Surface cell flow paths for a test case representing a small catchment with an internal lake. The interior area of the depression is shown in dark grey and the buffer cells with forced flow directions are shown in light grey. The reservoir cell is identified by "R" and the outlet cell by "O". Source: *Paniconi et al. [2003]*

sections situated along the length of a stream.

For description purposes, in Figure 1.12 cross sections A and B represent two points on a river at low discharge, while C and D are the same sections at higher discharge. These sections are shown at the right, as A, B, C, and D, in their relation to the full length of the river and to its watershed at both low and high discharge. These diagrams illustrate the conception that the width and depth of the channel increase at a given river cross section with increase in discharge. Variations in discharge follow a pattern in time that is peculiar to the position of the cross section and to the river. The different discharges at a given cross section vary in frequency, which in turn is a function of the watershed and its hydrologic and physical characteristics.

Under the condition of low discharge represented by the diagram in the upper right corner of Figure 1.12, it is postulated that every point along the river is experiencing a discharge that is small for that point; or, if all points along a river system are experiencing a relatively low discharge, the frequency of the rate of discharge at any one point is about the same as the

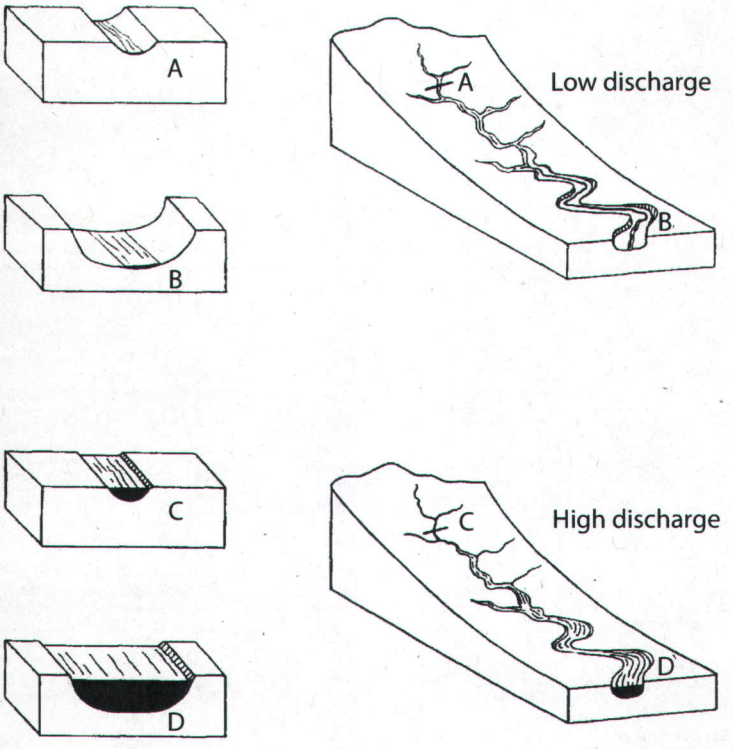

Figure 1.12: Illustration of the hydraulic geometry concept: comparison of different rates of discharge at a given river cross section and at points downstream. Source: *Leopold and Maddock Jr. [1953].*

frequency of the rate at any other point. Of course the rate of discharge, not its frequency, will generally be much greater near the mouth of a river draining a large area than at some headwater point. The same postulation is made for the condition of high discharge, as represented by the diagram in the lower right. The two diagrams of the watershed are introduced to emphasize the points, first, that at a given cross section different discharges have different frequencies; and second, that at cross sections situated at various points along the stream the rates of discharge are usually different from each other. Comparison of the various cross sections along a stream is made under the assumed condition that they are experiencing equal frequency of discharge. To reproduce the effects of the dynamic variations in channel and rill geometry, in the CATHY model the "at-a-station" and "downstream" scaling laws are combined (Appendix D) and incorporated in the diffusion wave model used for surface rounting (Appendix E).

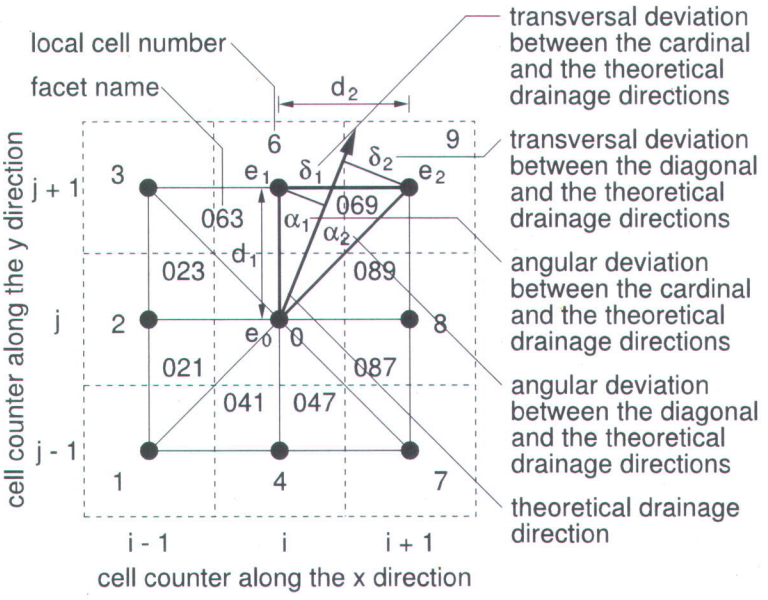

Figure 1.13: Sketch of the elementary computational system used to determine flow directions. Source: *Orlandini et al. [2003]*.

1.3.2 Improvements to the CATHY model pre-processor

In the new version of the model the terrain analysis and drainage network characterization procedure described above has been augmented by newer alternative algorithms, and these various options have been packaged as a pre-processing module for the CATHY model. This pre-processor, written in Fortran 90, includes the D8, D8-LTD, D_∞, and a combination of monodirectional (e.g., D8-LTD) and bidirectional (e.g., D_∞) algorithms, for extracting the drainage network and calculating the upslope drainage areas *[O'Callaghan and Mark, 1984; Marks et al., 1984; Tarboton, 1997; Orlandini et al., 2003; Orlandini and Moretti, 2009]*. The flow directions are calculated by using an elementary computational system based on eight triangular facets formed in a 3 × 3 pixel window centered on the pixel of interest (Figure 1.13). The use of triangular facets avoids the approximation involved in fitting a plane and the influence of higher neighbors on the downslope.

The distinction between hillslope and channel cells is performed by posing threshold values on upstream drainage area A (the approach of *Montgomery and Foufoula-Georgiou [1993]*) or on a function $A\,S^k$, S being the local terrain slope and k an exponent *[Montgomery and Dietrich, 1988, 1989]*, or by using a more elaborate criterion introduced by *Howard [1994]* and based on the gradient divergence normalized by the mean gradient. The procedure based on a constant critical support area assumes that sediment transport on hillslopes (slope dependent) gives rise to convex slopes, whereas sediment transport in channels (discharge and slope dependent)

gives rise to concave slope profiles. Thus, channel sources represent the transition in dominant sediment transport process from a convex longitudinal slope profile (on the hillslopes) to a concave longitudinal slope profile (for channels). The slope-dependent critical support area model assumes that channel heads represent an erosional threshold. This assumption implies that the channel source is the result of a change in sediment transport processes from distributed to concentrated flow, rather than a spatial transition in longitudinal slope profiles. The main differences between the networks defined by the constant and slope-dependent threshold methods is the spatial variability of slope. *Montgomery and Foufoula-Georgiou [1993]* report that with the slope-dependent threshold method, drainage density is greater in steeper portions of the catchment. They also indicate that for the case of a catchment with little spatial variability in slope, the constant and slope-dependent threshold methods converge and predict similar channel networks for the same mean source-area size.

Methods based on the definition of a critical support area are usable for drainage networks within areally uniform topography but are inappropriate for landforms with large areal variation in local relief *[Tribe, 1992]*. To handle these cases, *Howard [1994]* proposed a method based on the values of the normalized (with respect to the average catchment slope) profile curvature K_p which is calculated as:

$$K_p = \frac{z_{xx}z_y^2 + 2z_{xy}z_xz_y + z_{yy}z_x^2}{(z_x^2 + z_y^2)(z_x^2 + z_y^2 + 1)^{3/2}} \tag{1.1}$$

where z_x and z_y are the first-order derivatives of the surface topography that describe the rate of change of elevation with distance along the x and y axes, or the slope in those directions; z_{xx} and z_{yy} are the second-order derivatives that describe the rate of change of the first derivative in the x and y directions, or the curvature in those directions; z_{xy} is a mixed second-order derivative that describes the rate of change of the x derivative in the y direction, or the twisting of the surface. Profile curvature is negative for slope increasing downhill (convex flow profile, typically on upper slopes) and positive for slope decreasing downhill (concave, typically on lower slopes). Thus by posing zero as a threshold value, the heads of channel networks are located where there is a change in the shape of the profile from convex to concave (Figure 1.14).

Amongst the three methods implemented in the pre-processor for the extraction of channel cells, the constant threshold area method appears more practical for hydrological modeling applications, as is evidenced by its widespread use. The current preference for this method can be attributed to the fact that local slope and curvature values require either a high resolution DEM (less than 30 m) or field measurements which are often difficult to obtain.

The hydraulic characterization of the drainage network in the new version of the CATHY model has been improved by applying the "hydraulic concept" to the surface resistance

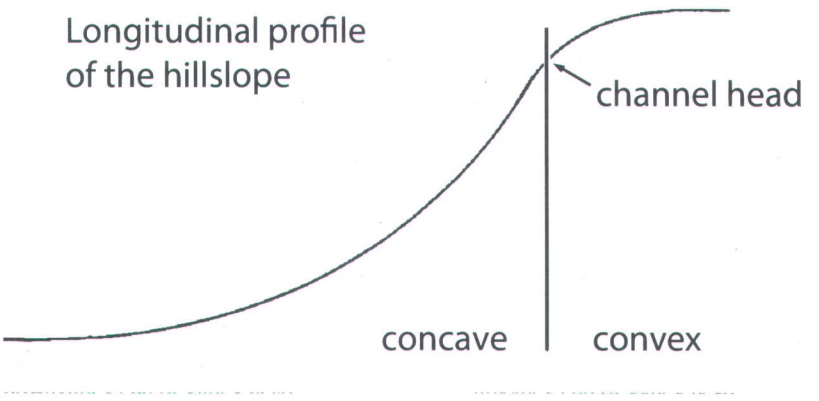

Figure 1.14: Longitudinal section of a hillslope used to show the passage from rill to sheet flow conditions.

coefficient *[Orlandini, 2002]*:

$$k_s(A,Q) = \underbrace{k_s(A_s,Q_f)\,Q_f(A_s)^{-y'}\left(\frac{A}{A_s}\right)^{w(y''-y')}}_{\text{spatial variation}} \overbrace{Q^{y'}}^{\text{temporal variation}} \tag{1.2}$$

where k_S [$L^1/3/T$] is the Gauckler-Strickler coefficient, A_s is the drainage area at a selected site, the exponents y' and y'' are characteristics of the rill/channel network as a whole, w [-] is the exponent of the scaling relationship for the selected frequency discharge Q_f with drainage area A. The roughness coefficients can thus be dynamically varied in space and time. In equation (1.2) the spatial variation term is calculated through the pre-processor, whereas the temporal one is dynamically calculated at each time step of the surface routing module of the CATHY model.

Finally, in the new version of the CATHY model surface runoff propagation has been simplified through the definition of an ordering system based on the descending elevation value of the cells, which allows for a faster and more straightforward processing of the DEM.

1.3.3 Applying the CATHY model pre-processor

Application of the pre-processor is divided into four conceptual steps: *(i)* dimensioning (i.e., definition of the grid spacing, definition of DEM size along the x- and y-directions, and

```
--------------------------------------------------------------------------------
STRUCTURAL PARAMETERS
--------------------------------------------------------------------------------
Grid spacing along the x-direction =                          180.00
Grid spacing along the y-direction =                          180.00
DEM rectangle size along the x-direction =                    180
DEM rectangle size along the y-direction =                    218
Number of cells within the catchment =                      21706
X low left corner coordinate =                            581776.59388597
Y low left corner coordinate =                           4973076.56002260
--------------------------------------------------------------------------------
TERRAIN ANALYSIS PARAMETERS
--------------------------------------------------------------------------------
Depit threshold slope =                                       0.130E-03
Drainage directions method (LAD:1,LTD:2) =                    2
Upstream deviation memory factor (CBM:0,PBM:1) =              0.100E+01
Threshold on the contour curvature (NDM:-1E10;DM:+1E10) =     -0.100E+11
Nondispersive channel flow (0:not-required;1:required) =      0
Channel initiation method (A:1,AS**k:2,ND:3) =                1
Threshold on the support area (A) =                           0.207360000E+07
Threshold on the AS**k function =                           16000.00
Exponent k of the AS**k function =                            2.00
Threshold on the normalized divergence (ND) =                -0.100E-01
Path threshold slope =                                        0.100E-03
Drainage direction of the outlet cell (if necessary...)  =    8
Boundary channel constraction (No:0,Yes:1) =                  0
Coefficient for boundary channel elevation definition =       0.50
Coefficient for outlet cell elevation definition =            0.50
--------------------------------------------------------------------------------
RIVULET NETWORK PARAMETERS (HYDRAULIC GEOMETRY OF THE SINGLE RIVULET)
--------------------------------------------------------------------------------
Rivulet spacing =                                  180.000
Reference drainage area (As_rf) =                   0.1296000000000E+06
Flow discharge (Qsf_rf,w_rf) =                      1.000                 1.000
Water-surface width (Wsf_rf,b1_rf,b2_rf) =          1.000     0.2600      0.500
Resistance coefficient (kSsf_rf,y1_rf,y2_rf) =      0.500     0.000       0.000
Initial flow discharge (Qsi_rf) =                   0.000
--------------------------------------------------------------------------------
CHANNEL NETWORK PARAMETERS
--------------------------------------------------------------------------------
Reference drainage area (As_cf) =                   0.691804800000E+09
Flow discharge (Qsf_cf,w_cf) =                    100.000                 1.000
Water-surface width (Wsf_cf,b1_cf,b2_cf) =         50.000     0.200       0.300
Resistance coefficient (kSsf_cf,y1_cf,y2_cf) =     18.000     0.000       0.000
Initial flow discharge (Qsi_cf) =                   0.000
--------------------------------------------------------------------------------
```

Figure 1.15: Snapshot of the parameter file (*hap.in*) required by the pre-processor.

computation of "active" cells) and georeferencing of the study area; *(ii)* selection of the drainage method for the definition of flow directions; *(iii)* selection of the method for the distinction between hillslope and channel cells; and *(iv)* hydraulic characterization of the drainage network (i.e., implementation of the hydraulic geometry concept to channel and overland flow). The pre-processor, through the definition of the drainage directions, can be also used as a stand-alone tool for identification of the catchment and relative subcatchments of a considered study area.

Two files are needed to accomplish the four steps described above: a raster file (named *dtm_13.val*) containing the DEM of the study area and a text file (named *hap.in*; see an example in Figure 1.15) containing the parameters to perform the terrain analysis. The output from the pre-processing procedure is stored in two binary files (named *basin_b* and

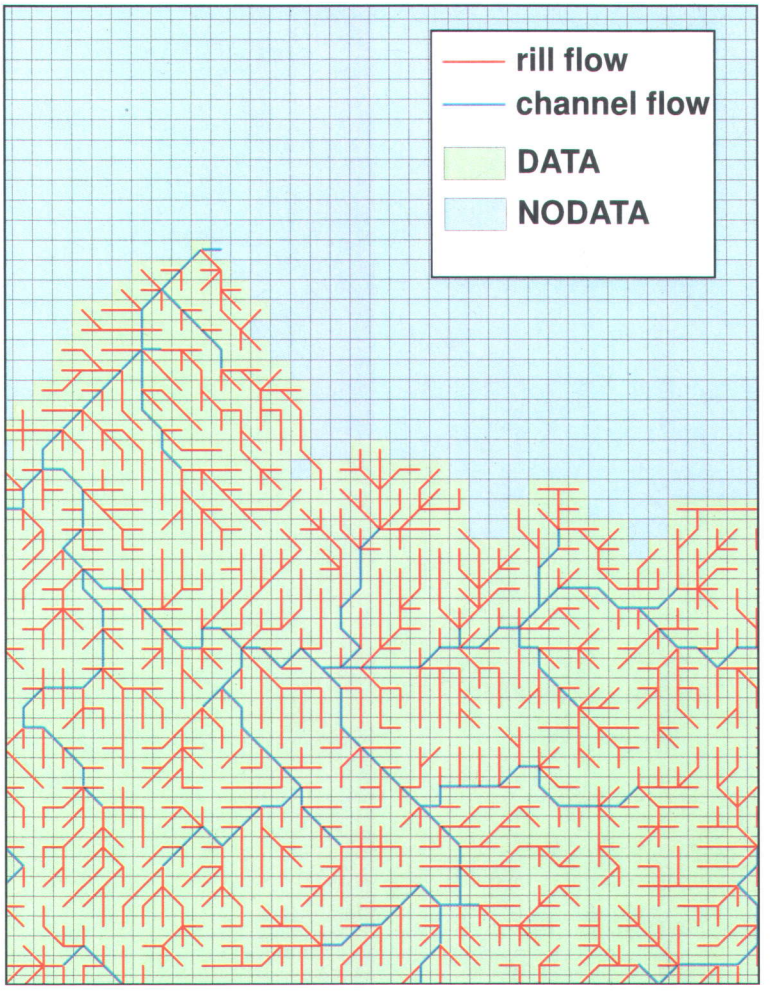

Figure 1.16: Snapshot of a visualization of the vector data produced by the pre-processor.

basin_i) which in turn can be queried to produce both the input files needed by the CATHY model and two vector files (named *cells* and *river_net*) which allow an easy visualization (Figure 1.16) of the terrain analysis results through GIS. The indirect link between the output of the pre-processor and a GIS that facilitates the creation, manipulation, and analysis of the input files prior to conducting model simulations could be further improved by configuring the pre-processor as an internal option of the GIS. An additional future improvement would be to integrate within the suite of programs of the pre-processor those procedures which to date are internally implemented in the CATHY model and which concern the creation of the mesh and the assignment of boundary conditions for the subsurface flow solver.

We present below two examples that illustrate the functionalities of the pre-processor and some of the implications for hydrological modeling of using different options, such as classical D8 vs D8-LTD and D8-LTD vs a hybrid D_∞ for the determination of flow directions. The two examples are based on a simple planar slope and the DEM for a portion of the des Anglais

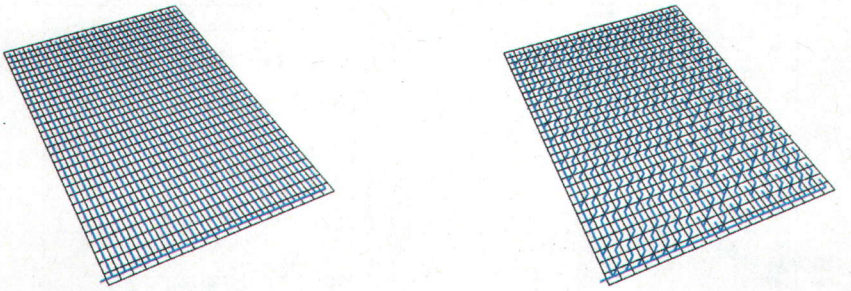

Figure 1.17: Drainage network for the planar slope obtained with the classical D8 (left) and D8-LTD (right) methods. Note that the view angle does not correspond to the real orientation of the planar slope.

river basin.

1.3.3.1 Synthetic drainage system

The earliest and simplest method for specifying drainage directions in grid-based DEMs is to assign a pointer from each cell to one of its eight neighbors, either adjacent or diagonal, in the direction of the steepest downward slope. This method is commonly designated as D8 (eight drainage directions). The main disadvantage of this method is that the drainage direction from each DEM cell is restricted to only eight possibilities, separated by $\pi/4$ rad when square cells are used, whereas in theory it could continuously vary between 0 and 2π. Thus, whenever the steepest drainage direction is not a multiple of $\pi/4$, an error is committed in the determination of the drainage direction from gridded elevation data.

The novelty of the D8-LTD (least transverse deviation) method proposed by *Orlandini et al. [2003]*, and contained in the pre-processor for CATHY, is that the bias arising from selectining a single direction from each DEM cell is reduced by the introduction of cumulative (path-based) deviations (angular and transversal) between selected and theoretical drainage directions. These deviations are accounted for through the definition of a dampening factor (λ) that can assume values varying between 0 and 1 (with 0 if memory is not accounted for, i.e., the classical D8 scheme, and 1 in the case of full memory of the deviations calculated for upstream pre-processed cells).

The planar slope (Figure 1.17) has been generated with an aspect Ψ_{FD} (orientation of the line of steepest descent) of 270.38 degrees clockwise from north and calculated as:

$$\Psi_{FD} = 180 - arctan\left(\frac{z_y}{z_x}\right) + 90\left(\frac{z_x}{|z_x|}\right) \tag{1.3}$$

where z_x and z_y are the derivatives of the topographic surface estimated using centered finite differences. Note that the aspect is an attribute for all the cells of the plane, and that it can be associated to the theoretical (steepest) drainage direction.

The D8 and D8-LTD ($\lambda = 1$) methods are compared by visually examining the synthetic drainage network. As shown in Figure 1.17, the D8-LTD method reproduces the drainage paths significantly better than the classical D8. For instance, it is clear that the drainage paths resulting from the classical D8 appear affected by grid orientation and form patterns characterized by parallel lines, whereas those obtained with the D8-LTD method follow more closely the related surface topography, with a drainage path more in agreement with the aspect feature of the planar slope.

1.3.3.2 Real catchment drainage system

The classical D8 or the D8-LTD allows flow from a cell to only one of the eight nearest neighbors based on the theoretical (steepest) flow direction. Because flow can accumulate into a cell from several upslope cells, but can only flow out into a single cell, these methods can model flow convergence in valleys, but not flow divergence in ridge areas. To overcome this limitation, the pre-processor for CATHY includes a multiple flow directions method denoted as D_∞ *[Tarboton, 1997]*, and a combination of single and multiple flow directions method *[Orlandini and Moretti, 2009]*. In the first method, the flow from a pixel is apportioned between the two downslope pixels according the closeness of the flow angle to the direct angle to that pixel center. In the second method, single or multiple flow directions are selected at each grid cell depending on whether the value of the plan curvature (K_c) exceeds or not a fixed threshold value K_{ct}. For instance, by setting K_{ct} equal to zero, the algorithm selects single flow directions over locally convergent terrains and multiple flow directions over locally divergent terrains.

The plan curvature (K_c) is calculated using the 3×3 subgrid mask sketched in Figure 1.13 as:

$$K_c = \frac{z_{xx} z_y^2 - 2 z_{xy} z_x z_y + z_{yy} z_x^2}{(z_x^2 + z_y^2)^{3/2}} \tag{1.4}$$

where all terms are as defined for equation 1.1. The derivatives are estimated using centered finite differences.

Figure 1.18 shows the upslope area for a portion of the des Anglais river basin calculated using D8-LTD, D_∞-LTD, and a hybrid of these two methods obtained by setting K_c equal to zero. The differences at this scale are quite subtle, but it is possible to see more streakiness associated with the grid from the D8-LTD procedure than with that from the D_∞-LTD and

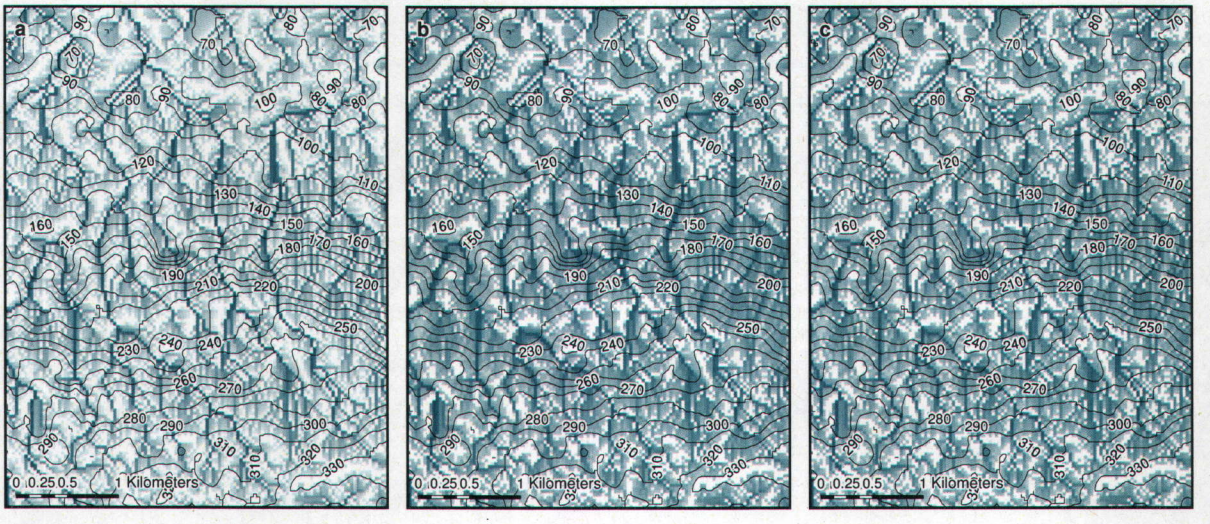

Figure 1.18: Map of a portion of the des Anglais river basin showing logarithmically transformed (base 10) drainage areas contributing to each cell as obtained from (a) the D8-LTD flow direction method, (b) the D_∞-LTD flow direction method, and (c) a hybrid of these two methods obtained by setting the threshold plan curvature (K_c) equal to 0. White cells denote source cells with an upslope drainage area equal to zero. The grid cell size is 30 m; the contour interval is 10 m.

the hybrid combination. The results shown in Figure 1.18 also indicate that multiple flow direction (dispersive) algorithms provide a better spatial pattern of the drainage area than that provided by single flow direction (nondispersive) algorithms, which display numerous source grid cells scattered across the terrain rather than only at ridges and peaks.

Two main issues that have important implications in distributed hydrological modeling arise from application of the different drainage methods. First, it is important that flow directions and consequently upslope drainage area be accurately determined free from grid artifacts, because such values are used in the automatic demarcation of channels relying on the notion of a critical support area, and thus have an impact on the parameterization of the hydrological model. Second, the artificial dispersion inherent in any technique for the delineation of the drainage network should be minimized. This condition is especially important when distributed flow predictions are to be used for modeling solute and sediment propagation.

Chapter 1

Synthèse de recherche

La recherche décrite dans cette thèse vise à mettre en lumière les interactions entre les eaux de surface et souterraines à différentes échelles spatiales et temporelles. Ce premier chapitre fait la synthèse des principaux résultats de recherche, ceux-ci sont ensuite décrits en détail aux chapitres 2, 3, et 4 et ont été soumis, respectivement, aux revues scientifiques suivantes:

- "A comparison of two physics-based numerical models for simulating surface water–groundwater interactions", Mauro Sulis, Steven B. Meyerhoff, Claudio Paniconi, Reed M. Maxwell, Mario Putti, and Stefan J. Kollet, *Adv. Water Resour.*, 33(4), 456–467, 2010

- "Assessment of climate change impacts at the catchment scale with a detailed hydrological model of surface/subsurface interactions, and comparison with a land surface model", Mauro Sulis, Claudio Paniconi, Christine Rivard, Richard Harvey, and Diane Chaumont. *Water Resour. Res.*, resoumis avec "révisions mineures à modérées" en juillet 2010

- "Impact of grid resolution on the integrated and distributed response of a coupled surface–subsurface hydrological model", Mauro Sulis, Claudio Paniconi, and Matteo Camporese, *Hydrol. Process.*, doit être resoumis avec corrections mineures, révisions reçues en août 2010

La première section de cette synthèse présente quelques concepts de base ainsi qu'une revue de littérature des principaux thèmes de la recherche et des questions soulevées. La deuxième section résume les principaux résultats. La troisième et dernière section présente un résumé des travaux de recherche additionnels réalisés au cours du doctorat, qui n'ont pas été présentés

dans les trois articles, dont une description du préprocesseur du modèle hydrologique qui a spécialement été développé pour les besoins de cette recherche.

1.1 Introduction

1.1.1 Interactions entre eaux de surface et eaux souterraines

Les eaux de surface et souterraines ne sont pas des composantes isolées du cycle hydrologique, mais interagissent en réponse aux facteurs topographiques, pédologiques, géologiques et climatiques *[Eagleson, 1978]*. Ces interactions ont été étudiées à la fois à petite échelle (du lit d'un ruisseau au versant d'une colline) *[Harvey and Bencala, 1993; Tonina and Buffington, 2007]* et à grande échelle (d'un bassin hydrographique à l'échelle continentale) *[Levine and Salvucci, 1999; Syed et al., 2005; Günter et al., 2007; Lemieux et al., 2008]*. Ces interactions ont également été explorées en laboratoire au moyen de bacs de sable et par l'intermédiaire d'études détaillées de parcelles sur le terrain *[Abdul and Gillham, 1984; VanderKwaak and Loague, 2001]*. Les diverses questions soulevées par l'étude de ces phénomènes incluent le rôle géomorphologique de l'érosion des eaux souterraines *[Howard and McLane, 1998]*, les stratégies intégrées de gestion de l'eau *[Illangasekare and Morel-Seytoux, 1982]* et l'évaluation de la qualité de l'eau dans un cadre de gestion intégrée *[Bencala, 1984; Castro and Hornberger, 1991]*. Les interactions entre les eaux de surface et souterraines peuvent se produire via un écoulement de sous-surface latéral dans un sol non saturé et par infiltration vers les zones saturées ou par exfiltration à partir de celles-ci. De plus, dans le cas de terrains karstiques ou fracturés, les interactions peuvent se produire dans les canaux de dissolution ou les fractures/fissures. Lors d'un orage, différents mécanismes peuvent provoquer du ruissellement dans différentes parties d'un bassin versant. La réponse du bassin peut être dominée par un seul mécanisme ou par une combinaison de mécanismes, selon l'importance de l'événement pluvial, les conditions antérieures d'humidité du sol et l'hétérogénéité des propriétés hydrauliques du sol *[Beven, 2000b]*. Le ruissellement de surface par excès d'infiltration (mécanisme de saturation de Horton, Figure 1.1(a)-1.1(b)) se produit lorsque l'intensité des précipitations dépasse la capacité d'infiltration du sol. Ce mécanisme peut être dominant dans les zones urbanisées, ainsi que dans celles qui reçoivent typiquement des précipitations de forte intensité et qui sont caractérisées par une couche de faible perméabilité en surface. Le ruissellement de surface par excès de saturation (mécanisme de saturation de Dunne) se produit habituellement dans des secteurs relativement restreints, lorsque le taux de précipitation est inférieur à la conductivité hydraulique saturée du sol, mais que la nappe phréatique atteint la surface du sol. Si la nappe phréatique (et donc la frange capillaire) est proche de la surface du sol, alors seule une petite quantité d'eau supplémentaire est nécessaire pour

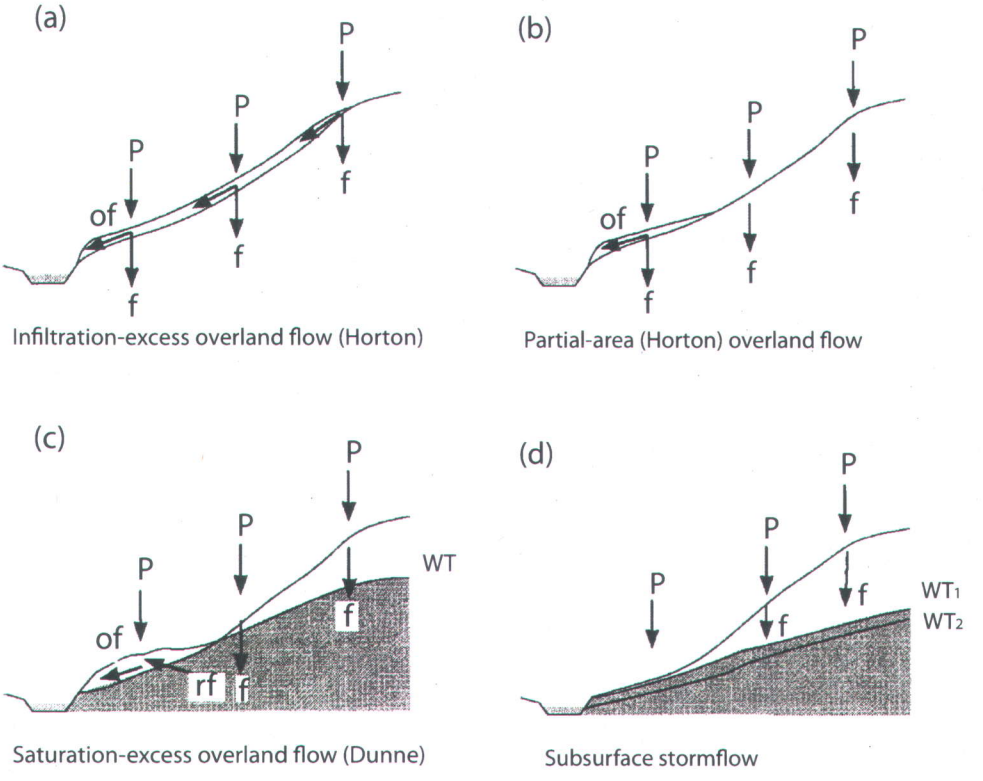

Figure 1.1: Mécanismes de formation du ruissellement. "P" sont les précipitations, "f" l'infiltration, "of" l'écoulement de surface, "rf" le reflux, et "WT" la nappe phréatique. Adapté de *Beven [2000b]*.

saturer complètement le sol. Cet excès d'eau peut faire résurgence en tant qu'écoulement restitué (*return flow*) (Figure 1.1(c)) ou peut également atteindre un cours d'eau suffisamment rapidement pour contribuer directement à la réponse de l'événement (Figure 1.1(d)). Une vue d'ensemble des mécanismes causant le ruissellement dans différents environnements et pouvant être dominants à l'échelle du versant est présentée à la Figure 1.2.

Les échanges entre l'eau souterraine et l'eau de surface dans un réseau hydrographique sont régis par *(i)* les conductivités hydrauliques et leur distribution spatiale, à la fois du lit des cours d'eau et des sédiments de la plaine alluviale; *(ii)* le niveau du cours d'eau et celui de la nappe adjacente; et *(iii)* la géométrie et la position du chenal dans la plaine alluviale *[Woessner, 2000]*. La direction des processus d'échange varie en fonction des charges hydrauliques, tandis que leur vitesse dépend aussi de la conductivité hydraulique des sédiments. Les précipitations et leurs patrons saisonniers modifient la charge hydraulique et induisent de ce fait des changements dans la direction et la vitesse de l'écoulement. Habituellement, on différencie les relations qui peuvent exister entre l'écoulement de surface et souterrain en

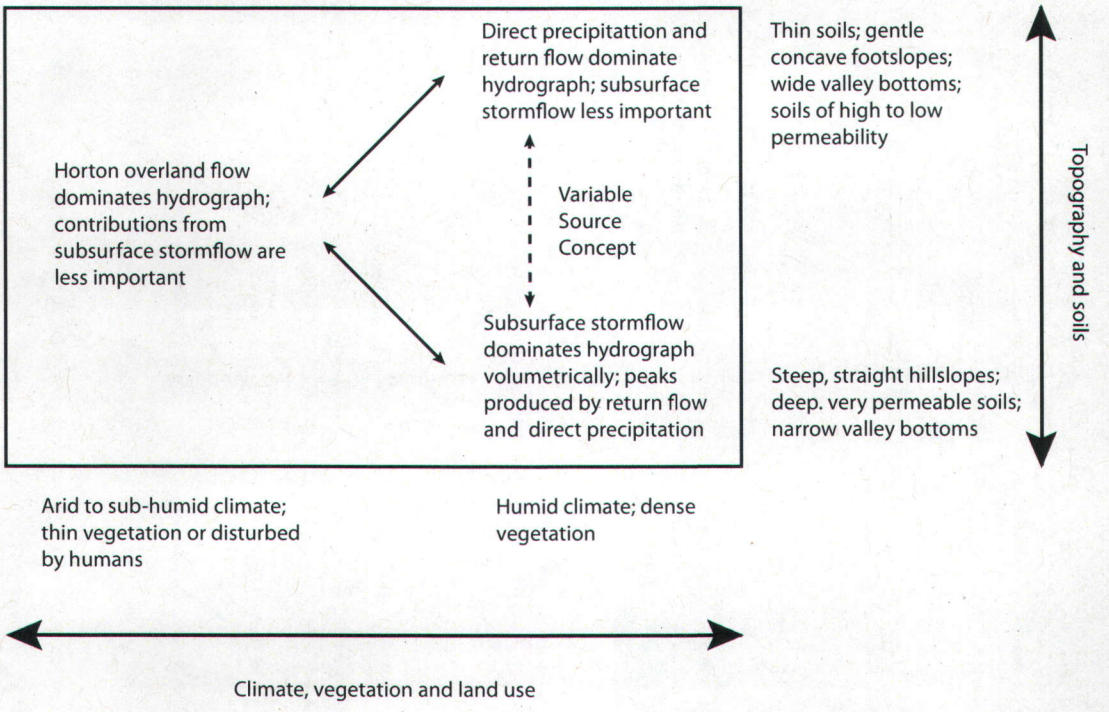

Figure 1.2: Processus dominants dans la réponse des hauts de pente aux précipitations. Adapté de *Dunne [1978]*.

fonction des deux directions nettes d'écoulement: *(i)* la condition affluente, où l'eau de surface contribue à l'écoulement souterrain; et *(ii)* la condition effluente, où l'eau souterraine fait résurgence dans les cours d'eau. Selon cette représentation, les relations cours d'eau–aquifère peuvent être définies comme permanentes, intermittentes, ou éphémères. Dans les cours d'eau permanents, le débit de base est continu tout au long de l'année (Figure 1.3(a)). Ces cours d'eau peuvent également recevoir et perdre simultanément de l'eau souterraine (Figure 1.3(d)). Les cours d'eau intermittents reçoivent de l'eau à certaines périodes de l'année seulement et peuvent donc tour à tour alimenter les nappes et être alimentés par les nappes au cours d'une année (Figure 1.3(a)–1.3(b)). Pour les cours d'eau éphémères, le niveau des eaux souterraines est toujours situé sous le lit. Dans ce cas, les cours d'eau alimentent la nappe lorsqu'ils coulent (Figure 1.3(c)).

Les interactions entre les eaux de surface et souterraines jouent également un rôle critique dans le cycle de l'eau entre la terre et l'atmosphère *[Liang et al., 2003; Gulden et al., 2007; Maxwell et al., 2007]*. À l'exception des déserts, où elles peuvent être profondes et déconnectées de la surface, les nappes sont rechargées au cours des périodes humides et peuvent combler les déficits en eau lors des périodes sèches *[Sophocleous, 2002]*. Ainsi, l'eau souterraine peut influencer la teneur en eau du sol près de la surface et dans la zone racinaire, qui à son tour joue un rôle clé dans la répartissant des précipitations en infiltration,

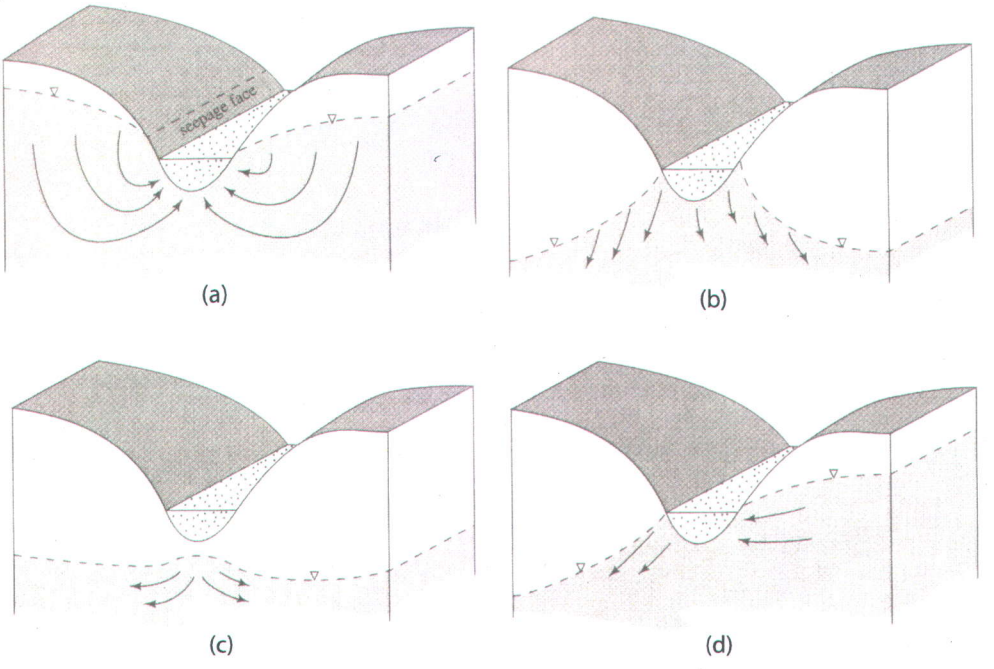

Figure 1.3: Relations cours d'eau–aquifère. (a) Le cours d'eau reçoit de l'eau de l'écoulement souterrain local, intermédiaire, ou régional; (b) le cours d'eau perdant de l'eau est relié à la nappe phréatique; (c) le cours d'eau perdant de l'eau est perché au-dessus de la nappe phréatique; (d) l'eau coule à travers le cours d'eau. Source: *Dingman [2002].*

ruissellement, évapotranspiration et percolation dans la zone non saturée vers l'aquifère. La teneur en eau du sol en surface contrôle également la répartition de l'énergie entre les flux de chaleur sensible et latente à la surface du sol, ce qui influence les mécanismes d'interaction sol–atmosphère *[Brubaker and Entekhabi, 1996; Eltahir, 1998].*

Un sommaire des processus complexes de rétroaction impliqués dans le lien entre les composantes atmosphériques et terrestres du cycle hydrologique est présenté sous forme de diagramme classique de Forrester à la Figure 1.4. Ce diagramme montre la direction de certains mécanismes de rétroaction qui résultent d'un changement dans la teneur en eau des couches de sol en surface. Ainsi, on peut voir que l'humidité du sol et le rayonnement net sont reliés par huit processus rétroactifs, quatre provoquant une rétroaction positive globale et les quatre autres une rétroaction négative. Les directions des flèches présentées dans ce diagramme sont basées sur lès considérations suivantes: *(i)* la relation entre le taux d'humidité du sol et deux propriétés de base de la surface terrestre, l'albédo et le rapport de Bowen (le rapport entre les flux de chaleur sensible et latente); *(ii)* le bilan radiatif de la surface; *(iii)* le bilan énergétique à la frontière terre–atmosphère; *(iv)* le bilan énergétique de la condition frontière atmosphérique; et *(v)* les processus thermodynamiques et dynamiques qui relient

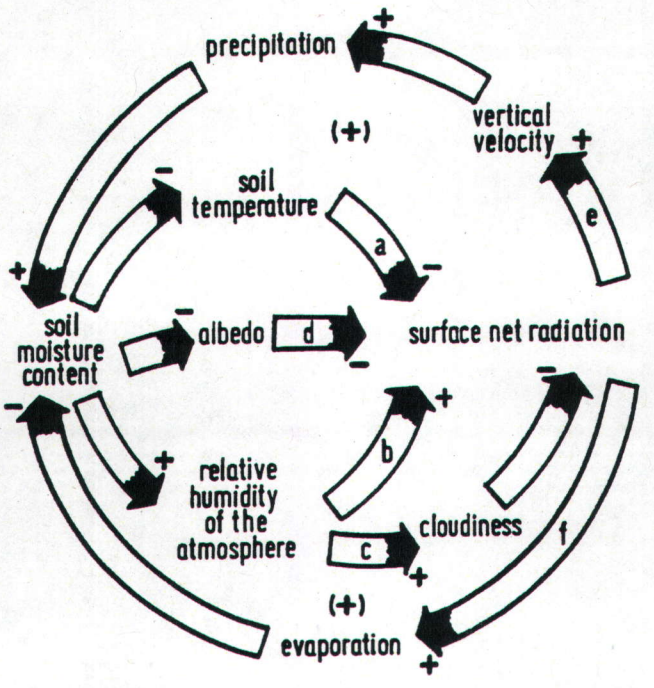

Figure 1.4: Schéma des mécanismes de rétroaction entre la surface terrestre et la couche limite atmosphérique. Source: *Dooge [1989]*.

les conditions de la couche limite et les précipitations subséquentes. Par exemple, les lois de physique suggèrent que l'eau absorbe significativement plus de rayonnement solaire qu'un sol sec. Ainsi, l'albédo est négativement corrélé avec la teneur moyenne en eau du sol. La relation négative entre la teneur en eau du sol et l'albédo implique qu'un taux élevé d'humidité dans le sol aura tendance à faire augmenter le rayonnement solaire net à la surface.

1.1.2 Modélisation des interactions eau de surface / eau souterraine

La reconnaissance de l'influence potentiellement significative des interactions eau souterraine–eau de surfac–atmosphère sur la variabilité spatiale et temporelle du climat a entraîné ces dernières années une augmentation des études portant sur ces interactions en hydrologie, en hydrométéorologie terrestre et dans d'autres domaines. De plus en plus d'attention est portée à l'amélioration de la représentation des processus hydrologiques de sous-surface au sein des modèles eau-végétation–atmosphère (*land surface model*) à grande échelle, allant d'un paramétrisation simple *[Manabe et al., 1965]* à des paramétrisations plus sophistiquées *[Lee and Abriola, 1999; Yeh and Eltahir, 2005; Niu et al., 2007]*. Bien que les chercheurs

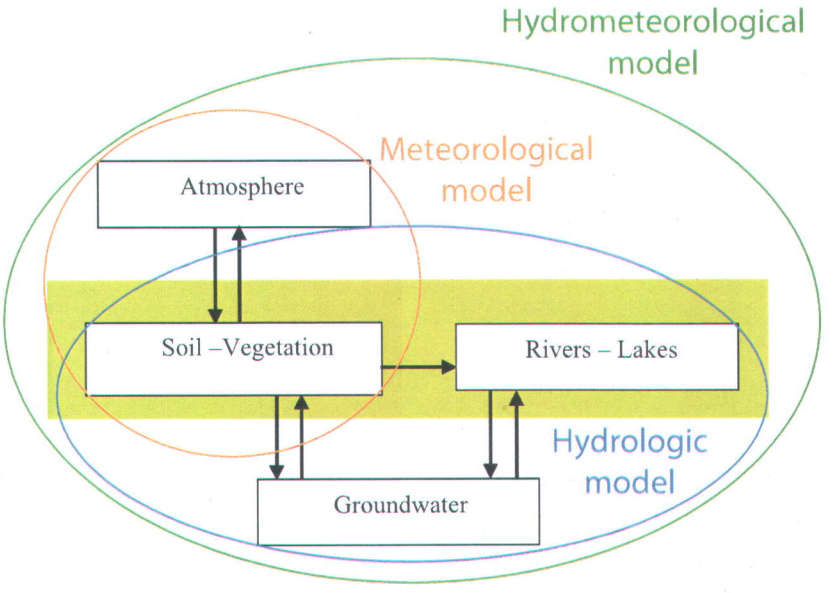

Figure 1.5: Schéma illustrant les différentes communautés de simulation impliquées dans la modélisation des interactions entre l'eau de surface et l'eau souterraine. Adapté de *Miguez-Macho et al. [2007]*.

en sciences de l'atmosphère se soient tournés de plus en plus vers l'hydrologie pour proposer de meilleures paramétrisations terre–atmosphère afin d'améliorer les modèles de climat et la prévision météorologique, les modèles eau-végétation–atmosphère sont encore limités au transport vertical d'humidité dans la colonne de sol et n'incluent pas une représentation adéquate du transport latéral de surface et souterrain causé par les gradients de topographie et/ou d'humidité du sol. Pour leur part, les hydrologues ont concentré leurs efforts sur le développement d'outils de modélisation qui vont des modèles conceptuels globaux *[Crawford and Linsley, 1966; Todini, 1996]* aux modèles détaillés de la physique de l'écoulement de l'eau *[Abbott et al., 1986; Refsgaard and Storm, 1995]*. Le point commun entre ces modèles hydrologiques est une définition simplifiée de la condition limite en surface destinée à représenter les flux d'eau liés aux processus comme l'infiltration et l'évapotranspiration. Ces écoulements sont souvent simplifiés, non couplés et parfois même remplacés par une moyenne dans le temps et l'espace, ce qui ne permet pas de tenir compte de la dynamique des principaux processus de rétroaction entre la surface terrestre et la couche limite atmosphérique décrite précédemment.

L'accroissement de l'intérêt vis-à-vis les changements climatiques et l'étude de leur impact a mis en évidence le besoin d'un paradigme unifié de simulation hydroclimatologique comme celui présenté à la Figure 1.5. Dans cette perspective, la capacité à incorporer différentes

variables et paramètres spatialement distribuées, incluant les données atmosphériques, les propriétés hydrogéologiques, les caractéristiques topographiques, les effets de l'ombre et de l'aspect sur la réponse hydrologique ainsi que celles liées à l'utilisation du sol, permet aux modèles ayant une base physique (*physically-based*) de constituer des outils adéquats pour comprendre les principales influences et rétroactions des nombreuses variables d'état et processus physiques des bilans hydrologique et énergétique.

Dans la classe des modèles à base physique, les approches qui requièrent le plus de temps de calcul utilisent des équations spécifiques pour les premiers mètres de sol afin de décrire l'écoulement superficiel, c.-à-d., une approximation à une ou deux dimensions des équations de Saint-Venant pour l'écoulement en surface ou canalisé, couplée à une composante de l'équation de l'écoulement souterrain à saturation variable en trois-dimensions, c.-à-d. l'équation de Richards *[Freeze, 1972; Sudicky et al., 2000; VanderKwaak and Loague, 2001; Morita and Yen, 2002; Panday and Huyakorn, 2004; Therrien et al., 2004; Kollet and Maxwell, 2006].* D'autres approches plus simples, impliquent des approximations utilisant des moyennes spatiales *[Anderson, 2005; Gunduz and Aral, 2005]* ou des techniques analytiques ou de linéarisation *[Fan and Bras, 1998; Ni and Capart, 2006].*

Les modèles hydrologiques couplés exigent un certain ajustement pour tenir compte des interactions entre la surface terrestre et le sous-sol. Une solution d'intégration des équations de surface et du sous-sol est la technique entièrement implicite de résolution simultanée des deux équations régissant le système et des interactions entre les écoulements. Cette approche a été entre autres proposée par *Panday and Huyakorn [2004]* et *VanderKwaak and Loague [2001].* Une seconde façon de coupler les équations de surface et du sous-sol est de les résoudre séparément et de façon itérative à chaque étape. La convergence de cette solution est obtenue lorsque le terme d'échange atteint une tolérance prescrite. On trouve des exemples de cette approche dans les travaux de *Govindaraju and Kavvas [1991]* et de *Morita and Yen [2002].* Une troisième approche de modélisation couplée a été proposée récemment par *Kollet and Maxwell [2006].* Dans ce dernier cas, les deux équations régissant le système sont couplées directement selon les principes de continuité à la surface du sol, l'équation d'écoulement de surface étant intégrée à celle du sous-sol comme condition aux limites. Le résultat est une approche entièrement intégrée comprenant une seule équation à résoudre à chaque étape.

Les modèles couplés surface–sous-sol diffèrent également dans la manière dont l'écoulement de surface y est représenté. Dans la plupart des modèles, le ruissellement de surface d'un bassin est représenté comme un écoulement en nappe (*sheet flow*). Selon ces modèles, l'eau disponible à la surface est considérée comme étant distribuée uniformément. En supposant une distribution uniforme de l'eau dans les unités de calcul, un couplage numérique simple est possible entre les modèles d'écoulement superficiel et du sous-sol. Cependant, dans la nature, l'écoulement de surface tend à être concentré le long d'un réseau complexe de pe-

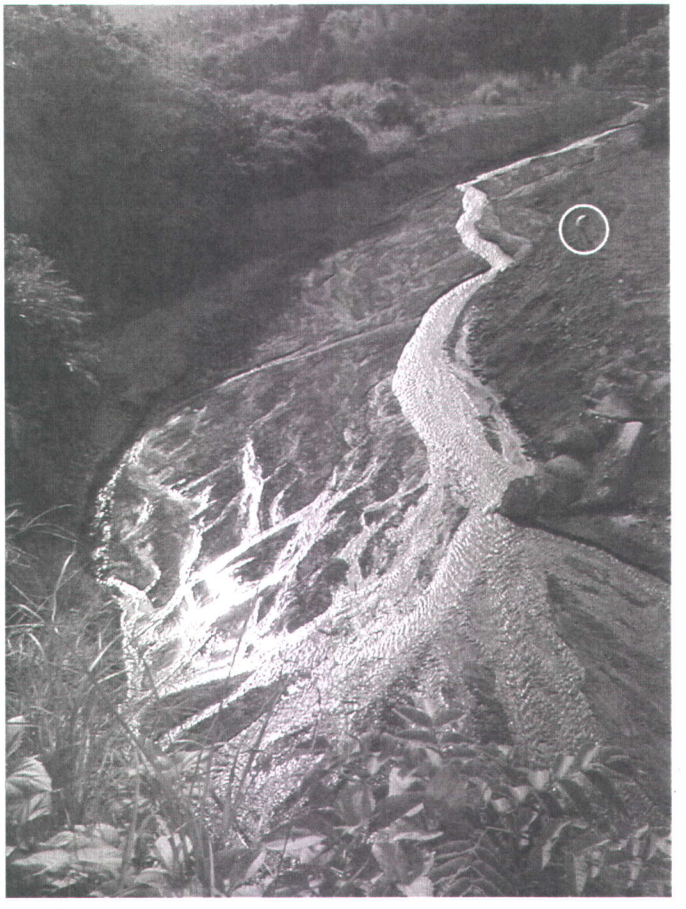

Figure 1.6: Réseau de chenaux et de petits ruisseaux creusés dans un terrain inégal. Source: *Ni and Capart [2006].*

tits ruisseaux et chenaux, tel qu'illustré à la Figure 1.6. Ce réseau se forme en raison des irrégularités topographiques ou des différences d'érodibilité du sol, et il se creuse et s'élargit lors d'événements de ruissellement en fonction de la pente, des caractéristiques du ruissellement et de l'érodibilité du sol *[Emmett, 1978; Li et al., 1980].*

L'importance de la formation de rigoles (*rills* ou *rivulets*) dans les processus d'érosion et dans la dynamique de l'écoulement est maintenant bien connue grâce à plusieurs études expérimentales *[par exemple, Abrahams et al. [1989]; Abrahams and Parsons [1990]; Hairsine and Rose [1992b]; Abrahams et al. [1994]]*. Des exemples de modélisation d'une surface avec rigoles et de la relation entre la géométrie des rigoles et les propriétés hydrologiques sont rapportés dans les travaux de *Moore and Burch [1986]*, *Govindaraju and Kavvas [1992]*, et *Tayfur and Kavvas [1994]*. Cependant, en dépit du fait qu'il soit plus réaliste, l'utilisation du concept de l'écoulement en rigoles (*rill flow*) pour représenter la propagation du ruissellement de surface pose le problème structurel de l'identification des paramètres, c.-à-d., la

correspondance entre la complexité du modèle et la possibilité réelle d'obtenir les paramètres associés lors de relevés de terrain. En effet, il n'existe actuellement aucun bon exemple illustrant comment caractériser un réseau de drainage à l'échelle des versants à partir d'études sur le terrain. Ainsi, d'autres travaux expérimentaux et théoriques doivent être réalisés pour comprendre complètement le phénomène complexe des structures en rigoles sur les versants et pour les quantifier.

1.1.3 Discrétisation, calage et autres questions de modélisation

La disponibilité croissante des données de précipitations distribuées dans l'espace, de données sur les propriétés distribuées des bassins versants, ainsi que des ressources informatiques peu coûteuses encouragent l'utilisation des modèles hydrologiques basés sur la physique pour une vaste gamme d'applications. À la suite de cette augmentation d'activité, il y a également eu un certain nombre de discussions dans la littérature au sujet de questions liées à l'utilisation de tels modèles hydrologiques basés sur la physique *[Beven, 1989, 1993, 2000a; Beven and Binley, 1992; Grayson et al., 1992b; Smith et al., 1994; Abbott, 1996; Loague and VanderKwaak, 2004]*. Les questions soulevées par ces discussions peuvent être résumées comme suit: *(i)* il y a un risque important que la rigueur théorique à la base de ces modèles engendre une croyance dans leurs prédictions qui ne serait pas critique *[Beven, 1989]*; *(ii)* les valeurs des paramètres sont souvent choisies sans tenir compte de leur nature physique et de leur variabilité, considérations essentielles dans le cas de modèles distribués basés sur la physique *[Grayson et al., 1992b]*; *(iii)* leur facilité d'utilisation mène souvent à une évaluation moins critique de leurs limites *[Loague and VanderKwaak, 2004]*. En général, une juste utilisation des modèles physiques exige une attention particulière aux aspects (par exemple, les options de maillage) touchant la résolution numérique des équations différentielles partielles fondamentales décrivant l'écoulement superficiel et souterrain et aux effets d'attribution des paramètres (par exemple, l'unicité) sur la fiabilité de la réponse des modèles.

Il a été démontré par *Ross [1990]* et *El-Kadi and Ling [1993]* qu'il est nécessaire un'équation de Richards avec une résolution verticale fine pour simuler des fronts de mouillage marqués dans les sols initialement secs. *Smirnova et al. [1997]* et *Dam and Feddes [2000]* ont montré de quelle façon le nombre de cellules de la grille verticale et sa taille influencent le calcul de l'humidité du sol et des flux hydrologiques. Pour l'écoulement de surface, les problèmes numériques apparaissent lors de la résolution des équations complètes de Saint-Venant pour étudier le mouvement de l'onde de crue lorsque les amplitudes des différents termes de l'équation de la quantité de mouvement varient considérablement *[Ferrick, 1985]*. En analysant différents types d'ondes, *Ferrick [1985]* a proposé l'utilisation d'équations appropriés pour obtenir des solutions exactes sans faire face aux problèmes numériques et il a argumenté que l'utilisation d'équations plus complètes peut ne pas donner des simulations

plus précises des ondes en rivière pour tous les types d'ondes. Les questions de précision et de stabilité liées à la résolution des équations d'ondes de diffusion par la méthode des différences finies ainsi que la définition des critères pour le choix des algorithmes numériques et des intervalles appropriés d'espace et de temps ont été examinées par *Moussa and Bocquillon [1996a,b]*.

Les études mentionnées précédemment ont décrit de façon exhaustive la précision, la robustesse, et autres éléments de performance des modèles numériques de surface et du sous-sol, mais ne fournissent pas d'aperçu des problèmes numériques découlant du couplage de telles équations à l'échelle du bassin versant. En comparaison avec l'échelle de parcelle de terrain, à l'échelle du bassin versant les effets de facteurs tels que la résolution verticale et horizontale sont compliqués par les caractéristiques topographiques locales prononcées, les divers mécanismes qui causent le ruissellement, les effets des eaux souterraines sur le ruissellement, et les caractéristiques hétérogènes du bassin versant. *Downer and Ogden [2004]* ont réalisé l'une des quelques études rigoureuses en ce sens. Grâce à une étude de convergence spatiale, *Downer and Ogden [2004]* ont identifié la résolution appropriée décrivant correctement la solution avec une efficacité de calcul maximale en utilisant des valeurs physiquement réalistes pour les paramètres. Une des remarques finales de leur travail, cependant, est que la discrétisation appropriée et l'épaisseur de la couche près de la surface dépendent du type d'application et du bassin versant étudié. Ainsi, on n'a pas encore une bonne idée de la robustesse qu'ont les modèles physiques de réponse hydrologique au sujet de questions telles que la résolution spatiale et temporelle, en particulier en ce qui concerne la simulation de la réponse hydrologique distribuée. Cependant, la question d'une discrétisation appropriée est d'importance fondamentale dans le cas où les simulations hydrologiques basées sur la physique doivent fournir une base fiable afin d'étudier les processus physiques pour lesquels la réponse hydrologique distribuée est importante.

Par définition, un modèle physique entièrement distribué ne contient que des paramètres qui peuvent être obtenus par des mesures sur le terrain. Ceci implique qu'en principe, lorsque suffisamment de données sont disponibles, il n'est pas nécessaire de caler le modèle. Cependant, ces modèles sont fréquemment utilisés à des échelles différentes de celle pour laquelle les équations ont été développées et validées. En raison de cette différence dans les échelles, du manque de données et des erreurs de mesure, ces modèles doivent habituellement être calés. Le but du procédé de calage pour les modèles physiques est de trouver un ensemble optimal de valeurs physiquement réalistes pour les paramètres simulant aussi précisément que possible le comportement du bassin *[Sooroshian and Gupta, 1995]*. Pour accomplir cela, des contraintes basées sur la physique doivent être spécifiées pour les valeurs des paramètres sur la base de l'information disponible.

Le calage d'un modèle hydrologique basé sur la physique peut toutefois mener à des résultats

inadéquats. *Refsgaard and Storm [1996]* ont distingué six raisons différentes de cet échec: *(i)* des erreurs aléatoires et/ou systématiques dans les données d'entrée et de calage; *(ii)* des erreurs dues à un ensemble non optimal de paramètres; *(iii)* des erreurs mathématiques dans le modèle en lien avec les bases physiques et mathématiques du code informatique; *(iv)* des erreurs conceptuelles dans le modèle, par exemple, des conditions aux limites incorrectes; *(v)* des erreurs numériques inhérentes à la solution de l'algorithme, par exemple, une dispersion numérique découlant de la discrétisation; et *(vi)* des erreurs d'interprétation des résultats prédits. Ainsi, il est important de distinguer les diverses sources d'incertitude pour ne pas changer les valeurs des paramètres au-delà des limites physiques acceptables dans le but de compenser d'autres sources d'erreur.

Un des attraits supposés des modèles physiques est que, en théorie, les équations régissant le système, les conditions aux limites, et les valeurs des paramètres calées pour un registre hydrologique court devraient s'appliquer à la majorité des conditions hydrologiques, et ce, même au-delà de l'étendue des conditions testées avec succès *[Abbott et al., 1986; Bathurst and O'Connell, 1992]*. La possibilité que la réponse hydrologique puisse également être simulée pour une période de validation en dehors de la période de calage soulève la question de l'unicité (*uniqueness*). La définition de l'unicité *[Neuman, 1973; Carrera and Neuman, 1986]* implique qu'un seul ensemble de valeurs de paramètres puisse être estimé à partir d'un ensemble donné d'observations et que cet ensemble de paramètres doit également être représentatif du comportement observé dans d'autres conditions hydrologiques. Lors de l'utilisation d'un modèle distribué, la réponse hydrologique simulée devrait être comparée aux observations distribuées des variables d'état (state variables) du bassin versant *[Beven, 1989; Grayson et al., 1992a,b]*. Il est important de porter une attention particulière à la réponse distribuée dans le cas d'une simulation basée sur la physique en raison du nombre élevé de degrés de liberté (par exemple, paramètres, conditions aux limites) qui peuvent causer l'équifinalité (*equifinality*) lorsque seule la réponse intégrée (c.-à-d., débit ou concentrations de solutés) est utilisée pour l'évaluation *[par exemple, Beven [1989, 2006]; Ebel and Loague [2006]]*. Une question additionnelle se pose: L'unicité dans la simulation de la réponse intégrée indique-t-elle que l'unicité sera également atteinte pour la réponse distribuée?

En dépit de l'importance d'utiliser à la fois des observations intégrées (par exemple, débit) et distribuées (par exemple, piézométriques, teneur en eau du sol, ou profondeur d'eau à la surface) pour l'évaluation de la réponse hydrologique simulée au cours d'une période de validation, il y a relativement peu d'études qui abordent cette question. *Refsgaard [1997]* a montré que lors d'une application d'un modèle hydrologique basé sur la physique, le débit et la réponse piézométrique se sont avérés non uniques pour une période de validation suivant une période de calage. *Feyen et al. [2000]* ont constaté que le débit à l'exutoire du bassin était simulé correctement au cours d'une période de validation après calage, mais que les débits internes et les niveaux de la nappe phréatique n'étaient pas simulés correctement durant la

période de validation. *Anderton et al. [2002]* ont rapporté que lors de simulations basées sur la physique, les résultats obtenus étaient moins bons au cours de la période de validation suivant une période de calage dans le cas du débit, de la teneur en eau du sol et des niveaux de la nappe phréatique. *Downer and Ogden [2003]* ont examiné le niveau de sophistication requis pour un modèle calé sur l'écoulement observé pour représenter de façon réaliste les processus au niveau des cellules. En utilisant une caractérisation développée à partir de simulations basées sur des événements pour faire une simulation continue à long terme à partir d'un modèle physique, *Heppner et al. [2008]* ont constaté que les composantes du bilan hydrique, le débit de pointe et le transport de sédiment étaient tous simulés correctement alors que les teneurs en eau du sol distribuées ne l'étaient pas.

Les études citées ci-dessus démontrent comment l'application pratique d'un modèle physique à paramètres distribués n'est pas toujours évidente. Cela est attribuable à la difficulté d'obtenir des données de terrain pour la paramétrisation des modèles (écoulement superficiel et souterrain) pour de vastes secteurs, ce qui mène souvent à l'utilisation de valeurs fournies dans la littérature. Une difficulté associée est le manque d'informations détaillées pour intégrer correctement les écoulements internes ou latéraux, ce qui mène souvent à l'utilisation d'un modèle simple dans lequel on suppose qu'il n'y aucun écoulement aux frontières latérales comme condition aux limites. Ces questions sont liées à des thèmes fortement débattus dans la communauté scientifique, comme les effets de la complexité du modèle et de l'attribution des paramètres sur la fiabilité des estimations du modèle, et représentent un défi constant pour les modélisateurs en hydrologie.

Pour donner leur plein potentiel, les modèles physiques distribués requièrent une vaste gamme de mesures des variables d'état et des paramètres distribués, ceux-ci étant difficiles à mesurer et coûteux à obtenir. En raison de ce manque de données, ces modèles ont surtout été utilisés à des fins de recherche afin de formaliser les connaissances sur les systèmes hydrologiques et beaucoup moins comme outils opérationnels d'aide à la décision pour des problèmes hydrologiques réels. Cette situation pourrait toutefois changer dans les années à venir grâce à une plus grande disponibilité des données de télédétection et de senseurs automatisés au sol, et par l'utilisation de techniques avancées basées sur des traceurs géophysiques et environnementaux pour la caractérisation hydrogéologique d'un bassin. L'utilisation de ces techniques pourra ultimement fournir des estimations à grande échelle spatiale et temporelle des variables d'état comme l'humidité du sol *[Leconte et al., 2004; Thoma et al., 2006]*, le débit *[Koblinsky et al., 1993; Bjerklie et al., 2005]*, la couverture de neige et l'équivalent en eau de la neige *[Romanov et al., 2003; Dong et al., 2007]*, et des paramètres des modèles tels que la conductivité hydraulique *[Cook et al., 1996; Dafflon et al., 2009]* et la rugosité de la surface *[Järvelä, 2004; Antonarakis et al., 2009]*. Dans cet effort, un rôle important sera également joué par le développement de plates-formes basées sur des ordinateurs de haute performance en parallèle reliés par des connexions réseau rapides (par exemple, GRID;

[Beven, 2003]) et par l'établissement de consortiums pour augmenter le partage de données hydrologiques (CUAHSI; *[Consortium of Universities for the Advancement of Hydrological Science]*). Ce nouveau cadre devra à son tour consacrer plus d'attention aux méthodes intelligentes pour traiter et intégrer une grande quantité d'information dans les modèles de simulation hydrologique (par exemple, les techniques d'assimilation de données; *[McLaughlin, 2002; Camporese et al., 2009]*), et pour supporter le partage de données entre les différentes plates-formes (par exemple, NetCDF; *[Rew and Davis, 1990]*).

1.1.4 Le modèle CATHY (CATchment HYdrology)

La présente recherche a été réalisée en utilisant le modèle CATHY (CATchment HYdrology), un modèle physique, couplé et distribué spatialement pour les simulations de surface et du sous-sol *[Bixio et al., 2000; Camporese et al., 2010]*. Le modèle est basé sur la résolution séparée et séquentielle de l'équation tridimensionnelle de Richards pour l'écoulement souterrain dans des sols à saturation variable *[Paniconi and Wood, 1993; Paniconi and Putti, 1994]* et sur une approximation de l'onde de diffusion de l'équation de Saint-Venant pour l'écoulement en surface et canalisé *[Orlandini and Rosso, 1996, 1998]*. Les interactions hydrologiques entre les eaux superficielles et souterraines sont prises en charge par un algorithme de permutation automatisé des conditions aux limites agissant sur le terme source/puits de l'équation de l'écoulement souterrain *[Putti and Paniconi, 2004]*. Une description plus détaillée des principaux éléments du modèle (par exemple, la formulation mathématique, l'approche de couplage surface–sous-sol et la conceptualisation du ruissellement de surface) est présentée au Chapitre 2, alors que les aspects traitant spécifiquement des courbes caractéristiques du sol (Annexe A), de la discrétisation numérique des équations de surface et du sous-sol (Annexes B et C) de la paramétrisation de l'équation de l'écoulement de surface (Annexes D et E) et représentation de l'hétérogénéité du bassin versant des Anglais (Annexe F) sont décrits dans les annexes à la fin de la thèse. En outre, l'ensemble des données de simulation a été inclu dans un CD-ROM (Annexe G).

1.2 Résumé des principaux résultats de recherche

L'analyse des interactions entre les eaux de surface et les eaux souterraines a été initialement abordée prenant en considération des cas d'étude simples afin d'illustrer les caractéristiques du modèle CATHY et particulièrment l'algorithme permettant de varier les conditions de frontières, pour une variété de conditions. Ces différentes cas, décrits dans le premier chapitre de la thèse, traitent des différents processus de formation du ruissellement superficiel

(mécanisme de saturation de Dunne et Horton), sur la condition d'écoulement restitué (*return flow*) pendant des épisodes de précipitation et évaporation et sur d'autres processus physiques constituant la réponse hydrologique intégrée du bassin versant. En outre, la simulation des événements pluvieux uniques à l'aide d'une paramétrisation simple, a permis d'évaluer avec justesse l'influence de facteurs tels que la résolution verticale et horizontale, la taille du pas de temps et l'angle de pente sur l'exactitude et le temps de calcul de la réponse du modèle. À ce titre, ces simulations simples ont également été considérées comme un exercice préliminaire à l'application du modèle CATHY, tel que décrit dans le deuxième et troisième chapitre de cette thèse (chapitre 3 et 4), pour un bassin versant réel avec une géométrie et une topographie plus complexes, sous une longue série d'épisodes de précipitation et d'évaporation et avec un temps de calcul coûteux.

1.2.1 Analyse comparative des modèles CATHY et ParFlow (Chapitre 2)

La première partie du travail de recherche a été consacrée à une comparaison entre les modèles CATHY et ParFlow, un modèle couplé présenté par *Kollet and Maxwell [2006]*. Les équations régissant le système dans ParFlow sont l'équation tridimensionnelle de Richards pour l'écoulement souterrain dans des sols à saturation variable et l'approximation d'onde cinématique de l'équation de Saint-Venant pour l'écoulement de surface. En comparaison avec le couplage séquentiel et le procédé de permutation des conditions aux limites utilisés dans CATHY, ParFlow utilise une approche entièrement couplée basée sur une continuité des pressions et des écoulements à la surface pour résoudre les interactions surface–sous-sol. En plus des différentes méthodes de couplage et de résolution des échanges d'écoulement, les deux modèles conceptualisent différemment le routage de surface: écoulement en nappe dans ParFlow; écoulement en rigoles dans CATHY (Figure 1.7). Bien que n'étant pas inhérentes aux questions de couplage, ces différences supplémentaires ont également été considérées dignes d'évaluation étant donné le grand intérêt d'appliquer les modèles hydrologiques couplés aux échelles du bassin versant où les caractéristiques du terrain (pente, rugosité, etc.), et par conséquent les conditions d'écoulement en surface, peuvent varier considérablement.

La comparaison de ces deux modèles très différents a constitué une première occasion de faire un examen critique de certains éléments clés des modèles hydrologiques couplés, mais aussi d'établir un ensemble de cas simples à utiliser comme références pour le développement à venir du modèle CATHY. Ces essais numériques, sur un plan incliné et une aire de captage en V également inclinée, ont permis d'examiner le ruissellement produit par excès de saturation et d'infiltration dans des conditions homogènes et hétérogènes ainsi que la dynamique du processus de reflux décrit précédemment. Le but de ces essais était d'étudier les effets des

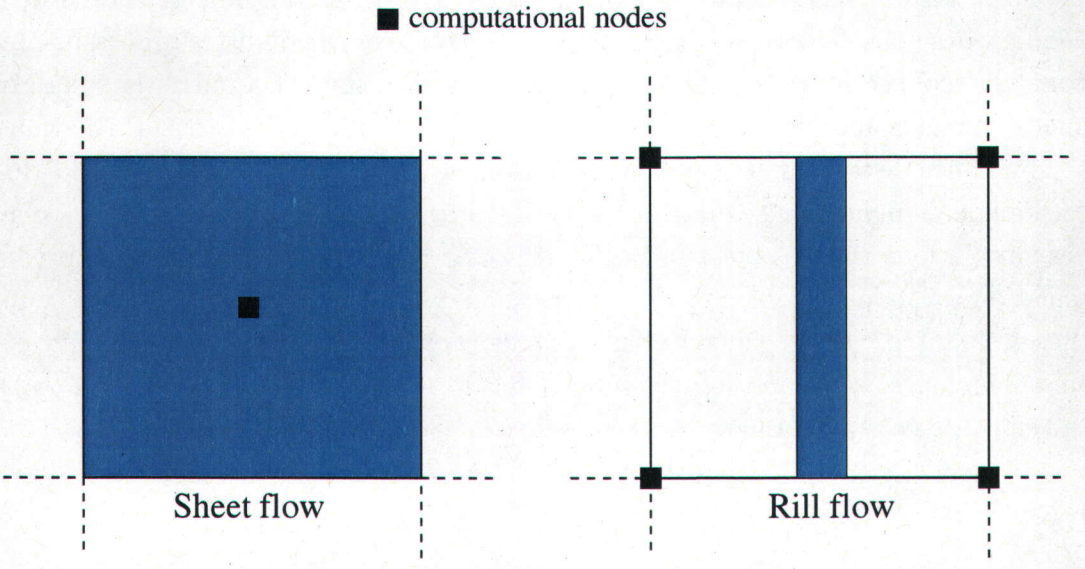

Figure 1.7: Croquis des conceptualisations de l'écoulement de surface intégrées dans ParFlow (gauche) et CATHY (droite).

facteurs tels que la discrétisation par grille (horizontale et verticale), la durée de l'intervalle de temps et l'angle de la pente sur la réponse couplée surface–sous-sol de ces deux modèles.

De façon générale, les tests de simulation pour les deux modèles ont montré une faible sensibilité à la discrétisation verticale et à la durée de l'intervalle de temps dans le cas d'un excès de saturation en conditions homogènes. Dans le cas d'un excès d'infiltration en conditions hétérogènes, une sensibilité plus grande et des différences plus importantes dans la réponse ont été observées, ceci en raison des différentes approches de couplage et méthodes de discrétisation spatiale utilisées (par différences finies dans ParFlow et par éléments finis dans CATHY). En particulier, pour la simulation des mécanismes d'excès de saturation et d'infiltration en conditions hétérogènes, la résolution simultanée des équations de surface et du sous-sol dans ParFlow produit un hydrogramme plus marqué et plus localisé qui est moins influencé par la discrétisation temporelle. Dans CATHY, d'autre part, le procédé de résolution séquentiel implique, par exemple, qu'une fois que la surface devient saturée à certains nœuds localisés (et la condition aux limites pour ces nœuds change de Neumann à Dirichlet), toute l'eau est dirigée vers le bas de la pente pour la durée d'un intervalle de temps, retardant toute possibilité de réinfiltration jusqu'au prochain (sous-sol) intervalle de temps. Ainsi, l'hydrogramme du modèle CATHY apparaît un peu plus tôt que celui de ParFlow et le front de réinfiltration est plus étendu tôt dans la simulation. Dans le cas du comportement de reflux, nous avons trouvé que les modèles étaient généralement en accord, les plus grandes divergences ont été observées dans la phase de récession où les réponses des modèles sont

dominées par le routage de surface et ainsi attribuables aux différentes paramétrisations de la diffusion dans les structures de propagation de l'eau en surface.

L'étude comparative a également examiné les différences dans la réponse hydrologique pour les paramétrisations de l'écoulement en rigoles et en nappe intégrées dans les modèles CATHY et ParFlow, respectivement. Les effets de ces deux conceptualisations étaient accentués pour le débit de décharge et les charges de pression à la surface (*ponding heads*). Les tests de simulation ont montré qu'avec des paramétrisations "équivalentes" d'écoulement en nappe, les modèles CATHY et ParFlow produisent des hydrogrammes très similaires à l'exutoire du bassin et des profils de profondeur d'écoulement comparables. D'autres tests de simulation ont mis en évidence les réponses différentes pour les hydrogrammes et les profils de profondeur d'eau causées par les paramétrisations d'écoulement en rigoles et en nappe dans CATHY (plus accentué dans l'espace et plus rapide dans le cas de la paramétrisation de l'écoulement en rigoles), soulignant les différences dans le potentiel d'érosion et la capacité de transport de sédiments entre les deux conceptualisations.

Un but plus général de cette partie de la recherche était d'encourager des efforts additionnels d'évaluation de modèles couplés surface–sous-sol étant donné la variété de formulations et d'approches proposées récemment pour représenter les interactions de l'écoulement et autres processus. D'autres études comparatives démontrant clairement les différences et les similitudes entre les modèles dans des conditions physiques complexes (en incluant la géométrie et la topographie) et pour des bassins réels seront nécessaires pour pousser plus loin ce travail de recherche et pour créer des cas de référence appropriés.

1.2.2 Évaluation des impacts des changements climatiques à l'échelle du bassin (Chapitre 3)

Dans la deuxième partie de la thèse, les interactions entre les eaux de surface et souterraines on été examinées à plus grande échelle spatiale et temporelle en appliquant le modèle CATHY sur une période de 30 ans afin d'évaluer les impacts des changements climatiques dans un bassin de taille moyenne (690 km^2). Le bassin versant à l'étude est celui de la rivière des Anglais, situé dans le sud-ouest du Québec, qui est un sous-bassin du bassin versant transfrontalier de la rivière Châteauguay (Figure 1.8). L'aspect nouveau de cet objectif de recherche était l'utilisation d'un modèle physique couplé surface–sous-sol pour mettre en évidence le rôle joué par les importantes rétroactions hydrodynamiques entre les zones de la surface, du sol, et de l'eau souterraine. L'utilisation d'un modèle détaillé distribué spatialement comme CATHY nous a également permis de montrer comment l'hétérogénéité locale dans la topographie, les sols et la géologie peut causer des variations spatiotemporelles significatives dans la réponse

d'un bassin aux changements climatiques.

Une étape préliminaire de cet objectif de recherche était le traitement des variables climatiques (précipitation et températures minimale/maximale) générées par le Modèle régional canadien du climat (MRCC) pour un scénario passé (1961-90) et futur (2041-70). Une analyse statistique a été utilisée pour vérifier l'hypothèse nulle d'aucune tendance dans la série chronologique et pour construire le jeu de données de projections du climat futur pour les simulations du modèle hydrologique. L'analyse statistique a été réalisée avec le test de Mann-Kendall sur des valeurs moyennes mensuelles et annuelles. Les résultats de cette analyse ont indiqué une tendance positive significative dans la température (et par conséquent dans l'évapotranspiration potentielle), mais aucune tendance significative dans les précipitations. La tendance positive dans la température était particulièrement forte pour les mois d'hiver et le début de l'été pour le scénario futur. Ces résultats étaient conformes à ceux d'une étude précédente basée sur un jeu de données d'observations pour tout le pays. Pour construire le jeu de données de projections du climat futur pour les simulations du modèle hydrologique, nous avons appliqué une méthode de transfert, celle habituellement utilisée, la méthode de changement delta (*delta change method*), qui consiste à perturber les données météorologiques de base avec des valeurs mensuelles modifiées. Les valeurs mensuelles modifiées ont été calculées par la différence entre les sorties de variables atmosphériques du MRCC pour deux périodes climatiques de 30 ans, une passée et une future.

L'évaluation des impacts des changements climatiques a été effectuée en intégrant dans le modèle hydrologique CATHY les données observées pour 1961-90 (précipitation et température minimale et maximale journalières) pour la simulation passée, et en utilisant ce même jeu de données, mais perturbé selon la méthode de changement delta pour la projection future. L'évaluation a examiné en particulier les impacts sur le débit de la rivière, l'alimentation de l'aquifère et le stockage de l'eau dans le sol près de la surface. Les résultats des simulations ont montré qu'à l'exutoire principal, les impacts des changements climatiques étaient les plus significatifs au cours de la période hivernale maximale en raison de la combinaison de précipitations et températures plus élevées (et par conséquent un ratio plus élevé des pluies par rapport aux chutes de neige) et lors des mois d'été en raison d'une augmentation marquée des températures (et par conséquent de l'évaporation). Les résultats ont également montré des variations spatiotemporelles significatives dans la réponse aux changements climatiques du débit de la rivière dues à une partition différente de l'hydrogramme entre les composantes du ruissellement de surface et du débit de base, ce dernier compensant la diminution marquée du débit durant l'été. L'alimentation en eau de l'aquifère augmente de manière significative durant la saison hivernale grâce à un rapport pluie/neige plus grand causé par des températures plus élevées, tandis que l'alimentation diminue au printemps en raison d'une période de fonte de la neige plus hâtive et moins intense, et au cours de la période estivale, due à une augmentation de l'évaporation. Une analyse spatiale des patrons

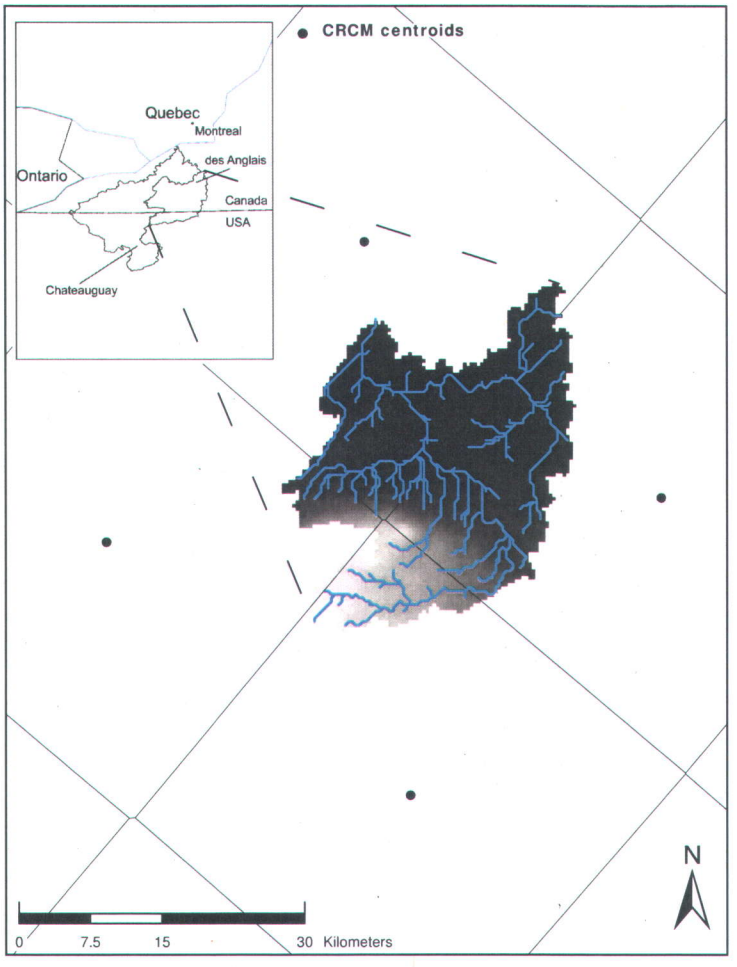

Figure 1.8: Carte du bassin de la rivière des Anglais montrant la localisation des centroïdes de la grille du MRCC.

d'alimentation a montré que l'on s'attend à observer les plus grandes variations tout au long de l'année dans la partie méridionale du bassin, là où les altitudes sont les plus élevées. Cette analyse a également mis en évidence une inversion possible, durant les mois d'été, dans les interactions rivière-eau souterraine en réponse aux déficits de stockage d'eau souterraine.

Comparés au débit des rivières et à l'alimentation des aquifères, les volumes de stockage d'eau sont moins sensibles aux changements climatiques. Les variations de stockage se font le plus sentir près de la surface, qui est directement exposée aux fluctuations de précipitation et d'évapotranspiration, et ces variations diminuent progressivement à mesure que la profondeur du sol augmente. À partir d'une analyse spatiale des variations d'humidité du sol, il a été possible d'observer des patrons d'organisation qui suivent les caractéristiques topographiques et pédologiques du bassin. Par ailleurs, grâce un examen de la relation entre la courbure tangentielle de la surface et les variations de la teneur en eau du sol, effectué pour une

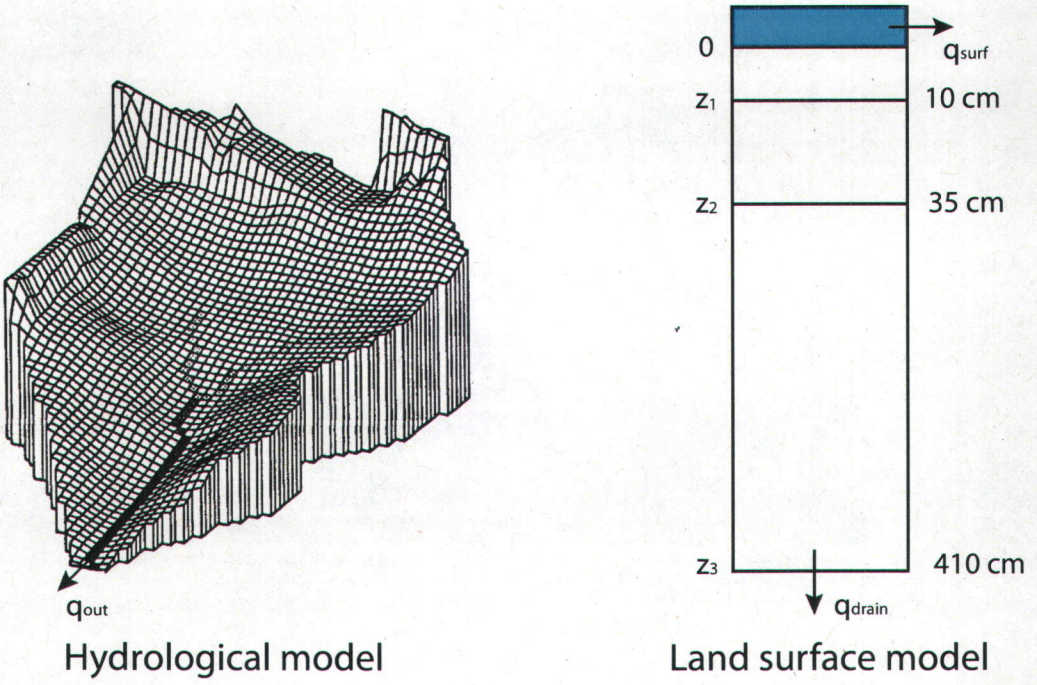

Figure 1.9: Conceptualisation 3D basée sur le MDT et 1D à 3 couches utilisées dans les modèles CATHY et CLASS, respectivement.

section du bassin près de l'exutoire, nous avons constaté que les cellules des versants situées le long des parties convergentes du bassin avaient tendance à subir une augmentation de la teneur en eau du sol en février et mars en réponse aux changements climatiques, et moins de variation vers la fin de l'été et au début de l'automne (août à octobre).

Un objectif additionnel de cette étude était de comparer les prédictions obtenues avec CLASS (*Canadian Land Surface Scheme*), le modèle de la surface terrestre couplé au MRCC, à celles du modèle CATHY pour les projections de changements climatiques passés et futurs. CLASS et CATHY représentent deux classes très différentes de modèles hydrologiques, et cette étude était une première occasion instructive de mettre en lumière certaines de leurs différences principales. Nous avons constaté que CLASS produit des estimations plus élevées que CATHY pour le ruissellement de surface et souterrain durant tout le cycle annuel pour les scénarios passés et futurs, la plus grande différence se produisant au moment du débit de pointe lors de la fonte de la neige. Les facteurs clés contribuant à ces divergences étaient le niveau différent de détails physiques inclus dans les paramétrisations de surface et souterraine (le modèle 1D Green-Ampt *versus* l'équation 3D de Richards) et les différentes résolutions spatiales des deux modèles qui influencent la capacité de modéliser les caractéristiques topographiques impor-

tantes et les hétérogénéités souterraines qui influencent fortement la réponse du bassin (Figure 1.9). Pour le stockage de l'eau dans le sol, CLASS et CATHY se sont révélés généralement en accord en ce qui concerne la variabilité intra-annuelle de la teneur en eau dans les deux premières couches du sol (0-0.10 m et 0.10-0.35 m), en particulier pour la couche supérieure dans laquelle les variations d'eau sont le plus directement influencées par les événements de pluie et par les changements journaliers de température entre les périodes d'orages. Les plus grandes différences entre les deux modèles se sont produites dans la troisième couche (0.35-4.10 m), CATHY prédisant des conditions de sol plus humides pour toute la période de simulation et des fluctuations d'humidité de beaucoup plus faible amplitude. Les causes probables de ce comportement sont une sous-estimation de l'infiltration dans CLASS, combinée à l'absence d'un réservoir sous-jacent d'eau souterraine causant un déficit en eau plus rapide dans la couche inférieure.

1.2.3 Étude des impacts de la grille sur la réponse du modèle CATHY (Chapitre 4)

La troisième partie du travail de recherche a été consacrée à étudier la sensibilité de la réponse hydrologique à la résolution des cellules du modèle altimétrique numérique (*digital elevation model, DEM*), en s'attardant en particulier à l'impact de la discrétisation de la grille sur les facteurs qui régissent la partition et les autres interactions entre l'eau de surface et souterraine. Les effets de la taille de la grille ont été examinés à la fois pour la réponse intégrée (débit à l'exutoire principal et en deux points internes) et distribuée (profondeur de la nappe phréatique, saturation de surface et stockage de l'eau dans sol) du bassin de la rivière des Anglais.

Une étape préliminaire du travail consistait à faire une analyse de terrain basée sur des distributions de fréquence de la pente locale, de la courbure de niveau, de l'aire de drainage, et de l'indice topographique pour des DEM de 180, 360, et 720 m de résolution. Une comparaison des distributions de ces attributs topographiques a permis d'évaluer directement l'influence de la taille de la grille sur la représentation du paysage. Les principaux résultats de cette analyse sont: *(i)* la pente locale diminue systématiquement à mesure que la taille de la grille du DEM augmente; *(ii)* la gamme de courbures de niveau diminue à mesure que la taille de la grille du DEM augmente; *(iii)* une grille de plus grande taille cause un biais en faveur d'aires contributives de plus grande taille; et *(iv)* une grille de plus petite taille cause un déplacement dans la distribution cumulative de l'indice topographique vers des valeurs plus faibles.

Les résultats de la simulation avec CATHY ont montré que les volumes d'eau augmentent

lorsque le DEM devient plus grossier, et qu'un DEM plus grossier est aussi en général plus humide en ce qui a trait à la profondeur de la nappe phréatique et au stockage de l'eau dans le sol. Les causes de ces tendances incluent une augmentation de l'aire totale de drainage du bassin pour un DEM ayant des cellules plus grandes, due à des effets d'agrégation des cellules aux limites du bassin, et une diminution des variations de la pente locale et de la courbure de niveau, qui à son tour limite la capacité du bassin versant à transporter l'eau latéralement et vers le bas de la pente.

Une analyse des volumes d'eau simulés en différents points du bassin a révélé des variations spatiotemporelles significatives dans la sensibilité du débit de la rivière à la résolution du DEM causées par une partition différente entre les composantes du ruissellement de surface et du débit de base de l'hydrogramme, la partie du bassin caractérisée par des sols perméables et une topographie plane étant moins sensible aux effets de la résolution de la grille en raison de la dominance de l'écoulement de surface. Une analyse de l'humidité du sol à la fin d'une période de dix jours de pluie (octobre 2005) et à la fin d'une période sèche de dix jours (août 2003) a démontré que les effets de la résolution de la grille sont moins prononcés au cours des périodes sèches. Ceci parce que les différences dans la teneur en eau du sol au cours des périodes humides sont provoquées par le transport latéral de l'eau, et ce processus est dominé par la courbure de niveau. À l'opposé, l'évaporation est le facteur principal dans la perte d'humidité au cours des périodes sèches et il y a peu de transport latéral, la courbure de niveau joue alors un rôle de moindre importance.

1.3 Recherche supplémentaire

En plus du travail de recherche des 3 chapitres résumés ci-dessus, un certain effort a été également fait afin d'apporter des changements au modèle CATHY dans le but d'améliorer la modularité du modèle et d'ajouter des options de pointe en ce qui a trait à la délinéation du réseau de drainage et à sa caractérisation. Ce travail a été réalisé en extériorisant complètement le préprocesseur basé sur le DEM, une amélioration qui facilite également l'échange d'informations entre le modèle et les systèmes d'information géographique (SIG) tels qu'ArcGIS ou GRASS.

L'analyse de l'impact de la modélisation hydrologique sur de tels modèles, basée sur des simulations numériques et supportée par des données mesurées, est jugée au-delà de la portée de cette thèse. Toutefois, un domaine de simulation semblable à celui utilisé dans le premier article ainsi qu'une partie du MNT du bassin versant réel utilisé dans le deuxième et troisième articles, sont considérés pour illustrer brièvement certaines des améliorations apportées par ce travail de recherche auxiliaire sur la définition du réseau de drainage. Dans

l'application pratique du pré-processeur, telle que décrite dans les articles du deuxième et troisième chapitre de la thèse, le choix parmi les différentes options pour la délimitation et la caractérisation du réseau de drainage a été limité par la résolution du MNT disponible et par le manque des mesures sur le terrain.

1.3.1 Délinéation du réseau de drainage pour le modèle CATHY

Dans la version préalable de CATHY, le réseau de drainage était extrait de façon automatisée à partir d'un DEM en appliquant la méthode D8 (huit directions de drainage) proposée par *O'Callaghan and Mark [1984]* et *Marks et al. [1984]*. L'écoulement de surface se propageait vers l'aval à partir de la cellule la plus élevée du DEM par un réseau conceptuel de chenaux définis par un système de classement où deux nombres étaient attribués à chaque cellule (Figure 1.10): l'ordre de la cellule (OC) et le nombre du lien de la cellule (NL). L'OC est la somme des ordres des cellules voisines supérieures et à partir desquelles la cellule peut recevoir de l'eau (un ordre de 1 est attribué aux cellules sources). Le NL identifie la première cellule de chaque lien dans le système de drainage. Il est égal à l'ordre de la cellule pour la cellule la plus élevée du lien et à zéro pour toutes autres cellules liées. La distinction entre les cellules de versants pour des réseaux en rigoles et en chenaux était basée sur le concept d'"aire critique de support constante" (*constant critical support area*) décrit par *Montgomery and Foufoula-Georgiou [1993]*. Dans cette méthode, on suppose un écoulement en rigoles pour toutes les cellules pour lesquelles l'aire de drainage en amont A ne dépasse pas une valeur seuil constante A_t, alors qu'on suppose un écoulement en chenaux pour toutes les cellules pour lesquelles A égal ou dépasse A_t.

Les procédures d'extraction automatisée du réseau de drainage ne peuvent pas prendre en compte les dépressions topographiques isolées, ou fosses (*pits*). Ainsi, une technique de depitting est utilisée dans le préprocesseur afin de modifier les valeurs d'élévation et de régulariser le DEM. Cette technique est un processus récursif qui soulève les élévations des cellules situées dans des secteurs plats ou affaissés afin de s'assurer de la direction du drainage en fonction d'une faible pente positive (du haut vers le bas) pour toutes les cellules du bassin.

Cependant, lorsque les dépressions jouent un rôle important dans la formation des écoulements de surface et souterrain, le processus de depitting introduit des directions d'écoulement contradictoires et ne reproduit pas correctement les effets de stockage et de retardement des réservoirs et des lacs sur la réponse du bassin. Ceci se produit habituellement dans des secteurs relativement plats où la configuration de l'écoulement est fortement influencée par de petits changements de pente. Une fois les dépressions topographiques localisées (cette tâche peut être effectuée en utilisant des cartes numérisées), une procédure de "suivi des

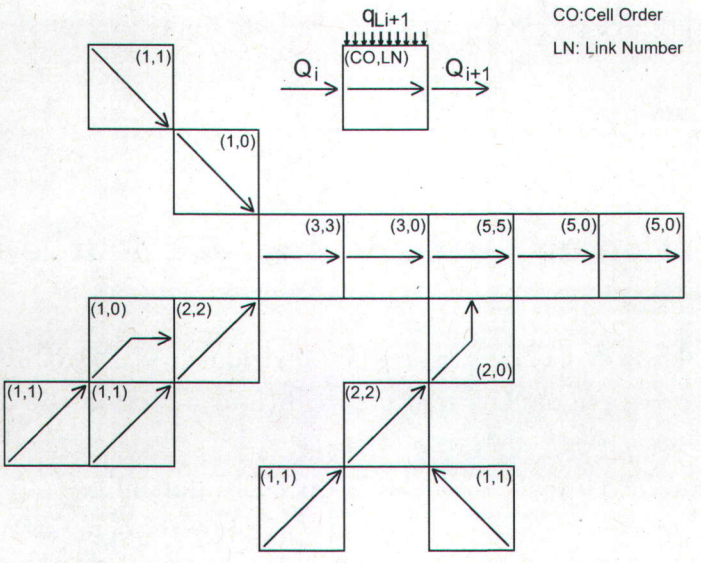

Figure 1.10: Croquis du système de classement du réseau de drainage basé sur le DEM dans la version préalable du modèle CATHY. Source: *Orlandini and Rosso [1998].*

contours du lac" *[Mackay and Band, 1998]* est utilisée pour isoler et corriger les ruptures potentielles dans la subséquente extraction du réseau de drainage. Dans cette procédure, chaque cellule le long des contours de la fosse (aussi appelées "cellules tampons") agit en tant que point de dépression pour toutes les cellules du bassin s'écoulant dans la fosse (Figure 1.11). Pour assurer une circulation adéquate de l'écoulement dans la zone, la direction de drainage de toutes les cellules tampons est forcée de s'écouler dans une seule cellule (cellule exutoire ou "réservoir" du lac). Un algorithme de circulation de l'écoulement, combiné à une procédure de correction basée sur une "tolérance de pente" pour tenir compte des dépressions erronées restantes, est ensuite appliqué au DEM modifié qui exclut les cellules centrales de la dépression. Les effets de stockage et de retardement de la fosse sont pris en compte en transférant avec une vitesse infinie toute l'eau drainée par les cellules tampons vers la cellule exutoire du lac, qui est maintenant traitée comme un réservoir. Dans la présente version du préprocesseur, les dépressions topographiques sont identifiées "manuellement" à partir de l'analyse du DEM. Une procédure d'identification automatisée est envisagée dans les améliorations à venir pour le préprocesseur.

La caractérisation hydraulique du réseau de drainage a été réalisée en appliquant le concept de "géométrie hydraulique" *[Leopold and Maddock Jr., 1953].* Cette expression réfère aux relations entre la forme moyenne du chenal d'un cours d'eau et le débit moyen tous deux "en une station" (*at-a-station*) et "dans une direction aval" (*downstream*) le long du réseau d'un cours d'eau. La forme du chenal inclut la géométrie moyenne en coupe (par exemple,

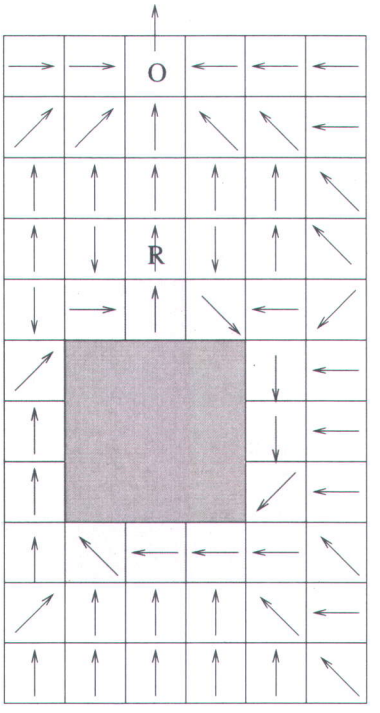

Figure 1.11: Trajectoires d'écoulement de surface des cellules d'un cas représentatif d'un petit bassin contenant un lac. La zone intérieure de la dépression est en gris foncé et les cellules tampons avec des directions forcées d'écoulement en gris pâle. La cellule réservoir est identifiée par "R" et la cellule exutoire par "O". Source: *Paniconi et al. [2003]*

la largeur) et les variables hydrauliques qui incluent les moyennes de la pente, de la friction, et de la vitesse pour un afflux donné d'eau. L'expression "en une station" est employée pour signifier en une section transversale donnée, et l'expression "dans une direction aval" se rapporte aux sections transversales situées sur la longueur d'un cours d'eau.

Dans un but descriptif, les coupes transversales A et B dans la Figure 1.12 représentent deux points sur une rivière de faible débit, alors que C et D sont les mêmes coupes pour un débit plus élevé. La relation entre ces sections et l'ensemble de la rivière et du bassin versant est montrée à droite, pour un débit faible (A et B) et fort (C et D). Ces diagrammes illustrent le concept que dit que la largeur et la profondeur du chenal augmentent avec l'augmentation du débit pour une section transversale de rivière donnée. Les variations du débit suivent un patron temporel qui dépend de la position de la section transversale et de la rivière. Les différents débits en une section transversale donnée varient en fréquence, qui à son tour est fonction du bassin versant et de ses caractéristiques hydrologiques et physiques.

Dans le cas d'un faible débit tel que présenté dans le schéma supérieur droit de la Figure

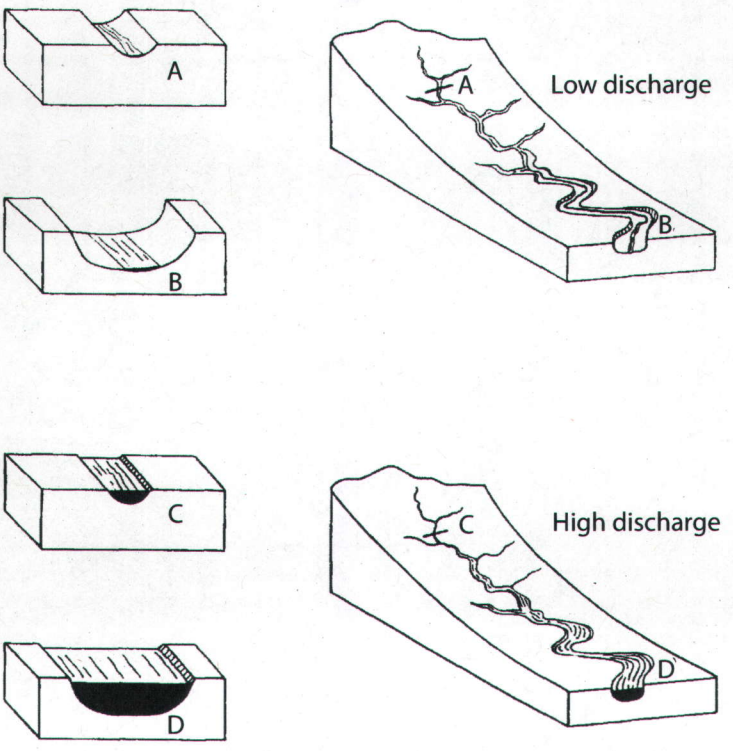

Figure 1.12: Illustration du concept de géométrie hydraulique: comparaison des différents débits d'une section transversale donnée d'une rivière et de points en aval. Source: *Leopold and Maddock Jr. [1953].*

1.12, on postule qu'en chaque point le long de la rivière, le débit est faible pour ce point; ou, si tous les points le long d'une rivière ont un débit relativement faible, la fréquence du débit en n'importe quel point est à peu près similaire à celle de n'importe quel autre point. Naturellement le débit, et non sa fréquence, sera généralement beaucoup plus fort près de l'embouchure d'une rivière drainant de vastes secteurs qu'en un certain point plus près de la tête de la rivière. Le même postulat est fait pour la condition de fort débit, tel que présenté dans le schéma inférieur droit.

Les deux schémas du bassin versant sont présentés pour mettre en évidence deux éléments, le premier étant que pour une section transversale donnée, les différents débits ont différentes fréquences; et le second, que les débits des sections transversales situées en divers points le long du cours d'eau sont habituellement différents. On compare les diverses sections transversales le long d'un cours d'eau en supposant qu'elles ont les mêmes fréquences de débit. Dans le modèle CATHY, pour reproduire les effets des variations dynamiques de la géométrie du chenal et des rigoles, les lois d'échelle "en une station" et "dans une direction aval" sont combinées (Annexe D) et intégrées dans le modèle d'onde de diffusion utilisé pour

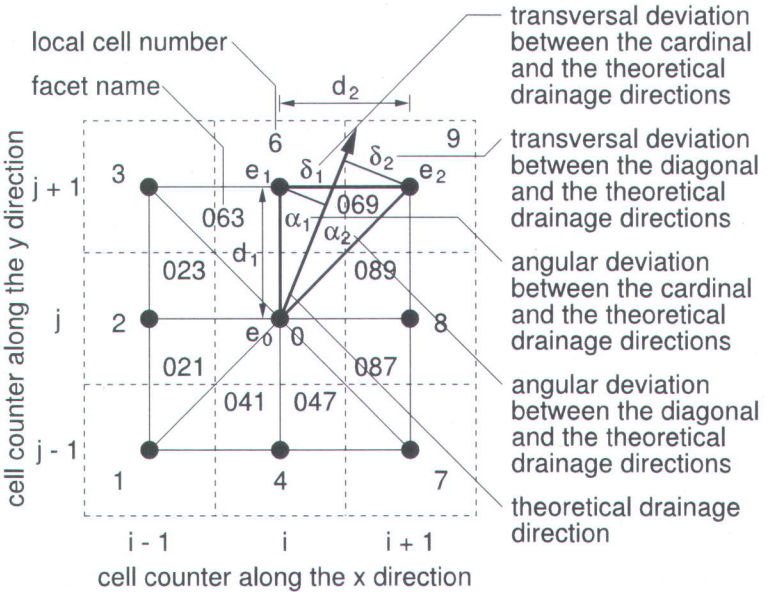

Figure 1.13: Croquis du système informatique élémentaire utilisé pour déterminer les directions d'écoulement. Source: *Orlandini et al. [2003]*.

le routage de surface (Annexe E).

1.3.2 Améliorations au préprocesseur du modèle CATHY

Dans la nouvelle version du modèle, la procédure d'analyse de terrain et de caractérisation du réseau de drainage décrite ci-dessus a été bonifiée par l'ajout de nouveaux algorithmes alternatifs, et ces diverses options ont été intégrées comme module de prétraitement dans le modèle CATHY. Ce préprocesseur, écrit en Fortran 90, inclut les D8, D8-LTD, D_∞, et une combinaison d'algorithmes monodirectionnels (par exemple, D8-LTD) et bidirectionnels (par exemple, D_∞) pour extraire le réseau de drainage et calculer les aires de drainage du haut des pentes *[O'Callaghan and Mark, 1984; Marks et al., 1984; Tarboton, 1997; Orlandini et al., 2003; Orlandini and Moretti, 2009]*. Les directions d'écoulement sont calculées en utilisant un système informatique élémentaire basé sur huit facettes triangulaires formées par une fenêtre de 3 × 3 pixels centrée sur le pixel d'intérêt (Figure 1.13). L'utilisation de facettes triangulaires évite l'approximation d'adaptation d'un plan et l'influence des voisins plus élevés sur le bas de la pente.

La distinction entre les cellules de versant et de chenal est faite en utilisant des valeurs seuils pour l'aire de drainage en amont A (l'approche de *Montgomery and Foufoula-Georgiou [1993]*) ou pour une fonction $A\,S^k$, où S est la pente locale du terrain et k un exposant *[Mont-*

gomery and Dietrich, 1988, 1989], ou en utilisant un critère plus élaboré, présenté par *Howard [1994]*, basé sur la divergence du gradient normalisée par le gradient moyen. La procédure basée sur une aire critique de support constante suppose que le transport de sédiments sur les versants (dépendant de la pente) produit des pentes convexes, tandis que le transport de sédiments dans des chenaux (dépendant du débit et de la pente) produit des profils concaves de pente. Ainsi, les sources du chenal représentent une transition dans le processus dominant de transport de sédiments entre un profil longitudinal de pente convexe (sur les versants) et un profil longitudinal concave (pour les chenaux). Le modèle d'aire critique de support dépendant de la pente suppose que les têtes de chenaux représentent un seuil érosionnel. Cette supposition implique que la source du chenal est le résultat d'un changement de processus de transport de sédiments entre un écoulement distribué et concentré, plutôt qu'une transition spatiale dans les profils longitudinaux de pente. La principale différence entre les réseaux définis par les méthodes constante et d'un seuil dépendant de la pente est la variabilité spatiale de la pente. *Montgomery and Foufoula-Georgiou [1993]* rapportent qu'avec la méthode d'un seuil dépendant de la pente, la densité de drainage est plus forte dans les parties plus raides du bassin. Ils indiquent également que dans le cas d'un bassin avec peu de variabilité spatiale dans la pente, les méthodes constante et d'un seuil dépendant de la pente convergent et prédisent des réseaux de chenaux similaires pour une aire contributive source de même taille moyenne.

Les méthodes basées sur la définition d'une aire critique de support sont utilisables pour des réseaux de drainage dont la topographie est uniforme mais sont inadéquates pour des paysages possédant une grande variabilité de relief local *[Tribe, 1992]*. Pour traiter ces cas, *Howard [1994]* a proposé une méthode basée sur les valeurs normalisées (en ce qui concerne la pente moyenne du bassin) de la courbure du profil K_p calculé comme suit:

$$K_p = \frac{z_{xx}z_y^2 + 2z_{xy}z_x z_y + z_{yy}z_x^2}{(z_x^2 + z_y^2)(z_x^2 + z_y^2 + 1)^{3/2}} \tag{1.1}$$

où z_x et z_y sont les dérivées de premier ordre de la topographie de surface décrivant le taux de variation de l'élévation avec la distance le long des axes x et y, ou la pente dans ces deux directions; z_{xx} et z_{yy} sont les dérivées de second ordre décrivant le taux de variation de la première dérivée dans les directions de x et de y, ou la courbure dans ces deux directions; z_{xy} est une dérivée mixte de second ordre décrivant le taux de variation de la dérivée de x dans la direction de y, ou la déformation de la surface. La courbure du profil est négative pour une pente augmentant vers le bas (profil d'écoulement convexe, typique du haut des pentes) et positif pour une pente diminuant vers le bas (concave, typique du bas des pentes). Ainsi, en utilisant zéro comme valeur seuil, les têtes des réseaux de chenaux sont localisées là où il y a un changement de profil de convexe à concave (Figure 1.14).

Parmi les trois méthodes intégrées dans le préprocesseur pour l'extraction des cellules du chenal, la méthode de l'aire constante de seuil semble plus pratique pour les applications

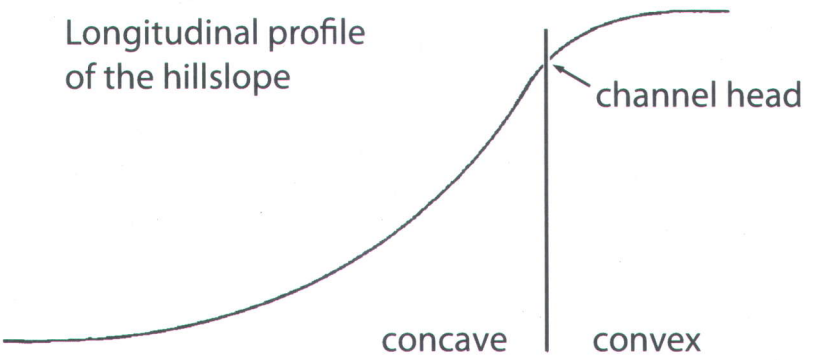

Figure 1.14: Section longitudinale d'une pente montrant la transition entre des conditions d'écoulement en rigoles et en nappe.

de modélisation hydrologique, comme le démontre son utilisation répandue. La présente préférence pour cette méthode peut être attribuée au fait qu'obtenir des valeurs locales de pente et de courbure exigent soit un DEM de haute résolution (moins de 30 m) ou des mesures sur le terrain qui sont souvent difficiles à réaliser.

La caractérisation hydraulique du réseau de drainage dans la nouvelle version du modèle CATHY a été améliorée en appliquant le "concept hydraulique" au coefficient de résistance de surface *[Orlandini, 2002]*:

$$k_s(A,Q) = \underbrace{k_s(A_s,Q_f)\,Q_f(A_s)^{-y'}\left(\frac{A}{A_s}\right)^{w(y''-y')}}_{\text{variation spatiale}} \overbrace{Q^{y'}}^{\text{variation temporelle}} \tag{1.2}$$

où k_S [$L^1/3/T$] est le coefficient de Gauckler-Strickler, A_s est l'aire de drainage en un site choisi, les exposants y' et y'' sont caractéristiques du réseau rigoles/chenal dans son ensemble, et w [-] est l'exposant de la relation d'échelle de la fréquence de débit sélectionnée Q_f pour l'aire de drainage A. Les coefficients de rugosité peuvent varier de façon dynamique dans l'espace et dans le temps. Dans l'équation (1.2) le terme pour la variation spatiale est calculé par le préprocesseur, tandis que celui pour la variation temporelle est calculé de façon dynamique à chaque intervalle de temps du module de routage de surface du modèle CATHY.

En conclusion, dans la nouvelle version du modèle CATHY, la propagation du ruissellement de surface a été simplifiée par la définition d'un système de classement basé sur la valeur de

```
--------------------------------------------------------------------------------
STRUCTURAL PARAMETERS
--------------------------------------------------------------------------------
Grid spacing along the x-direction =                          180.00
Grid spacing along the y-direction =                          180.00
DEM rectangle size along the x-direction =                    180
DEM rectangle size along the y-direction =                    218
Number of cells within the catchment =                      21706
X low left corner coordinate =                            581776.59388597
Y low left corner coordinate =                           4973076.56002260
--------------------------------------------------------------------------------
TERRAIN ANALYSIS PARAMETERS
--------------------------------------------------------------------------------
Depit threshold slope =                                       0.130E-03
Drainage directions method (LAD:1,LTD:2) =                    2
Upstream deviation memory factor (CBM:0,PBM:1) =              0.100E+01
Threshold on the contour curvature (NDM:-1E10;DM:+1E10) =     -0.100E+11
Nondispersive channel flow (0:not-required;1:required) =      0
Channel initiation method (A:1,AS**k:2,ND:3) =                1
Threshold on the support area (A) =                           0.207360000E+07
Threshold on the AS**k function =                           16000.00
Exponent k of the AS**k function =                            2.00
Threshold on the normalized divergence (ND) =                -0.100E-01
Path threshold slope =                                        0.100E-03
Drainage direction of the outlet cell (if necessary...)  =    8
Boundary channel constraction (No:0,Yes:1) =                  0
Coefficient for boundary channel elevation definition =       0.50
Coefficient for outlet cell elevation definition =            0.50
--------------------------------------------------------------------------------
RIVULET NETWORK PARAMETERS (HYDRAULIC GEOMETRY OF THE SINGLE RIVULET)
--------------------------------------------------------------------------------
Rivulet spacing =                                  180.000
Reference drainage area (As_rf) =                   0.1296000000000E+06
Flow discharge (Qsf_rf,w_rf) =                      1.000                 1.000
Water-surface width (Wsf_rf,b1_rf,b2_rf) =          1.000     0.2600      0.500
Resistance coefficient (kSsf_rf,y1_rf,y2_rf) =      0.500     0.000       0.000
Initial flow discharge (Qsi_rf) =                   0.000
--------------------------------------------------------------------------------
CHANNEL NETWORK PARAMETERS
--------------------------------------------------------------------------------
Reference drainage area (As_cf) =                   0.691804800000E+09
Flow discharge (Qsf_cf,w_cf) =                    100.000                 1.000
Water-surface width (Wsf_cf,b1_cf,b2_cf) =         50.000     0.200       0.300
Resistance coefficient (kSsf_cf,y1_cf,y2_cf) =     18.000     0.000       0.000
Initial flow discharge (Qsi_cf) =                   0.000
--------------------------------------------------------------------------------
```

Figure 1.15: Instantané du fichier de paramètres (*hap.in*) requis par le préprocesseur.

diminution de l'élévation des cellules, ce qui permet un traitement plus rapide et plus facile du DEM.

1.3.3 Application du préprocesseur du modèle CATHY

L'application du préprocesseur est divisée en quatre étapes conceptuelles: *(i)* calcul des dimensions (c.-à-d., définition de l'espacement de la grille, définition de taille du DEM dans les direction x et y, et calcul des cellules "actives") et géoréférencement de l'aire d'étude; *(ii)* choix de la méthode de drainage pour la définition des directions d'écoulement; *(iii)* choix de la méthode pour distinguer entre les cellules de versant et de chenal; et *(iv)* caractérisation hydraulique du réseau de drainage (c.-à-d., application du concept de géométrie hydraulique

à l'écoulement canalisé et en surface). Le préprocesseur, par la définition des directions de drainage, peut également être utilisé comme outil autonome pour l'identification du bassin et des sous-bassins de l'aire d'étude considérée.

Deux fichiers sont nécessaires pour accomplir les quatre étapes décrites ci-dessus: un fichier matriciel (appelé *dtm 13.val*) contenant le DEM de l'aire d'étude et un fichier texte (appelé *hap.in*; voir un exemple à la Figure 1.15) contenant les paramètres pour réaliser l'analyse de terrain. La sortie du préprocesseur est contenue dans des deux fichiers binaires (appelés *basin_b* et *basin_i*) qui à leur tour peuvent être interrogés pour produire les fichiers d'entrée requis par le modèle CATHY et deux fichiers vectoriels (appelés cells et river net) qui permettent une visualisation facile (Figure 1.16) des résultats de l'analyse de terrain. Le lien indirect entre la sortie du préprocesseur et le SIG qui facilite la création, manipulation, et analyse des fichiers d'entrée avant d'exécuter les simulations du modèle pourrait être encore amélioré en configurant le préprocesseur comme une option interne du SIG. Une amélioration additionnelle serait d'intégrer dans la suite des programmes du préprocesseur les procédures qui jusqu'à maintenant sont intégrées à l'intérieur du modèle CATHY et qui concernent la création du maillage et l'attribution des conditions aux limites pour l'écoulement souterrain.

Nous présentons ci-dessous deux exemples qui illustrent les fonctionnalités du préprocesseur et de certaines des implications pour la modélisation hydrologique d'utiliser les différentes options, telles que D8 standard versus D8-LTD et D8-LTD versus D_∞ hybride pour déterminer les directions d'écoulement. Ces deux exemples sont basés sur un plan incliné simple et le DEM d'une partie du bassin de la rivière des Anglais.

1.3.3.1 Système de drainage synthétique

La méthode la plus simple utilisée pour spécifier les directions de drainage dans les DEM basés sur une grille est d'attribuer à chaque cellule un pointeur vers une de ses huit voisines, adjacentes ou diagonales, dans la direction de la plus forte pente descendante. Cette méthode est généralement appelée D8 (huit directions de drainage). L'inconvénient principal de cette méthode est que la direction de drainage de chaque cellule du DEM est limitée à seulement huit possibilités, séparées par $\pi/4$ rad lorsque des cellules carrées sont utilisées, alors qu'en théorie la direction pourrait varier sans interruption entre 0 et 2π. Ainsi, toutes les fois que la direction de drainage la plus raide n'est pas un multiple de $\pi/4$, une erreur est introduite dans la détermination de la direction de drainage des données d'élévation de la grille.

La nouveauté de la méthode D8-LTD (least transverse deviation) proposée par *Orlandini et al. [2003]*, et contenue dans le préprocesseur de CATHY, est que le biais résultant de

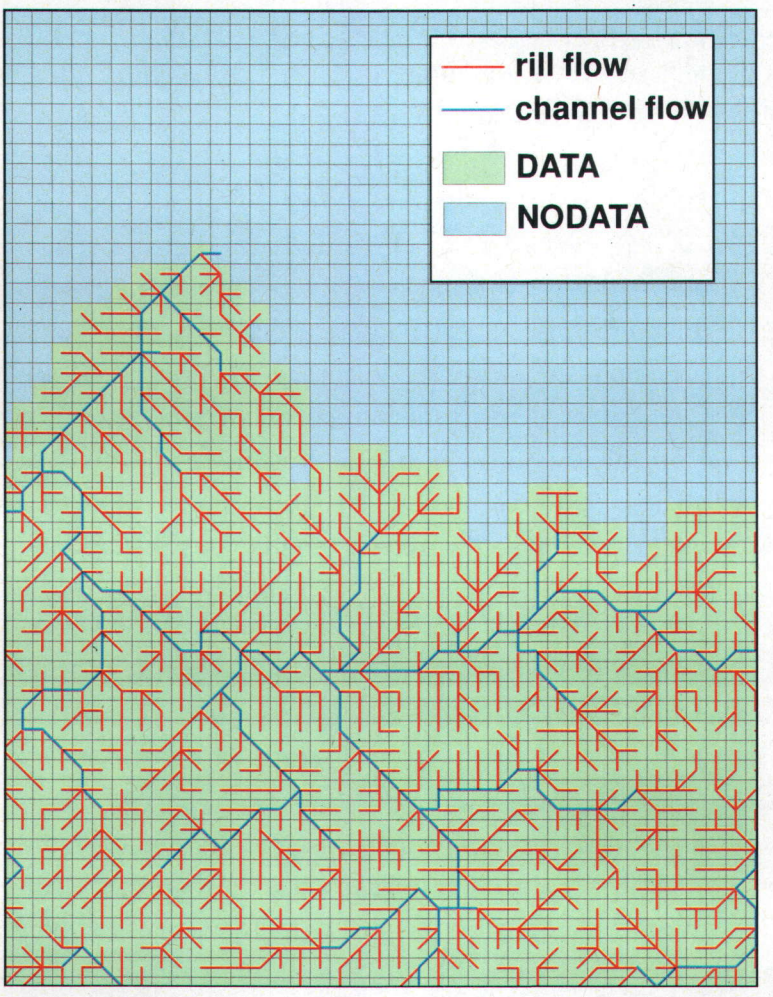

Figure 1.16: Instantané d'une visualisation des données vectorielles produites par le préprocesseur.

la sélection d'une seule direction pour chaque cellule du DEM est réduit par l'introduction de déviations (angulaires et transversales) cumulatives (basées sur la trajectoire) entre les directions de drainage sélectionnées et théoriques. Ces déviations sont prises en compte par la définition d'un facteur d'amortissement (λ) qui peut prendre des valeurs entre 0 et 1 (0 si on ne tient pas compte de la mémoire, c.-à-d., la méthode standard D8, et 1 dans le cas d'une mémoire complète des déviations calculées pour les cellules supérieures prétraitées).

Le plan incliné (Figure 1.17) a été généré avec une orientation Ψ_{FD} (orientation de la ligne descendante la plus raide) de 270.38 degrés dans le sens des aiguilles d'une montre à partir du nord calculée comme suit:

$$\Psi_{FD} = 180 - arctan\left(\frac{z_y}{z_x}\right) + 90\left(\frac{z_x}{|z_x|}\right) \tag{1.3}$$

où z_x et z_y sont les dérivées de la surface topographique estimées par différences finies centrées.

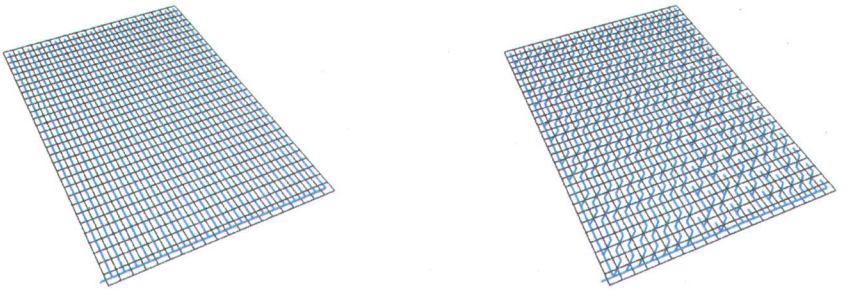

Figure 1.17: Réseau de drainage d'un plan incliné obtenu avec la méthode standard D8 (gauche) et la D8-LTD (droite). Noter que l'angle de vue ne correspond pas à l'orientation réelle du plan incliné.

Il faut noter que l'orientation est un attribut de toutes les cellules d'un plan et qu'elle peut être associée à la direction de drainage théorique (la plus raide).

Les méthodes D8 et D8-LTD ($\lambda = 1$) sont comparées en examinant visuellement le réseau synthétique de drainage. Comme on le voit à la Figure 1.17, la méthode D8-LTD reproduit les trajectoires de drainage significativement mieux que la méthode standard D8. Par exemple, il est évident que les trajectoires de drainage résultant de la méthode D8 standard semblent influencées par l'orientation de la grille et forment des patrons caractérisés par des lignes parallèles, tandis que celles obtenues avec la méthode D8-LTD suivent plus de près la topographie de la surface associée, avec une trajectoire de drainage davantage en accord avec l'orientation du plan incliné.

1.3.3.2 Système de drainage d'un bassin réel

La méthode standard D8 ou la D8-LTD permettent l'écoulement à partir d'une cellule vers seulement une de ses huit voisines les plus proches en se basant sur la direction d'écoulement théorique (la plus raide). Puisque l'écoulement de plusieurs cellules supérieures peut s'accumuler dans une cellule, mais de là ne peut s'écouler que vers une seule cellule, ces méthodes peuvent modéliser la convergence de l'écoulement dans des vallées, mais pas la divergence de l'écoulement sur des crêtes. Pour surmonter cette limitation, le préprocesseur de CATHY inclut une méthode à directions d'écoulement multiples dénotée D_∞ *[Tarboton, 1997]*, et une combinaison des méthodes de directions simples et multiples de l'écoulement *[Orlandini and Moretti, 2009]*. Dans la première méthode, l'écoulement d'un pixel est réparti entre les deux pixels inférieurs selon la proximité de l'angle d'écoulement avec l'angle direct vers le centre de ce pixel. Dans la deuxième méthode, des directions d'écoulement simples ou multiples sont sélectionnées pour chaque cellule de la grille selon que la valeur de la courbure du plan (K_c)

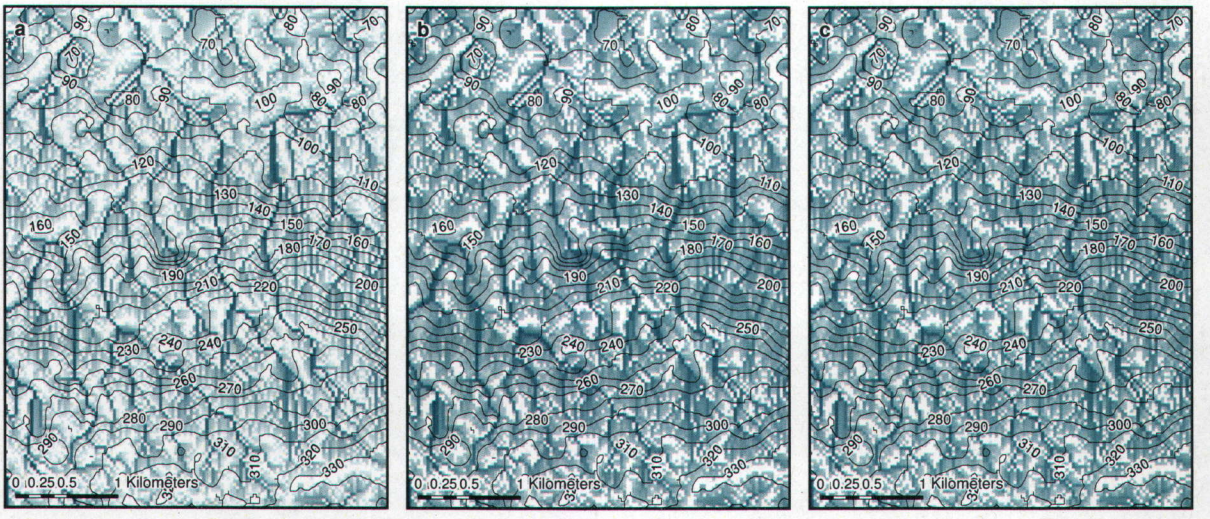

Figure 1.18: Carte d'une partie du bassin de la rivière des Anglais montrant les aires de drainage transformées logarithmiquement (base 10) contribuant à chaque cellule et obtenues à partir de (a) la méthode des directions d'écoulement D8-LTD, (b) la méthode des directions d'écoulement D_∞-LTD, et (c) un hybride de ces deux méthodes utilisant une valeur seuil de la courbure du plan (K_c) égale à 0. Les cellules blanches représentent des cellules sources ayant une aire supérieure de drainage égale à zéro. La taille des cellules de la grille est de 30 m; l'intervalle des contours est de 10 m.

dépasse ou non une valeur seuil fixée (K_{ct}). Par exemple, lorsque K_{ct} égal zéro, l'algorithme sélectionne des directions d'écoulement simples pour les terrains localement convergents et des directions multiples pour les terrains localement divergents.

La courbure du plan (K_c) est calculée en utilisant la sous-grille 3 × 3 schématisée à la Figure 1.13 comme ce qui suit:

$$K_c = \frac{z_{xx}z_y^2 - 2z_{xy}z_x z_y + z_{yy}z_x^2}{(z_x^2 + z_y^2)^{3/2}} \tag{1.4}$$

où tous les termes sont définis comme dans l'équation 1.1. Les dérivées sont estimées par différences finies centrées.

La Figure 1.18 montre l'aire du haut de la pente pour une partie du bassin de la rivière des Anglais calculé en utilisant D8-LTD, D_∞-LTD, et un hybride de ces deux méthodes obtenu en fixant K_c égal à zéro. Les différences à cette échelle sont assez subtiles, mais il est possible de voir plus de stries dans la grille de la méthode D8-LTD que dans celle de D_∞-LTD et de la combinaison hybride. Les résultats présentés à la Figure 1.18 indiquent également que les algorithmes de directions multiples de l'écoulement (dispersifs) produisent une meilleure représentation spatiale de l'aire de drainage que les algorithmes de direction simple (non

dispersifs), qui montrent de nombreuses cellules sources dispersées sur le terrain plutôt que seulement sur les crêtes et les sommets.

Deux questions principales ayant des implications importantes pour la modélisation hydrologique distribuée sont soulevées par l'application des différentes méthodes de drainage. D'abord, il est important que les directions d'écoulement, et par conséquent l'aire de drainage du haut de la pente, soient déterminées adéquatement libres de tout artéfact de la grille, puisque ces valeurs sont utilisées dans la délimitation automatisée des chenaux basée sur la notion d'aire critique de support, et ont donc un impact sur la paramétrisation du modèle hydrologique. En second lieu, la dispersion artificielle inhérente à toute technique de délinéation du réseau de drainage devrait être réduite au minimum. Cette condition est particulièrement importante lorsque des prédictions d'écoulement distribué doivent être utilisées pour modéliser la propagation de solutés et de sédiments.

Chapter 2

A comparison of two physics-based numerical models for simulating surface water–groundwater interactions

Abstract

Problems in hydrology and water management that involve both surface water and groundwater are best addressed with simulation models that can represent the interactions between these two flow regimes. In the current generation of coupled models, a variety of approaches is used to resolve surface–subsurface interactions and other key processes such as surface flow propagation. In this study we compare two physics-based numerical models that use a 3D Richards equation representation of subsurface flow. In one model, surface flow is represented by a fully 2D kinematic approximation to the Saint-Venant equations with a sheet flow conceptualization. In the second model, surface routing is performed via a quasi-2D diffusive formulation and surface runoff follows a rill flow conceptualization. The coupling between the land surface and the subsurface is handled via an explicit exchange term resolved by continuity principles in the first model (a fully-coupled approach) and by special treatment of atmospheric boundary conditions in the second (a sequential approach). Despite the significant differences in formulation between the two models, we found them to be in good agreement for the simulation experiments conducted. In these numerical tests, on a sloping plane and a tilted V-catchment, we examined saturation excess and infiltration excess runoff production under homogeneous and heterogeneous conditions, the dynamics of the return flow process,

the differences in hydrologic response under rill flow and sheet flow parameterizations, and the effects of factors such as grid discretization, time step size, and slope angle. Low sensitivity to vertical discretization and time step size was found for the two models under saturation excesss and homogeneous conditions. Larger sensitivity and differences in response were observed under infiltration excess and heterogeneous conditions, due to the different coupling approaches and spatial discretization schemes used in the two models. For these cases, the sensitivity to vertical and temporal resolution was greatest for processes such as reinfiltration and ponding, although the differences between the hydrographs of the two models decreased as mesh and step size were progressively refined. In return flow behavior, the models are in general agreement, with the largest discrepancies, during the recession phase, attributable to the different parameterizations of diffusion in the surface water propagation schemes. Our results also show that under equivalent parameterizations, the rill and sheet flow conceptualizations used in the two models produce very similar responses in terms of hydrograph shape and flow depth distribution.

2.1 Introduction

Surface and subsurface waters are not isolated components of the hydrologic cycle, but instead interact in response to topographic, soil, geologic, and climatic factors *[Eagleson, 1978]*. The study of these interactions has been addressed at both small (field and hillslope) (e.g., *Abdul and Gillham [1984]; Tonina and Buffington [2007]*) and large (watershed to global) scales (e.g., *Levine and Salvucci [1999]; Syed et al. [2005]*). A number of hydrological models that incorporate some representation of groundwater–surface water interactions have been developed over the past decades, including physically-based, distributed-parameter models. This latter class of models, more rigorous but also more computationally intensive than empirical or semi-empirical approaches, uses the shallow water equations to describe surface flow, i.e., one- or two-dimensional approximations of the Saint-Venant equations for overland and/or channel flow, coupled with a subsurface component that solves the three-dimensional equation for variably saturated flow, i.e., Richards' equation (e.g., *VanderKwaak and Loague [2001]; Morita and Yen [2002]; Panday and Huyakorn [2004]; Jones et al. [2008]*). A comprehensive description of the types of process representation in distributed models and their inherent assumptions and limitations, together with a discussion of comparison and assessment issues, is provided in *Kampf and Burges [2007]*, *Clarke [2008]*, *Furman [2008]*, *Ebel et al. [2009]*, and *Maxwell [2009]*.

For physically-based coupled models, which are the focus of this study, various schemes have been proposed for solving the system of surface and subsurface equations and for resolving the interactions across the land surface. The solution approaches can be broadly classified

as full coupling, sequential coupling, and loose coupling, whereas the formulations for the exchange fluxes are based on continuity principles, diffusion paradigms, boundary conditions switching, or other schemes. In full coupling (e.g., *VanderKwaak and Loague [2001]; Panday and Huyakorn [2004]; Kollet and Maxwell [2006]*), the governing equations are solved simultaneously; in sequential coupling (e.g., *Govindaraju and Kavvas [1991]; Morita and Yen [2002]; Camporese et al. [2010]*), they are solved separately, with an explicit discretization used for at least one of the equations or with an iterative cycle superposed on the overall system; in loose coupling (e.g., *Smith and Woolihser [1971]; Downer and Ogden [2003]*), the equations are again solved separately, with the output from one regime (e.g., surface flow) simply passed as input to the other, without iteration or other conditions imposed.

Whereas the accuracy, robustness, and other performance features of surface and subsurface numerical models have been extensively documented (e.g., *Ponce et al. [1978]* and *Viera [1983]* for Saint-Venant approximations; *Huyakorn et al. [1986]* and *Nieber and Feddes [1999]* for Richards' equation), there have been very few assessments of coupled models based on these equations. The purpose of this study is to provide such an assessment via a comparative analysis of two process-based groundwater–surface water models. One model, ParFlow *[Kollet and Maxwell, 2006, 2008]*, uses a full coupling approach and continuity of pressures and fluxes across the land surface to resolve the surface–subsurface interactions; the other model, CATHY *[Bixio et al., 2000; Camporese et al., 2010]*, is based on sequential coupling with boundary condition switching to partition atmospheric fluxes into infiltration (or exfiltration) and a change in surface water storage. A comparison of these two very different models provides a first opportunity to critically examine some key features of coupled hydrological models. In addition to different schemes for coupling and exchange flux resolution, the two models use different conceptualizations of surface routing: sheet flow representation and a kinematic wave equation in ParFlow; rill flow representation and a diffusion wave equation in CATHY. Although not directly inherent to coupling issues, these additional differences are also worthy of assessment, given the high interest in applying coupled hydrological models at catchment and river basin scales where terrain features (slope, roughness, etc), and consequently surface flow conditions, can vary greatly. Other differences between the models (e.g., ParFlow uses a finite difference/finite volume discretization whereas CATHY uses finite elements for the subsurface and finite differences for the surface) will also have an effect on the intercomparison tests and will be duly considered.

The intercomparison study is carried out through a series of simple test cases subjected to step functions of rainfall followed by a recession or evaporation period. The test cases involve a sloping plane (*Gottardi and Venutelli [1993]*) and a tilted V-catchment (*Panday and Huyakorn [2004]*). The simulations are designed to clearly expose model differences and similarities under complex and realistic physical conditions. The first tests focus on the different treatments of the exchange fluxes between the subsurface and surface domains and

their sensitivity to factors such vertical mesh resolution, time step size, and slope angle. A second set of tests is intended to evaluate the impact of the different conceptualizations for propagation of surface runoff in terms of water depth distribution at the ground surface and timing and shape of the hydrograph.

2.2 Description of the models

The governing equations for the ParFlow model *[Kollet and Maxwell, 2006; Maxwell and Kollet, 2008]* are the three-dimensional (3D) Richards equation for subsurface flow in variably saturated soils and the kinematic wave approximation of the Saint-Venant equation for overland and channel flow:

$$S_s S_w \frac{\partial \psi}{\partial t} + \phi \frac{\partial S_w}{\partial t} = -\nabla \cdot \mathbf{q} + q_s \tag{2.1}$$

$$\mathbf{q} = -K_s K_r \nabla(\psi - z) \tag{2.2}$$

$$\frac{\partial \psi_s}{\partial t} = \nabla \cdot (\psi_s \vec{\nu}) + q_r(x) \tag{2.3}$$

$$S_{f,i} = S_{o,i} \tag{2.4}$$

where S_s is the specific storage coefficient $[1/L]$, $S_w = S_w(\psi)$ is the relative saturation $[-]$, ψ is the subsurface pressure head $[L]$, t is time $[T]$, ϕ is the porosity $[-]$, ∇ is the gradient operator, q is the Darcy flux $[L/T]$, q_s is a general source/sink term $[1/T]$, K_s is the saturated hydraulic conductivity tensor $[L/T]$, $K_r = K_r(\psi)$ is the relative hydraulic conductivity function $[-]$, z is the vertical coordinate pointing downward $[L]$, ψ_s is the pressure at the ground surface (surface ponding depth) $[L]$, $\vec{\nu}$ is the depth-averaged velocity vector $[L/T]$, q_r is the rainfall rate $[L/T]$, and $S_{f,i}$ and $S_{o,i}$ are the gravity forcing and friction slope terms, respectively $[-]$, with i indicating the x and y directions.

The governing equations for the CATHY model *[Bixio et al., 2000; Camporese et al., 2010]* are the 3D Richards equation and the diffusion wave approximation of the Saint-Venant equation:

$$S_s S_w \frac{\partial \psi}{\partial t} + \phi \frac{\partial S_w}{\partial t} = \nabla \cdot [K_s K_r(\psi) (\nabla \psi + \eta_z)] + q_{ss} \tag{2.5}$$

$$\frac{\partial Q}{\partial t} + c_k \frac{\partial Q}{\partial s} = D_h \frac{\partial^2 Q}{\partial s^2} + c_k q_s, \tag{2.6}$$

where $\eta_z = (0, 0, 1)^T$ (the vertical coordinate is positive upward), q_{ss} represents distributed source (positive) or sink (negative) terms $[L^3/L^3T]$, Q is the discharge along the channel link $[L^3/T]$, c_k is the kinematic wave celerity $[L/T]$, s is the hillslope/channel link coordinate $[L]$, D_h is the hydraulic diffusivity $[L^2/T]$, and q_s is the inflow (positive) or outflow (negative) from the subsurface to the surface $[L^3/LT]$.

2.2.1 Subsurface flow

The three-dimensional Richards equation is solved in ParFlow using a cell-centered finite difference scheme with harmonic averages of the saturated hydraulic conductivity and a one-point upstream weighting of the relative permeability function. CATHY uses a Galerkin finite element spatial integrator using tetrahedral elements and linear basis function. Both models employ an implicit backward Euler scheme for the discretization in time of Richards' equation. The resulting discrete equation is solved in ParFlow by a Newton-Krylov nonlinear solver *[Jones and Woodward, 2001]* and in CATHY by Picard or Newton iteration *[Paniconi and Putti, 1994]*.

2.2.2 Surface routing

The kinematic wave equations (2.3) and (2.4) in ParFlow are discretized in space with an upwind finite volume scheme and in time with an implicit backward Euler method. The surface flow equation is solved by posing two types of boundary conditions: the gradient and critical depth outlet conditions, consisting respectively in a prescribed flux and water depth condition. In CATHY the diffusion wave equation (2.6) is discretized in space and time with a matched artificial dispersivity (MAD) scheme *[Syriopoulou and Koussis, 1991]*.

ParFlow uses a two-dimensional sheet flow conceptualization for surface routing, whereby flow is assumed to be distributed in a uniform sheet over a plane surface. The different dynamics of overland and channel flow are handled by assigning different Manning's roughness coefficients to each regime, and there is no need for parameters related to flow geometry. In CATHY surface routing is conceptualized as rill flow along a one-dimensional drainage network of connected linear segments. This network is automatically extracted by a digital elevation model (DEM)-based pre-processor *[Orlandini et al., 2003]*. To differentiate between overland and channel flow regimes, different hydraulic parameters (resistance/conductance coefficient and water-surface width) and dynamic scaling properties are assigned to hillslope and channel cells, which have been distinguished in the pre-processing step based on threshold criteria linked, for example, to upstream drainage area *[Montgomery and Foufoula-Georgiou,*

1993]. Hydraulic characterization of the drainage network is achieved by applying the *Leopold and Maddock Jr. [1953]* power law relations that relate water-surface width and roughness coefficient to discharge *[Orlandini, 2002]*:

$$W(A,Q) = W(A_s,Q_f)\,Q_f(A_s)^{-b'}\;(A/A_s)^{w(b''-b')} \cdot Q^{b'} \tag{2.7}$$

$$k_S(A,Q) = k_S(A_s,Q_f)\,Q_f(A_s)^{-y'}\;(A/A_s)^{w(y''-y')} \cdot Q^{y'} \tag{2.8}$$

where W $[L]$ is the water-surface width, k_S $[L^{1/3}/T]$ is the Gauckler-Strickler coefficient, A_s is the drainage area at a selected site, the exponents b', b'', y', y'' are characteristics of the rill/channel network as a whole, and w $[-]$ is the exponent of the scaling relationship of the selected frequency discharge Q_f with drainage area A. The width and roughness coefficients are thus dynamically varied in space and time, with water-surface width for instance ranging from a present minimum value up to the cell size.

The temporal solution is globally implicit in ParFlow, using backward Euler for both the surface and subsurface equations. The time step size can be constant or it can vary based on an exponential growth method. In CATHY the time step size for the surface routing module is computed based on a Courant number accuracy criterion. The explicit in time nature of the MAD scheme allows sequential resolution of the surface and subsurface equations and a nested time stepping approach, whereby for each subsurface time step, one or more sub-steps (depending on the Courant estimate) are taken for the surface routing module.

2.2.3 Coupling and resolution of exchange fluxes

As detailed in *Kollet and Maxwell [2006]*, ParFlow simulates fully-coupled surface and subsurface flow via an overland flow boundary condition. The approach takes equation (2.3) and adds a flux for subsurface exchanges, $q_e(x)$:

$$\frac{\partial \psi_s}{\partial t} = \nabla \cdot (\psi_s \vec{v}) + q_r(x) + q_e(x) \tag{2.9}$$

Continuity of pressure at the top cell of the boundary between the surface and subsurface systems is then assigned by setting pressure head ψ in equation (2.1) equal to the vertically-averaged surface pressure ψ_s as follows:

$$p = \psi_s = \psi \tag{2.10}$$

This relationship is then substituted back into equation (2.9) as follows:

$$\frac{\partial \parallel p, 0 \parallel}{\partial t} = \nabla \cdot (\parallel p, 0 \parallel \vec{v}) + q_r(x) + q_e(x) \tag{2.11}$$

where the $\| p, 0 \|$ operator chooses the greater of the two quantities, p and 0. By posing now the continuity of the fluxes ($q_{bc} = q_e$, where q_{bc} is a boundary condition of Neumann type for the subsurface equation) at the ground surface:

$$-K_s K_r(p)\nabla(p - z) = \frac{\partial \| p, 0 \|}{\partial t} - \nabla \cdot (\| p, 0 \| \vec{v}) - q_r(x) \tag{2.12}$$

equation (2.1) and equation (2.2) can be re-written in the following combined form:

$$S_s S_w \frac{\partial \psi}{\partial t} + \phi \frac{\partial S_w(\psi)}{\partial t} = -\nabla \cdot [-K_s K_r(p)\nabla(p - z)] + q_s \tag{2.13}$$

When the pressure at the top cell of the subsurface domain has a ponded depth and is thus greater than zero (Dirichlet boundary condition), the kinematic wave equation is active through the left term in equation (2.12) and the depth-averaged velocity calculated through Manning's depth-discharge relationship. On the other hand, when the pressure at the top cell of the subsurface is lower than zero (Neumann boundary condition), the overland flow boundary condition is turned off and equation (2.13) is solved as a standard Richards equation. This approach results in both systems (surface and subsurface) solved over a common grid in a fully-integrated, fully-mass conservative manner.

In CATHY the source/sink terms q_{ss} and q_s in equations (2.5) and (2.6) represent the exchanges between the subsurface and surface modules. At any given time t, atmospheric forcing inputs are imposed as land surface boundary conditions on the subsurface equation, which is solved first. After solution, a balance is performed at each surface node between the atmospheric water supply (rainfall) or demand (potential evaporation), the capacity of the soil to accept (infiltrate) or deliver (exfiltrate) this water, and the amount of water already present at the surface (ponding). The boundary condition is updated to reflect whether, after this balance, the soil capacity exceeds or not the water supply (or demand), including any water held as surface storage (ponded). Exceedance implies a Neumann (specified flux) boundary condition, equivalent to an atmosphere-controlled process, whereas in the converse case a Dirichlet (specified head) condition applies and the process is soil-limited. This boundary condition switching procedure is an extension to the case of ponding (and thus interaction with a surfacing routing model) of the method commonly used in Richards' equation-based subsurface models to perform rainfall-runoff partitioning and to restrict water loss when the soil becomes too dry. One of the appealing features of this procedure is that it automatically tracks both infiltration excess (Hortonian) and saturation excess (Dunnian) runoff generation mechanisms. In the ponding extension, the parameter *Pond_head_min* is introduced in CATHY as the threshold pressure head (or ponding) value a surface node must attain before water can be routed by the surface flow module. This parameter represents, for instance, the amount of water that can be stored in microtopographic depressions on the land surface.

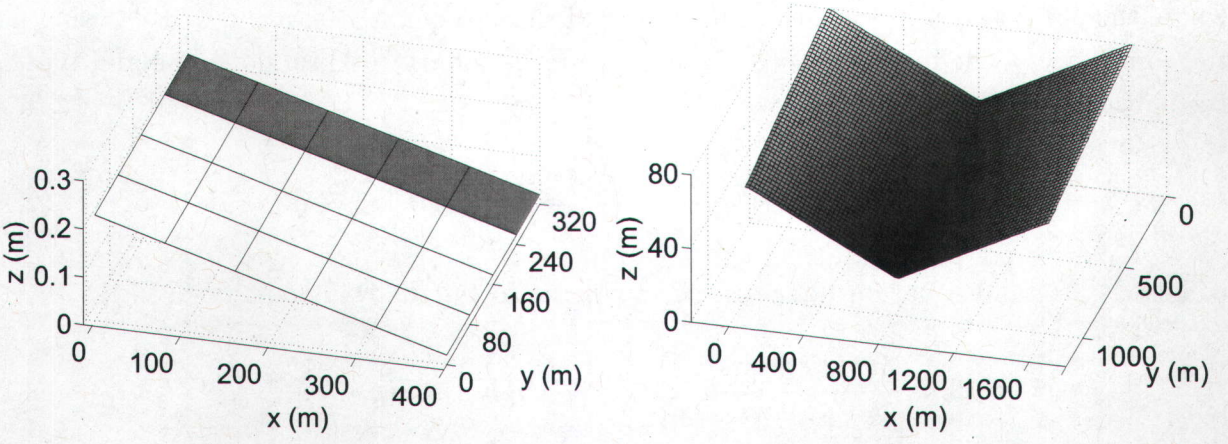

Figure 2.1: The sloping plane catchment (left) and the tilted V-catchment (right). Model outflow results for the sloping plane are for the grey strip of cells.

To illustrate the boundary condition switching approach consider a rainfall event on an initially unsaturated soil. The surface boundary condition will be of Neumann type until the pressure head at the surface, computed by the model, becomes zero. At this time the boundary condition is switched to Dirichlet type, allowing the model to compute the actual rate at which water enters the soil. If during the course of the rainfall period the actual flux becomes larger than the potential rate (as could happen for instance if there is a fall in precipitation intensity), the boundary condition is switched back to Neumann type. In the interaction with the surface module, any water that accumulates at the surface (in excess of *Pond_head_min*) when the boundary condition is of Dirichlet type becomes available for routing.

Switching between Neumann and Dirichlet boundary conditions according to the saturation status of a surface node, as done in CATHY, resembles the way in which the boundary condition equation (2.12) in ParFlow takes on different forms depending on whether the surface pressure head is positive or not. A key difference in the coupling approach for the two models is that, by embedding the surface flow equation into the subsurface equation, ParFlow resolves the exchange between surface and subsurface at the same time level, whereas in CATHY, where the explicit nature of the MAD scheme allows sequential and noniterative resolution of the coupled system, there is a time level lag when solving the surface equation following the subsurface one.

2.3 Test case descriptions

In the sloping plane simulations, surface–subsurface interactions were investigated for the infiltration excess (Horton) and saturation excess (Dunne) runoff generation mechanisms under homogeneous and heterogeneous conditions, and for the return flow process under homogeneous conditions. Rill flow vs sheet flow routing for overland flow was also examined for this test case (channel flow was not considered for this test). The test catchment (Figure 2.1) is 400 m long by 320 m wide. A surface grid of 5 × 4 cells, or 80 m resolution, was used for the homogeneous tests of Horton and Dunne processes and for the overland flow cases, a grid of 40 × 32, or 10 m resolution, was used for the heterogeneous tests, and a grid of 80 × 64, or 5 m resolution, was used for the return flow cases. The soil depth is 5 m and van Genuchten relationships *[van Genuchten and Nielsen, 1985]* are used to describe the soil hydraulic characteristics, with saturated moisture content $\theta_{sat} = 0.4$, residual moisture content $\theta_{res} = 0.08$, $\alpha = 1.0$, and $n = 2.0$. For CATHY the Gauckler-Strickler conductance coefficient (k_S) was kept fixed in space and time at $3.0{\times}10^3$ $m^{1/3}/min$ (i.e., $y'{=}y''{=}0$ in equation (2.8)) and the exponent w was kept fixed at 1.0. This parameterization corresponds in ParFlow to a Manning's roughness coefficient of $3.3{\times}10^{-4}$ $m^{-1/3}min$. In order to have a consistent basis for intercomparison, the coupled simulations in the runoff generation tests were run with the CATHY model parameterized as sheet flow, using a constant water-surface width (equation (2.7)) equal to the grid resolutions for the 80 m and 10 m grids. The bottom and vertical sides of the domain are no-flow boundaries for the subsurface in both models. ParFlow uses a gradient condition at the catchment outlet for the overland flow simulator, while CATHY, with an overland simulator based on a hyperbolic equation, does not need to specify a boundary condition at the outlet. The simulation consists of a 200-min rainfall event (at a uniform intensity of $3.3{\times}10^{-4}$ m/min) followed by 100 min of drainage for the runoff generation and overland flow tests, whereas for the return flow cases a 200 min rainfall event (at a uniform intensity of $1.5{\times}10^{-4}$ m/min) followed by 200 min of evaporation (at a uniform rate of $5.4{\times}10^{-6}$ m/min) was used. For the runoff generation tests two inclinations of the plane (in the x direction) are used, of 0.05% and 5% (the slope in the y direction is zero), together with a range of uniform vertical discretizations from 0.0125 m (400 layers) to 0.2 m (25 layers). For the return flow cases inclinations of 0.5% and 5% and a uniform vertical discretization of 0.05 m (100 layers) are used, and for the overland flow tests the slope inclination is 0.05%. Reported outflow rates for the two models are with reference to the grey strip of cells shown in Figure 2.1.

In the tilted V-catchment only surface flow processes are considered, but we now consider both overland and channel flow. The catchment consists of two identical sloping planes of length 800 m and width 1000 m joined by a 20 m wide, 1000 m long channel. The x direction follows the hillslope length and channel width while the y direction is along the channel length

Table 2.1: Parameter values for the sloping plane and tilted V-catchment test cases.

	Sloping plane				V-catchment
	Homogeneous			Heterogeneous	
	Saturation excess	Infiltration excess	Return flow	slab	
Horizontal mesh size, $\Delta x = \Delta y$ (m)	80	80	5	10, 1	20
Vertical mesh size, Δz (m)	0.0125, 0.025, 0.05, 0.1, 0.2	0.0125, 0.025, 0.05, 0.1, 0.2	0.05	0.05	*na*
Water table depth at time 0, WT (m)	0.5, 1.0	1.0	0.5	1.0	*na*
Saturated hydraulic conductivity, K_{sat} (m/min)	6.94×10^{-4}	6.94×10^{-6}, 6.94×10^{-5}	6.94×10^{-2}	6.94×10^{-4}, 6.94×10^{-6}	*na*
Rainfall rate, q_r (m/min)	3.3×10^{-4}	3.3×10^{-4}	1.5×10^{-4}	3.3×10^{-4}	1.8×10^{-4}
Evaporation rate, q_e (m/min)	0	0	5.4×10^{-6}	0	0
Gauckler-Strickler conductance coefficient, k_s ($m^{1/3}$/min):					
– hillslope cells	3.0×10^{3}	3.0×10^{3}	3.0×10^{3}	3.0×10^{3}	4.0×10^{3}
– channel cells	*na*	*na*	*na*	*na*	4.0×10^{2}
Manning's roughness coefficient, n ($m^{-1/3}$min):					
– hillslope cells	3.3×10^{-4}	3.3×10^{-4}	3.3×10^{-4}	3.3×10^{-4}	2.5×10^{-4}
– channel cells	*na*	*na*	*na*	*na*	2.5×10^{-3}

and hillslope width (Figure 2.1). The Gaukler-Strickler conductance coefficient is constant in space and time at 4.0×10^{3} $m^{1/3}$/min for hillsope cells and 4.0×10^{2} $m^{1/3}$/min for channel cells, which correspond in ParFlow to a Manning's roughness coefficient of 2.5×10^{-4} $m^{-1/3}$min and 2.5×10^{-3} $m^{-1/3}$min, respectively. The simulation consists of a 90-min rainfall event (at a uniform intensity of 1.8×10^{-4} m/min) followed by 90 min of drainage.

A summuary of the parameter values for the different test cases is given in Tables 2.1 and 2.2.

2.4 Results and discussion

2.4.1 Sloping plane

2.4.1.1 Runoff generation mechanisms, homogeneous conditions

Surface-subsurface water exchanges under Dunne and Horton saturation processes were first investigated for the homogeneous case. In the saturation excess test two initial water table configurations, at 0.5 m and 1.0 m from the ground surface, were simulated with a saturated hydraulic conductivity K_s of 6.94×10^{-4} m/min. In the infiltration excess test the

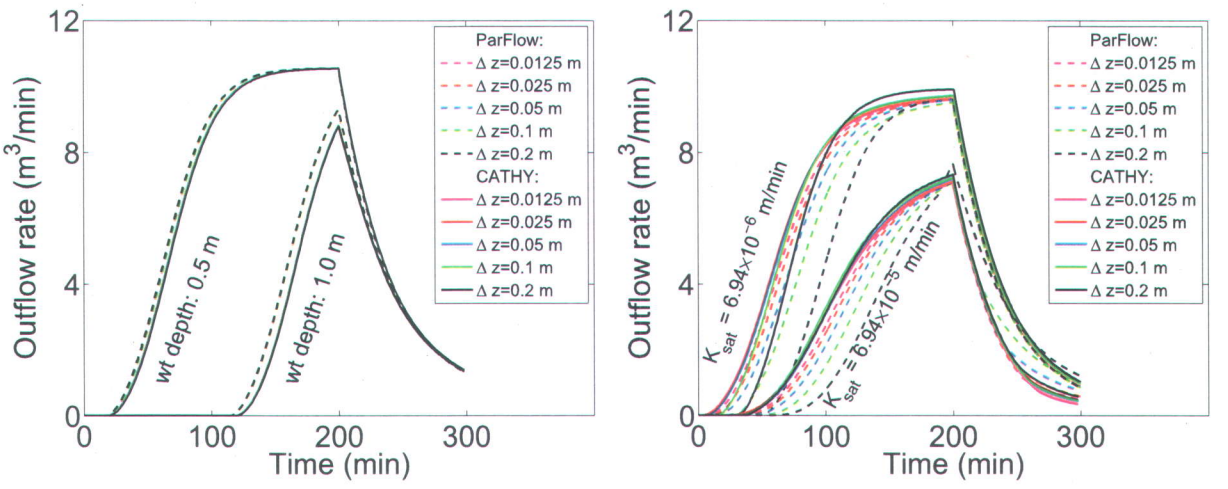

Figure 2.2: Outflow response for the homogeneous sloping plane test case under conditions of saturation excess runoff generation with two initial water table configurations (left) and under conditions of infiltration excess runoff generation with two values of saturated hydraulic conductivity (right).

initial water table depth was fixed at 1.0 m and two K_s values were used, 6.94 $\times 10^{-5}$ and 6.94 $\times 10^{-6}$ m/min. The influence of vertical mesh size resolution is explored for both processes by varying the vertical discretization from 0.0125 m (400 layers) to 0.2 m (25 layers).

Figure 2.2 shows the ParFlow and CATHY outflow rates for the two sub-cases in each of the direct runoff tests. In the saturation excess case the results for the two models compare quite well, with an excellent match in the timing and shape of the recession portion of the hydrograph and with percentage differences in total outflow volume (relative to ParFlow totals) ranging from 1.4% (finest discretization, 0.0125 m, and 0.5 m initial water table depth) to 9% (coarsest discretization, 0.2 m, and 1 m initial water table depth). The CATHY results show a slight lag with respect to ParFlow in the rising portion, becoming more pronounced for the deeper initial water table configuration. This discrepancy is due to the slight difference in time to ponding. There is little sensitivity to vertical discretization in both models for the saturation excess case. In the infiltration excess case ParFlow and CATHY again agree quite well, especially in the time to peak and in the recession curve. Total outflow differences for this case range from 2.7% (higher conductivity, 0.0125 m discretization) to 23% (lower conductivity, 0.2 m discretization). There is a greater sensitivity to vertical grid resolution for both models in this case, and in particular for ParFlow, illustrating the importance of a fine near-surface mesh in accurately capturing the advent (rising limb) of Horton runoff generation. The reasons for this sensitivity to Δz are however different for the two models. In ParFlow (finite difference discretization), the solutions differ because of the finite storage volume that must be saturated at the top model layer for ponding to occur, resulting in a

shift in time in the rising limbs of the hydrographs. In CATHY (finite element discretization), a thicker top layer element (larger Δz) will be drier at its base than a thin element during an infiltration excess process, resulting in a lower hydraulic conductivity (since K_r is calculated from the nodal values over that element), resulting in a smaller volume of infiltrated water.

In Figure 2.3 it is verified that the numerical results converge as the vertical resolution is refined. Plotted in this figure are relative differences in outflow as a function of resolution expressed as total discharge volume. These are computed with respect to the solution obtained at the finest mesh ($\Delta z = 0.0125$ m) as:

$$\varepsilon_i = \sqrt{\sum_{j=1}^{N} \left[\left(Q_j^{(i)} - Q_j^{(f)} \right) \Delta t \right]^2} \tag{2.14}$$

where $Q^{(i)}$ is the flow discharge for the ith vertical discretization, $Q^{(f)}$ is the flow discharge for the finest discretization, N is the number of time steps, and Δt is the step size (the same constant Δt was used for all runs). Note that the true solution is unknown. We show only the differences between solutions obtained at a given resolution with that of the finest resolution simulated by that code. In this way, we may use ϵ as a quantitative measure to test the relative effect of vertical resolution. The results show that the differences are lower for the saturation excess mechanism and larger for the smaller conductivity sub-case (bottom-left graph in Figure 2.3), i.e., the near-surface vertical discretization needs to be finer as the infiltration excess mechanism becomes more prominent. Vertical discretization effects are also explored in *Downer and Ogden [2004]*, for a Richards equation subsurface model, and related issues connected to coupling formulations are addressed in *Ebel et al. [2009]*.

In Figure 2.4 the influence of temporal discretization is examined for the 0.05% slope angle of the previous tests with the finest vertical discretization (i.e. $\Delta z = 0.0125$ m), and also for a much steeper sloping plane (5%). Very good agreement between the ParFlow and CATHY models is obtained for the entire time step size range and for both Horton and Dunne surface–subsurface exchange processes.

For ParFlow, a constant time step size of 1, 5, and 10 min was used during the whole simulation for both runoff processes. For CATHY, a constant step size was used for the Δt = 1 min case; for the other simulations, given an initial, minimum, and maximum (Δt_{max}) time step size, the step size for the subsurface module was adapted based on the convergence behavior of the iterative scheme (Picard in this paper) that is used to linearize Richards' equation *[Paniconi and Putti, 1994]*. When convergence is rapid (less than five iterations in this paper) the step size is increased, and when it is slow (more than 10 iterations) Δt is decreased. A higher Δt_{max} in CATHY generally results in a higher average subsurface time

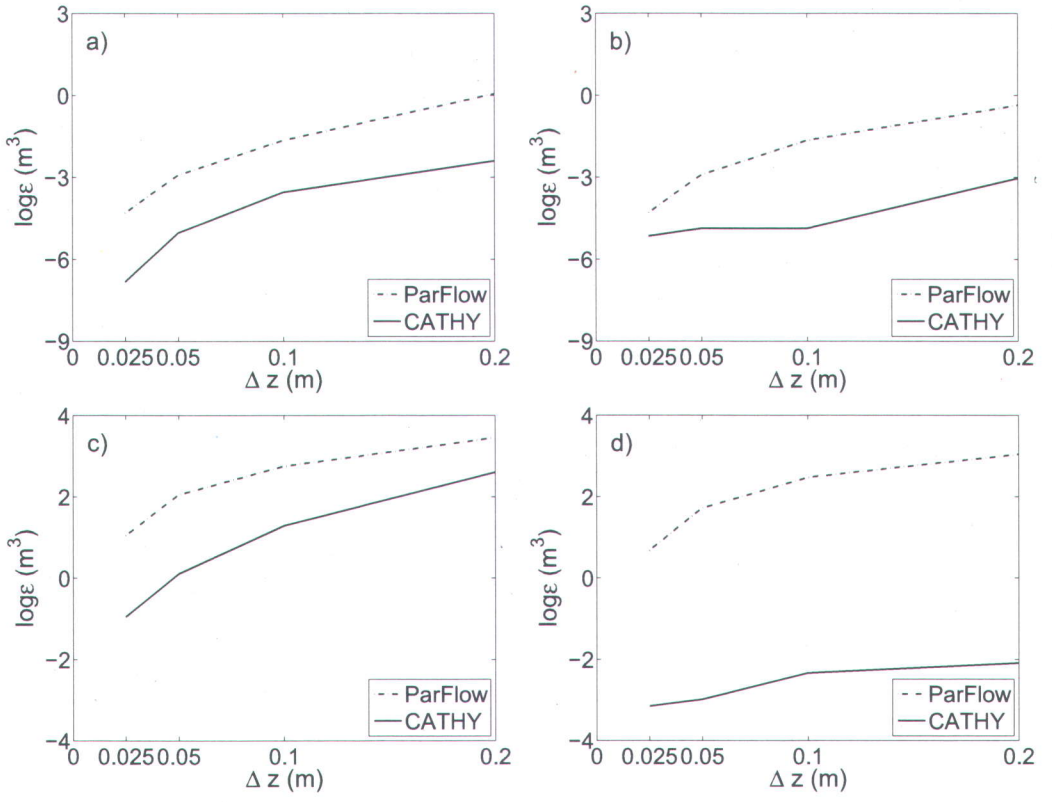

Figure 2.3: Relative discharge differences, as defined in equation 2.14, as a function of vertical discretization for the homogeneous sloping plane test case. Top: saturation excess runoff generation with initial water table depth of 0.5 m (a) and 1 m (b). Bottom: infiltration excess runoff generation with saturated hydraulic conductivity $K_s = 6.94 \times 10^{-6}$ m/min (c) and $K_s = 6.94 \times 10^{-5}$ m/min (d).

step size (Δt_{avg}) for the overall simulation, but at the possible expense of a greater number of nested time steps to solve the surface routing equation. For the results reported in Figure 2.4 this tradeoff was only apparent for the saturation excess case, and somewhat significant only for the higher slope angle (as could be expected, since the faster surface routing in this case requires smaller time steps). The maximum number of nested time steps for each of the CATHY runs in Figure 2.4 is as follows: one (i.e., no nesting needed) for the smallest Δt_{avg} at both slope angles for both the Horton and Dunne cases; two for the higher Δt_{avg} for both the Horton and Dunne case at the lower slope; seven for the highest Δt_{avg} for the Horton case at the higher slope angle; eight for the highest Δt_{avg} for the Dunne case at the higher slope angle.

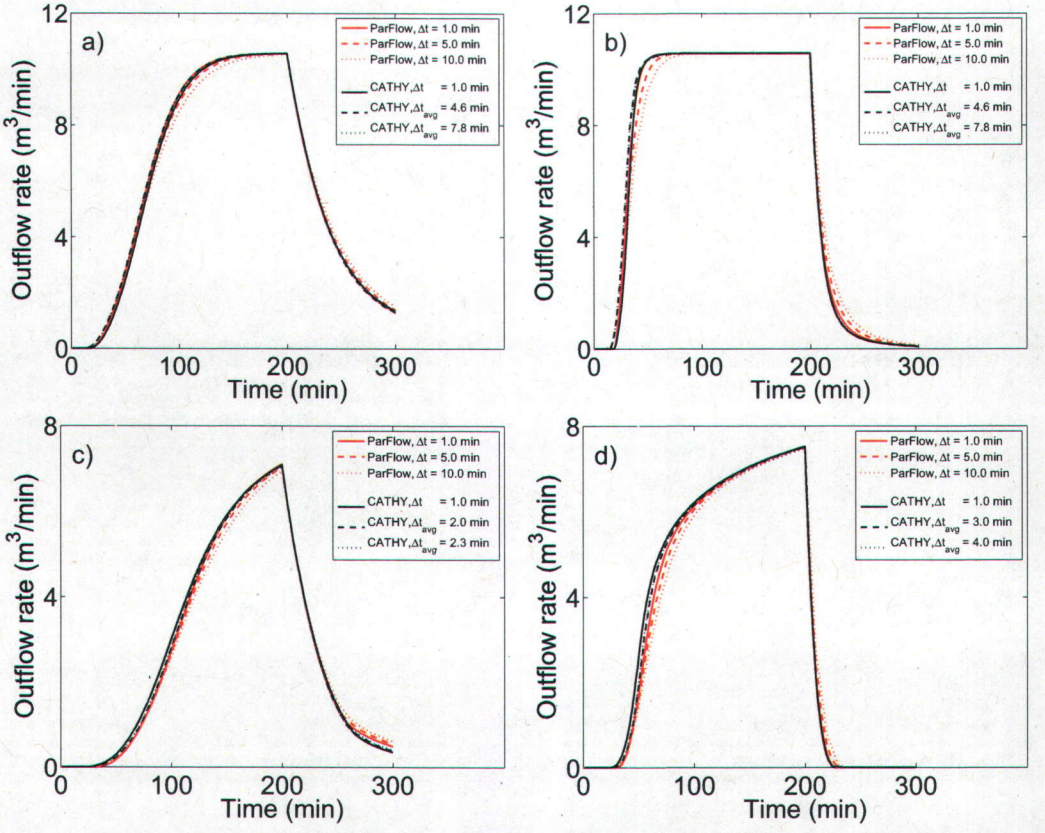

Figure 2.4: Influence of slope angle and time step size for the homogeneous sloping plane test case. Top: saturation excess runoff generation (with initial water table depth of 0.5 m) for slope angles 0.05% (a) and 5% (b). Bottom: infiltration excess runoff generation (with $K_s = 6.94 \times 10^{-5}$ m/min) for slope angles 0.05% (c) and 5% (d).

2.4.1.2 Runoff generation mechanisms, heterogeneous conditions

For the heterogeneous sloping plane the slope angle was 0.05%, the vertical discretization was 0.05 m (100 layers), and the initial water table depth was 1 m. A 100 m long slab of low conductivity ($K_s = 6.94 \times 10^{-6}$ m/min) was placed in the middle of the slope (from x = 150 m to x = 250 m, for all y). The slab was 0.05 m thick and occupied the first layer. The hydraulic conductivity outside of the slab was 6.94×10^{-4} m/min. Two different DEM resolutions were used, 10 m and 1 m, and simulations were conducted using a constant time step size (1.0 min and 3.0 min) for ParFlow and variable (adaptive) time stepping (Δt_{avg} = 1.0 min and 3.0 min) for CATHY. All other parameters and simulation conditions are as reported for the homogeneous sloping plane.

The stepped hydrograph shown in Figure 2.5 is a result of the different infiltration–runoff dynamics occurring upslope and downslope of the slab and on the slab itself. Reinfiltration

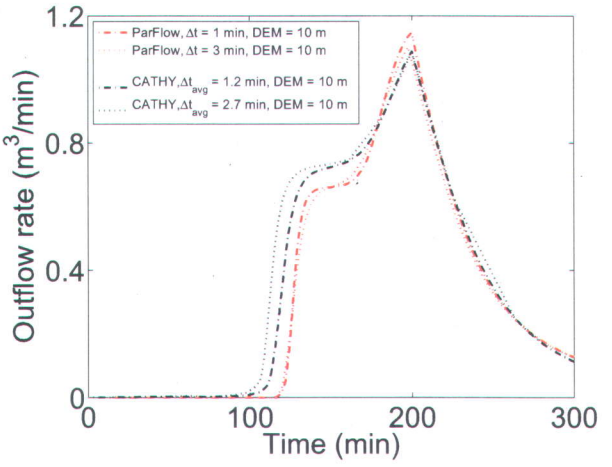

Figure 2.5: Outflow response for the heterogeneous sloping plane test case at 10 m DEM resolution under variable (CATHY) and uniform (ParFlow) time discretizations.

of water that runs off the slab causes earlier saturation of the downslope portion, producing the first plateau in the hydrograph, while later saturation of the upslope portion contributes to the second peak. The reasonable similarity of the curves plotted in Figure 2.5 demonstrates that both models are able to capture surface–subsurface interactions for this difficult test problem, while at the same time the discrepancies highlight the algorithmic differences between the coupling approaches used in ParFlow and CATHY. Simultaneous solution of the surface and subsurface equations in ParFlow produces a sharper, more localized response that is less influenced by the temporal discretization. In CATHY, the sequential solution procedure implies, for instance, that once the slab surface becomes saturated (and the boundary condition for these nodes is switched from Neumann to Dirichlet), all of this water is routed downslope for the duration of one time step, delaying any possible reinfiltration until the next (subsurface) time step. Thus the CATHY hydrograph appears a little bit earlier than ParFlow's, and the outflow for the first rising limb is more disperse. A similar situation is observed in the subsurface, as shown in Figure 2.6. The greater spreading of the reinfiltration front for CATHY early in the simulation is apparent, and indeed at the coarser DEM resolution this spreading can also be seen in the mesh strip immediately upslope of the slab and by the higher value reached at the first rising limb of the hydrograph. This effect is due to the loss of accuracy in passing information from nodes (subsurface) to cells (surface) and can be alleviated by a finer horizontal discretization, as can be seen in Figure 2.6. The higher value reached by the CATHY model at the first rising limb of the hydrograph is again connected to the different spatial discretization schemes implemented in the two models. This results in a smaller volume of infiltrated water above the slab for CATHY, causing in turn a lower degree of saturation beneath the slab.

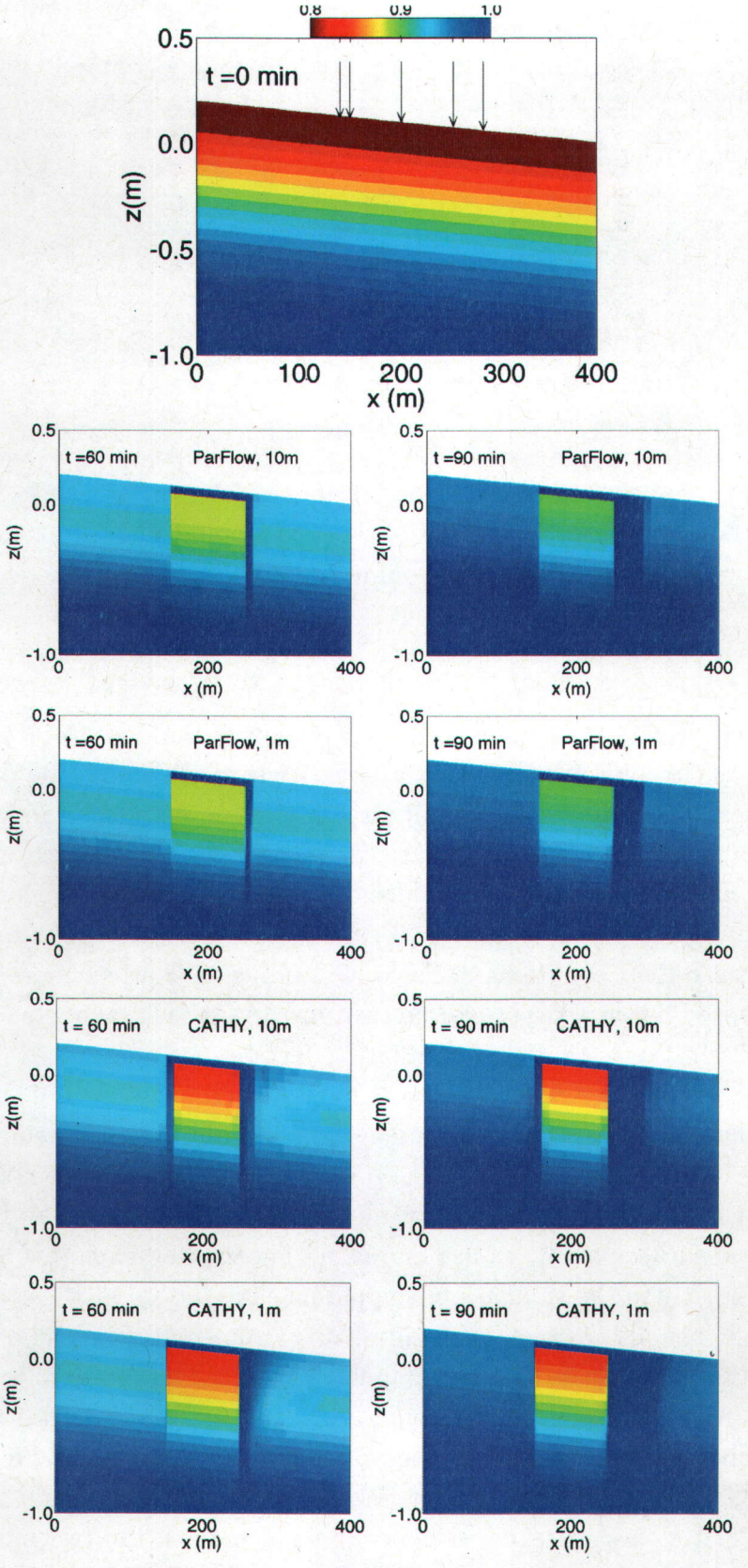

Figure 2.6: Saturation (S_w) profiles in cross section (at y = 200 m) for the heterogeneous sloping plane test case at grid cell resolutions of 10 m and 1 m and with a variable time discretization. In the top figure the initial conditions are shown, as well as the location along the transect of the five vertical profiles plotted in Figure 2.7.

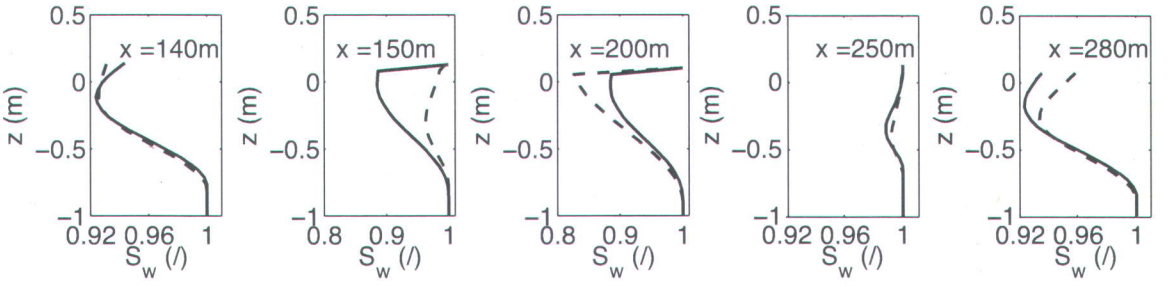

Figure 2.7: Vertical saturation profiles for the heterogeneous sloping plane test case at the five locations indicated in Figure 6. The output is taken at time 60 min, the simulations used a grid cell resolution of 10 m, and the temporal discretization was variable. ParFlow results are the solid lines and CATHY results are the dashed lines.

The differences in behavior of the ParFlow and CATHY models at and in the vicinity of the slab can be seen more clearly in Figure 2.7, where, for the coarse DEM case, vertical profiles of saturation (S_w) are shown 60 min into the simulation for the five points indicated in Figure 2.6. The profiles are identical or very similar at the downslope edge of the slab (x = 250 m, high wetness due to reinfiltration from the slab) and farther away from the slab in the upslope direction (x = 140 m, dry profiles). The ParFlow and CATHY profiles are most different in the center of the slab (x = 200 m, saturated at the surface and a sharp drop in wetness below the surface), at the upslope edge of the slab (x = 150 m), and further downslope of the slab (x = 280 m), due to greater reinfiltration front spreading for the CATHY model.

2.4.1.3 Return flow dynamics, homogeneous conditions

In this set of simulations the dynamics of return flow processes is evaluated by tracking the evolution of the point of intersection (or exit point) between the water table and the land surface during a storm-interstorm simulation consisting of 200 min of rain followed by 200 min of evaporation. The high conductivity values used for the test case (6.94×10^{-2} m/min) allow a rapid rise and fall of the water table and a consequently fast expansion and contraction of the sloping plane's partial contributing area. Two slope angles of 0.5% and 5.0% were simulated, with an initial water table depth of 0.5 m and a constant time step of 0.5 min. For each of the slope angles, in addition to the ParFlow simulations (representing a sheet flow parameterization of overland routing), two CATHY simulations were run, with surface parameterizations corresponding to sheet flow and rill flow (these parameterizations are described in the next subsection).

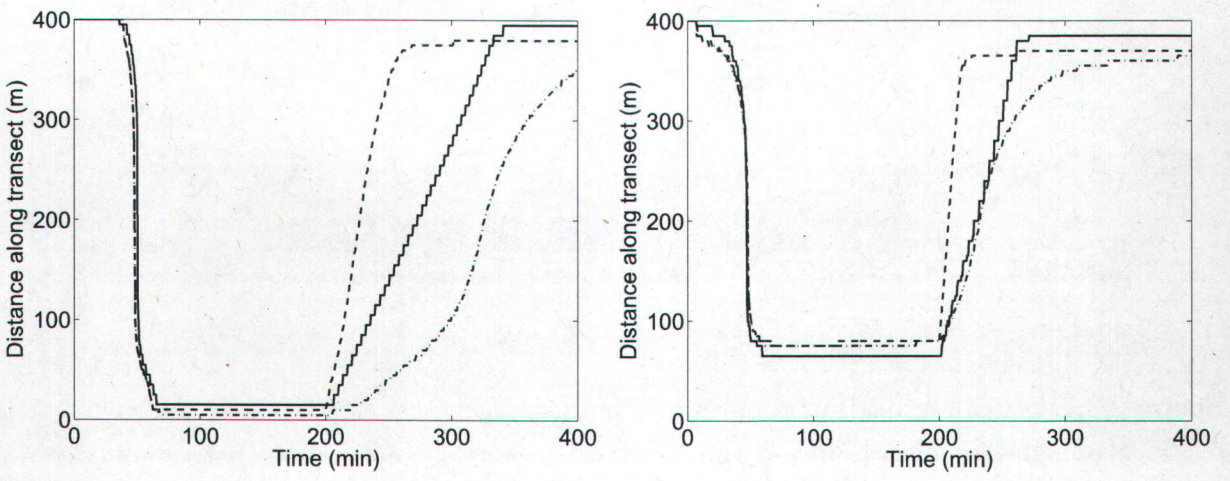

Figure 2.8: Evolution of the point of intersection between the water table and the land surface for the sloping plane test case with slope angles 0.5% (left) and 5.0% (right). The outlet face is at x = 400 m. ParFlow results are the solid lines and CATHY results are the dashed-dotted lines (sheet flow) and dashed lines (rill flow)

The simulation results are shown in Figure 2.8 for the transect in the middle of the sloping plane. At gentler slopes, infiltration and subsurface flow remain predominantly vertical, thus the water table rise is relatively uniform over the catchment, and slower than at the downslope nodes of the steeper case. It thus takes longer for the exit point to move upslope, but when it does so it is more abrupt than for the steeper slope, and it reaches a higher position upslope (saturating almost the entire catchment). When rainfall ceases, on the other hand, gentler-sloping catchments drain more slowly than steep catchments, and thus we observe that during the recession phase the exit point recedes downslope more slowly than for the steep plane. As can be seen in Figure 2.8, ParFlow and CATHY agree quite well for both slopes in the timing of the water table intersection with the ground surface and in its evolution during the entire rainfall period. A more marked discrepancy (especially for the 0.5% slope) was instead found for the evaporation period, with the CATHY model sheet flow case characterized by a slower downward recession of the exit point. This discrepancy may be attributed to the different parameterizations of the routing scheme diffusion process in the two models. The close match between ParFlow and both CATHY parameterizations during the rainfall period clearly indicates that the dynamics of the return flow process is controlled by the subsurface domain during this phase, whereas surface routing dominates the process during the recession phase. It is interesting to observe that, despite the differences in ParFlow and CATHY response during the recession period, the ParFlow result nonetheless lies within the envelope defined by the CATHY rill and sheet flow extremes.

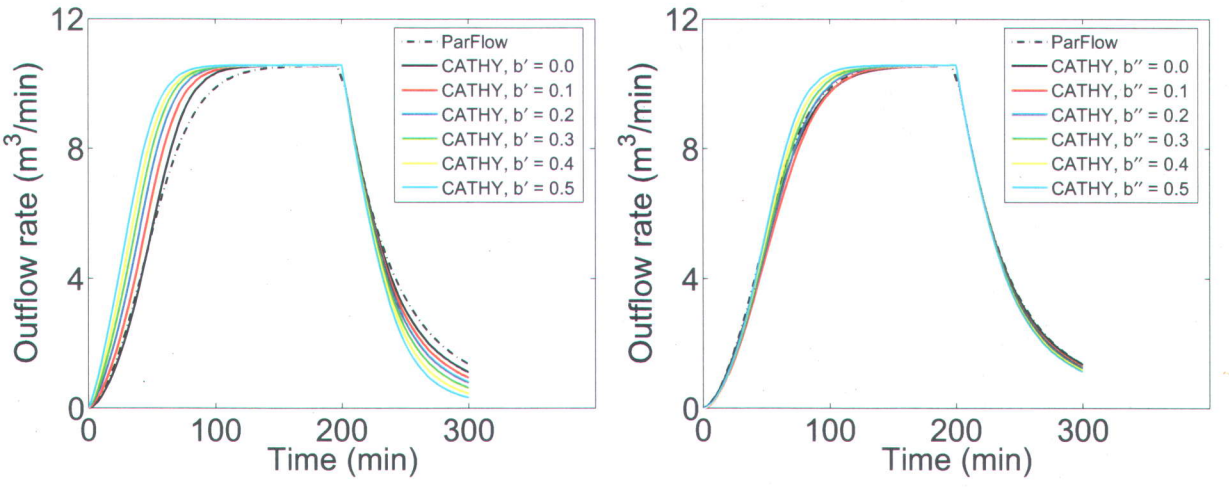

Figure 2.9: Sloping plane test case: comparison of outflow responses for sheet flow (ParFlow) and rill flow (CATHY) surface routing models. For CATHY a range of "at-a-station" (b', left) and "downstream" (b'', right) *Leopold and Maddock Jr. [1953]* scaling exponents was used.

2.4.1.4 Overland flow routing

The representation of surface runoff as two-dimensional sheet flow or as one-dimensional rill flow can have a strong effect on ponding heads, surface flow velocities, and outlet hydrographs *[Grayson et al., 1992a]*, and on connected overland and channel flow processes such as soil erosion and sediment transport *[Moore and Burch, 1986; Hairsine and Rose, 1992a,b]*. In this next set of simulations on the sloping plane (with DEM resolution 80 m and slope angle 0.05%), the influence of hydraulic geometry parameters was investigated, as well as the possibility of setting "equivalent" parameterizations between the sheet flow conceptualization used in ParFlow and the rill flow representation in CATHY.

In CATHY the water-surface width of each cell of the river network is scaled in space as a function of the upstream drainage area according to the following relationship:

$$W(A,1) = W(A_s, Q_f)\, Q_f(A_s)^{-b'}\, (A/A_s)^{w(b''-b')} \tag{2.15}$$

where $W(A,1)$ is the water-surface width at a site draining area A for a unit-flow discharge. This unit-flow water-surface width is dynamically varied in time as a function of the simulated flow discharge Q by multiplying equation (2.15) by $Q^{b'}$ (see equation (2.7)). In the simulations presented here we set $W(A_s, Q_f)$ to 80 m, with A_s= 3.2×10^4 m^2 being the drainage area at the outlet cell and Q_f= 10.56 m^3/min being the steady state outlet discharge obtained from a simulation with b' and b'' equal to zero, i.e., with a water-surface width of 80 m over the

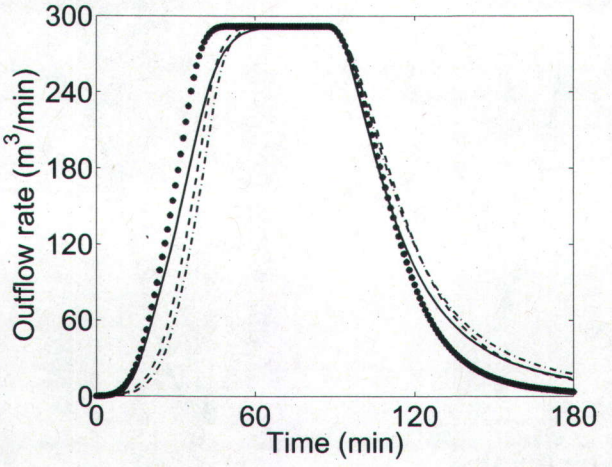

Figure 2.10: Outflow response for the tilted V-catchment test case: ParFlow (solid line), CATHY with sheet flow parameterization (dashed-dotted line), CATHY with rill flow parameterization (dotted line), and CATHY with combined sheet and rill flow parameterization, for the channel and hillslope, respectively (dashed line).

entire catchment and through the entire simulation. This set of values, with the water-surface width constant and equal to the DEM resolution, should correspond most closely to a sheet flow representation. With these values of A_s, Q_f, and $W(A_s, Q_f)$, different surface width parameterizations were then simulated in CATHY by using different values of the *Leopold and Maddock Jr. [1953]* "at-a-station" (b') and "downstream" (b'') scaling exponents. The results of these tests are presented in Figure 2.9, on the left for fixed b'' (0.5) and varying b' (from 0.0 to 0.5 in increments of 0.1) and on the right for fixed b' (0.0) and varying b'' (from 0.0 to 0.5 in increments of 0.1). When b'=0.0 the water-surface width is time-invariant and when b'=b'' it is space-invariant. The upper value of 0.5 for both the b' and b'' ranges is taken from *Orlandini and Rosso [1996]*. For increasing b' we get decreasing water-surface

Table 2.2: CATHY surface parameters for the tilted V-catchment test case.

	$W(A_s, Q_f)$ [m]	A_s [m^2]	Q_f [m^3/min]	b', b'' [/]
Sheet flow:				
– hillslope and channel cells	20	1.62×10^6	291.6	0, 0
Rill flow:				
– hillslope cells	6.5	1.6×10^4	2.88	0.36, 0.50
– channel cells	20	1.62×10^6	291.6	0.36, 0.50
Combined rill/sheet flow:				
– hillslope cells	20	1.6×10^4	2.88	0.36, 0.50
– channel cells	20	1.62×10^6	291.6	0, 0

widths, and thus faster routing and hydrograph response, as can be seen in Figure 2.9. For increasing b'' (with b'=0) we also get decreasing water-surface widths and again faster hydrograph response. Figure 2.9 shows that the CATHY model is more sensitive to the "at-a-station" scaling exponent than to the "downstream" exponent, which is to be expected for a sloping plane, where the drainage area varies linearly with elevation.

As alluded to above, the combination b'=0, b''=0 in Figure 2.9 does indeed produce the closest match with the ParFlow (sheet flow) results. It is thus possible in this test case to parameterize a rill flow conceptualization that accurately mimics a sheet flow model. It is notable that this good match was obtained despite the different approximations of the Saint-Venant equation (kinematic and diffusion waves) implemented in the ParFlow and CATHY models, and despite the gentle slope of the plane catchment, which favors diffusion-dominated overland flow (compensated for in kinematic wave models by the introduction of numerical diffusion *[Chow et al., 1988]*).

2.4.2 Tilted V-catchment

For the tilted V-catchment rill and sheet flow conceptualizations are again examined. In this case three different water-surface width parameterizations for the CATHY model are compared against the sheet flow results obtained with ParFlow. In the first parameterization a sheet flow representation was used for the entire catchment, in the second a rill flow representation, and in the third case sheet flow was used for the channel cells and rill flow for the hillslope cells. In the first case we set b' and b'' to zero and $W(A_s, Q_f)$ to 20 m (equal to the DEM resolution), with $A_s = 1.62 \times 10^6$ m^2 being the drainage area of the entire catchment and $Q_f = 291.6$ m^3/min being the steady state outlet discharge obtained for this combination of parameter values. In the rill flow parameterization for the entire catchment (second case) we set b'=0.36 and b''=0.50, with, for the hillslope portion of the catchment surface, $W(A_s, Q_f) = 6.5$ m (water-surface width at the uppermost channel cell at steady state), $A_s = 1.6 \times 10^4$ m^2 (the drainage area at the hillslope outlet cell), and $Q_f = 2.88$ m^3/min (the steady state discharge at the hillslope outlet cell), and for the channel portion of the catchment domain, $W(A_s, Q_f) = 20$ m, $A_s = 1.62 \times 10^6$ m^2, and $Q_f = 291.6$ m^3/min. In the third case (combined sheet and rill flow) we set $b' = b'' = 0$ for the channel cells and b'= 0.36, b''= 0.50 for the hillslope cells, with $W(A_s, Q_f) = 20$ m (water-surface width at channel cells at steady state condition), $A_s = 1.6$ x 10^4 m^2, and $Q_f = 2.88$ m^3/min for the hillslope cells and $W(A_s, Q_f) = 20$ m, $A_s = 1.62 \times 10^6$ m^2, and $Q_f = 291.6$ m^3/min for the channel cells.

The results in Figure 2.10 for the ParFlow model and for the three surface routing parameterizations in CATHY show that the ParFlow hydrograph lies between the CATHY rill flow

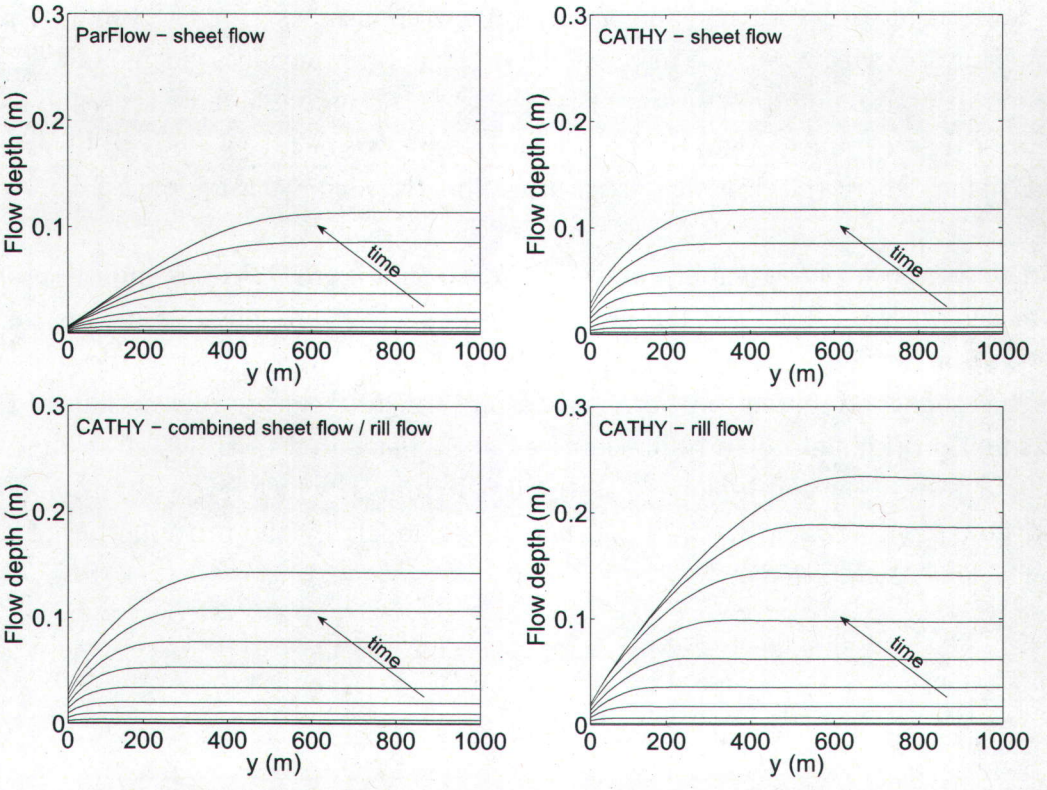

Figure 2.11: Tilted V-catchment test case: evolution of surface flow depth along the channel ($x = 800$ m) during the first 30 min of the rainfall period for CATHY (using three different surface routing parameterizations) and for ParFlow. The catchment outlet is at $y = 1000$ m.

case (fastest response) and the CATHY sheet flow case (slowest response). The sheet flow and combined sheet flow/rill flow responses are very similar, and are closer to ParFlow's sheet flow hydrograph, suggesting that the channel flow segment of the catchment dominates the response for this test case. The differences between rill flow and sheet flow dynamics are highlighted in Figure 2.11, which traces the evolution of ponding heads (surface flow depths) along the channel during the first 30-min of rainfall for CATHY (three different parameterizations) and for ParFlow. The flow depths are lowest for the sheet flow conceptualization, about 50% higher for the combined sheet/rill flow case, and about two times higher (relative to the combined case) for the rill flow parameterization. The energy gradients are also much stronger in the rill flow case, in particular along the first 600 m of the channel reach. This is due to the nonlinearity of the stage-discharge relationship for the three simulated flow conditions. These differences in water depth profiles (steeper in space and faster in time for the rill flow parameterization) underscore the differences in erosion potential and sediment transport capacity between the two conceptualizations.

2.5 Conclusions

Two physically-based, spatially-distributed models of conjunctive surface and subsurface flow, ParFlow and CATHY, have been compared. The analysis has been focused on examining the coupling approaches implemented in the two models and the different conceptualizations used to describe the propagation of surface runoff. The theoretical and numerical bases for ParFlow and CATHY were briefly presented, highlighting key features and differences between the models, and two test problems were simulated under a variety of configurations and parameter combinations to explore runoff generation, surface routing, and other dynamics, and the impact of heterogeneity, grid resolution, and other factors on this dynamics.

ParFlow and CATHY were both found to be quite sensitive to vertical discretization for scenarios of infiltration excess runoff generation, with some differences in behavior between the two models due also to the different discretization schemes used (finite difference and finite element). For both models, convergence of the solutions under mesh refinement was demonstrated. The CATHY model was found to be more sensitive to temporal discretization, in particular for the heterogeneous test case, owing to the sequential coupling approach used in this model. It was shown that under "equivalent" sheet flow parameterizations the CATHY and ParFlow models produce very similar hydrograph responses at the catchment outlet, and differences in CATHY model response under rill flow and sheet flow conceptualizations were highlighted.

A broader goal of this study is to encourage additional efforts to assess coupled surface–subsurface models, given the variety of formulations and approaches that have recently been proposed for representing flow interactions and other processes. Suitable benchmark test cases will need to be devised to extend the work presented here, for instance larger catchments with more complex geometry and topography.

Chapter 3

Assessment of climate change impacts at the catchment scale with a detailed hydrological model of surface/subsurface interactions, and comparison with a land surface model

Abstract

A process-based model that incorporates the hydrodynamic feedbacks between the land surface, soil, and groundwater zones is used to assess the sensitivity of the hydrological response (river discharge, aquifer recharge, and soil water storage) to future climate conditions for the des Anglais catchment located in southwestern Quebec (Canada). The application of the coupled hydrological model (CATHY) to the study basin reveals significant spatio-temporal variations in the river discharge response to climate change owing to a different partitioning between the overland runoff and baseflow components of the hydrograph, with the latter alleviating the marked decrease in discharge during the summer period. A spatial analysis of recharge patterns shows that the greatest variations are expected to occur, throughout the year, in the southern portion of the catchment, where the elevations are highest. Compared to river discharge and aquifer recharge, the soil water storage volumes are less sensitive to climate changes. From a spatial analysis of soil moisture variations it was possible to observe organizational patterns that follow the topographic and pedologic characteristics of the catchment. In addition to these analyses, we also compare predictions obtained with CLASS, the land

surface scheme that is coupled to the CRCM model, to those from the detailed catchment model for past and future climate change projections. An examination of the runoff and soil water storage response is used to highlight some of the key differences in the two models. CLASS produces higher estimates than CATHY of surface and subsurface runoff throughout the annual cycle for both past and future projections. For soil water storage, the two models are in general agreement in terms of the intra-annual variability of moisture content at shallower soil layers, whereas a larger difference is found for the deepest layer, with CATHY predicting wetter soil conditions over the entire simulation period and moisture fluctuations of much smaller amplitude.

3.1 Introduction

The Intergovernmental Panel on Climate Change (IPCC) has found evidence that recent regional climate changes, particularly temperature increases, have already affected many physical and biological systems *[Intergovernamental Panel on Climate Change (IPCC), 2007]*. General circulation models (GCMs), aided by appropriate downscaling techniques, have long been used to simulate changes in regional climate systems over wide spatio-temporal scales, and to allow information from large scale atmospheric simulations to be used in smaller scale hydrological models *[Wilby and Wigley, 1997; Arnell et al., 2003]*.

Changes in future climate will alter regional hydrological cycles with a subsequent impact on the quantity and quality of regional water resources *[Gleick, 1989]*. While climate change affects surface water directly through changes in long-term climate variables, the impacts on groundwater are more difficult to assess *[Jyrkama and Sykes, 2007]*. To address this issue a number of studies have been undertaken. *Dooge et al. [1999]* explored the sensitivity of runoff to climate change for three scenarios using a very simple hydrological model. *Arora and Boer [2001]* studied the impact of future climate change on the hydrology of 23 major river basins using a GCM coupled to a simple 1-layer surface scheme and a river routing algorithm that included surface and groundwater reservoirs. *Caballero et al. [2007]* investigated the sensitivity during low-flow periods of a regional scale basin with a hydrometeorological modeling system. *York et al. [2002]* and *Scibek and Allen [2006]* studied climate change impacts on groundwater recharge while *Tague et al. [2008]* highlighted the role of groundwater in maintaining baseflow under an altered climate. *Quilbe et al. [2008]* and *van Roosmalen et al. [2009]* examined the combined effects of future climate and land use changes on agricultural watersheds. Despite these studies, very few assessments of climate change impacts on freshwater resources have been conducted using fully coupled numerical models that consider the important hydrodynamic feedbacks between the land surface, soil, and groundwater zones.

Interactions between surface and subsurface water play a critical role in the hydrological cycle *[e.g., Liang et al., 2003; Gulden et al., 2007; Maxwell et al., 2007]*. Improving the representation of infiltration and soil moisture processes in current land surface models is considered essential for accurate simulation of energy and moisture fluxes. Soil moisture plays a key role in partitioning precipitation into infiltration, surface runoff, and drainage to groundwater, and it also controls the partitioning of energy into sensible and latent heat fluxes at the ground surface, affecting the coupling between the land surface and the atmospheric boundary layer *[Brubaker and Entekhabi, 1996; Eltahir, 1998]*. Although land surface models have evolved from simple *[Manabe et al., 1965]* to more sophisticated parameterizations *[Lee and Abriola, 1999; Wang et al., 2002; Pitman, 2003; Yeh and Eltahir, 2005]*, they are still limited to vertical moisture transport in the soil column and lack an adequate representation of surface and subsurface lateral transport due to topography or moisture gradients. Lateral processes and a better surface–subsurface coupling, commonly considered at small hillslope and catchment scales *[Singh and Woolhiser, 2002; Furman, 2008]*, can also play an important role at larger regional scales, especially if latent heat flux–soil moisture feedbacks and shallow water table dynamics are embedded in fully integrated hydrometeorological models *[Fan et al., 2007; Kollet and Maxwell, 2008]*.

This work presents an assessment of climate change impacts for a medium-sized catchment (690 km^2) based on numerical simulations with a coupled physically-based model of surface and groundwater flow. A distributed model of this type allows us to investigate in detail the role of feedbacks between near-surface and deeper hydrological processes, the influence of factors such as topography and subsurface heterogeneity in amplifying or attenuating eventual impacts, and the ways in which processes that control the catchment dynamics can be altered in response to climate changes. The study area is the des Anglais river basin located in southwestern Quebec (Canada). The future climate projection (2041-2070) was constructed by applying to an observed daily dataset (1961-1990) a monthly deviation factor extracted from projections generated by the Canadian Regional Climate Model (CRCM) *[Music and Caya, 2007]*. This approach eliminates biases in the climate simulations (differences between observed and simulated climate), especially in precipitation, and it allows incorporation of detailed meteorological information contained in site-specific data *[Rivington et al., 2008]*.

An additional objective of this study was to compare results from the process-based catchment hydrological model with those obtained from the land surface model that has recently been coupled to the CRCM. Land surface schemes have been extensively evaluated against observed data and through intercomparison studies *[e.g., Bowling et al., 2003; Boone et al., 2004]*. For the des Anglais study, the surface–subsurface runoff and soil water predictions obtained from the Canadian LAnd Surface Scheme (CLASS) *[Verseghy, 1991; Verseghy et al., 1993]* are compared to those obtained with the CATHY (CATchment HYdrology) coupled groundwater–surface water model *[Camporese et al., 2010]*. The size of the study area, rel-

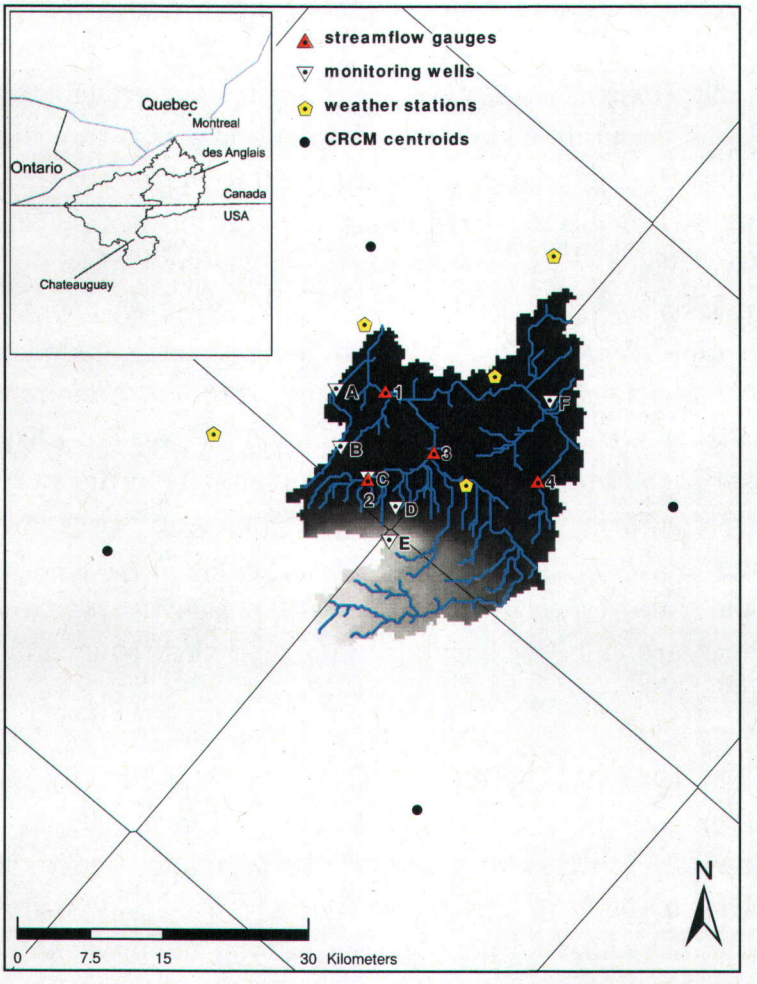

Figure 3.1: Topographic map of the des Anglais river basin (highest elevations in light grey) showing the network of weather stations, streamflow gauges, and monitoring wells, and the centroids of the CRCM grid with their Thiessen polygons.

atively large for a detailed surface–subsurface model and comparatively small for a land surface model, is a convenient spatial scale at which to investigate the importance of a three-dimensional representation of a catchment that takes into account a mathematical description of surface and subsurface processes and of factors such as topography and water table dynamics.

3.2 Study Area

The des Anglais river basin (Figure 3.1) has a drainage area of 690 km^2 and an average discharge of 300 $\times 10^6$ m^3 per year at its outlet. It is the largest sub-catchment of the

transboundary Chateauguay River watershed, and has an elevation range from 30 m to 400 m. The Chateauguay basin constitutes the northern part of Adirondack mountain range and initiates the physiographical region of the St. Lawrence Platform. The aquifer system in this region is part of the St. Lawrence Lowlands and consists of Cambrian to Middle Ordovician sedimentary rocks that are slightly deformed and fractured. Unconsolidated sediments of glacial and post-glacial origin (Wisconsinan period and Champlain sea event) overlay the bedrock aquifer and are of varying thickness, reaching 40 m in the northernmost portion *[Tremblay, 2006]*. These sediments are in turn overlain by Quaternary deposits of silty till, compact and dense at the base and reworked and more permeable above. The soils are characterized as mainly weathered Quaternary sediments *[Lamontagne, 2005]*, with the exception of bogs and swamps that overly Champlain sea sediments in the northeastern part of the catchment. These wetlands correspond to closed depressions with a thick accumulation of organic material.

Water table fluctuations in the des Anglais catchment are mainly driven by springtime snowmelt and by rainfall in the fall. The groundwater recession typically extends from June to the end of the growing season (September-October). Mean annual water table fluctuations are about 2.7 m under unconfined or semi-confined conditions and about 1.6 m under confined conditions *[Côté et al., 2006]*. The study area belongs to the Great Lakes and St. Lawrence climate region, characterized by a semi-humid climate with cold winters and humid summers. The annual mean temperature is 6.3 °C, with monthly variations from -10 °C in January to 20 °C in July *[Environment Canada, 2004]*. These temperatures result in frost conditions from mid-November to the end of March. The average annual precipitation is 958 mm, relatively uniformly distributed within the watershed, with snowfall prevalent from December to March when temperatures are below 0 °C.

3.3 Simulation Models

3.3.1 Catchment Hydrological Model

CATHY is a coupled physically-based spatially-distributed model for surface–subsurface simulations *[Camporese et al., 2010]*. The model is based on resolution of a one-dimensional diffusion wave approximation of the Saint-Venant equation for overland and channel routing nested within a solver for the three-dimensional equation for subsurface flow in variably saturated porous media (i.e., Richards equation). The routing scheme derives from a discretization of the kinematic wave equation based on the Muskingum-Cunge or matched artificial dispersivity method. Surface runoff is propagated through a 1D drainage network

of rivulets and channels automatically extracted by a digital elevation model (DEM)-based pre-processor and characterized using hydraulic geometry scaling relationships. The distinction between overland and channel flow regimes is made using threshold-type relationships based on, for instance, upstream drainage area criteria. Lakes and other topographic depressions are identified and specially treated as part of the DEM pre-processing procedure. The subsurface solver is based on Galerkin finite elements in space, a weighted finite difference scheme in time, and linearization via Newton or Picard iteration.

A boundary condition switching procedure is used to partition potential (atmospheric) fluxes into actual fluxes across the land surface and changes in surface storage. This scheme resolves the coupling term in the CATHY equations that represents the interactions between surface and subsurface waters. The switching procedure distinguishes four possible states for a given surface node: ponded, saturated, unsaturated, and air-dry. The distinction between ponded and saturated is based on a threshold parameter that represents the minimum water depth before surface routing can occur (the threshold would be zero for instance for perfectly smooth surfaces and higher for increasingly rough surfaces). An air-dry state is the evaporative analog to rainfall saturation in triggering a switch from an atmosphere-controlled process (and a Neumann boundary condition in the model) to a soil-limited stage (and a Dirichlet condition).

3.3.2 Regional Climate and Land Surface Models

The CRCM is a limited area, three-dimensional, nested grid–point atmospheric model based on the fully elastic nonhydrostatic Euler equations *[Caya and Laprise, 1999; Music and Caya, 2007]*. The equations are solved by noncentered semi-implicit and semi-Lagrangian numerical schemes. The model is run over a regional domain (on typical scales of 100s to 1000s of kilometers) cast on a horizontal grid that is uniform on a polar stereographic projection. A typical horizontal resolution is 45 km. Time-dependent data are provided at the lateral boundaries of the regional domain by reanalyses of observational data or GCM output at coarser horizontal resolutions. The vertical resolution is variable and uses a Gal-Chen scaled terrain following vertical coordinate.

Within the CRCM, turbulent exchanges of energy, water, and momentum at the surface–atmosphere interface are computed by CLASS, a physically based soil–snow–vegetation land surface scheme *[Verseghy, 1991; Verseghy et al., 1993]*. CLASS is commonly referred to as a second generation scheme (see *Pitman [2003]* for a comprehensive review) that uses an explicit representation of temperature and liquid and frozen soil moisture for three soil layers (a 10 cm surface layer, a 25 cm vegetation root zone layer, and a 3.75 m deep soil layer), an explicit vegetation canopy allowing stomatal and root zone control of evapotranspiration, and

a thermally and hydrologically distinct snow pack present during the cold seasons, acting in effect as a fourth separate "soil" layer. For the soil layers, CLASS solves the one-dimensional Darcy equation for vertical fluid flow in porous media (with both suction and gravity terms) and thermal conduction equations for soil temperatures. Water infiltration into the upper soil layer is treated as a downward propagating square wave *[Green and Ampt, 1911; Mein and Larson, 1973]*. When the infiltration capacity is exceeded, water is considered to be ponded at the surface up to a maximum surface retention capacity, which varies according to land cover, and beyond which surface runoff occurs. Subsurface runoff is crudely simulated as a "bottom drainage" out from the deepest soil layer (0.35–4.10 m depth), parameterized via an empirical power relation linking the saturated hydraulic conductivity and volumetric liquid water content *[Clapp and Hornberger, 1978]*. As CLASS was meant first and foremost to provide adequate boundary conditions to a coupled atmospheric model through surface fluxes of water, energy, and momentum, it does not explicitly account for the water table depth, lateral groundwater flow, and surface or subsurface routing to streams, and its soil domain remains within the vadose (unsaturated) zone.

3.4 Methodology

3.4.1 Analysis of the Climate Data

Climate projections for past and future conditions were taken from CRCM (version 4.2.3) driven by atmospheric fields from the Canadian General Circulation Model (CGCM, version 3.1), whose atmospheric component is described by *Scinocca et al. [2008]* and whose ocean and sea-ice components and coupling scheme are described by *Flato and Boer [2001]*. The model run used was ensemble member #3 based on the IPCC Special Report on Emission Scenario (SRES) A2 scenario *[Nakicenovic and Swart, 2000]*. The simulations were run over the regional domain covering North America (AMNO with 200×192 grid points) with a horizontal grid-size mesh of 45 km (polar stereographic projection, true at 60 N). The past CRCM simulation was run over the period 1958-2000 and used the observed greenhouse gas and aerosol concentrations until 2000. The future run was run over the period 2038-2070 and used the post-2000 SRES A2 greenhouse gas and aerosol projected evolution *[Nakicenovic and Swart, 2000]*. The same evolutions were used by the driving CGCM. Model output was archived on a 6-hourly basis over the periods considered. The spectral nudging technique *[Riette and Caya, 2002]* was applied within the interior of the regional domain to keep CRCM's large-scale flow close to its driving data. Both simulations have a three-year spin-up period for the climate system to reach equilibrium (the timescale of this equilibrium tends to be dominated by the land surface deep soil layer).

An important issue when considering adaptation and mitigation responses to climate change is the uncertainty in the prediction of future climate *[Christensen and Christensen, 2007]*. In addition to uncertainty derived from models formulation, there is that derived from natural climate variability and future atmospheric emissions. Thus, the use of data for multiple greenhouse gas emission scenarios from multiple climate models would be beneficial for the definition of an uncertainty envelope of future hydrologic conditions *[Prudhomme et al., 2003]*. Because the purpose of the present study is not to cover the full range of plausible future climates to propose adaptation measures for water management practices but rather to investigate the sensitivity of surface–subsurface interactions to climate change, the use of just one set of data from the CRCM model was deemed acceptable.

The simulated CRCM climate data were analyzed using the non-parametric Mann-Kendall statistical test *[Mann, 1945; Kendall, 1975]*, widely used in hydrological trend detection studies to verify the null hypothesis of no trend in a time series. In this study the test was applied to annual and mean monthly CRCM-generated values for both past and future periods. One problem associated with this test is that the result is affected by serial correlation in the time series. Specifically, if a positive serial correlation is present, the test will suggest a significant trend more often than it actually should *[von Storch and Navarra, 1995]*. To eliminate this effect without biasing the trend's magnitude, we applied the Mann-Kendall test to a pre-whitened time series obtained following the procedure proposed by *Yue et al. [2002]*, consisting first in removing the slope, then the lag-1 serial correlation from the time series, and finally putting back the slope.

The Mann-Kendall test statistic (S) is given by

$$S = \sum_{k=1}^{n-1} \sum_{j=k+1}^{n} \mathrm{sgn}(x_j - x_k) \tag{3.1}$$

where $\mathrm{sgn}(\theta)$ =1, 0, or -1 for θ positive, zero, or negative, respectively, n is the data set record length, and x_j and x_k are the sequential data values.

The Mann-Kendall test has two parameters that are important for trend detection: the significance level, which indicates the trend's strength, and the slope estimate, which indicates the direction as well as the rate of change. Under the null hypothesis that there is no trend in the data, the distribution of S is expected to have a mean of zero and a variance of $n(n-1)(2n+5)/18$.

Table 3.1: Summary of trend analysis for annual and monthly values of total precipitation and maximum and minimum temperature for the past simulation (1961-90).

	Precipitation			Max. temperature			Min. temperature		
	Test Z	Significance	Slope (β)	Test Z	Significance	Slope (β)	Test Z	Significance	Slope (β)
Annual	-0.694	*ns*	-2.350	2.195	**	0.033	2.32	**	0.035
Jan	-1.369	*ns*	-0.613	-1.332	*ns*	-0.091	-0.994	*ns*	-0.050
Feb	1.032	*ns*	0.530	0.844	*ns*	0.043	1.294	*ns*	0.093
Mar	1.144	*ns*	1.022	1.632	*ns*	0.063	1.519	*ns*	0.111
Apr	0.131	*ns*	0.124	0.356	*ns*	0.023	1.294	*ns*	0.068
May	-0.844	*ns*	-0.795	0.619	*ns*	0.033	0.957	*ns*	0.035
Jun	-1.632	*ns*	-0.958	1.444	*ns*	0.077	0.994	*ns*	0.029
Jul	-0.431	*ns*	-0.326	2.720	***	0.124	2.945	***	0.089
Aug	-1.482	*ns*	-1.14	2.444	*ns*	0.010	0.169	*ns*	0.006
Sep	-1.594	*ns*	-0.685	0.957	*ns*	0.039	0.469	*ns*	0.030
Oct	1.219	*ns*	0.397	1.219	*ns*	0.052	0.131	*ns*	0.009
Nov	0.694	*ns*	0.420	0.244	*ns*	0.008	0.319	*ns*	0.13
Dec	0.694	*ns*	0.427	0.244	*ns*	0.017	0.994	*ns*	0.050

$***$ and $**$ indicate significance levels of 0.01 and 0.05; *ns* indicates significance level exceeds 0.1

The normal Z-test statistic is calculated as

$$Z = \begin{cases} \dfrac{S-1}{\sqrt{\text{var}(S)}} & \text{if } S > 0 \\ 0 & \text{if } S = 0 \\ \dfrac{S+1}{\sqrt{\text{var}(S)}} & \text{if } S < 0 \end{cases}$$

The null hypothesis is rejected at significance level of α if $|Z| > Z_{(1-\alpha/2)}$, where $Z_{(1-\alpha/2)}$ is the value of the standard normal distribution with a probability of exceedance of $\alpha/2$. A positive value of Z indicates an upward trend while a negative value represents a downward trend.

Trend magnitude is estimated using a non-parametric median based slope method proposed by *Sen [1968]* and extended by *Hirsh et al. [1982]*:

$$\beta = \text{Median}\left[\frac{x_j - x_k}{j-k}\right] \text{ for all } k < j \tag{3.2}$$

where $1 < k < j < n$. β is the median of all possible combinations of pairs for the whole dataset.

Statistically significant trends in annual precipitation were not detected for either past or future periods (Tables 3.1 and 3.2). From the analysis of monthly values a significant negative trend was detected for late spring (May) and for two summer months (July and August) of the future period. Positive trends were found in annual mean values of minimum and maximum

Table 3.2: Summary of trend analysis for annual and monthly values of total precipitation and maximum and minimum temperature for the future projection (2041-70).

	Precipitation			Max. temperature			Min. temperature		
	Test Z	Significance	Slope (β)	Test Z	Significance	Slope (β)	Test Z	Significance	Slope (β)
Annual	-1.519	*ns*	-3.762	4.033	***	0.094	3.058	***	0.077
Jan	1.257	*ns*	0.744	3.170	***	0.161	2.307	**	0.170
Feb	0.056	*ns*	0.152	2.795	***	0.189	2.457	**	0.162
Mar	0.356	*ns*	0.444	0.732	*ns*	0.053	1.219	*ns*	0.112
Apr	0.019	*ns*	0.041	2.457	**	0.116	2.908	***	0.139
May	-2.007	**	-1.683	2.682	***	0.123	2.795	***	0.099
Jun	-0.919	*ns*	-0.784	2.682	***	0.106	3.020	***	0.083
Jul	-1.932	*	-1.671	1.707	*	0.107	0.957	*ns*	0.026
Aug	-2.908	***	-2.538	2.382	**	0.110	1.632	*ns*	0.056
Sep	-1.069	*ns*	-0.853	1.707	*	0.118	1.294	*ns*	0.062
Oct	0.657	*ns*	0.771	1.932	*	0.083	1.294	*ns*	0.060
Nov	0.319	*ns*	0.226	0.657	*ns*	0.046	0.994	*ns*	0.039
Dec	0.000	*ns*	0.000	-0.244	*ns*	-0.013	-0.469	*ns*	-0.032

$***$, $**$, and $*$ indicate significance levels of 0.01, 0.05, and 0.1; *ns* indicates significance level exceeds 0.1

temperatures for both periods, with a decrease in significance level from 5% to 1% from the past to the future projection. On a monthly basis, only July shows an increasing trend for the past period, for both min and max temperatures (Table 3.1). For the future projection most of the calendar months (9, spread over the four seasons) show significant increasing trends in maximum temperature, while 5 months (in winter, spring, and summer) do so for minimum temperatures (Table 3.2).

Overall, the trends detected in the CRCM-generated data for the past period are consistent with the results of a previous study based on an observation dataset for the entire country *[Zhang et al., 2000]*, i.e., a statistically significant positive trend found for annual maximum temperatures (and hence in potential evapotranspiration) and almost no statistically significant trend in annual precipitation. In a subsequent analysis of historical streamflow data for Canada, *Zhang et al. [2001]* found that the combination of stable precipitation and increasing temperatures produced a negative trend in annual mean streamflow, an earlier snow and ice melt, and, in addition, an increase in the rainfall proportion of total precipitation. This in turn produces more direct runoff and accelerates snowmelt as the wet snowpack absorbs more solar radiation. The consistency with national temperature and precipitation trends for the past period suggests that the CRCM-generated future projection will produce similar changes in streamflow for the des Anglais catchment if directly applied as atmospheric forcing input.

3.4.2 Hydrological Model Setup

3.4.2.1 Climate data

In climate change impact studies large scale atmospheric variables need to be related to local or station scale meteorological datasets. *Scibek and Allen [2006]* used a statistical downscaling model to extract monthly change factors from the CGCM and redistribute them to daily time series using a stochastic weather generator; *van Roosmalen et al. [2009]* applied a monthly deviation between future and past periods to overcome systematic biases in past data between observed and simulated (by a regional climate model) time series; *Chiew et al. [2009]* applied a daily downscaling method that considers changes in future mean seasonal rainfall and daily rainfall distribution to 15 GCM-generated datasets.

For the des Anglais river basin, the CRCM yielded estimates of mean monthly temperature that are comparable to observed data and mean monthly precipitation that vary somewhat from observed values (Figure 3.2). The observed data shown in this figure covers the same 1961-90 time period as the CRCM-generated past simulation. Weighted averaging is used to calculate the observed and CRCM data, in the former case using the five weather stations shown in Figure 3.1, and in the latter case according to the Thiessen polygons, also shown in Figure 3.1. In Figure 3.2 we observe in particular a marked overestimation of mean precipitation for late spring and summer. To construct the future climate projection dataset for the hydrological model simulations it was thus necessary to apply a transfer scheme such as the commonly used delta change method *[Hay et al., 2000; van Roosmalen et al., 2009]*, which consists in perturbing baseline meteorological data with monthly change values. The monthly change values are calculated as the difference in CRCM atmospheric outputs between the past and future 30-year climate periods. In applying the delta change method, it is assumed that the relative and/or absolute changes in precipitation and temperature between past and future climate simulations such as simulated by the CRCM have a strong physical basis, and that rainfall recurrence patterns remains the same between past and future periods. Thus scaled and baseline scenarios differ only in terms of their respective means, maxima, and minima; all other properties of the data, such as the range and variability, remain unchanged. The delta change method does not easily apply to precipitation records, because the multiplication of observed precipitation by CRCM precipitation changes does not affect the number of rain days. This means that the temporal sequencing of wet and dry days is unchanged, and so the method may not be helpful in circumstances where changes in spell lengths are important to the impact assessment. The importance for the des Anglais basin of snow accumulation and snowmelt processes alleviates this limitation to some extent. The CATHY hydrological model was thus driven by the observed 1961-90 dataset (daily precipitation and min and max temperatures) for the past simulation, and by this same

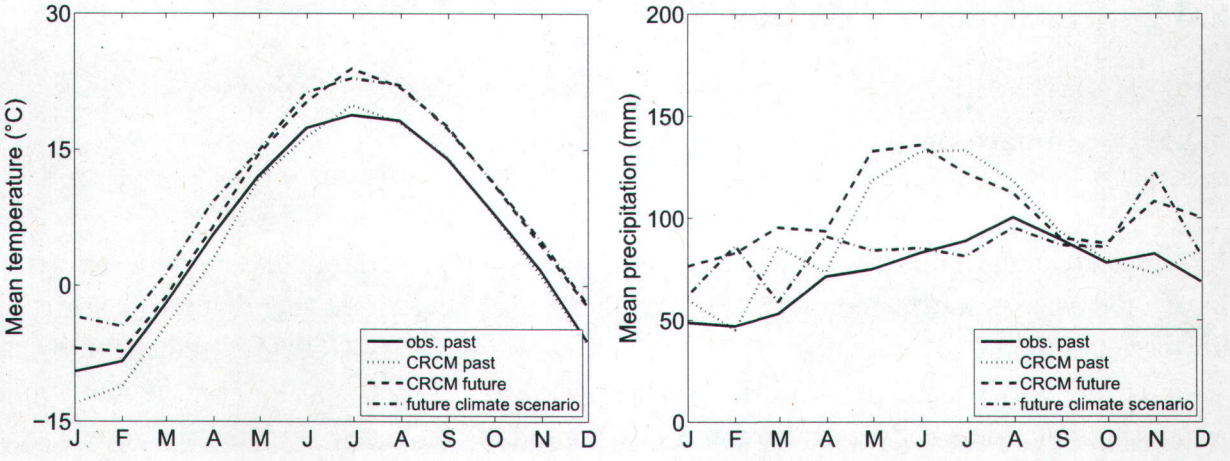

Figure 3.2: Mean monthly temperature and precipitation: observed past data (solid line), CRCM-generated values for the past simulation (dotted line), CRCM-generated values for the future projection (dashed line), and values for the future climate scenario based on the delta change method (dash-dotted line).

baseline dataset perturbed as per the delta change method for the future projection.

The precipitation input $P_\Delta(i,j,k)$ for day i, month j, and year k of the future projection is calculated as

$$P_\Delta(i,j,k) = \Delta_P(j) \times P_{obs}(i,j,k) \quad ; \quad i = 1,2,\ldots,31\,; j = 1,2,\ldots,12\,; k = 1,2,\ldots,30 \quad (3.3)$$

where P_{obs} is the observed past precipitation and Δ_P(j) is the delta method correction factor, calculated for each month j as $\overline{P_f}(j)/\overline{P_p}(j)$, where $\overline{P}(j)$ is the mean precipitation for month j averaged over the 30-year CRCM-generated past (p) and future (f) simulations.

In a similar manner, the minimum and maximum temperature inputs are calculated as

$$T_\Delta(i,j,k) = \Delta_T(j) + T_{obs}(i,j,k) \quad ; \quad i = 1,2,\ldots,31\,; j = 1,2,\ldots,12\,; k = 1,2,\ldots,30 \quad (3.4)$$

with correction factor $\Delta_T(j) = \overline{T_f}(j) - \overline{T_p}(j)$.

The results of applying the delta change method are shown in Figure 3.2. Compared to the baseline observation dataset, mean monthly temperatures increase for all months while mean monthly precipitation increases for all months except July, August, and September. The mean annual temperature for the future projection as corrected by the delta change method has increased by 3.8°C compared to the baseline case while the mean annual precipitation has increased by 135 mm, or 15%.

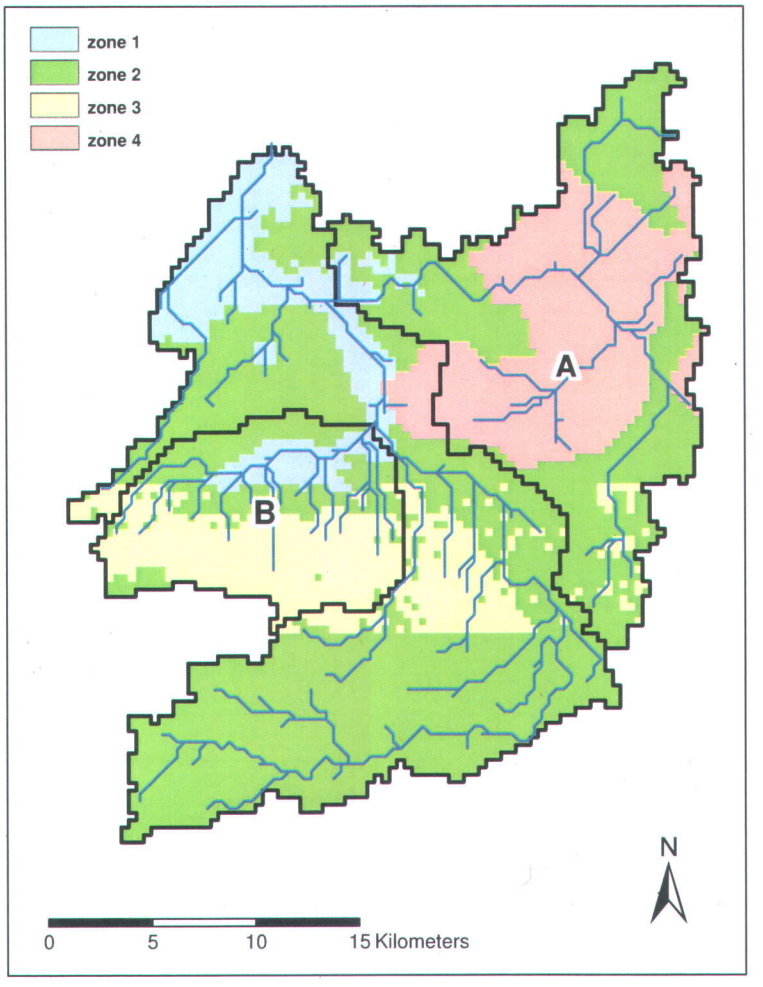

Figure 3.3: Map of the des Anglais watershed with four geopedologic zones and two sub-catchments (A, Norton and B, Rivière Noire).

The precipitation and min/max temperature time series for the observed (1961-1990) and future (2041-2070) climate projections were then used to derive potential evapotranspiration, using the method of *Oudin et al. [2005]*, and to reproduce snow accumulation and melting, based on the mixed degree-day energy budget method of *Turcotte et al. [2004]*. To account for the main land use classes in the des Anglais catchment (47% agriculture, 37% deciduous forest, 16% coniferous forest), the snow module was applied using three different values for the snow melting rate (8.37 mm/day°C for agriculture, 7.76 mm/day°C for deciduous forest, and 1.56 mm/day°C for coniferous forest) and for the threshold snow melting temperature (-0.92°C for agriculture, 2.10°C for deciduous forest, and 2.32°C for coniferous forest). These pre-processed time series of potential evapotranspiration and snow-corrected precipitation constitute the final form of the atmospheric input files passed to the CATHY model for simulation of the past and future climate simulations.

Table 3.3: Material properties for the 10 vertical layers and 4 geopedologic zones of the des Anglais catchment discretization.

Layer (top to bottom)		1	2	3	4	5	6	7	8	9	10
Layer thickness [m]		0.05	0.1	0.3	0.45	1.10	2.10	5.90	20	30	40
Zone 1	K_h [m/s]	5×10^{-4}	5×10^{-4}	5×10^{-4}	5×10^{-4}	1×10^{-4}	5×10^{-9}	5×10^{-9}	1×10^{-7}	5×10^{-8}	5×10^{-8}
	K_z [m/s]	3×10^{-4}	3×10^{-4}	3×10^{-4}	3×10^{-4}	5×10^{-4}	3×10^{-9}	3×10^{-9}	5×10^{-7}	5×10^{-8}	5×10^{-8}
	θ_s [/]	0.5	0.5	0.5	0.5	0.4	0.5	0.5	0.5	0.1	0.1
	S_s [m^{-1}]	1×10^{-5}	1×10^{-5}	1×10^{-5}	1×10^{-5}	1×10^{-4}	3×10^{-3}	3×10^{-3}	1×10^{-4}	1×10^{-6}	1×10^{-6}
Zone 2	K_h [m/s]	5×10^{-4}	5×10^{-4}	5×10^{-4}	5×10^{-4}	1×10^{-5}	1×10^{-5}	1×10^{-7}	5×10^{-8}	5×10^{-8}	5×10^{-8}
	K_z [m/s]	3×10^{-4}	3×10^{-4}	3×10^{-4}	3×10^{-4}	5×10^{-5}	5×10^{-5}	5×10^{-7}	5×10^{-8}	5×10^{-8}	5×10^{-8}
	θ_s [/]	0.5	0.5	0.5	0.5	0.5	0.5	0.5	0.1	0.1	0.1
	S_s [m^{-1}]	1×10^{-5}	1×10^{-5}	1×10^{-5}	1×10^{-5}	1×10^{-4}	1×10^{-4}	1×10^{-4}	1×10^{-6}	1×10^{-6}	1×10^{-6}
Zone 3	K_h [m/s]	5×10^{-4}	5×10^{-4}	5×10^{-4}	5×10^{-4}	1×10^{-4}	1×10^{-4}	2×10^{-6}	2×10^{-6}	2×10^{-6}	2×10^{-6}
	K_z [m/s]	3×10^{-4}	3×10^{-4}	3×10^{-4}	3×10^{-4}	5×10^{-4}	5×10^{-4}	5×10^{-8}	5×10^{-8}	5×10^{-8}	5×10^{-8}
	θ_s [/]	0.5	0.5	0.5	0.5	0.4	0.4	0.1	0.1	0.1	0.1
	S_s [m^{-1}]	1×10^{-5}	1×10^{-5}	1×10^{-5}	1×10^{-5}	1×10^{-4}	1×10^{-4}	1×10^{-6}	1×10^{-6}	1×10^{-6}	1×10^{-6}
Zone 4	K_h [m/s]	5×10^{-8}	5×10^{-8}	5×10^{-8}	5×10^{-8}	1×10^{-7}	1×10^{-7}	1×10^{-7}	5×10^{-8}	5×10^{-8}	5×10^{-8}
	K_z [m/s]	3×10^{-8}	3×10^{-8}	3×10^{-8}	3×10^{-8}	5×10^{-7}	5×10^{-7}	5×10^{-7}	5×10^{-8}	5×10^{-8}	5×10^{-8}
	θ_s [/]	0.9	0.9	0.9	0.9	0.5	0.5	0.5	0.1	0.1	0.1
	S_s [m^{-1}]	1×10^{-5}	1×10^{-5}	1×10^{-5}	1×10^{-5}	1×10^{-4}	1×10^{-4}	1×10^{-4}	1×10^{-6}	1×10^{-6}	1×10^{-6}

3.4.2.2 Discretization and parameterization

A 360 m DEM was used to delineate the des Anglais catchment, on the basis of which the 3D subsurface grid was constructed by subdividing each DEM cell into two triangles and then projecting this 2D surface mesh vertically for 100 m and 10 layers (the layer thicknesses are given in Table 3.3). The resulting 3D grid contains 61908 nodes and 320280 tetrahedral elements. The bottom and lateral boundaries of the domain were assumed to be impermeable.

According to calibration trials (described below) and to available pedologic and geologic information *[Lamontagne, 2005; Côté et al., 2006]*, different material properties were assigned both vertically and laterally. The four zones shown in Figure 3.3 represent distinct soil and Quaternary sediment types: the top 4 layers (0.9 m total thickness) are a loamy sand for zones 1, 2, and 3 and an organic soil for zone 4; the next layers are Quaternary stratigraphic sequences of fluvio-glacial coarse sand – marine clay and fine silt – till – bedrock for zone 1, reworked till – till – bedrock for zone 2, fluvio-glacial coarse sand – bedrock for zone 3, and till – bedrock for zone 4. Table 3.3 summarizes the saturated hydraulic conductivity (K_h, K_z), porosity (θ_s), and specific storage (S_s) attributed to each zone and layer of the discretized domain. A high degree of anisotropy (2 orders of magnitude) was attributed to the bottom 4 layers in zone 3 following indications of preferential horizontal flow paths in this region of the fractured bedrock aquifer *[Côté et al., 2006]*. Zone 3 includes Covey Hill, an elongated (east-west) plateau that is the most pronounced topographic feature in the Canadian part of the des Anglais river basin. The soil hydraulic properties were described by the *van Genuchten and Nielsen [1985]* relationships with residual moisture content θ_{res} = 0.07, air entry pressure head ψ_a= -0.2 m, and fitting exponent n = 2.0.

Table 3.4: Hydraulic geometry parameters for the surface routing module of the hydrological model.

Parameter	hillslope cells	channel cells
reference drainage area, A_s [m^2]	1.2×10^6	690×10^6
reference discharge, Q_f [m^3/s]	1	100
water-surface width, $W(A_s, Q_f)$ [m]	1	50
Gauckler-Strickler conductance coefficient, k_s [m$^{1/3}$/s]	0.5	18
"at-a-station" scaling exponents[a,b], b' and y' [/]	0.36, 0	0.26, 0
"downstream" scaling exponents[a,b], b'' and y'' [/]	0.5, 0	0.5, 0

[a] $W(A,Q) = W(A_s,Q_f)\,Q_f(A_s)^{-b'}\;(A/A_s)^{(b''-b')}\cdot Q^{b'}$

[b] $k_S(A,Q) = k_S(A_s,Q_f)\,Q_f(A_s)^{-y'}\;(A/A_s)^{(y''-y')}\cdot Q^{y'}$

The conditions of regional groundwater flow in the bedrock aquifer system were assessed on the basis of the physical properties of the unconsolidated sediments and their corresponding thicknesses. Confined flow prevails where more than 5 m of fine marine sediments with low hydraulic conductivity are present (zone 1 in Figure 3.3, representing about 10% of the catchment area, and layers 6 and 7 in Table 3.3). Semi-confined flow conditions are present in areas characterized by fine marine sediments of less than 5 m thickness or by at least 3 m of till (75% of the catchment, zones 2 and 4). Finally, areas with rock outcropping or where the bedrock is covered by less than 3 m of till, or by permeable sediments, regardless of their thickness, were designated as unconfined water table aquifers (15% of the catchment, zone 3)

The channel network was identified from the DEM of the catchment using an upstream drainage area threshold of 2.0 km^2, based on visual similarity between the extracted network and the streamlines depicted on topographic maps. Structural parameters for the channel and overland flow networks were calibrated using, for channel dynamics, the bankfull discharge measured at the main streamflow station (gauge 1 in Figure 3.1) as a reference value for the flow rate, and for overland (rivulet flow) dynamics, values reported in literature studies as a basis *[Emmett, 1978; Bathurst, 1986, 1993; Abrahams et al., 1994]*. The values obtained are reported in Table 3.4.

3.4.3 Hydrological Model Calibration

As mentioned, the CATHY model was calibrated for subsurface hydraulic conductivity (Table 3.3) and surface hydraulic geometry (Table 3.4) parameters. The observation data used was daily streamflow close to the outlet of the catchment (gauge 1 in Figure 3.1), and the simulation period was 12 months, from October 2001 to October 2002. The parameterization

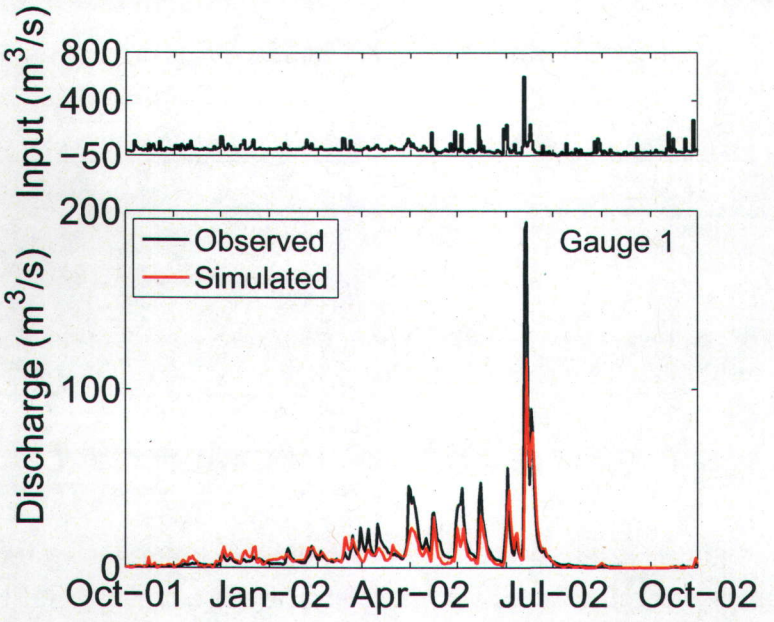

Figure 3.4: Observed (black line) and simulated (red line) discharge for the calibration period at the main streamflow gauge of the catchment.

was then verified for a 39-month simulation (October 2002 to January 2006) against daily streamflow at the outlet, for a 5-month simulation (August 2005 to January 2006) against daily streamflow at three internal stations (gauges 2, 3, and 4 in Figure 3.1), and for a 12-month simulation (May 2004 to May 2005) against daily groundwater level data at the six monitoring wells shown in Figure 3.1. We present here only the final results of the calibration and verification exercises.

Model performance was measured using the root mean squared error RMS for groundwater head and the RMS and Nash-Sutcliffe efficiency coefficient E, and the percentage error in peak PEP for stream discharge *[Nash and Sutcliffe, 1970; Anderson and Woessner, 1992; Jones et al., 2008]*:

$$E = 1 - \frac{\sum_{i=1}^{n}(\Omega_{obs,i} - \Omega_{sim,i})^2}{\sum_{i=1}^{n}(\Omega_{obs,i} - \overline{\Omega_{obs}})^2} \tag{3.5}$$

$$RMS = \sqrt{\frac{1}{n}\sum_{i=1}^{n}(\Omega_{obs,i} - \Omega_{sim,i})^2} \tag{3.6}$$

$$PEP_j = \left[\frac{max(\Omega_{obs,j}) - max(\Omega_{sim,j})}{max(\Omega_{obs,j})}\right] \times 100 \quad ; \quad j = 1, \ldots, m \tag{3.7}$$

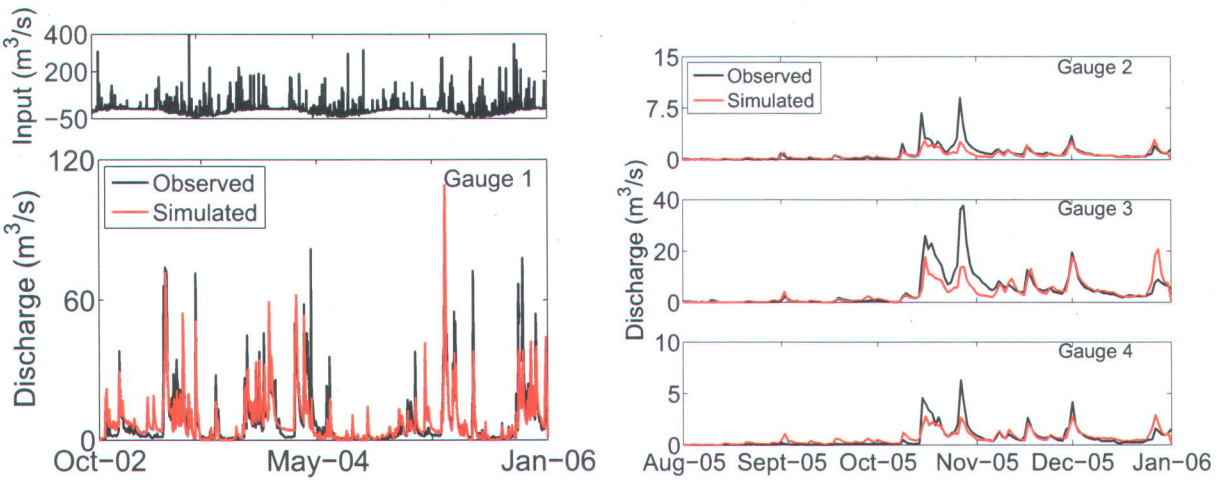

Figure 3.5: Observed (black line) and simulated (red line) discharge at the four gauges of the catchment for the verification period.

where Ω_{obs}, Ω_{sim}, and $\overline{\Omega_{obs}}$ are the observed, simulated, and average observed state variables (head, discharge), n is the number of observations, and m is the number of discharge events manually extracted for estimation of PEP. E=1 when there is a perfect match between simulated and observed values and is negative when the simulation is worse at capturing the observations than the mean value of the observed data. Similarly RMS and PEP are zero when the match is perfect and increases as the discrepancy between simulation and observation increases.

Figure 3.4 shows the simulated and observed hydrographs at the main gauging station for the calibration run, which produced performance measures of $E = 0.70$, $RMS = 9.7$ m^3/s for a mean observed discharge of 6.6 m^3/s, and an average PEP of 10% (underestimation), with a maximum of 39% reached for the event of Jun 10-16, 2002. Despite some disagreements in the peaks, the model captures the dynamics of the catchment quite well in both the rising and recession portions of the hydrograph. The good performance of the model was confirmed for the verification tests (Figures 3.5 and 3.6), where an efficiency index of $E = 0.69$ and an RMS value of 7.1 m^3/s resulted for the main streamflow gauge, and reasonable measures were also obtained at the internal streamflow stations ($E = 0.55$ and $RMS = 0.74$ m^3/s for gauge 2, $E = 0.6$ and RMS = 3.9 m^3/s for gauge 3, $E = 0.7$ and $RMS = 0.52$ m^3/s for gauge 4) and at the monitoring wells. In terms of peak flow errors, the average and maximum PEP values for the verification runs were 3% and 70%, respectively, at the main outlet, and 25% / 70% (average / maximum), 3% / 90%, and 13% / 56% at internal gauges 2, 3, and 4, respectively. The high PEP values obtained in the calibration and verification tests, with a prevalence of a negative bias, i.e., underestimation of peak discharges, can probably be attributed to uncertainty in the hydraulic parameters for the overland routing module, in

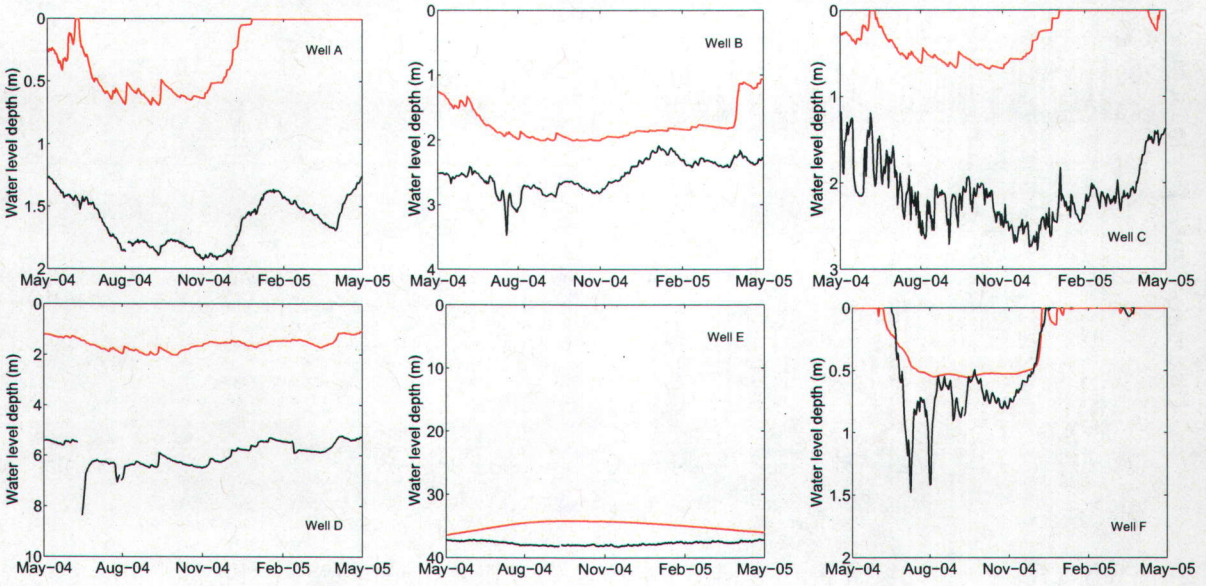

Figure 3.6: Observed (black line) and simulated (red line) water table depths at the six monitoring wells for the verification period.

particular the Gauckler-Strickler coefficient, which were estimated based on literature values, as already mentioned. Indeed the higher PEP values at the internal gauges are consistent with this hypothesis, since at smaller scales overland flow can become more prevalent in the overall hydrologic response of a catchment to storm events.

For the six well hydrographs (Figure 3.6) the RMS values ranged from 0.6 to 4.3 m, with the largest value occurring at the well located on the foothill of Covey Hill (well D in Figure 3.1), where the observed groundwater depth is about 6 m below ground surface. Although the RMS values are reasonable and the graphs in Figure 3.6 show that the model reproduces groundwater fluctuations reasonably well, it can also be seen that the simulated fluctuations are somewhat dampened for the deeper wells. This is probably due to the use of a coarser mesh in the model for the deeper layers (see Table 3.3) that diminishes the ability to capture local heterogeneities and fluctuations. It is also apparent in Figure 3.6 that there is systematic overprediction of groundwater levels, most probably attributable to a combination of the no-flow boundary condition assigned to the lateral boundaries of the subsurface domain, preventing regional (interbasin) groundwater flow, and the fact that no other outflow boundaries (e.g., seepage faces along incised streambanks) were assigned that could maintain water tables at a lower level. All subsurface water exits the catchment at the surface, as overland or channel flow and as evaporation. In the absence of field data to support accurate implementation of internal or lateral outflow boundaries, it was preferred to keep the model setup as simple as possible.

3.5 Simulations

The potential climate change impacts at the des Anglais river basin were assessed by running the calibrated CATHY model with the observed past atmospheric dataset and with the hypothetical future dataset obtained through the delta change transfer method. The assessment examines in particular the impacts on river discharge, aquifer recharge, and near-surface soil water storage. The fully coupled, distributed model is used to highlight the role played by feedback processes between the surface and subsurface and the influence of factors such as topography and heterogeneity. An additional set of simulations was performed, using directly the CRCM-generated past and future scenarios, to compare the CATHY and CLASS models in terms of surface and subsurface runoff and soil water storage.

3.5.1 Climate Change Impacts

3.5.1.1 River discharge

The sensitivity of river discharge to the changing atmospheric input was evaluated at the catchment outlet and at the outlet of two subcatchments having different physiographic features (the Norton and Rivière Noire subcathments in Figure 3.3). The Norton subcatchment, with a relatively flat topography, low-permeability organic soils, and semi-confined aquifer conditions, represents a case of weak interactions between surface and subsurface water, while the Rivière Noire, which includes Covey Hill, rock outcrops, and a fractured bedrock aquifer under unconfined conditions, is an area where we expect significant surface and subsurface interactions. Daily discharge values at the three outlets were averaged to obtain mean monthly values over the 1961-90 and 2041-70 periods. Mean monthly discharge ratios (future over past) were then calculated and plotted in Figure 3.7.

At the main outlet of the des Anglais catchment the climate change impacts are more significant during the peak winter (Jan-Feb) and summer (Jul-Aug) months, with a strong increase in future discharge in winter and a strong decrease in summer. The winter effect is due to the combination of more precipitation and higher temperatures, which increases the proportion of rainfall to snowfall. Higher temperatures also lead to a reduction in snow cover, resulting in a shift in spring freshet from April to March and a decrease in streamflow during the spring season. In the summer, the strong decrease in river discharge is the result of a slight decrease in total precipitation combined with a marked increase in evaporation due to higher temperatures. The watershed's response to increased precipitation in the fall for the future scenario is delayed (to late November) due to the storage deficit that developed in the basin

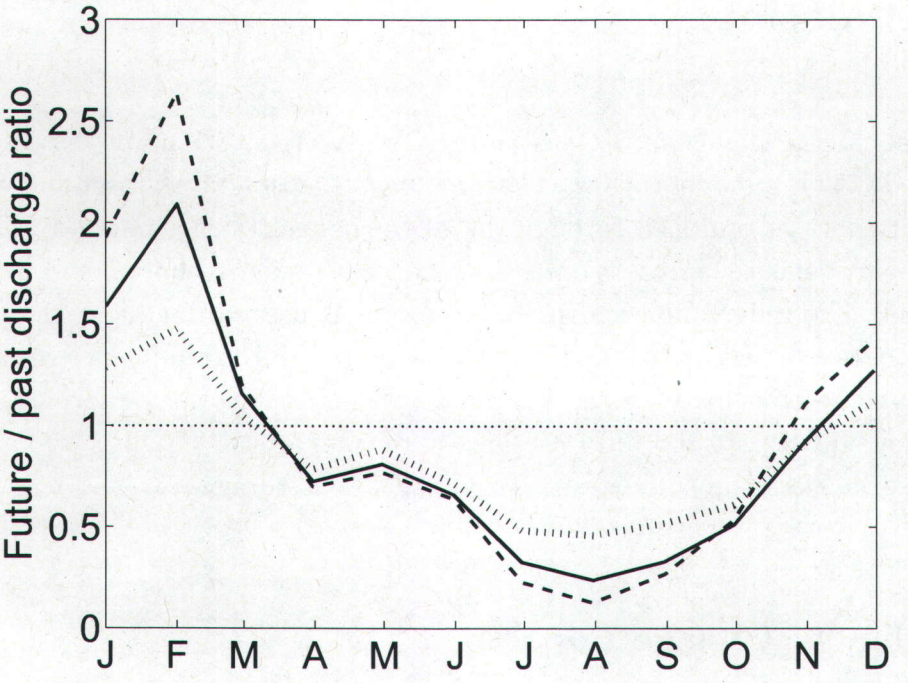

Figure 3.7: Ratio of mean monthly discharge simulated under future climate conditions to mean monthly discharge simulated under the past climate: des Anglais catchment outlet (solid line); Norton subcatchment outlet (dashed line); Rivière Noire subcatchment (dotted line).

over the summer period, resulting in more infiltration and recharge and less runoff in early fall.

The impacts on the two subcatchments generally follow the same trend detected at the main outlet, although marked differences in sensitivity to the changing climate can be observed in Figure 3.7, owing to a different partitioning between the overland runoff and baseflow components of the hydrograph. For the Rivière Noire subcatchment, the decrease in river discharge during the summer period is alleviated by a greater baseflow component as a result of the larger amount of water infiltrated in early spring. The Norton subcatchment, on the other hand, with its less permeable soils and weaker surface–subsurface connections, has a dominant overland flow component, resulting in a faster and sharper response to the forcing climate. This higher sensitivity is seen in Figure 3.7 in both the peak-winter discharge increase and the peak-summer low-flow period. The results at the different outlets indicate how local heterogeneity in topography, soils, and geology can result in significant spatio-temporal variations in a catchment's response to climate change.

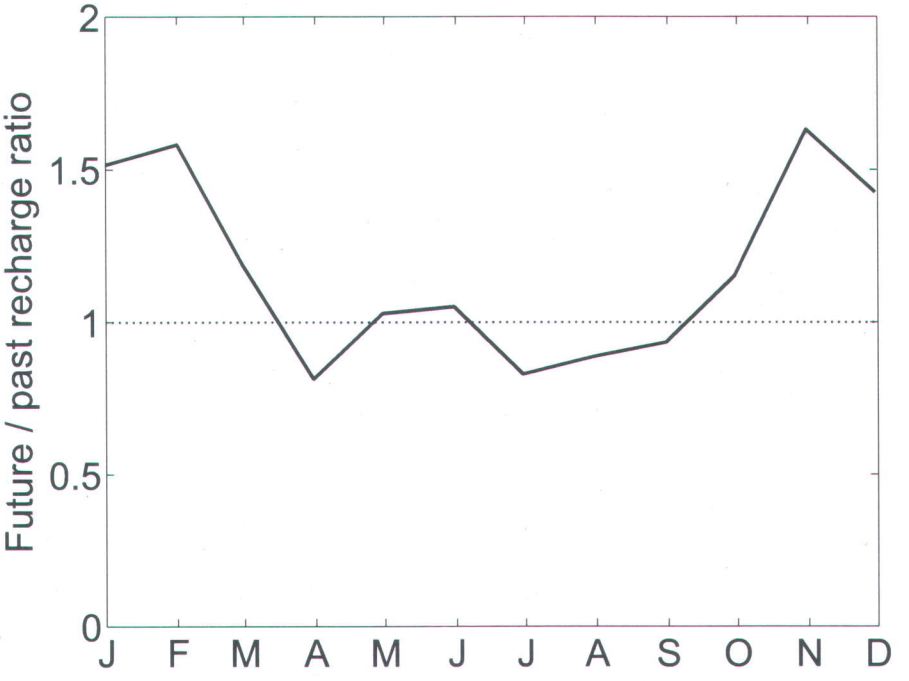

Figure 3.8: Ratio of mean monthly total recharge simulated under future climate conditions to mean monthly total recharge simulated under the past climate.

3.5.1.2 Recharge to the aquifer

Recharge is computed in the CATHY model as the downward flux of water across the water table. Daily nodal recharge values were spatially cumulated and temporally averaged to obtain mean monthly values for the past and future periods, and the future/past ratio was then calculated and plotted in Figure 3.8. The aquifer of the des Anglais basin receives most of its recharge in the spring and fall through snowmelt and heavier rainfall, respectively. In agreement with other studies *[Eckhardt and Ulbrich, 2003; Toews and Allen, 2009]*, Figure 3.8 shows that climate change for the des Anglais results in a significant increase in winter season recharge due to a higher rain/snow ratio caused by higher temperatures, less recharge in the spring due to an earlier and less intense snowmelt, a general decrease over the summer due to increased evaporation, and an increase in the fall due to increased precipitation. The important role of surface–subsurface interactions is evident in comparing the fall response for recharge (Figure 3.8) and for streamflow (Figure 3.7); the aquifer responds quickly to the increased precipitation, contributing to the lag in discharge response mentioned in the previous section.

Figure 3.9 shows the spatial distribution of the difference in mean monthly aquifer recharge

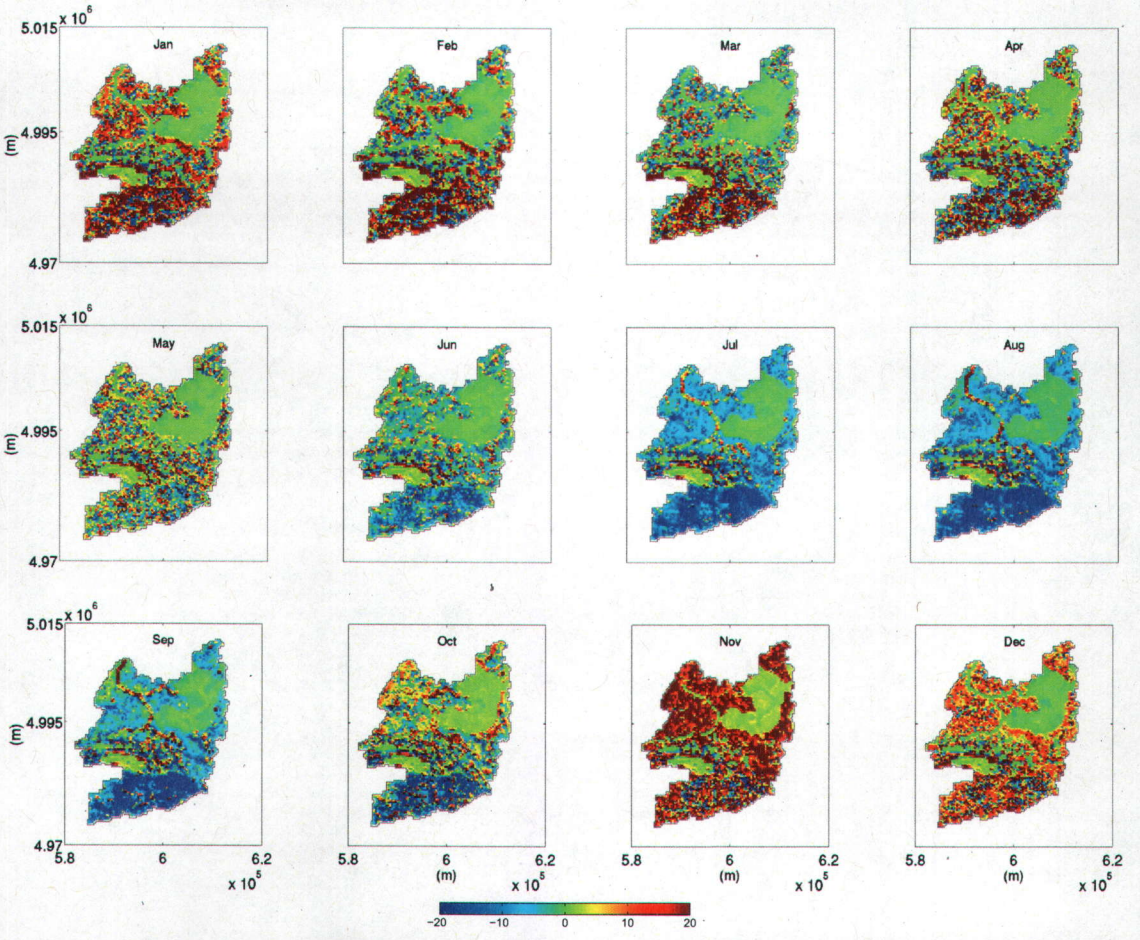

Figure 3.9: Distributed difference (mm) between mean monthly recharge simulated under future climate conditions and mean monthly recharge simulated under the past climate.

between the future and past climate simulations. General spatial and intra-annual patterns are clearly observable and are consistent with what was observed for the entire catchment, even though at the fine scale there are regions that show some strong variability from cell to cell, in particular in and around zones 1 and 3 where there are pockets of heterogeneity (from zone 2 cells) and in the southern portion of the catchment where the deeper water table lies within thicker grid layers. These factors can cause numerical difficulties (e.g., oscillations) in the subsurface flow solver. Figure 3.9 shows an increased future recharge in the winter and fall periods and a decrease in the summer. Zones 3 and 4 are the least sensitive to climate change in terms of recharge, due to the low aquifer porosity and high anisotropy in zone 3 and the low-permeability soils and aquifer in zone 4. The strongest response, throughout the year, is obtained for the southern portion of the catchment where elevations are highest. Recharge along the main branch of the des Anglais river, discernible throughout

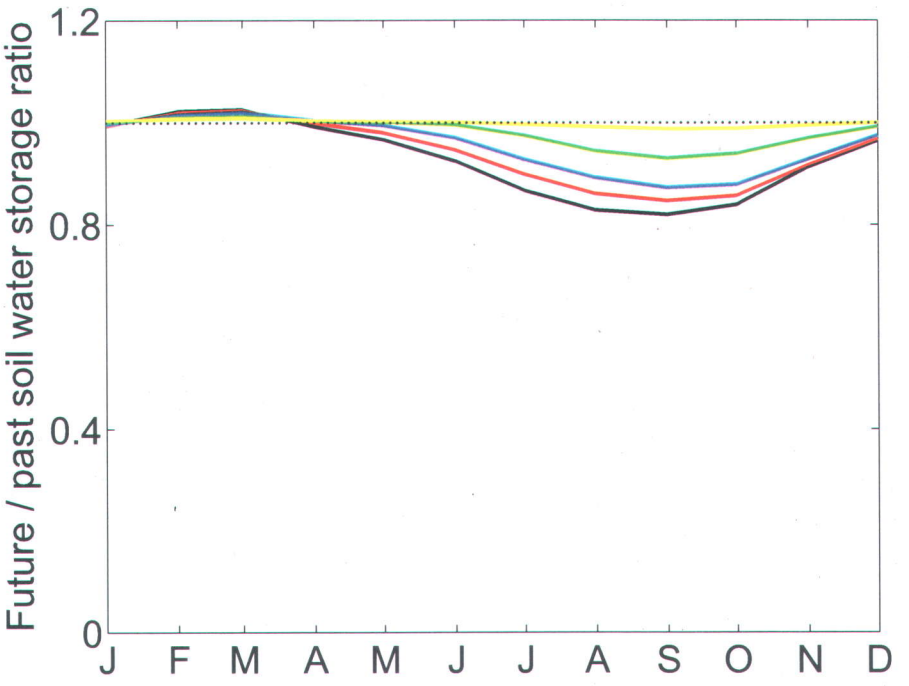

Figure 3.10: Ratio of mean monthly soil water storage simulated under future climate conditions to mean monthly soil water storage simulated under the past climate: 0.05 m depth (black line); 0.15 m depth (red line); 0.45 m depth (blue line), 0.90 m depth (green line), 2.0 m depth (yellow line).

the year in Figure 3.9, remains relatively insensitive to climate change, indicating that the river continues to be fed by the groundwater reservoir. However during the summer months (Jul-Sep), there are occurrences of a large positive change in recharge along this main branch of the channel network, suggesting a possible reversal in groundwater–river interaction in response to a groundwater storage deficit.

3.5.1.3 Soil water storage

The sensitivity of soil water storage to climate change was evaluated at the surface (top 5 cm) and at different soil depths (0.15, 0.45, 0.90, and 2.0 m). The daily values simulated at each node of the domain were averaged to obtain both aggregated and distributed mean monthly values for the catchment. The relative variation between past and future climate simulations for the entire catchment was assessed by computing an index ratio as in the previous analyses, and the results are plotted in Figure 3.10. Compared to water fluxes across a point or boundary (discharge at a catchment outlet in Figure 3.7 and recharge across the water table in Figure 3.8), water storage volumes are apparently less sensitive

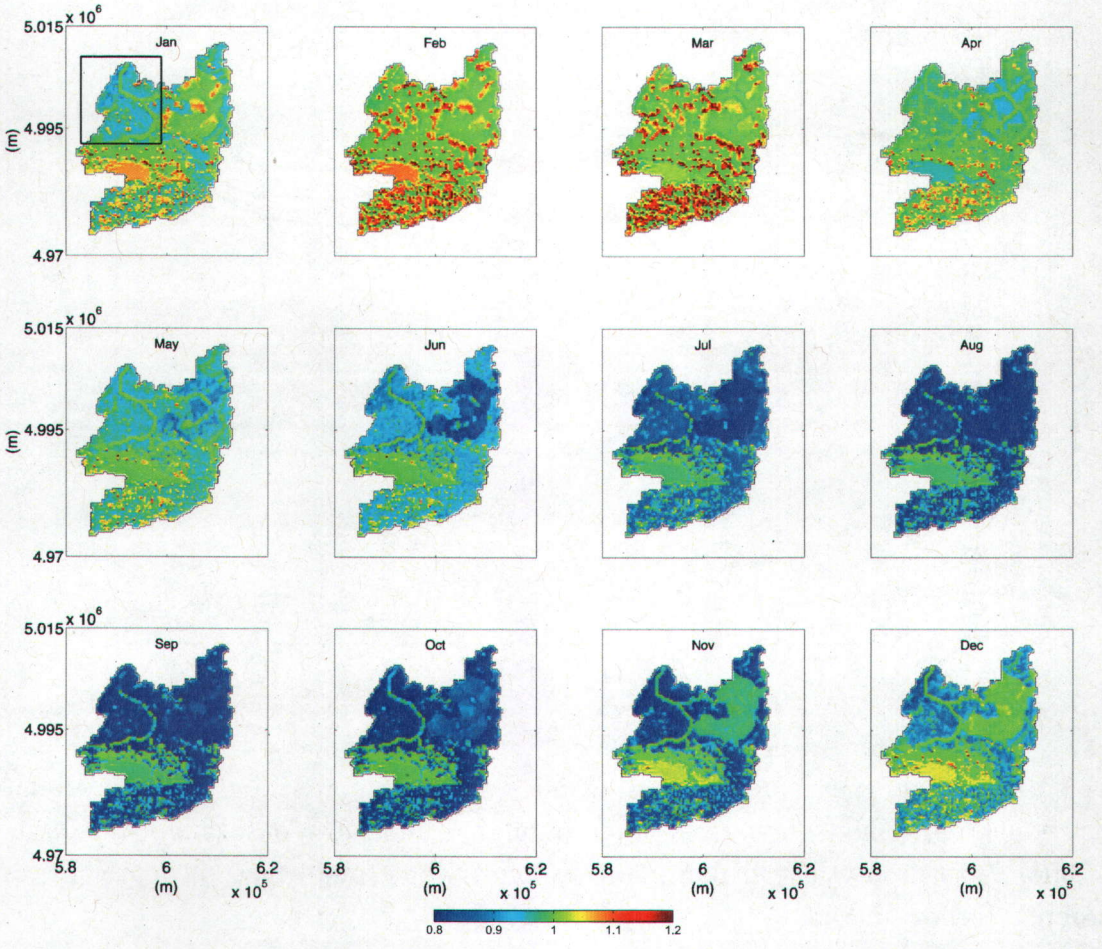

Figure 3.11: Distributed ratio of mean monthly surface soil moisture (5 cm depth) simulated under future climate conditions to mean monthly surface soil moisture simulated under the past climate.

to climate change. The changes from past to future climate shown in Figure 3.10 are most strongly felt nearest to the surface, which is directly exposed to variations in precipitation and evapotranspiration, and are progressively dampened as soil depth increases. In terms of intra-annual dynamics, the patterns are nonetheless similar to those observed for recharge and discharge, with all soil depths displaying a decrease in subsurface storage during the summer period and an increase (albeit very slight) over the peak winter and early spring months.

For the top layer of the model discretization (0-5 cm), the future/past soil water ratio computed above was also examined spatially. From a visual analysis of the plots in Figure 3.11 we can observe a spatial organization of soil moisture variability that follows the topographic

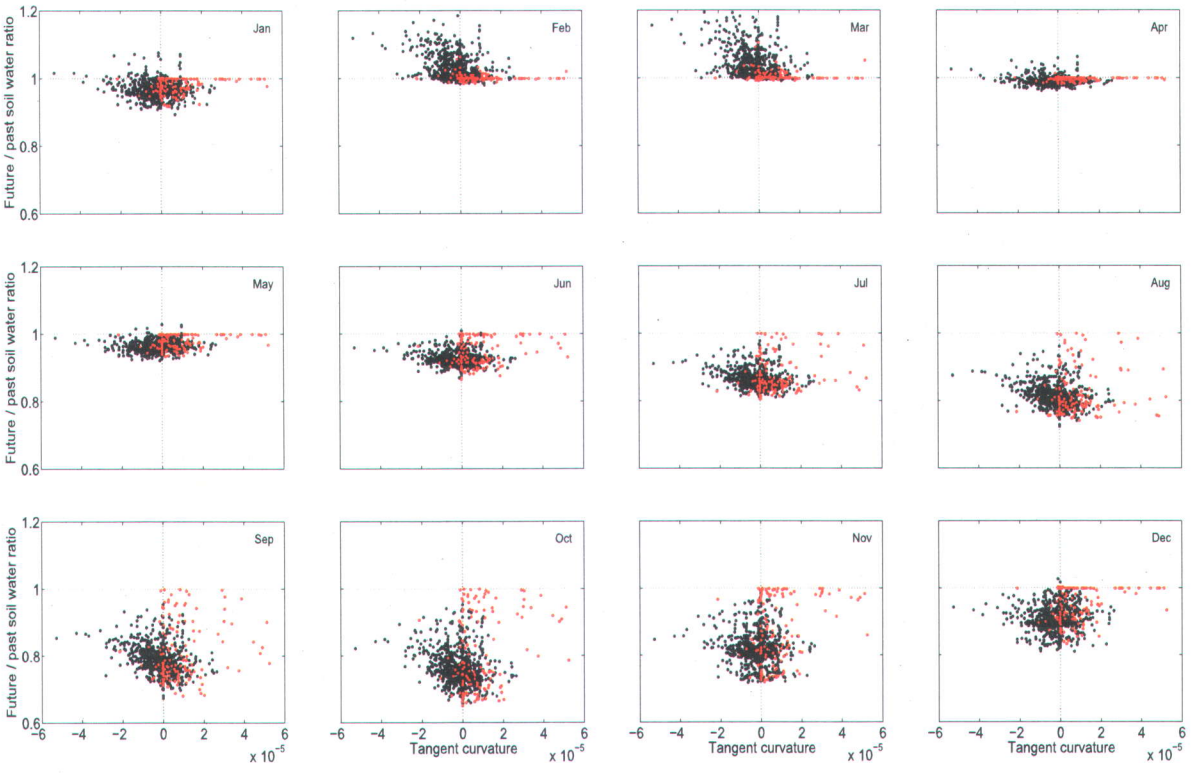

Figure 3.12: Scatter plot between the future / past surface soil water ratio and the tangent curvature for the channel (red points) and hillslope cells (black points). The analysis refers to the inset area of the catchment shown in Figure 3.11.

and pedologic characteristics (heterogeneity) of the catchment *[Western et al., 1999]*. In particular, the effect of a lateral redistribution of water is evident in the persistence of the main river network, discernible through most the year. The influence of the greater holding capacity (porosity = 0.90) of the organic soils in zone 4 can also be seen in the faster near-surface response of this region of the catchment in losing water under stress periods and regaining water under wetter conditions. In Figure 3.11 we can also discern a difference in hydrologic response between regions of the catchment where the exfiltration process during dry periods quickly becomes soil limited due to a deeper water table (for example Covey Hill) and areas with a shallower water table where exfiltration remains predominantly atmosphere controlled. In the latter areas more water is lost during the dry summer period, resulting in a greater soil moisture deficit compared to Covey Hill, and this deficit therefore persists longer into the fall when there is a return to wetter conditions.

To further explore the role of topography in describing the sensitivity of soil moisture to climate change, we investigated the relationship between the tangent curvature of the surface, as defined by *Mitasova and Hofierka [1993]*, and the mean monthly surface soil water ratio calculated earlier. This analysis was performed for the inset area depicted in Figure 3.11,

which from this previous figure demonstrates a varied response to climate change. Figure 3.12 shows the scatter plots between the tangent curvature of the surface and the monthly moisture, with the overland (hillslope) and channel cells plotted separately. It can be seen that there is a strong seasonal variation in the relationship between surface soil moisture and tangent curvature, and that this relationship is quite different between hillslope cells and channel cells. We found for instance that the hillslope cells having a negative curvature (and thus located along convergent parts of the catchment) are those that tend to experience an increase in soil moisture content for February and March in response to climate change, and less variation in the late summer and early fall (August to October). The correlation between the sensitivity of surface soil water content to climate change and the tangent curvature was quite weak for the other months of the year, when near-surface moisture variations are probably more controlled by factors such as evapotranspiration rather than lateral redistribution of water. The correlation was equally weak for channel cells, and this throughout the year, probably due to conditions of saturation or near-saturation that characterize these cells.

3.5.2 Comparison with the CLASS Model

As major components of the water cycle, surface and subsurface runoff and soil water storage play a critical role in the global/regional climate system. Many different models, operating over a range of scales from small field plots to continents, are used to simulate these and other hydrological processes. Climate models are continually evolving in terms of their spatial resolution and their parameterization of soil and groundwater flow components, while detailed process-based hydrological models are being increasingly used beyond the hillslope and subcatchment scale. These two classes of models are still far from any sort of convergence towards a unified hydroclimatological simulation paradigm, and it can be instructive to compare their formulations or predictive capabilities when opportunities to do so arise.

The CRCM model (using CLASS internally coupled to its atmospheric part) was used to provide predictions of runoff and soil water storage for the past and future climate simulations at the CRCM grid scale, for the 4 grid points shown in Figure 3.1. With appropriate averaging to ensure consistency, these outputs were compared to results produced by CATHY over the des Anglais river basin and at its outlet. The actual CRCM generated data was used (for the periods 1961-1990 and 2041-2070) instead of the observed past and delta change generated future data. In this way, both CLASS and CATHY are forced by the same precipitation input. For the actual evaporation, CLASS performs an energy balance at the ground surface while CATHY uses a threshold value of pressure head (ψ_{min}) that corresponds to the advent of stage-two evaporation *[Salvucci, 1997]*. The soil layer saturated hydraulic conductivity K_z and saturated porosity θ_s used in CLASS are related to soil texture information (percent sand) via empirical relationships presented in *Cosby et al. [1984]*, while bedrock depth is assigned

Table 3.5: Soil parameters for the CLASS model.

CRCM grid points		1	2	3	4
Layer 1 (0.00–0.10 m)	K_z [m/s]	2.84×10^{-5}	2.84×10^{-5}	1.22×10^{-6}	1.46×10^{-6}
	θ_s [/]	0.37	0.37	0.48	0.47
Layer 2 (0.10–0.35 m)	K_z [m/s]	3.05×10^{-5}	3.05×10^{-5}	1.10×10^{-6}	1.34×10^{-6}
	θ_s [/]	0.36	0.36	0.36	0.48
Layer 3 (0.35–4.10 m)	K_z [m/s]	3.44×10^{-5}	3.44×10^{-5}	1.11×10^{-6}	1.30×10^{-6}
	θ_s [/]	0.36	0.36	0.48	0.48
Bedrock depth (m)		3.0	3.0	1.7	1.2

for each CRCM grid point (Table 3.5). Moreover, for each of these grid points, four vegetation groups (needleleaf trees, broadleaf trees, crops, and grass) and urban areas are considered in CLASS. This information is obtained by making use of the global archive of *Wilson and Henderson-Sellers [1985]*, which contains listings of primary and secondary land covers at a resolution of 1° × 1°. The vegetation parameters considered are the fractional areal coverage ($FCAN$), the visible and near-infrared albedo ($ALVC$ and $ALIC$), the vegetation roughness length in logarithmic scale ($LNZ0$), the maximum and minimum leaf area index ($LAMX$ and $LAMN$), the canopy mass ($CMAS$), and the root depth ($ROOT$). The set of values used are reported in Table 3.6 while further details on the way CLASS is parameterized are provided in *Verseghy et al. [1993]*. In order to compare to the CRCM/CLASS simulations, CATHY was rerun using values for soil hydraulic properties, soil texture, and vertical discretization that are consistent with those in CLASS. In particular, CATHY's soil parameters for each Thiessen polygon (Figure 3.1) were set to the values used in CLASS (Table 3.5), while the bedrock aquifer was simulated by assigning a much lower hydraulic conductivity (5×10^{-8} m/s), as well as lower porosity and specific storage, to the layers below CLASS's bedrock depth. The CATHY parameterization is summarized in Table 3.7. As can be seen in this table, CATHY's layers 1-2 were assigned CLASS's layer 1, CATHY's layers 3-4 were assigned CLASS's layer 2, and CATHY's layers 5-8 were assigned CLASS's layer 3. CATHY's remaining layers 9-12 (beyond a depth of 4.1 m) are not part of CLASS's soil profile. Also, we can see that CATHY's bedrock starts at layer 8 (depth = 3 m) for CRCM grid points 1 and 2, at layer 7 (depth = 1.7 m) for grid point 3, and at layer 6 (depth = 1.2 m) for grid point 4.

3.5.2.1 Surface and subsurface runoff

The sum of surface and subsurface runoff simulated by CLASS at each CRCM grid point was spatially averaged according to the Thiessen polygons shown in Figure 3.1 and compared with the river discharge simulated by CATHY at the main outlet of the des Anglais catchment. The mean monthly values of this runoff and streamflow are shown in Figure 3.13 for the 1961-

Table 3.6: Vegetation parameters for the CLASS model.

CRCM grid points		1	2	3	4
Needleleaf trees	$FCAN$ [/]	0.41	0.03	0.09	0.14
	$ALVC$ [/]	0.03	0.03	0.03	0.03
	$ALIC$ [/]	0.23	0.23	0.23	0.23
	$LNZ0$ [/]	0.68	0.66	0.66	0.67
	$LAMX$ [/]	2.48	2.45	2.44	2.28
	$LAMN$ [/]	1.01	1.05	1.06	0.95
	$CMAS$ [kg/m^2]	15.91	15.63	15.59	14.56
	$ROOT$ [m]	1.48	1.45	1.44	1.35
Broadleaf trees	$FCAN$ [/]	0.42	0.96	0.82	0.26
	$ALVC$ [/]	0.05	0.05	0.05	0.05
	$ALIC$ [/]	0.29	0.29	0.29	0.29
	$LNZ0$ [/]	0.68	0.69	0.68	0.35
	$LAMX$ [/]	5.99	6.00	5.99	8.65
	$LAMN$ [/]	0.50	0.50	0.50	0.72
	$CMAS$ [kg/m^2]	19.95	20.00	19.95	28.28
	$ROOT$ [m]	1.99	2.00	1.99	2.84
Crops	$FCAN$ [/]	0.16	0.005	0.06	0.50
	$ALVC$ [/]	0.06	0.06	0.06	0.06
	$ALIC$ [/]	0.34	0.34	0.34	0.34
	$LNZ0$ [/]	-2.52	-2.52	-2.52	-2.52
	$LAMX$ [/]	4.00	4.00	4.00	3.22
	$LAMN$ [/]	0.00	0.00	0.00	0.00
	$CMAS$ [kg/m^2]	2.00	2.00	2.00	1.61
	$ROOT$ [m]	1.20	1.20	1.20	0.96
Grass	$FCAN$ [/]	0.004	0.005	0.02	0.05
	$ALVC$ [/]	0.04	0.04	0.04	0.05
	$ALIC$ [/]	0.29	0.28	0.29	0.31
	$LNZ0$ [/]	-3.07	-3.27	-3.20	-3.36
	$LAMX$ [/]	3.26	2.92	3.07	2.68
	$LAMN$ [/]	3.26	2.92	3.07	2.68
	$CMAS$ [kg/m^2]	2.07	1.91	1.92	1.48
	$ROOT$ [m]	0.99	0.87	0.90	0.75
Urban	$FCAN$ [/]	0.005	0.001	0.01	0.05
	$ALVC$ [/]	0.09	0.09	0.09	0.09
	$ALIC$ [/]	0.15	0.15	0.15	0.15
	$LNZ0$ [/]	0.30	0.30	0.30	0.30
	$LAMX$ [/]	*na*	*na*	*na*	*na*
	$LAMN$ [/]	*na*	*na*	*na*	*na*
	$CMAS$ [kg/m^2]	*na*	*na*	*na*	*na*
	$ROOT$ [m]	*na*	*na*	*na*	*na*

Table 3.7: CLASS-equivalent parameterization of the CATHY model for the 4 CRCM grid points of the des Anglais catchment.

Layer (top to bottom)		1-2	3-4	5	6	7	8	9-12
Layer thickness [m]		0.05-0.05	0.125-0.125	0.85	0.50	1.30	1.10	5.90-20-30-40
Grid point 1	$K_h = K_z$ [m/s]	2.84×10^{-5}	3.05×10^{-5}	3.44×10^{-5}	3.44×10^{-5}	3.44×10^{-5}	5.0×10^{-8}	5.0×10^{-8}
	θ_s [/]	0.37	0.36	0.36	0.36	0.36	0.1	0.1
	S_s [m^{-1}]	1×10^{-5}	1×10^{-5}	1×10^{-5}	1×10^{-5}	1×10^{-5}	1×10^{-6}	1×10^{-6}
Grid point 2	$K_h = K_z$ [m/s]	2.84×10^{-5}	3.05×10^{-5}	3.44×10^{-5}	3.44×10^{-5}	3.44×10^{-5}	5.0×10^{-8}	5.0×10^{-8}
	θ_s [/]	0.37	0.36	0.36	0.36	0.36	0.1	0.1
	S_s [m^{-1}]	1×10^{-5}	1×10^{-5}	1×10^{-5}	1×10^{-5}	1×10^{-5}	1×10^{-6}	1×10^{-6}
Grid point 3	$K_h = K_z$ [m/s]	1.22×10^{-6}	1.10×10^{-6}	1.11×10^{-6}	1.11×10^{-6}	5.0×10^{-8}	5.0×10^{-8}	5.0×10^{-8}
	θ_s [/]	0.48	0.36	0.48	0.48	0.1	0.1	0.1
	S_s [m^{-1}]	1×10^{-5}	1×10^{-5}	1×10^{-5}	1×10^{-5}	1×10^{-6}	1×10^{-6}	1×10^{-6}
Grid point 4	$K_h = K_z$ [m/s]	1.46×10^{-6}	1.34×10^{-6}	1.30×10^{-6}	5.0×10^{-8}	5.0×10^{-8}	5.0×10^{-8}	5.0×10^{-8}
	θ_s [/]	0.47	0.48	0.48	0.1	0.1	0.1	0.1
	S_s [m^{-1}]	1×10^{-5}	1×10^{-5}	1×10^{-5}	1×10^{-6}	1×10^{-6}	1×10^{-6}	1×10^{-6}

90 and 2041-70 periods. For reference (and mindful of the discrepancies between the observed and CRCM-generated datasets discussed earlier – see Figure 3.2), we also show, for the past period in Figure 3.13, the mean monthly streamflow observed over the period 1961–1990 and the CATHY results over this same period using the calibration described in section 3.4.3. As can be seen in Figure 3.13, CLASS produces higher estimates than CATHY of surface and subsurface runoff throughout the annual cycle for both past and future simulations, with the greatest difference occurring at peak flow during snowmelt. The important factors contributing to these discrepancies in model prediction most likely include the degree of physical detail included in the surface and subsurface parameterizations and the differing spatial resolutions of the two models (affecting for instance the ability to capture important topographic features and subsurface heterogeneities that strongly influence the response of the catchment). In CLASS, surface runoff is described by a two-stage infiltration model where the first stage predicts the volume of infiltration until surface ponding begins and the second stage, which is a modified Green-Ampt model, describes the subsequent infiltration down to the root zone. Compared to a 1D Richards equation, this simplified model can underestimate the infiltrated volume prior to runoff *[Mein and Larson, 1973]*, and this underestimation is amplified for steeper slope angles if, as in CLASS, slopes are not accounted for *[Chen and Young, 2006]*. A 3D Richards equation model such as CATHY provides additional byways for infiltration, through lateral subsurface moisture redistribution and, with surface coupling, through downslope reinfiltration.

To further illustrate differences in response between the CLASS and CATHY models, Figure 3.14 shows the results on a daily time step for one year (1979) of the 30-year past climate simulation. It is evident, particularly during wet periods (Feb-Mar and late-fall/early-winter), that CLASS produces a more intense hydrograph response (higher peaks of shorter duration) and a lower recession component (normally associated with subsurface contributions

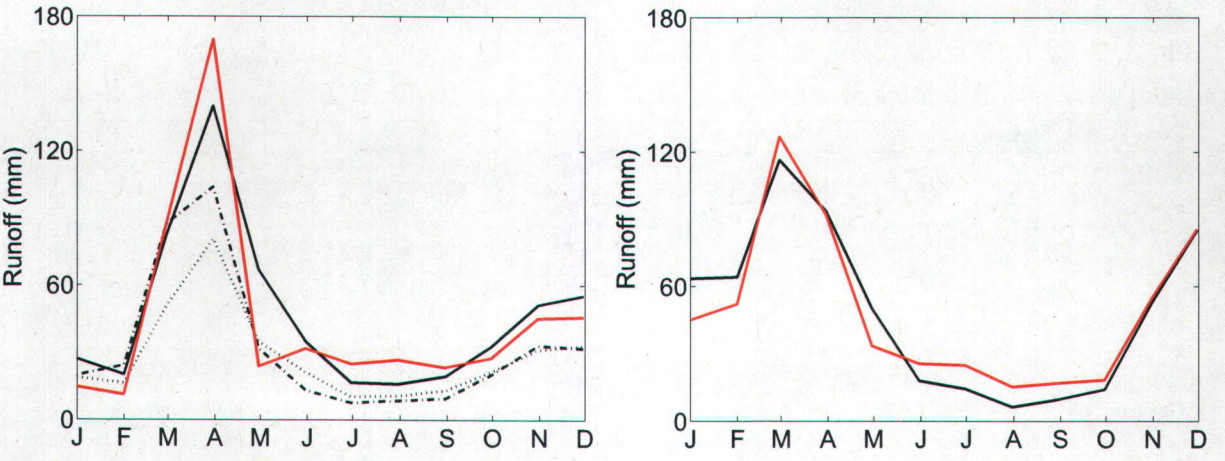

Figure 3.13: Mean monthly runoff for the past (left graph) and future (right graph) climate change projections: CLASS surface and subsurface runoff (red line); CATHY catchment outlet discharge (black line). The top graph also shows observed streamflow (dash-dotted line) and calibrated CATHY discharge (dotted line) for the period 1961-1990.

to runoff). Subsurface runoff in CLASS is computed as the flow out of the third soil layer (from 0.35 to 4.10 m depth). The higher peak runoff in CLASS is also partly due to the lack of attenuating processes such as explicit river routing and lake storage. The two models are better matched during the drier summer period.

3.5.2.2 Soil water storage

Groundwater dynamics and storage influence near-surface soil moisture and surface runoff. Water table fluctuations interact with soil moisture in the root zone and can affect evapotranspiration. In land surface models, the parameterization of subsurface processes falls within three broad classes: multi-layered and relatively shallow soil profile without an explicit representation of groundwater dynamics; multi-layered and deep soil profile that accounts for groundwater fluctuations even without an explicit representation; multi-layered soil column coupled in some way to an aquifer model. The CLASS model, with its three-layer discretization of the soil profile and no consideration of the water table dynamics, falls into the first category. For the past and future climate scenario simulations described above, the soil water storage computed by the CATHY and CLASS models within each of the three CLASS layers (0–0.10 m, 0.10–0.35 m, and 0.35–4.10 m) was plotted in Figure 3.15. CLASS and CATHY are in general agreement in terms of the intra-annual variability of moisture content in the first two soil layers, particularly for the top layer in which water variations are most directly affected by rainfall events and by diurnal temperature changes during interstorm periods.

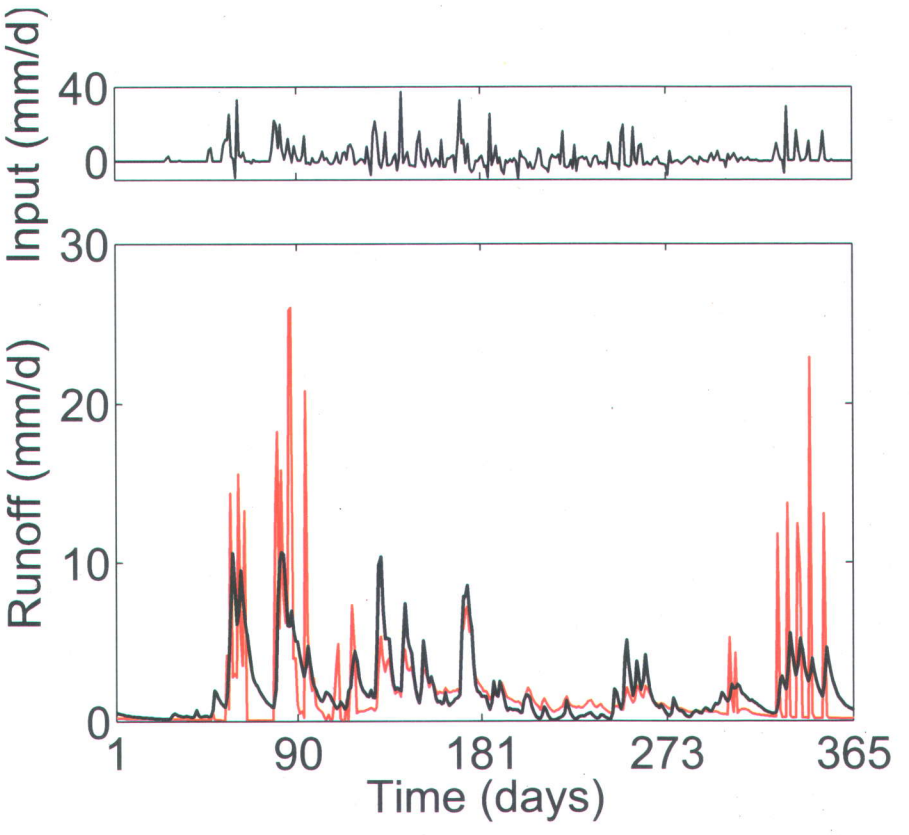

Figure 3.14: CLASS (red line) and CATHY (black line) daily runoff responses for year 1979 of the 30-year past climate simulation.

The largest differences between the two models occur in the third layer, with CATHY predicting wetter soil conditions over the entire simulation period and moisture fluctuations of much smaller amplitude. The causes of this behavior are underestimation of infiltration in CLASS (discussed earlier), together with the absence of an underlying groundwater reservoir that results in faster depletion of the bottom layer (in CLASS the bedrock is assumed to be an impermeable stratum with no water storage capacity).

CLASS and CATHY soil water storage, as well as runoff, are also analyzed in terms of mean monthly ratios (future climate over past climate), as plotted in Figure 3.16. For the CLASS model, with a higher surface contribution to the hydrograph, the runoff ratio is more sensitive to the relative variation in total precipitation between the future and past simulations, with the highest ratios observed in February. In terms of soil water storage, the changes from past to future climate in CATHY are most strongly felt nearest to the surface (first and second soil layers) and are progressively dampened as soil depth increases (third layer). CLASS on the other hand shows a less systematic response from shallow to deep layers, reflecting in part this model's more compartmentalized treatment of the subsurface.

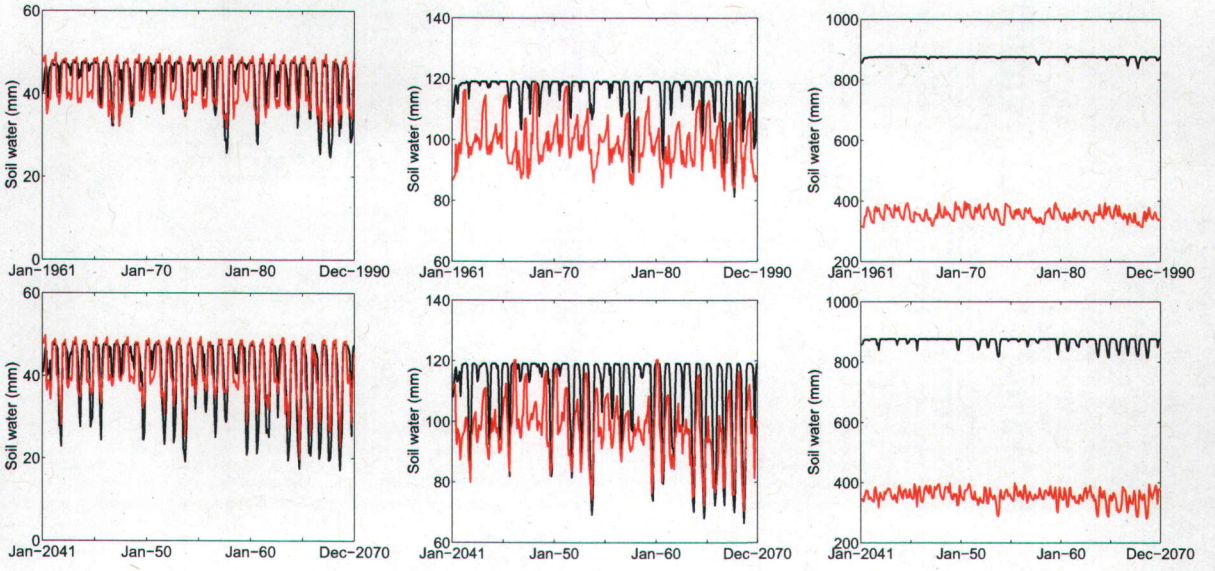

Figure 3.15: Monthly soil water content in the 0–0.10 m (left graphs), 0.10–0.35 m (middle graphs), and 0.35–4.10 m (right graphs) CLASS layers for the past (top graphs) and future (bottom graphs) climate change projections: CLASS (red line), CATHY (black line).

Overall, the differences in response between CLASS and CATHY highlight the importance of resolving soil and water table dynamics as a continuum when aquifers are relatively shallow, as is the case on average for a significant portion of the des Anglais river basin. For instance, over a depth range between 1 and 5 m *Kollet and Maxwell [2008]* found the land surface water and energy budgets to be very sensitive to groundwater storage for the Little Washita watershed in Central Oklahoma. *York et al. [2002]* found that for the shallow aquifer (less than 2 m) of Mill Creek in northeastern Kansas the water table depth affected the process of evapotranspiration. And *Gutowski et al. [2002]* found that for the Konza Prairie watershed in Kansas up to 33% of monthly evapotranspiration was derived from groundwater-supported exfiltration during dry periods. Further work is needed to assess the extent to which atmosphere and land surface processes are influenced by shallow and even deeper aquifers, and to improve both the subsurface representations in models such as CLASS and the land surface–atmosphere dynamics (e.g., energy budget) in models such as CATHY.

As a final remark, it is interesting to note that, despite the caveats described earlier in comparing two models as different as CATHY and CLASS, and despite significant differences in the detailed responses of the models, similarities in some other response characteristics, such as runoff timing and volume (Figures 3.13 and 3.14) and near-surface soil moisture fluctuations (Figure 3.15), suggest that the models have some elements of a common dynamic basis, and that a river basin with the size of des Anglais (690 km^2) is not a wholly inappropriate scale at which to intercompare and assess these two classes of model. Just as land surface models are evolving towards more sophisticated representations of subsurface flow processes,

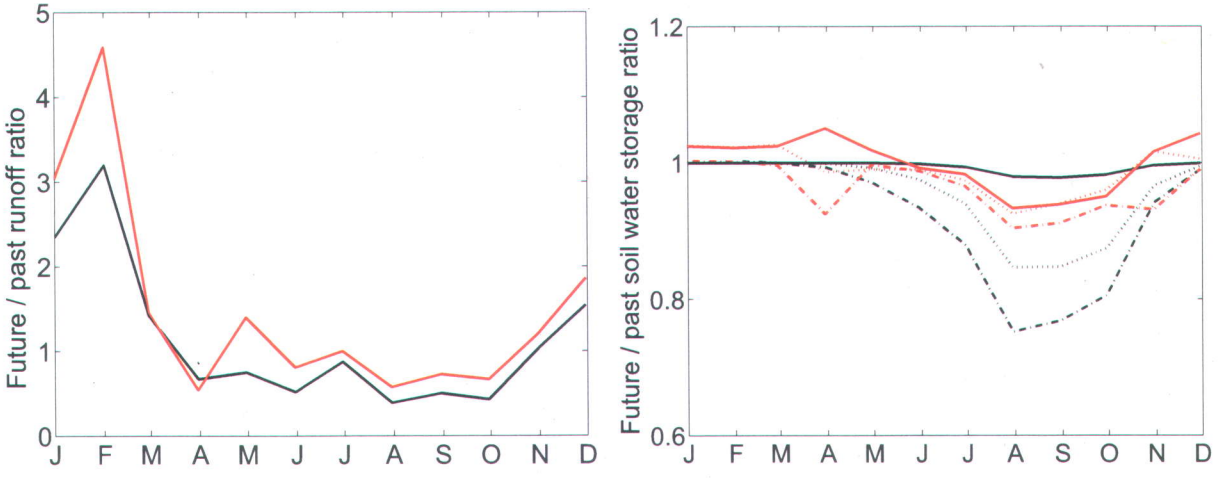

Figure 3.16: Ratio of mean monthly discharge (left graph) and soil water content (right graph) between future and past climates: CLASS (red lines) and CATHY (black lines). Soil storage results are shown for the 0–0.10 m (dash-dotted lines), 0.10–0.35 m (dotted lines), and 0.35–4.10 m (solid lines) CLASS layers.

so catchment and groundwater hydrological models are being extended to incorporate important exchange processes with the atmosphere, including energy and carbon fluxes. Both trends will enable simulation models to be more effectively used in assessing the impacts of climate change on freshwater resources.

3.6 Conclusions

This paper has investigated the sensitivity of the hydrological response (river discharge, aquifer recharge, and soil water storage) of a small river basin to different climate scenarios using a fully coupled numerical model of surface and subsurface flow. Climate variables (precipitation and min / max temperatures) were generated by the CRCM regional climate model for a past (1961-90) and future (2041-70) scenario. These data were further processed using the delta change transfer method and an observed dataset to ensure representativeness of the synthetic data on a monthly basis. A statistical analysis using the Mann-Kendall test was performed for the past and future CRCM datasets. The results of this analysis revealed a significant positive trend in temperature (and hence in potential evapotranspiration) and no significant trend in precipitation. The positive trend in temperature was particularly strong for the winter and early summer months of the future scenario. The numerical model, calibrated first against integrated values of streamflow for one gauge of the catchment, was then verified against integrated values of streamflow at different points within the catchment,

and against distributed observations of water level depth located in parts of the catchment having different pedologic and geologic characteristics. This model setup enabled a detailed investigation of the climate change impacts on different hydrologic response variables for the study basin.

The results of the simulations for the des Anglais river basin show that at the main outlet the climate change impacts are most significant during the peak winter period due to the combination of more precipitation and higher temperature (and hence an increased of rainfall to snowfall ratio) and during summer months due to a marked increase of temperature (and hence evaporation). The results also show significant spatio-temporal variations in the river discharge response to climate change owing to a different partitioning between the overland runoff and baseflow components of the hydrograph, with the latter alleviating the marked decrease in discharge during the summer period. Recharge to the aquifer increases significantly during the winter season due to a higher rain/snow ratio caused by higher temperatures, whereas it decreases in the spring due to an earlier and less intense snowmelt, and over the summer period due to increased evaporation. A spatial analysis of recharge patterns shows that the greatest variations are expected to occur, throughout the year, in the southern portion of the catchment, where the elevations are highest. This analysis also highlighted a possible reversal, during summer months, in groundwater–river interactions in response to groundwater storage deficits. Compared to river discharge and aquifer recharge, the water storage volumes are less sensitive to climate changes. Storage variations are most strongly felt nearest to the surface, which is directly exposed to fluctuations in precipitation and evapotranspiration, and are progressively dampened as soil depth increases. From a spatial analysis of soil moisture variations it was possible to observe organizational patterns that follow the topographic and pedologic characteristics of the catchment. Moreover, through an investigation of the relationship between the tangent curvature of the surface and the soil water variation, performed for a section of the catchment near the outlet, it was found that the hillslope cells located along convergent parts of the catchment tend to experience an increase in soil moisture content in February and March in response to climate change, and less variation in the late summer and early fall (August to October).

An additional objective of the study was to compare the predictions obtained with CLASS, the land surface scheme that is coupled to the CRCM model, to those from the CATHY hydrological model for past and future climate change projections. Differences in runoff and soil water storage response were used to highlight some of the key differences in the models. For instance, we found that CLASS produces higher estimates than CATHY of surface and subsurface runoff throughout the annual cycle for both past and future scenarios, with the greatest difference occurring at the peak flow during snowmelt. The key factors contributing to these discrepancies were the different degree of physical detail included in the surface and subsurface parameterizations (1D Green-Ampt model vs 3D Richards equation) and the

different spatial resolutions of the two models that affect the ability to capture important topographic features and subsurface heterogeneities that strongly influence the response of the catchment (e.g., lateral subsurface moisture redistribution). For soil water storage, CLASS and CATHY were found to be in general agreement in terms of the intra-annual variability of moisture content in the first two soil layers (0–0.10 m and 0.10–0.35 m), particularly for the top layer in which water variations are most directly affected by rainfall events and by diurnal temperature changes during interstorm periods. The largest differences between the two models occur in the third layer (0.35–4.10 m), with CATHY predicting wetter soil conditions over the entire simulation period and moisture fluctuations of much smaller amplitude. The probable causes of this behavior are underestimation of infiltration in CLASS, together with the absence of an underlying groundwater reservoir that results in faster depletion of the bottom layer.

Chapter 4

Impact of grid resolution on the integrated and distributed response of a coupled surface–subsurface hydrological model

Abstract

Digital elevation models (DEMs) at different resolutions (180, 360, and 720 m) are used to examine the impact of different levels of landscape representation on the hydrological response of a 690 km^2 catchment in southern Quebec. Frequency distributions of local slope, plan curvature, and drainage area are calculated for each grid size resolution. This landscape analysis reveals that DEM grid size significantly affects computed topographic attributes, which in turn explains some of the differences in the hydrological simulations. The simulations that are then carried out, using a coupled, process-based model of surface and subsurface flow, examine the effects of grid size on both the integrated response of the catchment (discharge at the main outlet and at two internal points) and the distributed response (water table depth, surface saturation, and soil water storage). The results indicate that discharge volumes increase as the DEM is coarsened, and that coarser DEMs are also wetter overall in terms of water table depth and soil water storage. The reasons for these trends include an increase in the total drainage area of the catchment for larger DEM cell sizes, due to aggregation effects at the boundary cells of the catchment, and to a decrease in local slope and plan curvature variations, which in turn limits the capacity of the watershed to transmit water downslope and laterally. The results obtained also shown that grid resolution effects are less pronounced during dry

periods when soil moisture dynamics are mostly controlled by vertical fluxes of evaporation and percolation.

4.1 Introduction

Physically-based distributed-parameter models are useful tools for simulating hydrologic response *[Kampf and Burges, 2007]*. The current generation of coupled surface–subsurface models *[e.g., Bixio et al., 2000; VanderKwaak and Loague, 2001; Panday and Huyakorn, 2004; Qu and Duffy, 2007; Jones et al., 2008; Camporese et al., 2010]* allows greater possibilities to analyze catchment scale processes and interactions in detail. Recent applications of such models have addressed research and practical problems in hydrogeomorphology *[Mirus et al., 2007]*, solute transport *[Sudicky et al., 2008]*, hydrograph separation *[Jones et al., 2006]*, and baseflow estimation *[Kollet and Maxwell, 2008]*.

The use of process-based distributed-parameter models raises issues related to parameterization and discretization *[e.g., Grayson et al., 1992b]*. For instance, *Downer and Ogden [2003]* showed that while adding complexity in model parameterization is beneficial and justified to accurately simulate distributed state variables such as soil moisture, the added complexity does not result in significantly improved predictions of runoff. *Mueller et al. [2007]* demonstrated that different parameterization approaches for incorporating small-scale variability influence not only the hydrograph at the main outlet but also the production of overland flow within the catchment. *Ebel et al. [2008]* addressed the issue of uniqueness (i.e., the ability of a set of parameter values estimated from given observations to also represent observed behavior under other hydrologic conditions) for both integrated (e.g., discharge) and distributed (e.g., piezometric) predictions, and they also found that the skill of a physically-based model in predicting outlet discharge does not necessarily imply accuracy in capturing physical processes within the catchment.

The increasing availability of digital elevation models (DEMs) and the development of tools that allow rapid analysis of topographic attributes for watershed delineation have contributed to advances in hydrological modeling and to the ease with which a wide diversity of models can be applied over a broad range of scales. Discretization issues related to DEM cell size are consequently quite important, and several studies have investigated this problem. Using a variable source area model based on TOPMODEL *[Beven and Kirkby, 1979]*, *Zhang and Montgomery [1994]* and *Wolock and Price [1994]* looked at how DEM grid size affected the computed topographic characteristics, wetness index, and outflow. Overall, both studies found that peak discharge increased as cell size increased. On the other hand, *Parsons et al. [1997]* found that for Hortonian overland flow, predicted discharge decreased with increasing

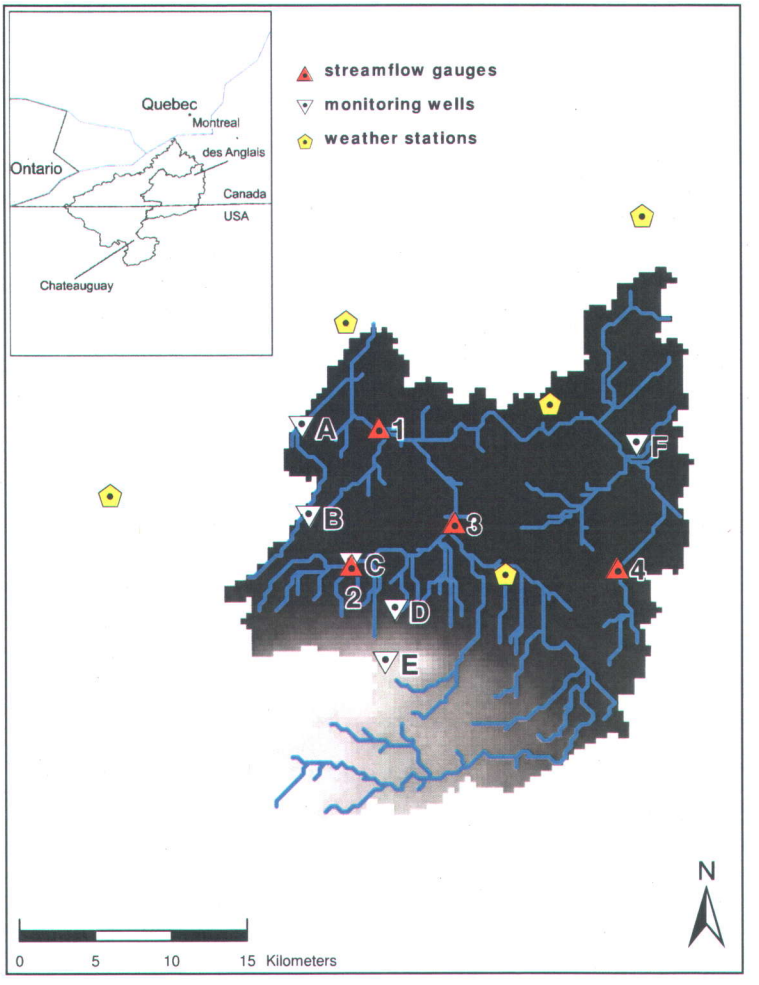

Figure 4.1: Topographic map of the des Anglais catchment at 360 m resolution (highest elevations in light grey) showing the network of weather stations, streamflow gauges, and monitoring wells.

cell size. In another study based on a variable source area model, *Kuo et al. [1999]* examined the loss of information in spatial variability of runoff and soil moisture when increasing not only the DEM grid size but also the land use and soil map grid sizes. As an alternative to uniformly gridded DEMs, terrain features can also be described using triangulated irregular networks (TINs). The effects of TIN resolution on distributed hydrological response have been addressed by *Vivoni et al. [2005]*. Given recent developments in catchment scale hydrological models, there is a need to conduct for coupled models analogous studies of the sensitivity of hydrologic response to DEM cell resolution, focusing in particular on the impact of grid discretization on the factors that control partitioning and other interactions between surface water and groundwater.

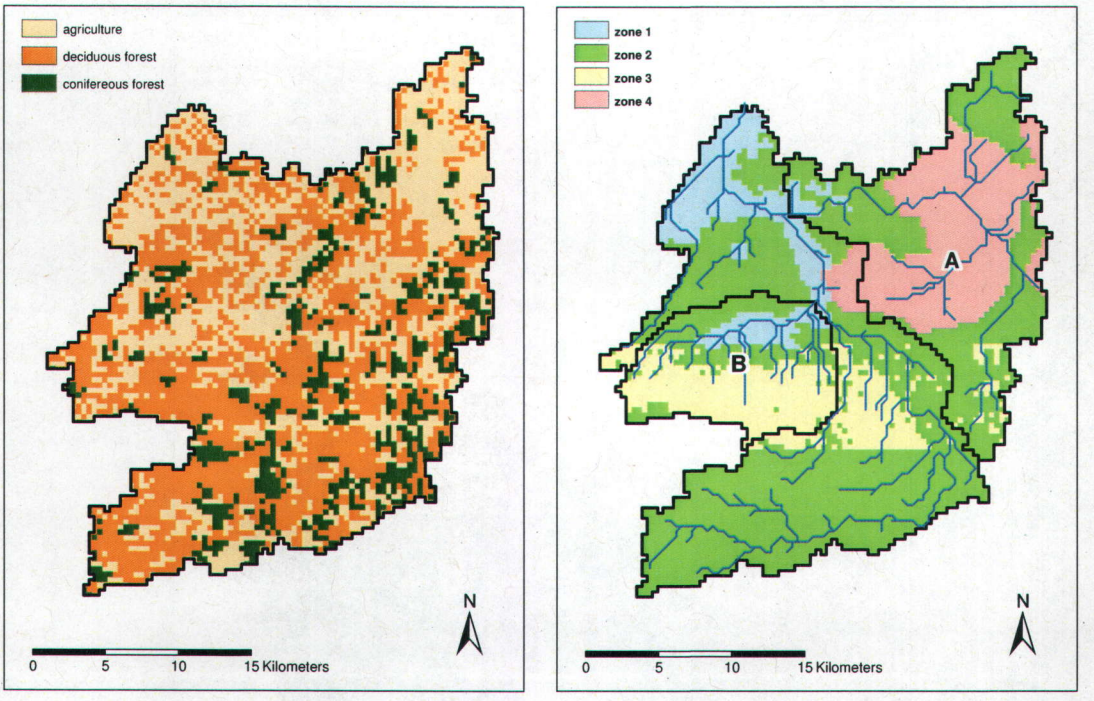

Figure 4.2: Land use and soil map of the des Anglais catchment at 360 m resolution showing also the delineation of the Norton (A) and Rivière Noire (B) subcatchments.

In this study we analyze the impact of DEM resolution for the distributed process–based surface–subsurface model CATHY *[Camporese et al., 2010]* applied to a 690 km^2 catchment in southwestern Quebec. We first present a terrain analysis based on frequency distributions of local slope, plan curvature, drainage area, and topographic index for DEMs of resolution 180, 360, and 720 m. We then examine the effects of grid size on both the integrated response of the catchment (discharge at the main outlet and at two internal points) and on the distributed response (water table depth, surface saturation, and soil water storage). The investigation is carried out using as base configuration a calibrated and verified implementation of the CATHY model for the test catchment at a DEM resolution of 360 m.

4.2 Methods

4.2.1 Study area

The des Anglais river basin (Figure 4.1) has a drainage area of 690 km^2 and an average annual discharge of 300 $\times 10^6$ m^3 at its outlet. It is the largest subcatchment of the trans-

Table 4.1: Material properties for the 10 vertical layers and 4 geopedologic zones of the des Anglais catchment discretization.

Layer (top to bottom)		1	2	3	4	5	6	7	8	9	10
Layer thickness [m]		0.05	0.1	0.3	0.45	1.10	2.10	5.90	20	30	40
Zone 1	K_h [m/s]	5×10^{-4}	5×10^{-4}	5×10^{-4}	5×10^{-4}	1×10^{-4}	5×10^{-9}	5×10^{-9}	1×10^{-7}	5×10^{-8}	5×10^{-8}
	K_z [m/s]	3×10^{-4}	3×10^{-4}	3×10^{-4}	3×10^{-4}	5×10^{-4}	3×10^{-9}	3×10^{-9}	5×10^{-7}	5×10^{-8}	5×10^{-8}
	θ_s [/]	0.5	0.5	0.5	0.5	0.4	0.5	0.5	0.5	0.1	0.1
	S_s [m^{-1}]	1×10^{-5}	1×10^{-5}	1×10^{-5}	1×10^{-5}	1×10^{-4}	3×10^{-3}	3×10^{-3}	1×10^{-4}	1×10^{-6}	1×10^{-6}
Zone 2	K_h [m/s]	5×10^{-4}	5×10^{-4}	5×10^{-4}	5×10^{-4}	1×10^{-5}	1×10^{-5}	1×10^{-7}	5×10^{-8}	5×10^{-8}	5×10^{-8}
	K_z [m/s]	3×10^{-4}	3×10^{-4}	3×10^{-4}	3×10^{-4}	5×10^{-5}	5×10^{-5}	5×10^{-7}	5×10^{-8}	5×10^{-8}	5×10^{-8}
	θ_s [/]	0.5	0.5	0.5	0.5	0.5	0.5	0.5	0.1	0.1	0.1
	S_s [m^{-1}]	1×10^{-5}	1×10^{-5}	1×10^{-5}	1×10^{-5}	1×10^{-4}	1×10^{-4}	1×10^{-4}	1×10^{-6}	1×10^{-6}	1×10^{-6}
Zone 3	K_h [m/s]	5×10^{-4}	5×10^{-4}	5×10^{-4}	5×10^{-4}	1×10^{-4}	1×10^{-4}	2×10^{-6}	2×10^{-6}	2×10^{-6}	2×10^{-6}
	K_z [m/s]	3×10^{-4}	3×10^{-4}	3×10^{-4}	3×10^{-4}	5×10^{-4}	5×10^{-4}	5×10^{-8}	5×10^{-8}	5×10^{-8}	5×10^{-8}
	θ_s [/]	0.5	0.5	0.5	0.5	0.4	0.4	0.1	0.1	0.1	0.1
	S_s [m^{-1}]	1×10^{-5}	1×10^{-5}	1×10^{-5}	1×10^{-5}	1×10^{-4}	1×10^{-4}	1×10^{-6}	1×10^{-6}	1×10^{-6}	1×10^{-6}
Zone 4	K_h [m/s]	5×10^{-8}	5×10^{-8}	5×10^{-8}	5×10^{-8}	1×10^{-7}	1×10^{-7}	1×10^{-7}	5×10^{-8}	5×10^{-8}	5×10^{-8}
	K_z [m/s]	3×10^{-8}	3×10^{-8}	3×10^{-8}	3×10^{-8}	5×10^{-7}	5×10^{-7}	5×10^{-7}	5×10^{-8}	5×10^{-8}	5×10^{-8}
	θ_s [/]	0.9	0.9	0.9	0.9	0.5	0.5	0.5	0.1	0.1	0.1
	S_s [m^{-1}]	1×10^{-5}	1×10^{-5}	1×10^{-5}	1×10^{-5}	1×10^{-4}	1×10^{-4}	1×10^{-4}	1×10^{-6}	1×10^{-6}	1×10^{-6}

boundary Chateauguay River watershed, and has an elevation range from 30 m to 400 m. The Chateauguay basin constitutes the northern part of Adirondack mountain range and initiates the physiographical region of the St. Lawrence Platform. The aquifer system in this region is part of the St. Lawrence Lowlands and consists of Cambrian to Middle Ordovician sedimentary rocks that are slightly deformed and fractured. Unconsolidated sediments of glacial and post-glacial origin (Wisconsinan period and Champlain sea event) overlay the bedrock aquifer and are of varying thickness, reaching 40 m in the northernmost portion *[Tremblay, 2006]*. These sediments are in turn overlain by Quaternary deposits of silty till, compact and dense at the base and reworked and more permeable above. The soils are characterized as mainly weathered Quaternary sediments *[Lamontagne, 2005]*, with the exception of bogs and swamps that overly Champlain sea sediments in the northeastern part of the catchment. These wetlands correspond to closed depressions with a thick accumulation of organic material.

Water table fluctuations in the des Anglais catchment are mainly driven by springtime snowmelt and by rainfall in the fall. The groundwater recession typically extends from June to the end of the growing season (September-October). Mean annual water table fluctuations are about 2.7 m under unconfined or semi-confined conditions and about 1.6 m under confined conditions *[Côté et al., 2006]*. The study area belongs to the Great Lakes and St. Lawrence climate region, characterized by a semi-humid climate with cold winters and humid summers. The annual mean temperature is 6.3 °C, with monthly variations from -10 °C in January to 20 °C in July *[Environment Canada, 2004]*. These temperatures result in frost conditions from mid-November to the end of March. The average annual precipitation is 958 mm, relatively uniformly distributed within the watershed, with snowfall prevalent from December to March when temperatures are below 0 °C.

Table 4.2: Hydraulic geometry parameters for the surface routing module of the hydrological model.

Parameter	hillslope cells	channel cells
reference drainage area, A_s [m^2]	1.2×10^6	690×10^6
reference discharge, Q_f [m^3/s]	1	100
water-surface width, $W(A_s, Q_f)$ [m]	1	50
Gauckler-Strickler conductance coefficient, k_s [m$^{1/3}$/s]	0.5	18
"at-a-station" scaling exponents[a,b], b' and y' [/]	0.36, 0	0.26, 0
"downstream" scaling exponents[a,b], b'' and y'' [/]	0.5, 0	0.5, 0

[a] $W(A,Q) = W(A_s,Q_f)\,Q_f(A_s)^{-b'}\;(A/A_s)^{(b''-b')}\cdot Q^{b'}$

[b] $k_S(A,Q) = k_S(A_s,Q_f)\,Q_f(A_s)^{-y'}\;(A/A_s)^{(y''-y')}\cdot Q^{y'}$

4.2.2 Description of the model

CATHY (CATchment HYdrology) is a coupled physically-based spatially-distributed model for surface–subsurface simulations *[Camporese et al., 2010]*. The model is based on resolution of a one-dimensional diffusion wave approximation of the Saint-Venant equation for overland and channel routing nested within a solver for the three-dimensional equation for subsurface flow in variably saturated porous media (i.e., Richards equation). The routing scheme derives from a discretization of the kinematic wave equation based on the Muskingum-Cunge or matched artificial dispersivity method. Surface runoff is propagated through a 1D drainage network of rivulets and channels automatically extracted by a DEM-based pre-processor and characterized using hydraulic geometry scaling relationships. The distinction between overland and channel flow regimes is made using threshold-type relationships based on, for instance, upstream drainage area criteria. Lakes and other topographic depressions are identified and specially treated as part of the DEM pre-processing procedure. The subsurface solver is based on Galerkin finite elements in space, a weighted finite difference scheme in time, and linearization via Newton or Picard iteration.

A boundary condition switching procedure is used to partition potential (atmospheric) fluxes into actual fluxes across the land surface and changes in surface storage. This scheme resolves the coupling term in the CATHY equations that represents the interactions between surface and subsurface waters. The switching procedure distinguishes four possible states for a given surface node: ponded, saturated, unsaturated, and air-dry. The distinction between ponded and saturated states is based on a threshold parameter that represents the minimum water depth before surface routing can occur (the threshold would be zero for instance for perfectly smooth surfaces and higher for increasingly rough surfaces). An air-dry state is the evaporative analog to rainfall saturation in triggering a switch from an atmosphere-controlled process (and a Neumann boundary condition in the model) to a soil-limited stage

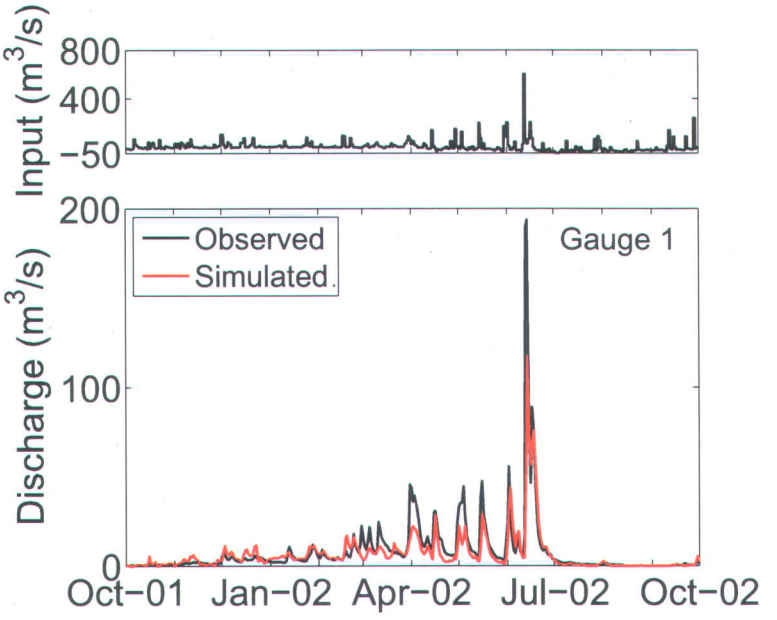

Figure 4.3: Observed (black line) and simulated (red line) discharge for the calibration period at the main streamflow gauge of the catchment.

(and a Dirichlet condition).

4.2.3 Atmospheric forcing term

The daily precipitation and min/max temperature time series for the des Anglais river basin are provided by five weather gauges located within or near the catchment (Figure 4.1). These time series were spatially distributed over the CATHY computational grid nodes through the inverse distance weighting method. The distributed data were then used to reproduce snow accumulation and melting with a model based on a mixed degree-day energy budget method *[Turcotte et al., 2004]*:

$$\frac{\Delta SWE}{\Delta t} = \frac{\Delta WR}{\Delta t} + R + S - M \tag{4.1}$$

$$\frac{\Delta U}{\Delta t} = u_s - u_r - u_c - u_{s-s} - u_{a-s} \tag{4.2}$$

where SWE (m) is the snow water equivalent, WR (m) is the water retained in the snow cover, R (m/s) is the liquid precipitation, S is the solid precipitation (m/s), M (m/s) is the melted water, U (J/m^2) is the heat deficit, u_s (J/m^{2}s) is the increase in heat deficit due to solid precipitation, u_r (J/m^{2}s) is the decrease in heat deficit due to liquid precipitation, u_c (J/m^{2}s) is the loss of heat via convection, u_{s-s} (J/m^{2}s) is the decrease in heat deficit due to the potential melt at the soil–snow interface, and u_{a-s} (J/m^{2}s) is the decrease in heat deficit

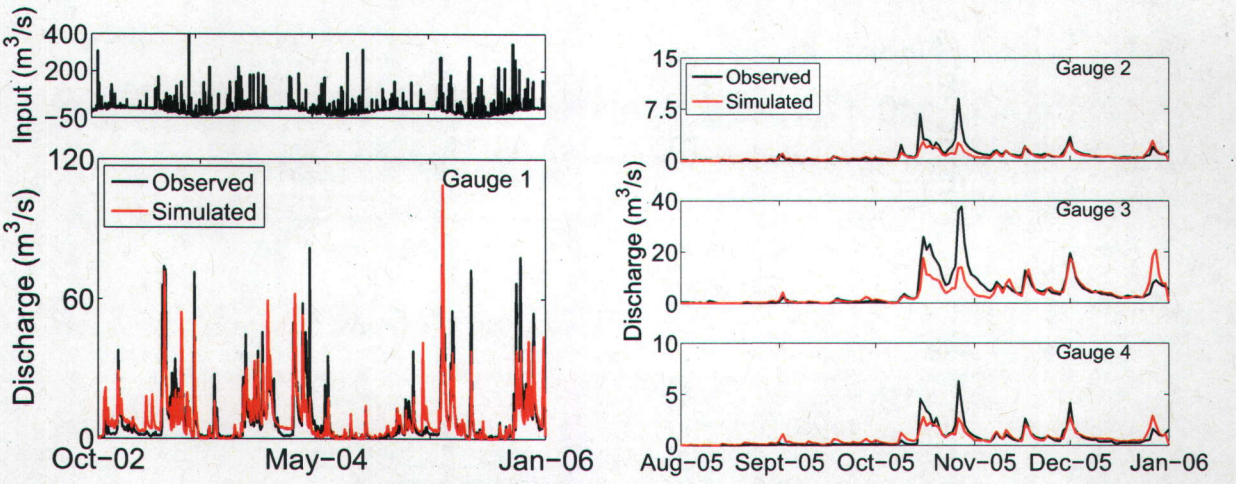

Figure 4.4: Observed (black line) and simulated (red line) discharge at the four gauges of the catchment for the verification period.

due to the potential melt at the air–snow interface. The melted water M is calculated from the heat surplus ($-U$) as:

$$M = \frac{-U}{\Delta t \rho_w C_f} \tag{4.3}$$

where C_f (J kg) is the latent heat of fusion of water, ρ_w (kg/m^3) is the density of water, and Δt (s) is the time step. The heat surplus is derived from equation (4.2), where in turn the different terms are estimated from equations based on known constants such as density of water, the specific heat of water and snow, and the latent heat of fusion of water and on a temperature index and calibrated parameters such as the melting rate and the threshold snow melting temperature.

To account for the different melting dynamics of the main land use classes (Figure 4.2) in the des Anglais catchment (47% agriculture, 37% deciduous forest, 16% coniferous forest), the snow module was applied using three different values for the snow melting rate (8.37 mm/day°C for agriculture, 7.76 mm/day°C for deciduous forest, and 1.56 mm/day°C for coniferous forest) and for the threshold snow melting temperature (2.32 °C for agriculture, -0.92°C for deciduous forest, and 2.10 °C for coniferous forest).

The distributed values of min and max temperature were then used to derive potential evapotranspiration PE (mm/day) using the method of *Oudin et al. [2005]*:

$$PE = \frac{R_e}{\lambda \rho} \frac{T_{avg} + 5}{100} \tag{4.4}$$

where R_e (MJ/m^2 day) is the extraterrestrial radiation , λ (MJ/kg) is the latent heat flux, ρ (kg/m^3) is the density of water, and T_{avg} (°C) is the mean daily air temperature.

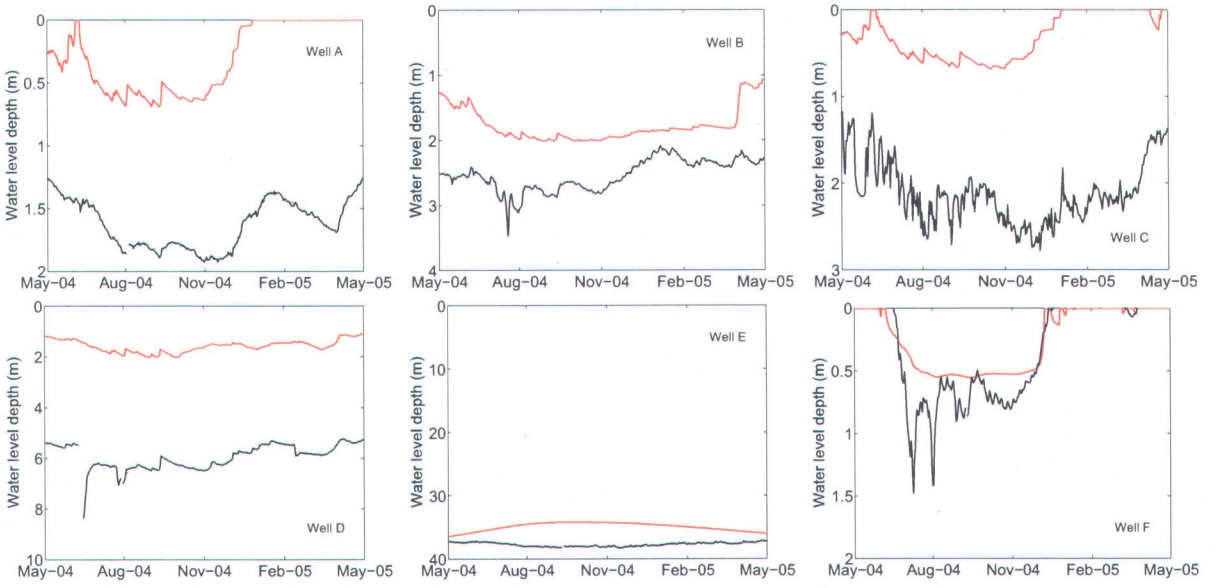

Figure 4.5: Observed (black line) and simulated (red line) water table depths at the six monitoring wells for the verification period.

These pre-processed time series of potential evapotranspiration and snow-corrected precipitation were spatially averaged to obtain the atmospheric input files for CATHY.

4.2.4 Model parameterization and calibration

The 3D subsurface grid for the des Anglais catchment was constructed by subdividing each DEM cell into two triangles and then projecting this 2D surface mesh vertically for 100 m and 10 layers (the layer thicknesses are given in Table 4.1). The resulting 3D grid contains 245454 nodes and 1302360 tetrahedral elements for the 180 m resolution DEM, 61908 nodes and 320280 tetrahedral elements for the 360 m DEM, and 17567 nodes and 87600 tetrahedral elements for the 720 m DEM. Model calibration was carried out for a single resolution (360 m, base configuration) and the calibrated set of parameters were then transferred to the other model resolutions.

According to calibration trials (described below) and to available pedologic and geologic information *[Lamontagne, 2005; Côté et al., 2006]*, the base configuration of the CATHY model was parameterized by assigning different material properties both vertically and laterally. The four zones shown in Figure 4.2 represent distinct soil and Quaternary sediment types that are described in more detail in *Sulis et al. [2010]*. Table 4.1 summarizes the values attributed to each zone and layer for saturated hydraulic conductivity in the horizontal

and vertical directions (K_h, K_z), porosity (θ_s), and specific storage (S_s). A high degree of anisotropy (2 orders of magnitude) was attributed to the bottom 4 layers in zone 3 following indications of preferential horizontal flow paths in this region of the fractured bedrock aquifer *[Côté et al., 2006]*. Zone 3 includes Covey Hill, an elongated (east-west) plateau that is the most pronounced topographic feature in the Canadian part of the des Anglais river basin. The soil hydraulic properties were described by the *van Genuchten and Nielsen [1985]* relationships with residual moisture content $\theta_{res} = 0.07$, air entry pressure head ψ_a= -0.2 m, and fitting exponent $n = 2.0$.

The channel network was identified from the DEM of the catchment using an upstream drainage area threshold of 2.0 km^2, based on visual similarity between the extracted network and the streamlines depicted on topographic maps. Structural parameters for the channel and overland flow networks were calibrated using, for channel dynamics, the bankfull discharge measured at the main streamflow station (gauge 1 in Figure 4.1) as a reference value for the flow rate, and for overland (rivulet flow) dynamics, values reported in literature studies as a basis *[Emmett, 1978; Bathurst, 1986, 1993; Abrahams et al., 1994]*. The values obtained are reported in Table 4.2.

As mentioned, the base case of the CATHY model was calibrated for subsurface hydraulic conductivity (Table 4.1) and surface hydraulic geometry (Table 4.2) parameters. The observation data used was daily streamflow close to the outlet of the catchment (gauge 1 in Figure 4.1), and the simulation period was 12 months, from October 2001 to October 2002. The parameterization was then verified for a 39-month simulation (October 2002 to January 2006) against daily streamflow at the outlet, for a 5-month simulation (August 2005 to January 2006) against daily streamflow at three internal stations (gauges 2, 3, and 4 in Figure 4.1), and for a 12-month simulation (May 2004 to May 2005) against daily groundwater level data at the six monitoring wells shown in Figure 4.1.

Model performance was measured using the root mean squared error (RMS) for groundwater head and the RMS and Nash-Sutcliffe efficiency coefficient (E) for stream discharge *[Nash and Sutcliffe, 1970; Anderson and Woessner, 1992]*:

$$E = 1 - \frac{\sum_{i=1}^{n} (\Omega_{obs,i} - \Omega_{sim,i})^2}{\sum_{i=1}^{n} (\Omega_{obs,i} - \overline{\Omega_{obs}})^2} \tag{4.5}$$

$$RMS = \sqrt{\frac{1}{n} \sum_{i=1}^{n} (\Omega_{obs,i} - \Omega_{sim,i})^2} \tag{4.6}$$

where Ω_{obs}, Ω_{sim}, and $\overline{\Omega_{obs}}$ are the observed, simulated, and average observed state variables

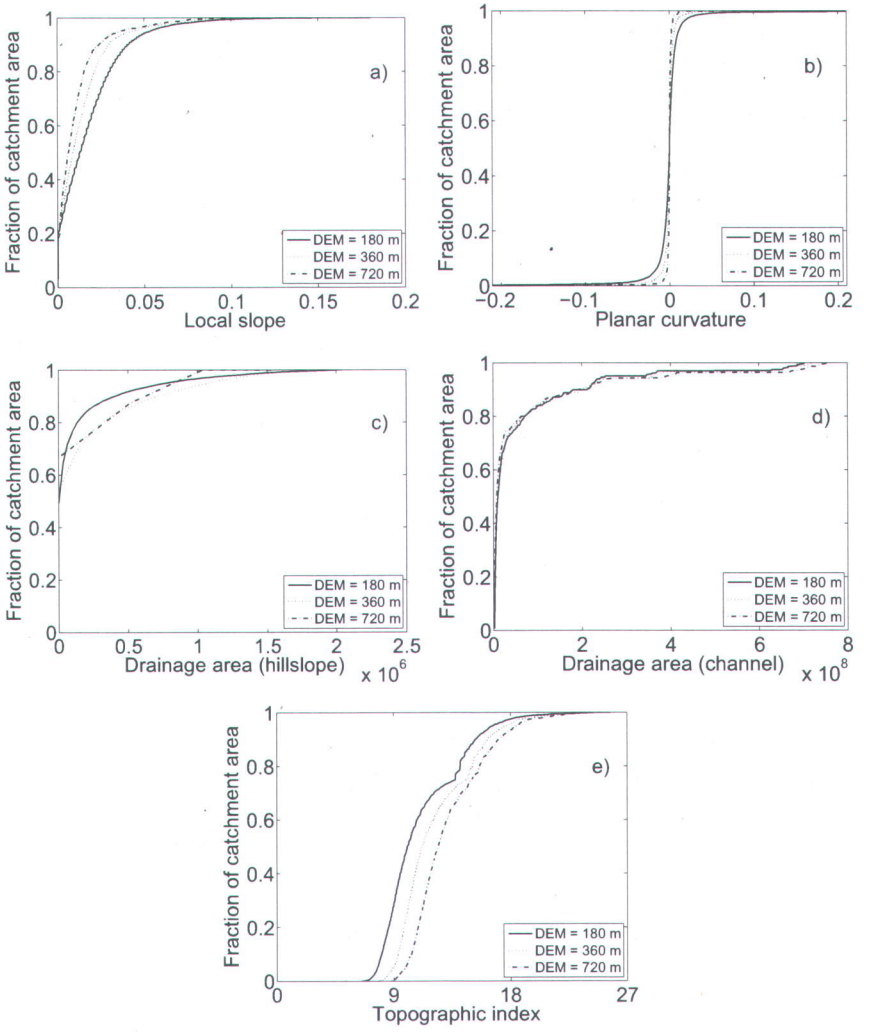

Figure 4.6: Cumulative frequency distributions of slope (a), plan curvature (b), drainage area (for hillslope and channel cells, c and d), and topographic index (e).

(head, discharge) and n is the number of observations. E=1 when there is a perfect match between simulated and observed values and is negative when the simulation is worse at capturing the observations than the mean value of the observed data. Similarly RMS=0 when the match is perfect and increases as the discrepancy between simulation and observation increases.

Figure 4.3 shows the simulated and observed hydrographs at the main gauging station for the calibration run, which produced performance measures of $E = 0.70$ and $RMS = 9.7$ m^3/s for a mean observed discharge of 6.6 m^3/s. Despite some disagreements in the peaks, the model captures the dynamics of the catchment quite well in both the rising and recession portions of the hydrograph. The good performance of the model was confirmed for the verification

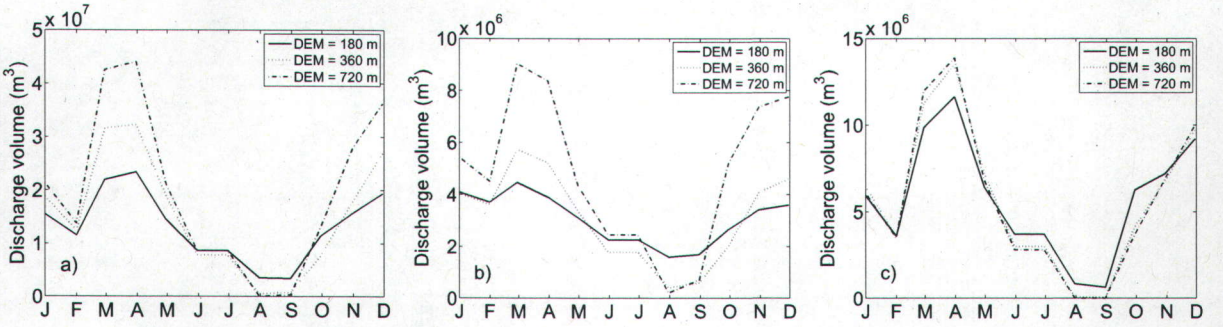

Figure 4.7: Average monthly values of discharge volume at three outlets: des Anglais catchment (a), Rivière Noire subcatchment (b), and Norton subcatchment (c).

tests (Figures 4.4 and 4.5), where an efficiency index of $E = 0.69$ and an RMS value of 7.1 m^3/s resulted for the main streamflow gauge, and reasonable measures were also obtained at the internal streamflow stations ($E = 0.55$ and $RMS = 0.74$ m^3/s for gauge 2, $E = 0.6$ and RMS = 3.9 m^3/s for gauge 3, $E = 0.7$ and $RMS = 0.52$ m^3/s for gauge 4) and at the monitoring wells.

For the six well hydrographs (Figure 4.5) the RMS values ranged from 0.6 to 4.3 m, with the largest value occurring at the well located at the foothill of Covey Hill (well D in Figure 4.1), where the observed groundwater depth is about 6 m below ground surface. Although the RMS values are reasonable and the graphs in Figure 4.5 show that the model reproduces groundwater fluctuations reasonably well, it can also be seen that there is systematic overprediction of groundwater levels. This is probably due to a combination of the no-flow boundary condition assigned to the lateral boundaries of the subsurface domain, preventing regional (interbasin) groundwater flow, and the fact that no other outflow boundaries (e.g., seepage faces along incised streambanks) were assigned that could maintain water tables at a lower level. All subsurface water exits the catchment at the surface, as overland or channel flow and as evaporation. In the absence of field data to support accurate implementation of internal or lateral outflow boundaries, it was preferred to keep the model setup as simple as possible.

Table 4.3: Surface areas (m^2) and cumulative discharge volumes (m^3) at the main outlet of the des Anglais catchment and at two subcatchment outlets.

	surface area			discharge volume		
	180 m	360 m	720 m	180 m	360 m	720 m
Main outlet	690.24×10^6	722.90×10^6	756.34×10^6	5.06×10^8	5.81×10^8	7.60×10^8
Norton	236.64×10^6	244.74×10^6	246.24×10^6	2.17×10^8	2.17×10^8	2.18×10^8
Rivière Noire	92.79×10^6	107.30×10^6	114.59×10^6	1.18×10^8	1.20×10^8	1.90×10^8

4.3 Results

4.3.1 Terrain analysis

Cumulative frequency distributions of local slope, plan curvature, drainage area, and topographic index determined for DEMs at different resolutions (180, 360, and 720 m) reflect changes in both mean and local values *[Zhang and Montgomery, 1994]*. A comparison of the distributions of these topographic attributes allows direct assessment of the influence of grid size on landscape representation, and will inform the analysis of these impacts that will be conducted through model simulations.

As shown in Figure 4.6, cumulative slope distributions are sensitive to DEM grid size. Indeed, the percent of the catchment steeper than a given slope systematically decreases as the DEM grid size increases, and the mean slope drops from 0.018 for the 180 m grid size to 0.010 for the 720 m case. Moreover, since the slope of a grid cell represents an average slope for the area covered by that cell, coarsening the DEM should reduce the ability to resolve the slope characteristics for those portions of the catchment with steeper and more dissected topography.

The plan curvature, expressed in radians per meter, is calculated as *[Zevenbergen and Thorne, 1987]*:

$$K_c = \frac{z_{xx}z_y^2 - 2z_{xy}z_x z_y + z_{yy}z_x^2}{(z_x^2 + z_y^2)^{3/2}} \tag{4.7}$$

where z_x and z_y are the first-order derivatives of the surface topography that describe the rate of change of elevation with distance along the x and y axes, in other words the slope in those directions, z_{xx} and z_{yy} are the second-order derivatives that describe the rate of change of the slope in the x and y directions, i.e., the curvature in those directions, and z_{xy} is a mixed second-order derivative that describes the twisting of the surface. These derivatives are estimated using centered finite differences.

Plan curvature measures topographic convergence (positive values) and divergence (negative values) and hence the tendency of water to converge as it flows across the land. Figure 4.6 shows that a larger grid size reduces the spectrum of plan curvature. Thus the impact of this terrain attribute during a DEM coarsening process will likely be to heighten values and reduce variability in spatially distributed state variables such as moisture content.

The cumulative frequency distributions for drainage area are evaluated separately for hillsope and channel cells in Figure 4.6. As can be seen, grid size effects are smaller for larger drainage areas, in other words where runoff hydrographs are dominated by channel routing. More

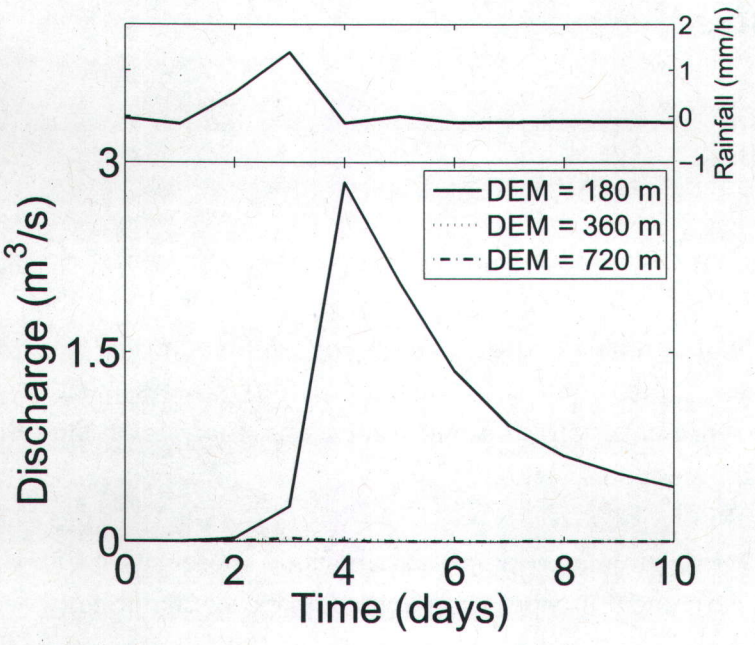

Figure 4.8: Discharge at the main outlet for the rainfall event of 2 September, 2005.

significant effects are encountered at the small hillslope scale, where Figure 4.6 shows that larger grid sizes lead to bias in favor of larger contributing areas. It is important to note that when the distinction between overland and channel cells is made using threshold-type relationships based on upstream drainage area *[Montgomery and Foufoula-Georgiou, 1993; Orlandini and Rosso, 1998]*, DEM resolution will also influence the partitioning between overland and channel cells, with a proportionately larger fraction of overland cells as the grid is refined.

The topographic index is defined as $\ln(a/\tan\beta)$, where a is the upslope area per unit contour length and $\tan\beta$ is the slope gradient. As illustrated in Figure 4.6, grid size significantly affects the cumulative frequency distributions of $\ln(a/\tan\beta)$. Decreasing grid size shifts the cumulative distribution toward lower values of $\ln(a/\tan\beta)$, with the greatest effect on smaller values. Again, computed frequency distributions systematically converge toward that of the finest grid. The mean $\ln(a/\tan\beta)$ value increases from 11.11 for the 180 m DEM to 13.20 for the 720 m DEM. High values of $\ln(a/\tan\beta)$ reflect drainage of large upslope areas and/or low gravitational gradients and thus a greater potential for development of saturation *[e.g., Beven and Kirkby, 1979; Wolock and Price, 1994; Lyon et al., 2006]*.

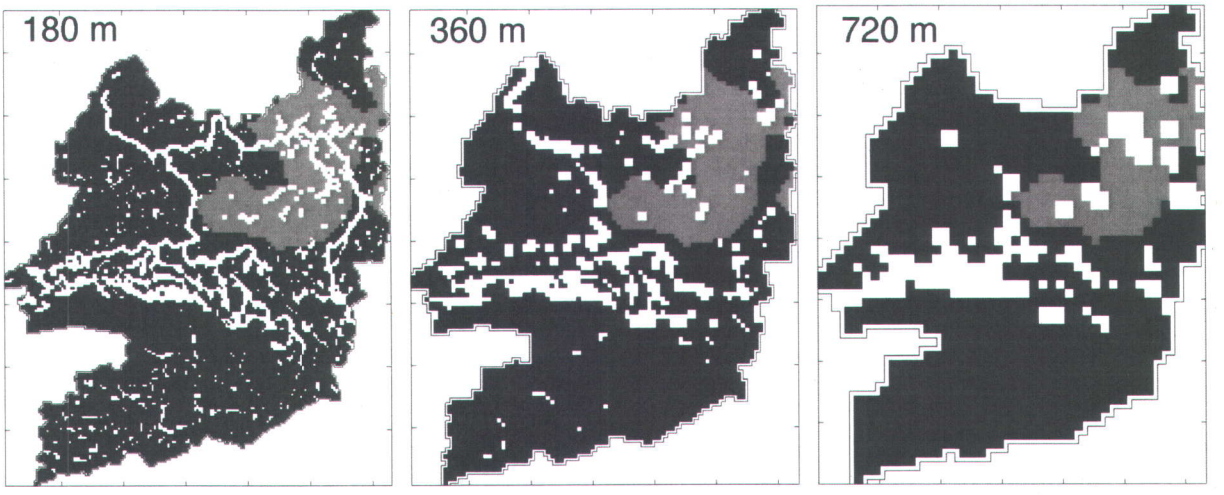

Figure 4.9: Saturation state for a sampled event (2 September, 2005). Black cells indicate unsaturated conditions, white cells are Dunne saturated, and grey cells are Horton saturated.

4.3.2 Hydrological simulations

To investigate the sensitivity of hydrologic response to DEM resolution we used the 39-month verification period (October 2002 to January 2006). This period includes a wide range of storm intensities and some extended wet and dry periods. The analysis examines in particular the grid size effects on integrated (river discharge) and distributed (water table depth, surface saturation, and soil water storage) model responses. A constant water table depth of 0.5 m was used as initial condition.

4.3.2.1 Integrated response

The sensitivity of river discharge to the different DEM resolutions was evaluated at the catchment outlet and at the outlet of two subcatchments having different physiographic features (the Norton and Rivière Noire subcatchments in Figure 4.2). The Rivière Noire catchment includes Covey Hill, the most important groundwater recharge region within the des Anglais river basin *[Côté et al., 2006]*, and thus an area where surface–subsurface interactions (e.g., rainfall-runoff-infiltration partitioning) play an important role.

The total discharge volumes over the simulation period for the three selected outlets are summarized in Table 4.3, where it can be seen that the cumulative discharge for the entire catchment increases significantly as the DEM resolution is coarsened (by 50% between the 720

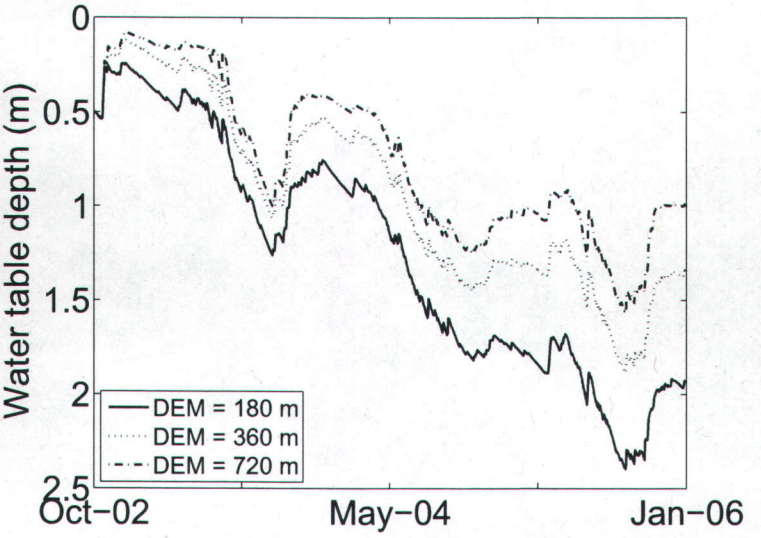

Figure 4.10: Catchment-averaged daily water table depth.

m and 180 m DEMs). The total discharge volume also increases for the two subcatchments, but to a lesser degree. The main reason for the increase is that for the coarser DEM the catchment area actually increases, because at the boundaries of the catchment, larger cells will englobe regions that fall outside of the catchment limits when the cell sizes are smaller. The same trend is obtained upon examination of average monthly discharge values (Figure 4.7), except during the low flow period in the summer and early fall. During this period of the year the catchment response is mainly controlled by the baseflow component of the hydrograph, which tends to increase as the DEM is refined due to higher local slopes (Figure 4.6(a)). The Rivière Noire and Norton subcatchments show the same monthly trends as the river basin, although there are marked differences in sensitivity between these two subcatchments. This is due to a different partitioning between the overland runoff and baseflow components of the hydrograph, with the Norton subcatchment, which is characterized by less permeable soils and a flatter topography, being less sensitive to grid resolution effects due to its dominant overland flow character.

In addition to examining average monthly and cumulative discharge volumes, we also looked at the different hydrograph responses generated by the 3 DEMs for a single low-intensity (1.4 mm/h) rainfall event that occurred on September 2, 2005 after an evaporation period. In Figure 4.8 it can be seen that only the fine resolution DEM produced a response to this event at the main outlet of the river basin, likely owing to the higher degree of connectivity in surface saturation for the finer DEM (see Figure 4.9) that is linked to the wider range in plan curvature and steeper local slopes that emerge at 180 m resolution. The larger extent of saturation implies greater overland flow, and thus a more significant peak or rapid response to the rain event. It is notable in Figure 4.9 that of the two surface runoff generation

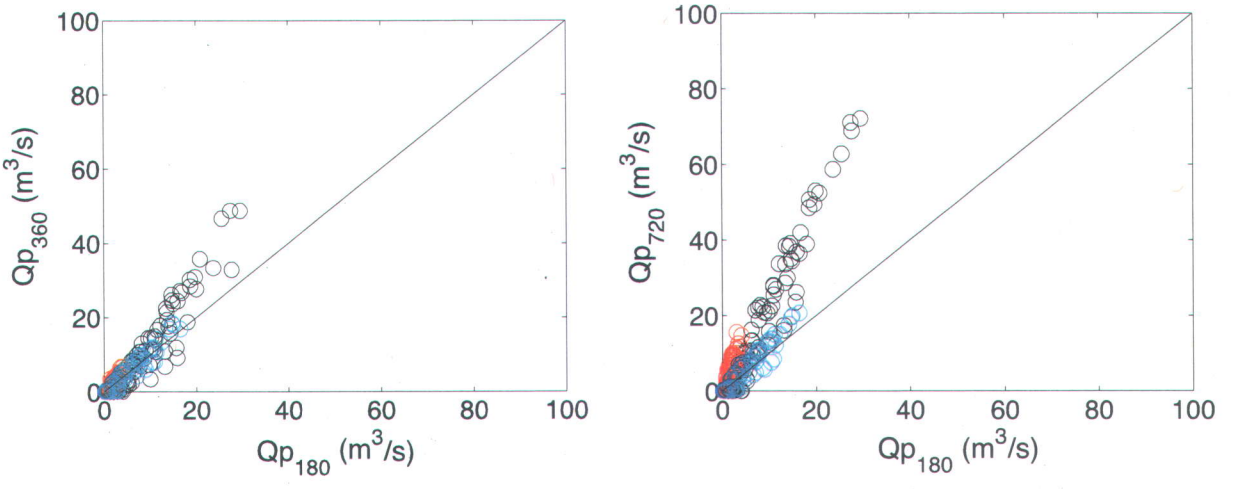

Figure 4.11: Scatter plots between peak flows at 180 m and 360 m DEM resolutions (left) and between peak flows at 180 m and 720 m DEM resolutions (right). Black circles correspond to the main outlet, red circles correspond to the Rivère Noire subcatchment, and blue circles correspond to the Norton subcatchment.

mechanisms, it is saturation excess (Dunne response) that is highly sensitive to DEM resolution. The area affected by infiltration excess (Horton) runoff remains quite constant for the 3 DEMs. This result is consistent with the plan curvature and local slope explanation, since Dunne saturation can be highly affected by these terrain features, whereas Horton saturation depends solely on the rapport between surface hydraulic conductivity and rainfall rate.

4.3.2.2 Distributed response

The water table depth is interpolated from CATHY pressure heads between the first two nodes (starting from the bottom) along each vertical profile for which the pressure head transitions from a positive value to a negative value. Proceeding from the bottom ensures that the water table corresponds to an aquifer, and not some localized (perched) area of saturation that can form for instance at the edge of an infiltration front. Daily averaged nodal values of water table depth for each DEM were spatially aggregated to obtain mean values for the catchment over the entire simulation period.

Figure 4.10 plots the evolution of the catchment-averaged water table depths for the three DEMs, and shows that the water tables are consistently shallower at coarser grid resolutions. During periods of continuous high-intensity precipitation, saturated source areas develop faster and more extensively for DEM resolutions that yield higher topographic index values

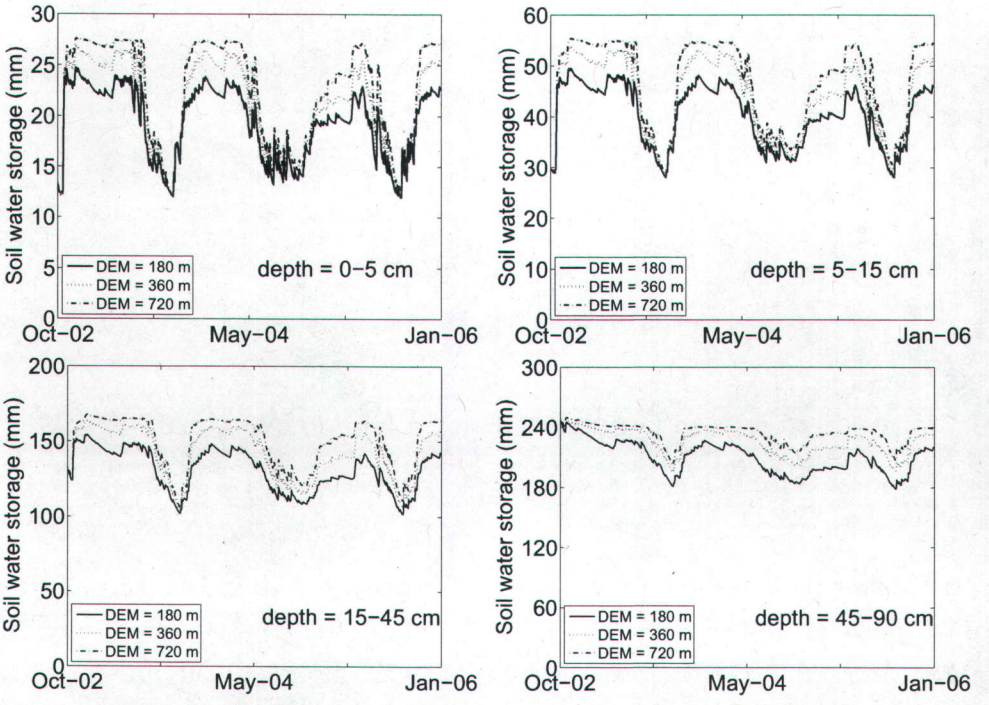

Figure 4.12: Average soil water storage at different depth intervals for the three DEM resolution.

(shallower water tables), resulting in higher peak flows as shown in Figure 4.11.

In Figure 4.12 catchment-averaged daily soil water storage (SWS) values are plotted. Four graphs of SWS are shown, representing soil moisture content vertically integrated over soil depths of 0-5 cm, 5-15 cm, 15-45 cm, and 45-90 cm. The results corroborate those obtained for the water table depths, with higher SWS values for the coarser grids. This increase is also related to the decrease in the variation of local slope and plan curvature, which tends to smooth the lateral redistribution of moisture content *[Kuo et al., 1999]*. As expected the grid size effects are most pronounced nearest to the surface and are progressively dampened as soil depth increases. Figure 4.13 shows the cumulative frequency distribution of soil moisture at the ground surface at the end of a 10-day rainfall period (in October, 2005) and at the end of a 10-day dry period (August, 2003). As seen with previous results, the catchment is wetter overall at coarser grid resolutions. We also see that grid sensitivity is much greater during the wet period than the dry period. Moisture content differences during wet periods are caused by lateral water transport, and this process is dominated by the plan curvature. During dry periods, evaporation is the main factor in moisture loss and lateral transport is small, thus plan curvature plays a lesser role. These findings are consistent with those of *Grayson et al. [1997]*, who showed that when the soil is dry, soil moisture content is primarily governed by vertical fluxes of percolation, rainfall, and evaporation at a particular location

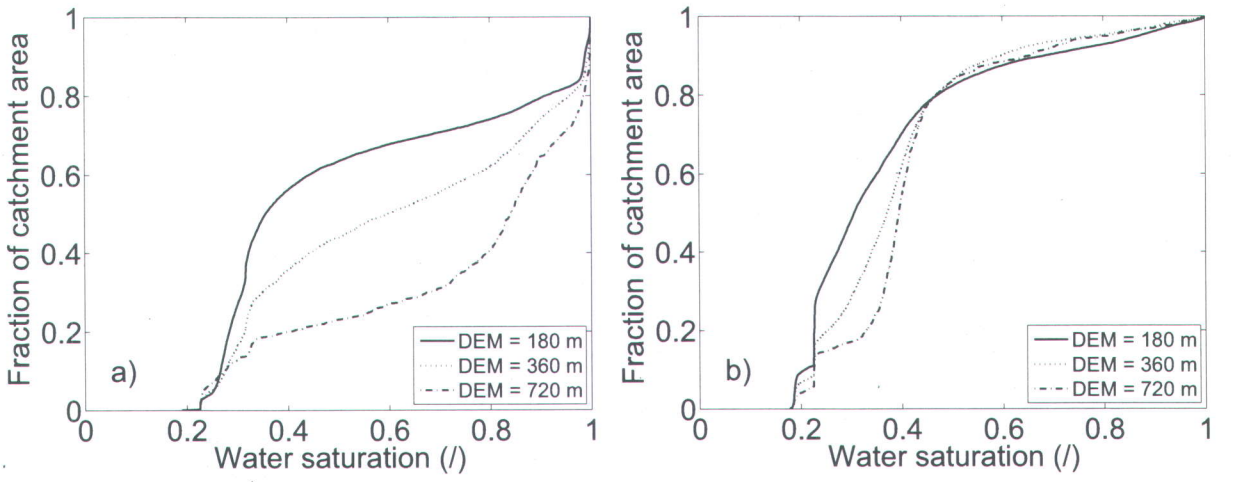

Figure 4.13: Cumulative frequency distribution of surface soil saturation at the end of a 10-day rainfall period (a) and at the end of a 10-day dry period (b).

and is thus independent of the curvature of the landscape.

4.4 Conclusions

The resolution of a DEM significantly affects both the representation of the land surface and hydrologic simulations based on this representation. As the grid is refined, landscape features are more accurately resolved. The sensitivity analysis presented in this study has demonstrated the differences in hydrologic response of a mid-sized catchment as the DEM resolution was varied from 180 m to 360 m to 720 m resolution. The simulations were conducted using a process-based numerical model of coupled groundwater and surface water flow. We identified a correspondence between the sensitivity in hydrologic response, the underlying surface–subsurface dynamics, and the terrain attributes, in particular local slope, plan curvature, and topographic index. Response variables that were examined include hydrograph discharge at the catchment outlet and at internal points, water table depths, soil water storage, and surface saturation.

The results show that simulated discharge volumes increase as the DEM is coarsened, and that coarser DEMs are also wetter overall in terms of water table depth and soil water storage. The reasons for these trends include an increase of the total drainage area of the catchment for larger DEM cell sizes, due to aggregation effects at the boundary cells of the catchment, and to a decrease in local slope and plan curvature variations, which in turn limits the capacity of the watershed to transmit water downslope and laterally. It was also shown

that the grid resolution effects are less pronounced during dry periods when soil moisture dynamics is mostly controlled by vertical fluxes of evaporation and percolation.

This work touches on important issues of scale invariance that arise in the use of DEM-based hydrological models. In addition to the factors examined here, the lack of scale invariance as a model's grid resolution is refined or coarsened can also result from the conceptualization and parameterization of different processes in a distributed model, such as the representation of the hydraulic geometry of rills and channels. These issues, and appropriate scaling relationships and downscaling techniques to resolve them, require further study.

Bibliography

M. B. Abbott. *Distributed Hydrological Modeling*, chapter Comment on 'A discussion of distributed hydrological modelling'. Kluwer Academic, 1996.

M. B. Abbott, J. C. Bathurst, J. A. Cunge, P. E. O'Connell, and J. Rasmussen. An introduction to the European Hydrological System — Système Hydrologique Européen, "SHE", 1: History and philosophy of a physically-based, distributed modelling system. *J. Hydrol.*, 87 (1–2):45–59, 1986.

A. S. Abdul and R. W. Gillham. Laboratory studies of the effects of the capillary fringe on streamflow generation. *Water Resour. Res.*, 20(6):691–698, 1984.

A. D. Abrahams and A. J. Parsons. Determining the mean depth of overland flow in field studies of flow hydraulics. *Water Resour. Res.*, 26(3):501–503, 1990.

A. D. Abrahams, A. J. Parsons, and S.-H. Luk. Distribution of depth of overland flow on desert hillslopes and its implication for modeling erosion. *J. Hydrol.*, 106(1):177–184, 1989.

A. D. Abrahams, G. Li, and A. J. Parsons. Rill hydraulics on semiarid hillslopes, southern Arizona. *Earth Surf. Proc. Land.*, 21(1):35–47, 1994.

E. I. Anderson. Modeling groundwater–surface water interactions using the Dupuit approximation. *Adv. Water Resources*, 28(4):315–327, 2005.

M. P. Anderson and W. W. Woessner. *Applied Groundwater Modeling.* Academic, 1992.

S. P. Anderton, S. P., J. Latron, S. M. White, P. Llorens, F. Gallart, C. Salvany, and P. E. O'Connell. Internal evaluation of a physically-based distributed model using data from a Mediterranean mountain catchment. *Hydrol. Earth Syst. Sci.*, 6(1):67–83, 2002.

A. S. Antonarakis, K. S. Richards, J. Brasington, and M. Bithell. Leafless roughness of complex tree morphology using terrestrial lidar. *Water Resour. Res.*, 45, W10401, doi:10.1029/2008WR007666, 2009.

N. W. Arnell, D. A. Hudson, and R. G. Jones. Climate change scenarios from a regional climate model: Estimating change in runoff in southern Africa. *J. Geophys. Res.*, 108(D16), 4519, doi:10.1029/2002JD002782, 2003.

V. K. Arora and G. J. Boer. Effects of simulated climate change on the hydrology of major river basins. *J. Geophys. Res.*, 106(D4):3335–3348, 2001.

J. C. Bathurst. Physically-based distributed modelling of an upland catchment using the Système Hydrologique Européen. *J. Hydrol.*, 87(1–2):79–102, 1986.

J. C. Bathurst. *Channel Network Hydrology*, chapter Flow resistance through the channel network, pages 69–98. John Wiley, New York, 1993.

J. C. Bathurst and P. E. O'Connell. Future of distributed modeling: The Systeme Hydrologique Europeen. *Hydrol. Process.*, 6(3):265–277, 1992.

K. E. Bencala. Interactions od solutes and streambed sediments; 2. A dynamic analysis of the coupled hydrologic and chemical processes that determine solute transport. *Water Resour. Res.*, 20(12):1804–1814, 1984.

K. Beven. Changing ideas in hydrology–The case of physically-based models. *J. Hydrol.*, 105 (1–2):157–172, 1989.

K. Beven. Prophecy, reality and uncertainty in distributed hydrological modelling. *Adv. Water Resources*, 16(1):41–51, 1993.

K. Beven. On the future of distributed modelling in hydrology. *Hydrol. Process.*, 14(16): 3183–3184, 2000a.

K. Beven. A manifesto for the equifinality thesis. *J. Hydrol.*, 320(1–2):18–36, 2006.

K. Beven and A. M. Binley. The future of distributed modelling: model calibration and uncertainty prediction. *Hydrol. Process.*, 6(3):279–298, 1992.

K. Beven and M. J. Kirkby. A physically based, variable contributing model of basin hydrology. *Hydrol. Sci. Bull.*, 24(1):43–69, 1979.

K. J. Beven. *Rainfall-Runoff Modeling: The Primer.* John Wiley, Hoboken, N. J., 2000b.

K. J. Beven. On environmental models of everywhere on the GRID. *Hydrol. Process.*, 17(1): 171–174, 2003.

A. C. Bixio, S. Orlandini, C. Paniconi, and M. Putti. Physically-based distributed model for coupled surface runoff and subsurface flow simulation at the catchment scale. In L. R. Bentley, J. F. Sykes, C. A. Brebbia, W. G. Gray, and G. F. Pinder, editors, *Computational Methods in Water Resources, Vol. 2*, pages 1115–1122, Rotterdam, The Netherlands, 2000. Balkema.

D. M. Bjerklie, D. Moller, L. C. Smith, and S. L. Dingman. Estimating discharge in rivers using remotely sensed hydraulic information. *J. Hydrol.*, 309(1–4):191–209, 2005.

A. Boone, F. Habets, J. Noilhan, D. Clark, P. Dirmeyer, S. Fox, Y. Gusev, I. Haddeland, R. Koster, D. Lohmann, S. Mahanama, K. Mitchell, O. Nasonova, G.-Y. Niu, A. Pitman, J. Polcher, A. B. Shmakin, K. Tanaka, B. van den Hurk, S. Vérant, D. Verseghy, P. Viterbo, and Z.-L Yang. The Rhone-aggregation land surface scheme intercomparison project: An overview. *J. Clim.*, 17(1):187–208, 2004.

L. C. Bowling, D. P. Lettenmaier, B. Nijssen, L. P. Graham, D. B. Clark, M. El Maayar, R. Essery, S. Goers, Y. M. Gusev, F. Habets, B. van den Hurk, J. Jin, D. Kahan, D. Lohmann, X. Ma, S. Mahanama, D. Mocko, O. Nasonova, G.-Y. Niu, P. Samuelsson, A. B. Shmakin, K. Takata, D. Verseghy, P. Viterbo, Y. Xia, Y. Xue, and Z.-L. Yang. Simulation of high latitude hydrological processes in the Torne-Kalix basin: PILPS Phase 2e. 1–Experimental description and summary intercomparisons. *Global Planet. Change*, 38 (1–2):1–30, 2003.

R. H. Brooks and A. T. Corey. Hydraulic properties of porous media. Hydrology Paper 3, Colorado State University, Fort Collins, CO, 1964.

K. L. Brubaker and D. Entekhabi. Analysis of feedback mechanisms in land-atmosphere interaction. *Water Resour. Res.*, 32(5):1343–1357, 1996.

Y. Caballero, S. Voirin-Morel, F. Habets, J. Noilhan, P. LeMoigne, A. Lehenaff, and A. Boone. Hydrological sensitivity of the Adour-Garonne river basin to climate change. *Water Resour. Res.*, 43, W07488, doi:10.1029/2005WR004192, 2007.

M. Camporese, C. Paniconi, M. Putti, and P. Salandin. Ensemble Kalman filter data assimilation for a process-based catchment scale model of surface and subsurface flow. *Water Resources Research*, 45, W10421, doi:10.1029/2008WR007031, 2009.

M. Camporese, C. Paniconi, M. Putti, and S. Orlandini. Surface–subsurface flow modeling with path-based routing, boundary condition-based coupling, and assimilation of multisource observation data. *Water Resour. Res.*, 46, W02512, doi:10.1029/2008WR007536, 2010.

J. Carrera and S. P. Neuman. Estimation of aquifer parameters under transient and steady state conditions: Uniqueness, stability, and solution alogorithms. *Water Resour. Res.*, 22 (2):211–227, 1986.

N. M. Castro and G. M. Hornberger. Surface–subsurface water interactions in an alluviated mountain stream channel. *Water Resour. Res.*, 27(7):1613–1621, 1991.

D. Caya and R. Laprise. A semi-implicit semi-lagrangian regional climate model: The Canadian RCM. *Mon. Wea. Rev.*, 127(3):341–362, 1999.

L. Chen and M. H. Young. Green-Ampt infiltration model for sloping surfaces. *Water Resour. Res.*, 42, W07420, doi:10.1029/2005WR004468, 2006.

F. H. Chiew, J. Teng, J. Vaze, D. A. Post, J. M. Perraud, D. G. C. Kirono, and N. R. Viney. Estimating climate change impact on runoff across south-east Australia: Method, results and implications of modelling method. *Water Resour. Res.*, 45, W10414, doi:10.1029/2008WR007338, 2009.

V. T. Chow, D. R. Maidment, and L. W. Mays, editors. *Applied Hydrology.* McGraw-Hill, New York, NY, 1988.

J. H. Christensen and O. B. Christensen. A summuary of the PRUDENCE model projections of changes in European climate by the end of this century. *Clim. Change*, 81 (supplement 1):7–30, doi:10.1007/s10584–006–9210–7, 2007.

R. B. Clapp and G. M. Hornberger. Empirical equations for some soil hydraulic properties. *Water Resour. Res.*, 14(4):601–604, 1978.

R. T. Clarke. Issues of experimental design for comparing the performance of hydrologic models. *Water Resour. Res.*, 44, W01409, doi:10.1029/2007WR005927, 2008.

Consortium of Universities for the Advancement of Hydrological Science. A National Center for Hydrologic Synthesis: Scientific objectives, structure, and implementation. Technical Report 5, Washington, D. C., 2003.

P. G. Cook, D. K. Solomon, W. E. Sanford, E. Busenberg, L. N. Plummer, and R. J. Poreda. Inferring shallow groundwater flow in saprolite and fractured rock using environmental tracers. *Water Resour. Res.*, 32(6):1501–1509, 1996.

B. J. Cosby, M. Hornberger, B. Clapp, and R. Ginn. A Statistical Exploration of the Relationships of Soil Moisture Characteristics to the Physical Properties of Soils. *Water Resour. Res.*, 20(6):682–690, 1984.

M.-J. Côté, Y. Lachance, C. Lamontagne, M. Nastev, R. Plamadon, and N. Roy. Atlas du bassin versant de la rivière Châteauguay. Technical report, Ministère du Développement durable, de l'Environnement et des Parcs, Québec, 2006.

N. H. Crawford and R. K. Linsley. Digital simulation in hydrology: Stanford watershed model iv. Technical Report 39, Dept. of Civil Eng., Stanford University, CA, 1966.

B. Dafflon, J. Irving, and K. Holliger. Use of high-resolution geophysical data to characterize heterogeneous aquifers: Influence of data integration method on hydrological predictions. *Water Resour. Res.*, 45, W09407, doi:10.1029/2008WR007646, 2009.

J. C. Van Dam and R. A. Feddes. Numerical simulation of infiltration, evaporation, and shallow groundwater levels with the Richards equation. *J. Hydrol.*, 233(1–4):72–85, 2000.

S. L. Dingman. *Physical Hydrology.* Waveland Press, Inc., Long Grove, Illinois, 2002.

J. Dong, J. P. Walker, P. R. Houser, and C. Sun. Scanning multichannel microwave radiometer snow water equivalent assimilation. *J. Geophys. Res.*, 112, D07108, doi:10.1029/2006JD007209, 2007.

J. C. I. Dooge. *The role of the hydrological cycle in climate.* Climate and Geosciences. Kluwer, Dardrecht, 1989.

J. C. I. Dooge, M. Bruen, and B. Parmentier. A simplified model for estimating the sensitivity of runoff to long-term changes in precipitation without change in vegetation. *Adv. Water Resources*, 23(2):153–163, 1999.

C. W. Downer and F. L. Ogden. Prediction of runoff and soil moistures at the watershed scale: Effects of model complexity and parameter assignment. *Water Resour. Res.*, 39(3), 1045, doi:10.1029/2002WR001439, 2003.

C. W. Downer and F. L. Ogden. Appropriate vertical discretization of Richards' equation for two-dimensional watershed-scale modelling. *Hydrol. Process.*, 18(1):1–22, 2004.

T. Dunne. *Hillslope Hydrology*, chapter Field studies of hillslope flow processes, pages 227–293. John Wiley, Chichester, 1978.

P. S. Eagleson. Climate, soil, and vegetation, 1, Introduction to water balance dynamics. *Water Resour. Res.*, 14(5):705–712, 1978.

B. A. Ebel and K. M. Loague. Physics-based hydrologic response simulation:Seeing through the fog of equifinality. *Hydrol. Process.*, 20(13):2887–2900, 2006.

B. A. Ebel, K. Loague, D. Montgomery, and W. E. Dietrich. Physics-based continuous simulation of long-term near-surface hydrologic response for the Coos Bay experimental catchment. *Water Resour. Res.*, 44, W07417, doi:10.1029/2007WR006442, 2008.

B. A. Ebel, B. B. Mirus, C. S. Heppner, J. E. VanderKwaak, and K. Loague. First-order exchange coefficient coupling for simulating surface water–groundwater interactions: parameter sensitivity and consistency with a physics-based approach. *Hydrol. Process.*, 23 (13):1949–1959, 2009.

K. Eckhardt and U. Ulbrich. Potential impacts of climate change on groundwater recharge and streamflow in a central European low mountain range. *J. Hydrol.*, 284(1–4):244–252, 2003.

A. I. El-Kadi and G. Ling. The Courant and Peclet number criteria for the numerical solution of the Richards equation. *Water Resour. Res.*, 29(20):3485–3494, 1993.

E. A. B. Eltahir. A soil moisture–rainfall feedback mechanism 1. Theory and observations. *Water Resour. Res.*, 34(4):765–776, 1998.

W. W. Emmett. Overland flow. In M. J. Kirkby, editor, *Hillslope Hydrology*, pages 145–176. John Wiley, New York, 1978.

Environment Canada, 2004. Canadian Daily Climate Data (CDCD). http://climate.weatheroffice.ec.gc.ca, 2004.

Y. Fan and R. L. Bras. Analytical solutions to hillslope subsurface storm flow and saturation overland flow. *Water Resour. Res.*, 34(4):921–927, 1998.

Y. Fan, G. Miguez-Macho, C. P. Weaver, R. Walko, and A. Robock. Incorporating water table dynamics in climate modeling: 1. Water table observations and equilibrium water table simulations. *J. Geophys. Res.*, 112, D10125, doi:10.1029/2006JD008111, 2007.

M. G. Ferrick. Analysis of River Wave Types. *Water Resour. Res.*, 21(2):209–220, 1985.

L. Feyen, R. Vásquez, K. Christiaens, O. Sels, and J. Feyen. Application of a distributed physically-based hydrological model to a medium size catchment. *Hydrol. Earth Syst. Sci.*, 4(1):47–63, 2000.

G.M. Flato and G. J. Boer. Warming asymmetry in climate change simulations. *Geophys. Res. Lett.*, 28(1):195–198, 2001.

R. A. Freeze. Role of subsurface flow in generating surface flow runoff 1. Base flow contributions to channel flow. *Water Resour. Res.*, 8(3):609–623, 1972.

A. Furman. Modeling Coupled Surface–Subsurface Flow Processes: A Review. *Vadose Zone J.*, 7(2):741–756, 2008.

P. H. Gleick. Climate change, hydrology, and water resources. *Rev. Geophys.*, 27(3):329–344, 1989.

G. Gottardi and M. Venutelli. A control-volume finite-element model for two-dimensional overland flow. *Adv. Water Resources*, 16(5):277–284, 1993.

R. S. Govindaraju and M. L. Kavvas. Dynamics of moving boundary overland flows over infiltrating surfaces at hillslopes. *Water Resour. Res.*, 27(8):1885–1898, 1991.

R. S. Govindaraju and M. L. Kavvas. Characterization of the rill geometry over straight hillslopes through spatial scales. *J. Hydrol.*, 130(1–4):339–365, 1992.

R. B. Grayson, I. D. Moore, and T. A. McMahon. Physically based hydrologic modeling 1. A terrain-based model for investigative purposes. *Water Resour. Res.*, 28(10):2639–2658, 1992a.

R. B. Grayson, I. D. Moore, and T. A. McMahon. Physically based hydrologic modeling 2. Is the concept realistic? *Water Resour. Res.*, 26(10):2659–2666, 1992b.

R. B. Grayson, A. W. Western, F. H. Chiew, and G. Blöschl. Preferred states in spatial soil moisture patterns: Local and nonlocal controls. *Water Resour. Res.*, 33(12):2897–2908, 1997.

W. H. Green and G. A. Ampt. Studies on soil physics: I. flow of air and water through soils. *J. Agr. Sci.*, 4:1–24, 1911.

L. E. Gulden, E. Rosero, Z.-L. Yang, M. Rodell, C. S. Jackson, G.-Y. Niu, P. J.-F. Yeh, and J. Famiglietti. Improving land-surface model hydrology: Is an explicit aquifer model better than a deeper soil profile? *Geophys. Res. Lett.*, 34, L09402, doi:10.1029/2007GL029804, 2007.

O. Gunduz and M. M. Aral. Rivernetworks and groundwater flow: A simultaneous solution of a coupled system. *J. Hydrol.*, 301(1–4):216–234, 2005.

A. Günter, J. Stuck, S. Werth, P. Döll, K. Verzano, and B. Merz. A global analysis of temporal and spatial variations in continental water storage. *Water Resour. Res.*, 43, W05416, doi:10.1029/2006WR005247, 2007.

W. J. Gutowski, Charles J. Vörösmarty, M. Person, Z. Ötles, B. Fekete, and J. York. A Coupled Land-Atmosphere Simulation Program (CLASP): Calibration and validation. *J. Geophys. Res.*, 107, D16, doi: 10.1029/2001JD000392, 2002.

P. B. Hairsine and C. W. Rose. Modeling water erosion due to overland flow using physical principles, 1, Sheet flow. *Water Resour. Res.*, 28(1):237–243, 1992a.

P. B. Hairsine and C. W. Rose. Modeling water erosion due to overland flow using physical principles, 2, Rill flow. *Water Resour. Res.*, 28(1):245–250, 1992b.

J. W. Harvey and K. E. Bencala. The effect of streambed topography on surface-subsurface water exchange in mountain catchments. *Water Resour. Res.*, 29(1):89–98, 1993.

L. E. Hay, R. L. Wilby, and G. H. Leavesley. A comparison of delta change and downscaled GCM scenarios for three mountainous basins in the United States. *J. Am. Water Resour. Assoc.*, 36(2):387–398, 2000.

C. S. Heppner, K. Loague, and J. E. VanderKwaak. Long-term InHM simulations of hydrologic response and sediment transport for the R-5 catchment. *Earth Surf. Processes Landforms*, 32(9):1273–1292, 2008.

R. M. Hirsh, J. R. Slack, and R. A. Smith. Techniques of trend analysis for monthly water quality data. *Water Resour. Res.*, 18(1):107–121, 1982.

A. D. Howard. A detachment-limited model of drainage basin evolution. *Water Resour. Res.*, 30(7):2261–2285, 1994.

A. D. Howard and C. F. McLane. Erosion of cohesionless sediment by groundwater seepage. *Water Resour. Res.*, 24(10):1659–1674, 1998.

P. S. Huyakorn, S. D. Thomas, and B. M. Thompson. Techniques for making finite elements competitive in modeling flow in variably saturated porous media. *Water Resour. Res.*, 20 (8):1099–1115, 1984.

P. S. Huyakorn, E. P. Springer, V. Guvanasen, and T. D. Wadsworth. A three-dimensional finite-element model for simulating water flow in variably saturated porous media. *Water Resour. Res.*, 22(13):1790–1808, 1986.

T. Illangasekare and H. J. Morel-Seytoux. Stream-aquifer influence coefficients as tools for simulation and management. *Water Resour. Res.*, 18(1):168–176, 1982.

Intergovernamental Panel on Climate Change (IPCC). *Climate Change 2007: Impacts, Adaptation and Vulnerability.* Contributions of Working Group 2 to the Fourth Assessment Report of the Intergovernmental Panel on Climate Change, Cambridge Univeristy Press, 2007.

J. Järvelä. Determination of flow resistance caused by non-submerged woody vegetation. *Int. J. River Basin Manage.*, 2(1):61–70, 2004.

J. E. Jones and C. S. Woodward. Newton-Krylov-multigrid solvers for large-scale, highly heterogeneous, variably saturated flow problems. *Adv. Water Resources*, 24(7):763–774, 2001.

J. P. Jones, E. A. Sudicky, A. E. Brookfield, and Y.-J. Park. An assessment of the tracer-based approach to quantifying groundwater contributions to streamflow. *Water Resour. Res.*, 42, W02407, doi:10.1029/2005WR004130, 2006.

J. P. Jones, E. A. Sudicky, and R. G. McLaren. Application of a fully integrated surface-subsurface flow model at the watershed scale: A case study. *Water Resour. Res.*, 44, W03407, doi:10.1029/2006WR005603, 2008.

M. I. Jyrkama and J. F. Sykes. The impact of climate change on spatially varying groundwater recharge in the Grand River watershed (Ontario). *J. Hydrol.*, 338(3–4):237–250, 2007.

S. K. Kampf and S. J. Burges. A framework for classifying and comparing distributed hillslope and catchment hydrologic models. *Water Resour. Res.*, 43, W05423, doi:10.1029/2006WR005370, 2007.

M. G. Kendall. *Rank Correlation Measures.* Charles Griffin, 1975.

C. J. Koblinsky, R. T. Clarke, A. C. Brenner, and H. Frey. Measurement of River Level Variations With Satellite Altimetry. *Water Resour. Res.*, 29(6):1839–1848, 1993.

S. J. Kollet and R. M. Maxwell. Integrated surface–groundwater flow modeling: A free-surface overland flow boundary condition in a parallel groundwater flow model. *Adv. Water Resources*, 29(7):945–958, 2006.

S. J. Kollet and R. M. Maxwell. Capturing the influence of groundwater dynamics on land surface processes using an integrated, distributed watershed model. *Water Resour. Res.*, 44, W02402, doi:10.1029/2007WR006004, 2008.

W-L. Kuo, T. S. Steenhuis, C. E. McCulloch, C. L. Mohler, D. A. Weinstein, S. D. DeGloria, and D. P. Swaney. Effect of grid size on runoff and soil moisture for a variable-source-area hydrology model. *Water Resour. Res.*, 35(11):3419–3428, 1999.

L. Lamontagne. Base de donnèes sur les propriétés physiques des sols du bassin versant de la rivière Châteauguay. Pedology and Precision Agriculture Laboratories, Agriculture and Agri-Food Canada, QC, CD-ROM., 2005.

R. Leconte, F. Brisette, M. Galarneau, and J. Rousselle. Mapping near-surface soil moisture with RADARSAT-1 synthetic aperture radar data. *Water Resour. Res.*, 40, W01515, doi:10.1029/2003WR002312, 2004.

D. H. Lee and L. M. Abriola. Use of the Richards equation in land surface parameterizations. *J. Geophys. Res.*, 104(D22):27519–27526, 1999.

J. M. Lemieux, E. A. Sudicky, W. R. Peltier, and L. Tarasov. Dynamics of groundwater recharge and seepage over the Canadian landscape during the Wisconsinian glaciation. *J. Geophys. Res.*, 113, F01011, doi:10.1029/2007JF000838, 2008.

L. B. Leopold and T. Maddock Jr. The hydraulic geometry of stream channels and some physiographic implications. Prof. Pap. 252, U.S. Geol. Surv., Washington, DC, 1953.

J. B. Levine and G. D. Salvucci. Equilibrium analysis of groundwater–vadose zone interactions and the resulting spatial distribution of hydrologic fluxes across a Canadian prairie. *Water Resour. Res.*, 35(5):1369–1383, 1999.

R. M. Li, V. M. Ponce, and D. B. Simons. Modeling rill density. *J. Irrig. Drain. Div. ASCE*, 106(1):63–67, 1980.

X. Liang, Z. Xie, and M. Huang. A new parameterization for surface and groundwater interactions and its impact on water budgets with the variable infiltration capacity (VIC) land surface model. *J. Geophys. Res.*, 108(D16), 8613, doi:10.1029/2002JD003090, 2003.

K. Loague and J. E. VanderKwaak. Physics-based hydrologic response simulation: platinum bridge, 1958 edsel, or useful tool. *Hydrol. Process.*, 18(15):2949–2956, 2004.

S. W. Lyon, A. J. Lembo, M. T. Walter, and T. S. Steenhuis. Defining probability of saturation with indicator kriging on hard and soft data. *Advances in Water Resources*, 29 (2):181–193, 2006.

D. S. Mackay and L. E. Band. Extraction and representation of nested catchment areas from digital elevation models in lake-dominated topography. *Water Resour. Res.*, 34(4): 897–901, 1998.

S. Manabe, J. Smagorinksy, and R. Strickler. Simulated climatology of a general circulation model with a hydrologic cycle. *Mon. Wea. Rev.*, 93(12):769–798, 1965.

H. B. Mann. Non-parametric tests against trend. *Econometrica*, 13(3):245–259, 1945.

D. Marks, J. Dozier, and J. Frew. Automated basin delineation from digital elevation data. *Geo. Processing*, 2(3):299–311, 1984.

R. M. Maxwell. Coupled surface–subsurface modeling across a range of temporal and spatial scales. *Vadose Zone J.*, 8(4):823–824, 2009.

R. M. Maxwell and S. J. Kollet. Quantifying the effects of three-dimensional subsurface heterogeneity on Hortonian runoff processes using a coupled numerical, stochastic approach. *Adv. Water Resources*, 31(5):807–817, 2008.

R. M. Maxwell, F. K. Chow, and S. J. Kollet. The groundwater–land-surface–atmosphere connection: Soil moisture effects the atmospheric boundary layer in fully-coupled simulations. *Adv. Water Resources*, 30(12):2447–2466, 2007.

D. McLaughlin. An integrated approach to hydrologic data assimilation: Interpolation, smoothing, and filtering. *Adv. Water Resources*, 25(8–12):1275–1286, 2002.

R. G. Mein and C. L. Larson. Modeling infiltration during a steady rain. *Water Resour. Res.*, 9(2):384–394, 1973.

G. Miguez-Macho, Y. Fan, C. P. Weaver, R. Walko, and A. Robock. Incorporating water table dynamics in climate modeling: 2. Formulation, validation, and soil moisture simulation. *J. Geophys. Res.*, 112, D13108, doi:10.1029/2006JD008112, 2007.

B. B. Mirus, B. A. Ebel, K. Loague, and B. C. Wemple. Simulated effect of a forest road on near-surface hydrologic response: redux. *Earth Surf. Process. Landforms*, 32(1):126–142, 2007.

H. Mitasova and J. Hofierka. Interpolation by regularized spline with tension, II, Application to terrain modeling and surface geometry analysis. *Math. Geol.*, 25(6):657–669, 1993.

D. R. Montgomery and W. E. Dietrich. Where do channels begin? *Nature*, 336(6196): 232–234, 1988.

D. R. Montgomery and W. E. Dietrich. Source areas, drainage density and channel initiation. *Water Resour. Res.*, 25(8):1907–1918, 1989.

D. R. Montgomery and E. Foufoula-Georgiou. Channel network source representation using digital elevation models. *Water Resour. Res.*, 29(12):3925–3934, 1993.

I. D. Moore and G. J. Burch. Sediment transport capacity of sheet and rill flow: Application of unit stream power theory. *Water Resour. Res.*, 22(8):1350–1360, 1986.

M. Morita and B. C. Yen. Modeling of conjunctive two-dimensional surface-three-dimensional subsurface flows. *J. Hydraul. Engrg. ASCE*, 128(2):184–200, 2002.

R. Moussa and C. Bocquillon. Criteria for the choice of flood-routing methods in natural channel. *J. Hydrol.*, 186(1–4):1–30, 1996a.

R. Moussa and C. Bocquillon. Algorithms for solving the diffusive wave flood routing equation. *Hydrol. Process.*, 10(1):105–123, 1996b.

E. N. Mueller, J. Wainwright, and A. J. Parsons. Impact of connectivity on the modeling of overland flow within semiarid shrubland environments. *Water Resour. Res.*, 43, W09412, doi:10.1029/2006WR005006, 2007.

B. Music and D. Caya. Evaluation of the Hydrological Cycle over the Mississippi River Basin as Simulated by the Canadian Regional Climate Model (CRCM). *J. Hydromet.*, 8 (5):969–988, 2007.

N. Nakicenovic and S. Swart, editors. *Emissions Scenarios.* A Special Report of Working Group III of the Intergovernmental Panel on Climate Change, Cambridge University Press, Cambridge, UK, 2000.

J. E. Nash and J. V. Sutcliffe. Riverflow forecasting through conceptual models: Part 1. A discussion of principles. *J. Hydrol.*, 10(3):282–290, 1970.

S. P. Neuman. Calibration of distributed parameter groundwater flow models viewed as a multi-objective decision process under uncertainty. *Water Resour. Res.*, 9(4):1006–1021, 1973.

W.-J. Ni and H. Capart. Groundwater drainage and recharge by networks of irregular channels. *J. Geophys. Res.*, 111, F02014, doi:10.1029/2005JF00410, 2006.

J. L. Nieber and R. A. Feddes. Solutions for combined saturated and unsaturated flow. In R. W. Skaggs and J. van Schilfgaarde, editors, *Agricultural Drainage*, volume 38 of *Agronomy Monograph*, chapter 5, pages 145–212. American Society of Agronomy, Crop Science Society of America, and Soil Science Society of America, Madison, WI, 1999.

G.-Y. Niu, Z.-L. Yang, R. E. Dickinson, L. E. Gulden, and H. Su. Development of a simple groundwater model for use in climate models and evaluation with Gravity Recovery and Climate Experiment data. *J. Geophys. Res.*, 112, D07103, doi:10.1029/2006JD007522, 2007.

J. F. O'Callaghan and D. M. Mark. The extraction of drainage networks from digital elevation data. *Comput. Vision Graph.*, 28(3):328–344, 1984.

S. Orlandini. On the spatial variation of resistance to flow in upland channel networks. *Water Resour. Res.*, 38(10):1197, 2002.

S. Orlandini and G. Moretti. Determination of surface flow paths from gridded elevation data. *Water Resour. Res.*, 44, W03417, doi:10.1029/2008WR007099, 2009.

S. Orlandini and R. Rosso. Diffusion wave modeling of distributed catchment dynamics. *J. Hydrol. Eng. Am. Soc. Civ. Eng.*, 1(3):103–113, 1996.

S. Orlandini and R. Rosso. Parameterization of stream channel geometry in the distributed modeling of catchment dynamics. *Water Resour. Res.*, 34(8):1971–1985, 1998.

S. Orlandini, G. Moretti, M. Franchini, B. Aldighieri, and B. Testa. Path-based methods for the determination of nondispersive drainage directions in grid-based digital elevation models. *Water Resour. Res.*, 39(6), 1144, doi:10.1029/2002WR001639, 2003.

L. Oudin, F. Hervieu, C. Michel, C. Perrin, V. Andréassian, F. Anctilb, and C. Loumagne. Which potential evapotranspiration input for a lumped rainfall–runoff model? Part 2—Towards a simple and efficient potential evapotranspiration model for rainfall–runoff modelling. *J. Hydrol.*, 303(1–4):290–306, 2005.

S. Panday and P. S. Huyakorn. A fully coupled physically-based spatially-distributed model for evaluating surface/subsurface flow. *Adv. Water Resources*, 27(4):361–382, 2004.

C. Paniconi and M. Putti. A comparison of Picard and Newton iteration in the numerical solution of multidimensional variably saturated flow problems. *Water Resour. Res.*, 30 (12):3357–3374, 1994.

C. Paniconi and E. F. Wood. A detailed model for simulation of catchment scale subsurface hydrologic processes. *Water Resour. Res.*, 29(6):1601–1620, 1993.

C. Paniconi, M. Marrocu, M. Putti, and M. Verbunt. Newtonian nudging for a Richards equation-based distributed hydrological model. *Adv. Water Resources*, 26(2):161–178, 2003.

A. J. Parsons, J. Wainwright, A. D. Abrahams, and J. R. Simanton. Distributed dynamic modelling of interrill overland flow. *Hydrol. Process.*, 11(14):1833–1859, 1997.

A. J. Pitman. The evolution of, and revolution in, land surface schemes designed for climate models. *Int. J. Climatol.*, 23(5):479–510, 2003.

V. M. Ponce, R. M. Li, and D. B. Simons. Applicability of kinematic and diffusion models. *J. Hydraul. Div. ASCE*, 104(3):353–360, 1978.

C. Prudhomme, D. Jakob, and C. Svensson. Uncertainty and climate change impact on 903 the flood regime of small UK catchments. *jhydro*, 277:1–23, 2003.

M. Putti and C. Paniconi. Time step and stability control for a coupled model of surface and subsurface flow. In C. T. Miller, M. W. Farthing, , W. G. Gray, and G. F. Pinder, editors, *Computational Methods in Water Resources, Vol. 2*, pages 1391–1402, Chapel Hill, NC, USA, 2004. Elsevier.

Y. Qu and C. J. Duffy. A semidiscrete finite volume formulation for multiprocess watershed simulation. *Water Resources Research*, 43, W08419, doi:10.1029/2006WR005752, 2007.

R. Quilbe, A. N. Rousseau, J. S. Moquet, S. Savary, S. Ricard, and M.S. Garbouj. Hydrological responses of a watershed to historical land use evolution and future land use scenarios under climate change conditions. *Hydrol. Earth Syst. Sci*, 12(1):101–110, 2008.

J. C. Refsgaard. Parameterisation, calibration and validation of distributed hydrological models. *J. Hydrol.*, 198(1–4), 1997.

J. C. Refsgaard and B. Storm. *Computer Models of Watershed Hydrology*, chapter MIKE SHE, pages 809–846. Water Res. Publ., Highlands Ranch, Colo., 1995.

J. C. Refsgaard and B. Storm. *Distributed Hydrological Modeling*, chapter Construction, calibration and validation of hydrological models, pages 41–54. Kluwer Academic, 1996.

R. Rew and G. Davis. NetCDF: An interface for scientific data access. *IEEE Trans. Comput. Graphics Appl.*, 10(4):76–82, 1990.

S. Riette and D. Caya. Sensitivity of short simulations to the various parameters in the new CRCM spectral nudging. Research Activities in Atmospheric and Oceanic Modelling. Technical Report 32, WMO/TD–No 1105, 2002.

M. Rivington, D. Miller, K. B. Matthews, G. Russell, G. Bellocchi, and K. Buchan. Evaluating regional climate model estimates against site-specific observed data in the uk. *Climate Change*, 88(2):157–185, 2008.

P. Romanov, D. Tarpley, G. Gutman, and T. Carroll. Mapping and monitoring of the snow cover fraction over North America. *J. Geophys. Res.*, 108(D16), 8619, doi:10.1029/2002JD003142, 2003.

P. J. Ross. Efficient numerical methods for infiltration using Richards' equation. *Water Resour. Res.*, 26(2):279–290, 1990.

G. D. Salvucci. Soil and moisture independent estimation of stage-two evaporation from potential evaporation and albedo or surface temperature. *Water Resour. Res.*, 33(1):111–122, 1997.

J. Scibek and D. M. Allen. Modeled impacts of predicted climate change on recharge and groundwater levels. *Water Resour. Res.*, 42, W11405, doi:10.1029/2005WR04742, 2006.

J. F. Scinocca, N. A. McFarlane, M. Lazare, J. Li, and D. Plummer. The CCCma third generation AGCM and its extension into the middle atmosphere. *Atmos. Chem. Phys*, 8 (23):7055–7074, 2008.

P. K. Sen. Estimates of the regression coefficient based on Kendall's tau. *J. Am. Stat. Assoc.*, 63(324):1379–1389, 1968.

V. P. Singh and D. A. Woolhiser. Mathematical modeling of watershed hydrology. *J. Hydrol. Eng.*, 7(4):270–292, 2002.

T. G. Smirnova, J. M. Brown, and S. G. Benjamin. Performance of different soil model configuration in simulating ground surface temperature and surface fluxes. *Mon. Wea. Rev.*, 125(8):1871–1884, 1997.

R. E. Smith and D. A. Woolihser. Overland flow on an infiltration surface. *Water Resour. Res.*, 7(4):899–913, 1971.

R. E. Smith, D. R. Goodrich, D. A. Woolhiser, and J. R. Simanton. Comment on 'Physically based hydrologic modelling, 2. Is the concept realistic? by R. B. Grayson, I. D. Moore and T. A. McMahon. *Water Resour. Res.*, 30(3):851–854, 1994.

S. Sooroshian and V. K. Gupta. *Computer Models of Watershed Hydrology*, chapter Model Calibration. Water Resources Publications, 1995.

M. Sophocleous. Interactions between groundwater and surface water: the state of the science. *Hydrogeol. J.*, 10(1):53–67, 2002.

E. A. Sudicky, J. P. Jones, R. G. McLaren, D. S. Brunner, and J. E. VanderKwaak. A fully coupled model of surface and subsurface water flow: Model overview and application to the Laurel Creek watershed. In L. R. Bentley, J. F. Sykes, C. A. Brebbia, W. G. Gray, and G. F. Pinder, editors, *Computational Methods in Water Resources, Vol. 2, Computational Methods, Surface Water Systems and Hydrology*, volume 2, pages 1093–1099, Rotterdam, The Netherlands, 2000. Balkema.

E. A. Sudicky, J. P. Jones, Y. J. Park, A. E. Brookfield, and D. Colautti. Simulating complex flow and transport dynamics in an integrated surface–subsurface modeling framework. *Geosciences Journal*, 12(2):107–122, 2008.

M. Sulis, C. Paniconi, C. Rivard, R. Harvey, and D. Chaumont. Assessment of climate change impacts at the catchment scale with a detailed hydrological model of surface/subsurface interactions, and comparison with a land surface model. *Water Resour. Res.*, 2010. submitted.

T. H. Syed, J. S. Famiglietti, J. Chen, M. Rodell, S. I. Seneviratne, P. Viterbo, and C. R. Wilson. Total basin discharge for the Amazon and Mississipi River basins from GRACE and a land-atmosphere water balance. *J. Geophys. Res.*, 32, L24404, doi.10.1029/2005GL024851, 2005.

D. Syriopoulou and A. D. Koussis. Two-dimensional modeling of advection-dominated solute transport in groundwater by the matched artificial dispersivity method. *Water Resour. Res.*, 27(5):865–872, 1991.

C. Tague, G. Grant, M. Farrell, J. Choate, and A. Jefferson. Deep groundwater mediates streamflow response to climate warming in the Oregon Cascades. *Clim. Change*, 86(1–2): 189–210, 2008.

D. G. Tarboton. A new method for the determination of flow directions and contributing areas in grid digital elevation models. *Water Resour. Res.*, 33(2):309–319, 1997.

G. Tayfur and M. L. Kavvas. Spatially averaged conservation equations for interacting rill-interrill area overland flows. *J. Hydraul. Engrg. ASCE*, 120(12):1426–1448, 1994.

R. Therrien, R. G. McLaren, E. A. Sudicky, and S. M. Panday. *HydroGeoSphere. A Three-dimensional Numerical Model Describing Fully-integrated Subsurface and Surface Flow and Solute Transport.* Univeristy of Waterloo, 2004.

D. P. Thoma, M. S. Moran, R. Bryant, M. Rahman, C., D. Holifield-Collins, S. Skirvin, E. E. Sano, and K. Slocum. Comparison of four models to determine surface soil moisture from C-band radar imagery in a sparsely vegetated semiarid landscape. *Water Resour. Res.*, 42, W01418, doi:10.1029/2004WR003905, 2006.

E. Todini. The ARNO rainfall-runoff model. *J. Hydrol.*, 175(1–4):339–382, 1996.

M. W. Toews and D. M. Allen. Evaluating different GCMs for predicting spatial recharge in an irrigated arid region. *J. Hydrol.*, 374(3–4):265–281, 2009.

D. Tonina and J. M. Buffington. Hyporheic exchange in gravel bed rivers with pool-riffle morphology: Laboratory experiments and three-dimensional modeling. *Water Resour. Res.*, 43, W01421, doi.10.1029/2005WR004328, 2007.

T. Tremblay. Hydrostratigraphie et géologie du Quaternaire dans le bassin-versant de la rivièré Châteauguay, Québec. Master's thesis, Université du Québec à Montréal, 2006.

A. Tribe. Problems in automated recognition of valley features from digital elevation models and a new method toward their resolution. *Earth Surf. Processes Landforms*, 17(5):437–454, 1992.

R. Turcotte, L.-G. Fortin, J.-P. Fortin, and J.-P Villeneuve. Operational analysis of the spatial distribution and the temporal evolution of the snowpack water equivalent in southern Québec, Canada. *Nordic Hydrology*, 38(3):211–234, 2004.

M. Th. van Genuchten and D. R. Nielsen. On describing and predicting the hydraulic properties of unsaturated soils. *Ann. Geophys.*, 3(5):615–628, 1985.

L. van Roosmalen, T. O. Sonnenborg, and K. H. Jensen. The impact of climate and land use change on the hydrology of a large-scale agricultural catchment. *Water Resour. Res.*, 45, W00A15, doi:10.1029/2007WR006760, 2009.

J. E. VanderKwaak and K. Loague. Hydrologic-response simulation for the R-5 catchment with a comprehensive physics-based model. *Water Resour. Res.*, 37(4):999–1013, 2001.

D. L. Verseghy. CLASS–A Canadian Land Surface scheme for GCMS: I. Soil Model. *Int. J. Climatol.*, 11(4):111–133, 1991.

D. L. Verseghy, N. A. McFarlane, and M. Lazare. CLASS–A Canadian Land Surface scheme for GCMS: II. Vegetation Model and Coupled Runs. *Int. J. Climatol.*, 13(4):347–370, 1993.

J. H. D. Viera. Conditions governing the use of approximations for the Saint-Vénant equations for shallow surface water flow. *J. Hydrol.*, 60(1–4):43–58, 1983.

E. R. Vivoni, V. Y. Ivanov, R. L. Bras, and D. Entekhabi. On the effects of triangulated terrain resolution on distributed hydrologic model response. *Hydrological Processes*, 19 (11):2101–2122, 2005.

H. von Storch and A. Navarra. *Analysis of Climate Variability–Applications of Statistical Techniques*. Springer-Verlag, 1995.

S. Wang, R. F. Grant, D. L. Verseghy, and T. A. Black. Modelling carbon-coupled energy and water dynamics of a boreal aspen forest in a general circulation model land surface scheme. *Int. J. Climatol.*, 22(10):1249–1265, 2002.

A. W. Western, R. B. Grayson, G. Blösh, G. R. Willgoose, and T. A. McMahon. Observed spatial organization of soil moisture and its relation to terrain indices. *Water Resour. Res.*, 35(3):797–810, 1999.

R. L. Wilby and T. M. L. Wigley. Downscaling general circulation model output: A review of methods and limitations. *Prog. Phys. Geogr.*, 21(4):530–548, 1997.

M. F. Wilson and A. Henderson-Sellers. A global archive of land cover and soils data for use in general circulation climate models. *J. Climatol.*, 5:119–143, 1985.

W. W. Woessner. Stream and fluvial plain groundwater interactions: rescaling hydrogeologic thought. *Ground Water*, 38(3):423–429, 2000.

D. M. Wolock and C. V. Price. Effects of digital elevation model map scale and data resolution on a topography-based watershed model. *Water Resour. Res.*, 35(11):3041–3052, 1994.

P. J.-F. Yeh and E. A. B. Eltahir. Representation of Water Table Dynamics in a Land Surface Scheme. Part I: Model Development. *J. Clim.*, 18(12):1861–1880, 2005.

J. P. York, M. Person, W. J. Gutowski, and T. C. Winter. Putting aquifers into atmospheric simulation models: an example from the Mill Creek Watershed, northeastern Kansas. *Adv. Water Resources*, 25(2):221–238, 2002.

S. Yue, P. Pilon, B. Phinney, and G. Cavadias. The influence of autocorrelation on the ability to detect trend in hydrological series. *Hydrol. Process.*, 16(9):1807–1829, 2002.

L.W. Zevenbergen and C. R. Thorne. Quantitative analysis of land surface topography. *Earth Surf. Processes Landforms*, 12(1):47–56, 1987.

W. Zhang and D. R. Montgomery. Digital elevation model grid size, landscape representation, and hydrologic simulation. *Water Resour. Res.*, 30(4):1019–1028, 1994.

X. Zhang, W. D. Hogg, and E. Mekis. Temperature and precipitation trends in Canada during the 20th century. *Atmos. Ocean*, 38(3):395–429, 2000.

X. Zhang, K. D. Harvey, W. D. Hogg, and T. R. Yuzyk. Trends in Canadian streamflow. *Water Resour. Res.*, 37(4):987–998, 2001.

Appendices

A Soil moisture characteristic equations

van Genuchten curves *[van Genuchten and Nielsen, 1985]*:

$$\theta(\psi) = \begin{cases} \theta_r + (\theta_s - \theta_r)[1+\beta]^{-m} & \psi < 0 \\ \theta_s & \psi \geq 0 \end{cases} \tag{A.1}$$

$$K_r(\psi) = \begin{cases} (1+\beta)^{-5m/2}[(1+\beta)^m - \beta^m]^2 & \psi < 0 \\ 1 & \psi \geq 0 \end{cases} \tag{A.2}$$

Brooks-Corey curves *[Brooks and Corey, 1964]*:

$$\theta(\psi) = \begin{cases} \theta_r + (\theta_s - \theta_r)(\psi_s/\psi)^{\beta} & \psi < \psi_s \\ \theta_s & \psi \geq \psi_s \end{cases} \tag{A.3}$$

$$K_r(\psi) = \begin{cases} (\psi_s/\psi)^{2+3\beta} & \psi < \psi_s \\ 1 & \psi \geq \psi_s \end{cases} \tag{A.4}$$

Huyakorn curves *[Huyakorn et al., 1984, 1986]*:

$$S_e(\psi) = \begin{cases} [1+\alpha^{\beta}(\psi_a - \psi)^{\beta}]^{-\gamma} & \psi < \psi_a \\ 1 & \psi \geq \psi_a \end{cases} \tag{A.5}$$

$$K_r(\psi) = K_r(S_e(\psi)) = S_e^{\mu} \tag{A.6}$$

where $\theta(\psi)$ is the volumetric moisture content, θ_s the saturated moisture content, θ_r the residual moisture content, $\beta = (\psi/\psi_s)^n$, where ψ_s is the capillary pressure head, $m = 1 - 1/n$ where n is an empirical constant ranging between 1.25 and 6, $K_r(\psi)$ the relative hydraulic conductivity, $S_e = (\theta - \theta_r)/(\theta_s - \theta_r)$ the effective saturation, and ψ_a the capillary pressure head. In the Brooks-Corey and Huyakorn curves α, β, γ, and μ are constants.

B Numerical discretization of the three-dimensional Richards equation

Let the exact solution ψ of equation (2.5) be approximated by $\hat{\psi}$ using linear basis functions $w(\mathbf{x})$ defined over a domain Ω discretized by E tetrahedral elements and N nodes:

$$\psi \approx \hat{\psi} = \sum_{j=1}^{N} \hat{\psi}_j(t) w_j(\mathbf{x}) \tag{B.1}$$

where $\hat{\psi}_j$ are the components of the nodal solution vector $\hat{\mathbf{\Psi}}$.

Recasting equation (2.5) in operator notation

$$L(\psi) = \nabla \cdot [K_s K_r(\psi) (\nabla\psi + \eta_z)] - \sigma(\psi)\frac{\partial\psi}{\partial t} + q = 0 \tag{B.2}$$

the error, or residual, represented by the finite element approximation (B.1) is given as $L(\hat{\psi}) - L(\psi)$, or simply $L(\hat{\psi})$. This error is minimized by imposing an orthogonality constraint between the residual and the basis functions, which yields the Galerkin integral

$$\int_\Omega L(\hat{\psi}) w_i(\mathbf{x}) d\Omega = 0 \qquad i = 1, \ldots, N \tag{B.3}$$

We assume that the coordinate directions are parallel to the principal directions of hydraulic anisotropy, so that the off-diagonal components of the conductivity tensor K are zero. Expanding equation (B.3) and applying Green's lemma to the spatial derivative term we get, for $i = 1, \ldots, N$

$$\begin{aligned} &-\int_\Omega K_r \left[K_s \left(\nabla\hat{\psi} + \eta_z\right) \cdot \nabla w_i\right] d\Omega + \int_\Gamma K_r \left[K_s \left(\nabla\hat{\psi} + \eta_z\right) \cdot \mathbf{n}\right] w_i d\Gamma \\ &\quad - \int_\Omega \sigma \frac{\partial\hat{\psi}}{\partial t} w_i d\Omega + \int_\Omega q w_i d\Omega = 0 \end{aligned} \tag{B.4}$$

Substituting equation (B.1) into this expression, changing sign, and making use of boundary condition to replace the boundary integral term above, we obtain the following system of ordinary differential equations

$$H(\hat{\mathbf{\Psi}})\hat{\mathbf{\Psi}} + P(\hat{\mathbf{\Psi}})\frac{d\hat{\mathbf{\Psi}}}{dt} + \mathbf{q}^*(\hat{\mathbf{\Psi}}) = \mathbf{0} \tag{B.5}$$

In the above equations, $H = \{h_{ij}\}$ is the flow stiffness matrix, $P = \{p_{ij}\}$ is the flow mass (or capacity) matrix, $\mathbf{q}^* = \{q_i^*\}$ accounts for the prescribed boundary flux, the withdrawal or injection rate, and the gravitational gradient term, and K_{sz} is the vertical component

of the saturated conductivity tensor. Dirichlet boundary conditions are imposed after the discretized system has been completely assembled.

Equation (B.5) is integrated in time by a ν-weighted finite difference scheme

$$\left(\nu H^{k+\nu} + \frac{P^{k+\nu}}{\Delta t_k}\right) \hat{\boldsymbol{\Psi}}^{k+1} = \left(\frac{P^{k+\nu}}{\Delta t_k} - (1-\nu) H^{k+\nu}\right) \hat{\boldsymbol{\Psi}}^{k} - \mathbf{q}^{*^{k+\nu}} \tag{B.6}$$

where k and $k+1$ denote the previous and current time levels, Δt_k is the time step size, and H, P, $\mathbf{q}^*$, and $\mathbf{r}^*$ are evaluated at pressure head $\hat{\boldsymbol{\Psi}}^{k+\nu} = \nu \hat{\boldsymbol{\Psi}}^{k+1} + (1-\nu)\hat{\boldsymbol{\Psi}}^{k}$ with $0 \leq \nu \leq 1$. Typically Crank-Nicolson ($\nu = 0.5$) or backward Euler ($\nu = 1$) time stepping is used.

In the case of Picard linearization, we obtain

$$\left(\nu H^{k+\nu,m} + \frac{1}{\Delta t_k} P^{k+\nu,m}\right) \mathbf{s}^m = -\mathbf{g}(\hat{\boldsymbol{\Psi}}^{k+1,m}) \tag{B.7}$$

while in the case of Newton linearization, we obtain

$$\mathbf{g}'(\hat{\boldsymbol{\Psi}}^{k+1,m})\mathbf{s}^m = -\mathbf{g}(\hat{\boldsymbol{\Psi}}^{k+1,m}) \tag{B.8}$$

where m is the iteration level, $\mathbf{s}^m = \hat{\boldsymbol{\Psi}}^{k+1,m+1} - \hat{\boldsymbol{\Psi}}^{k+1,m}$, and

$$\mathbf{g}\left(\hat{\boldsymbol{\Psi}}^{k+1}\right) = H^{k+\nu}\hat{\boldsymbol{\Psi}}^{k+\nu} + \frac{1}{\Delta t_k} P^{k+\nu}\left(\hat{\boldsymbol{\Psi}}^{k+1} - \hat{\boldsymbol{\Psi}}^{k}\right) + \mathbf{q}^{*^{k+\nu}} = \mathbf{0} \tag{B.9}$$

Convergence of these iterative schemes can be enhanced by introducing a relaxation (or damping) parameter ω of the form $\hat{\boldsymbol{\Psi}}^{m+1} = \hat{\boldsymbol{\Psi}}^{m} + \omega \mathbf{s}^m$. Equation (B.7) and (B.8) are solved, at each iteration, using standard preconditioned conjugate gradient methods for sparse linear systems.

C Numerical discretization of the one-dimensional kinematic flow equation

For the sake of convenience the extended formulation of the kinematic flow equation is rewritten in the following form:

$$\frac{\partial Q}{\partial t} + c_k \frac{\partial Q}{\partial s} = c_k q_L \tag{C.1}$$

Let discretize now the above equation (C.1) in space and in time:

$$\frac{\partial Q}{\partial t} \cong (1-X)\frac{Q_{i+1}^{j+1} - Q_{i+1}^{j}}{\Delta t} + X\frac{Q_i^{j+1} - Q_i^j}{\Delta t} \tag{C.2}$$

$$\frac{\partial Q}{\partial s} \cong \theta\frac{Q_{i+1}^{j+1} - Q_i^{j+1}}{\Delta s} + (1-\theta)\frac{Q_{i+1}^{j} - Q_i^j}{\Delta s} \tag{C.3}$$

where X and θ are the time- and space-weighting factors, Δt and Δs the temporal and space integration step.

Now replacing equation (C.2) and equation (C.3) in equation (C.1) we obtain:

$$(1-X)\frac{Q_{i+1}^{j+1} - Q_{i+1}^{j}}{\Delta t} + X\frac{Q_i^{j+1} - Q_i^j}{\Delta t} + c_k\left(\theta\frac{Q_{i+1}^{j+1} - Q_i^{j+1}}{\Delta s}X + (1-\theta)\frac{Q_{i+1}^{j} - Q_i^j}{\Delta s}\right) = c_k q_L \tag{C.4}$$

Recasting equation (C.4) in terms of Q_{i+1}^{k+1} for $\theta = 0.5$ then the well-know Muskingum formula is obtained:

$$Q_{i+1}^{k+1} = C_1\, Q_i^{k+1} + C_2\, Q_i^k + C_3\, Q_{i+1}^k + C_4\, q_{L_{i+1}}^k, \tag{C.5}$$

where:

$$\begin{aligned}
C_1 &= \frac{c_k\left(\frac{\Delta t}{\Delta s}\right) - 2X}{2(1-X) + c_k\left(\frac{\Delta t}{\Delta s}\right)} \\
C_2 &= \frac{c_k\left(\frac{\Delta t}{\Delta s}\right) + 2X}{2(1-X) + c_k\left(\frac{\Delta t}{\Delta s}\right)} \\
C_3 &= \frac{2(1-X) - c_k\left(\frac{\Delta t}{\Delta s}\right)}{2(1-X) + c_k\left(\frac{\Delta t}{\Delta s}\right)} \\
C_4 &= \frac{2c_k\Delta t}{2(1-X) + c_k\left(\frac{\Delta t}{\Delta s}\right)}
\end{aligned} \tag{C.6}$$

D Combination of at-a-station and downstream fluvial relationships

The variation of the water surface width W at a site of upstream drainage area A with flow discharge of different frequencies Q can be expressed in the simple power function form

$$W(A,Q) = a'\,Q^{b'}, \tag{D.1}$$

where a' is a scaling coefficient and b' is an exponent. The variation of W between sites of upstream drainage areas A with flow discharge Q_f of given frequency f can be expressed in the simple power function form

$$W(A,Q_f) = a''\,Q_f^{b''}, \tag{D.2}$$

where a'' is a scaling coefficient and b'' is an exponent. From (D.1) one can obtain that

$$\frac{W(A,Q)}{W(A,Q_f)} = \left(\frac{Q}{Q_f(A)}\right)^{b'} \tag{D.3}$$

and from (D.2) one can obtain that

$$\frac{W(A,Q_f)}{W(A_s,Q_f)} = \left(\frac{Q_f(A)}{Q_f(A_s)}\right)^{b''}, \tag{D.4}$$

where $W(A_s,Q_f)$ denotes the value of W at a site of fixed upstream drainage area A_s and for a flow discharge Q_f of fixed frequency f. Combining (D.3) and (D.4) yields

$$W(A,Q) = W(A_s,Q_f)\left(\frac{Q_f(A)}{Q_f(A_s)}\right)^{b''}\left(\frac{Q}{Q_f(A)}\right)^{b'}. \tag{D.5}$$

Using the relationship $Q_f = u\,A^w$ to express the variation of Q_f across a channel network, with the upstream drainage area A, one can obtain

$$\frac{Q_f(A)}{Q_f(A_s)} = \left(\frac{A}{A_s}\right)^{w}. \tag{D.6}$$

Now, we can rewrite (D.5) in the following form:

$$W(A,Q) = \underbrace{W(A_s,Q_f)\,Q_f(A_s)^{-b'}\left(\frac{A}{A_s}\right)^{w(b''-b')}}_{\text{spatial variation} = W(A,1)} \overbrace{Q^{b'}}^{\text{temporal variation}} \tag{D.7}$$

The same procedure can be utilized for combining the at-a-station and downstream fluvial relationship for the Gaukler-Strickler roughness coefficient:

$$k_s(A,Q) = \underbrace{k_s(A_s,Q_f)\,Q_f(A_s)^{-y'}\left(\frac{A}{A_s}\right)^{w(y''-y')}}_{\text{spatial variation} = k_s(A,1)} \overbrace{Q^{y'}}^{\text{temporal variation}} \tag{D.8}$$

E Incorporation of fluvial relationships in diffusion wave formulations

Let consider the continuity and momentum equation for the diffusion wave approximation:

$$\frac{\partial \Omega}{\partial t} + \frac{\partial Q}{\partial s} = q_L \qquad ; \qquad \frac{\partial (Y \cos\beta)}{\partial s} = S_0 - S_f \tag{E.1}$$

since $\partial\Omega/\partial t = \partial\Omega/\partial Y \partial Y \partial t$, and $\partial\Omega/\partial Y = W$, with Ω being the flow area, W and Y the water surface width and water depth, respectively, the continuity equation can be rewritten in the following form:

$$W\frac{\partial Y}{\partial t} + \frac{\partial Q}{\partial s} = q_L \tag{E.2}$$

Let derive now the momentum equation respect to t and the continuity equation respect to s:

$$\frac{\partial^2 Y}{\partial s \partial t} = -\frac{1}{\cos\beta}\frac{S_f}{\partial t} \tag{E.3}$$

$$\frac{\partial^2 Y}{\partial s \partial t} = \frac{1}{W}\left(\frac{\partial^2 Q}{\partial s^2} - \frac{\partial q_L}{\partial t} + \frac{\partial W}{\partial s}\frac{\partial Y}{\partial t}\right) \tag{E.4}$$

Equating (E.3) and (E.4) for $\partial q_L/\partial t = 0$ and $\partial W/\partial s\, \partial Y/\partial t = 0$:

$$\frac{\partial S_f}{\partial t} = \frac{\cos\beta}{W}\left(\frac{\partial^2 Q}{\partial s^2}\right) \tag{E.5}$$

The variation in time of the friction term in the momentum equation can be expressed as:

$$\frac{\partial S_f}{\partial t} = \frac{\partial S_f}{\partial Q}\frac{\partial Q}{\partial t} + \frac{\partial S_f}{\partial Y}\frac{\partial Y}{\partial t} \tag{E.6}$$

Incorporating now in (E.6), $\partial Y/\partial t = (q_L - \partial Q/\partial s)/W$ from (E.2), and $\partial S_f/\partial t = \cos\beta\,(\partial^2 Q/\partial s^2)\,/W$ from (E.5), we obtain:

$$\frac{\partial Q}{\partial t} - \frac{\partial S_f/\partial\Omega}{\partial S_f/\partial Q}\frac{\partial Q}{\partial s} = \left(\frac{W}{\cos\beta}\frac{\partial S_f}{\partial Q}\right)^{-1}\frac{\partial^2 Q}{\partial s^2} - \frac{\partial S_f/\partial\Omega}{\partial S_f/\partial Q}q_L \tag{E.7}$$

(E.7) is the diffusion wave equation (2.6) with the kinematic wave celerity and hydraulic diffusivity evaluated according the following expressions:

$$c_k = -\frac{\partial S_f/\partial\Omega}{\partial S_f/\partial Q} \tag{E.8}$$

$$D_h = \left(\frac{W}{\cos\beta}\frac{\partial S_f}{\partial Q}\right)^{-1} \tag{E.9}$$

Let consider now the Manning-Gaukler-Strickler (MGS) as flow resistance relationship:

$$Q = k_S \, W^{-2/3} \, \Omega^{5/3} \, S_f^{1/2} \tag{E.10}$$

where k_S is the Gaukler-Strickler resistance coefficient, W the surface water width, Ω the flow area, and S_f the frictional force term.

From (E.10) $S_f = Q^2 \, / \, (k_s^2 \, W^{-4/3} \, \Omega^{10/3})$ the derivatives of S_f respect to Ω and to Q are:

$$\frac{\partial S_f}{\partial \Omega} = \frac{5}{3} \frac{Q}{\Omega} \left(\frac{-2Q}{k_s^2 W^{-4/3} \Omega^{10/3}} \right) \tag{E.11}$$

$$\frac{\partial S_f}{\partial Q} = \frac{2Q \left(1 - \dfrac{Q}{k_s} \dfrac{dk_s}{dQ} + \dfrac{2}{3} \dfrac{Q}{W} \dfrac{dW}{dQ} \right)}{k_s^2 W^{-4/3} \Omega^{10/3}} \tag{E.12}$$

where variation of W and k_s with Q are expressed by equation (D.7) and (D.8).

F Representation of heterogeneity for the des Anglais catchment

The CATHY model allows the user to represent heterogeneity by layer (vertically) and by zone (laterally). This is depicted in Table F.1 and Figure F.1, which show the four horizontal zones and the eight vertical units identified for the des Anglais catchment. The zones represent lateral heterogeneity, as deduced from surficial geology data and Quaternary sediment information.

A parallel base was used for the bottom of the study area with a total thickness of 100 m. This base (with respect to the flat one) alleviated the coarsening of the layers in the most pronounced topographic feature of the catchment (see transect A-A in Figure F.2), where stronger surface–subsurface interactions are expected to occur. A total of 10 layers were used for the vertical discretization, with one or more layers for each major geological formation. Each layer is parallel to the surface and has a constant thickness. The thinnest layer (0.05 m) was that closest to the surface, needed to accurately resolve rainfall-runoff infiltration partitioning and in general to better capture the interactions between surface water and groundwater. The layers were progressively coarsened with depth (see Table F.1), to a maximum thickness of 40 m for the bottom-most layer.

Table F.1: Material properties for the 10 vertical layers and 4 geopedologic zones of the des Anglais catchment discretization.

Layer (top to bottom)		1	2	3	4	5	6	7	8	9	10
Layer thickness [m]		0.05	0.1	0.3	0.45	1.10	2.10	5.90	20	30	40
Zone 1	K_h [m/s]	5×10^{-4}	5×10^{-4}	5×10^{-4}	5×10^{-4}	1×10^{-4}	5×10^{-9}	5×10^{-9}	1×10^{-7}	5×10^{-8}	5×10^{-8}
	K_z [m/s]	3×10^{-4}	3×10^{-4}	3×10^{-4}	3×10^{-4}	5×10^{-4}	3×10^{-9}	3×10^{-9}	5×10^{-7}	5×10^{-8}	5×10^{-8}
	θ_s [/]	0.5	0.5	0.5	0.5	0.4	0.5	0.5	0.5	0.1	0.1
	S_s [m^{-1}]	1×10^{-5}	1×10^{-5}	1×10^{-5}	1×10^{-5}	1×10^{-4}	3×10^{-3}	3×10^{-3}	1×10^{-4}	1×10^{-6}	1×10^{-6}
Zone 2	K_h [m/s]	5×10^{-4}	5×10^{-4}	5×10^{-4}	5×10^{-4}	1×10^{-5}	1×10^{-5}	1×10^{-7}	5×10^{-8}	5×10^{-8}	5×10^{-8}
	K_z [m/s]	3×10^{-4}	3×10^{-4}	3×10^{-4}	3×10^{-4}	5×10^{-5}	5×10^{-5}	5×10^{-7}	5×10^{-8}	5×10^{-8}	5×10^{-8}
	θ_s [/]	0.5	0.5	0.5	0.5	0.5	0.5	0.5	0.1	0.1	0.1
	S_s [m^{-1}]	1×10^{-5}	1×10^{-5}	1×10^{-5}	1×10^{-5}	1×10^{-4}	1×10^{-4}	1×10^{-4}	1×10^{-6}	1×10^{-6}	1×10^{-6}
Zone 3	K_h [m/s]	5×10^{-4}	5×10^{-4}	5×10^{-4}	5×10^{-4}	1×10^{-4}	1×10^{-4}	2×10^{-6}	2×10^{-6}	2×10^{-6}	2×10^{-6}
	K_z [m/s]	3×10^{-4}	3×10^{-4}	3×10^{-4}	3×10^{-4}	5×10^{-4}	5×10^{-4}	5×10^{-8}	5×10^{-8}	5×10^{-8}	5×10^{-8}
	θ_s [/]	0.5	0.5	0.5	0.5	0.4	0.4	0.1	0.1	0.1	0.1
	S_s [m^{-1}]	1×10^{-5}	1×10^{-5}	1×10^{-5}	1×10^{-5}	1×10^{-4}	1×10^{-4}	1×10^{-6}	1×10^{-6}	1×10^{-6}	1×10^{-6}
Zone 4	K_h [m/s]	5×10^{-8}	5×10^{-8}	5×10^{-8}	5×10^{-8}	1×10^{-7}	1×10^{-7}	1×10^{-7}	5×10^{-8}	5×10^{-8}	5×10^{-8}
	K_z [m/s]	3×10^{-8}	3×10^{-8}	3×10^{-8}	3×10^{-8}	5×10^{-7}	5×10^{-7}	5×10^{-7}	5×10^{-8}	5×10^{-8}	5×10^{-8}
	θ_s [/]	0.9	0.9	0.9	0.9	0.5	0.5	0.5	0.1	0.1	0.1
	S_s [m^{-1}]	1×10^{-5}	1×10^{-5}	1×10^{-5}	1×10^{-5}	1×10^{-4}	1×10^{-4}	1×10^{-4}	1×10^{-6}	1×10^{-6}	1×10^{-6}

red = loamy sand; yellow = organic soil; blue = fluvio-glacial coarse sand; cyan = till; violet = reworked till; green = marine clay / fine silt; purple = bedrock; orange = bedrock with anisotropy

A 360 m DEM was used to determine the surface flow directions and area accumulations through the D8-LTD drainage method ($\lambda = 1$, full memory of the deviations calculated for upstream pre-processed cells) described in the introduction. The catchment was then delineated from the closest point to the outlet depicted on a topographic map. At 360 m resolution, the surface mesh for the catchment area contained 5338 cells on the basis of which the 3D subsurface grid was constructed by subdividing each DEM cell into two triangles and then projecting this 2D surface mesh vertically,i.e., the triangular mesh was then projected vertically into a tetrahedral grid, with 3 tetrahedra per triangle per layer. The resulting 3D grid contains 61908 nodes and 320280 tetrahedral elements. A grid of this size (on the order of 60000 nodes, or degrees of freedom) was the finest-feasible resolution for this study (calculation times of about two weeks for 30-year simulations run on a multi-processor desktop computer).

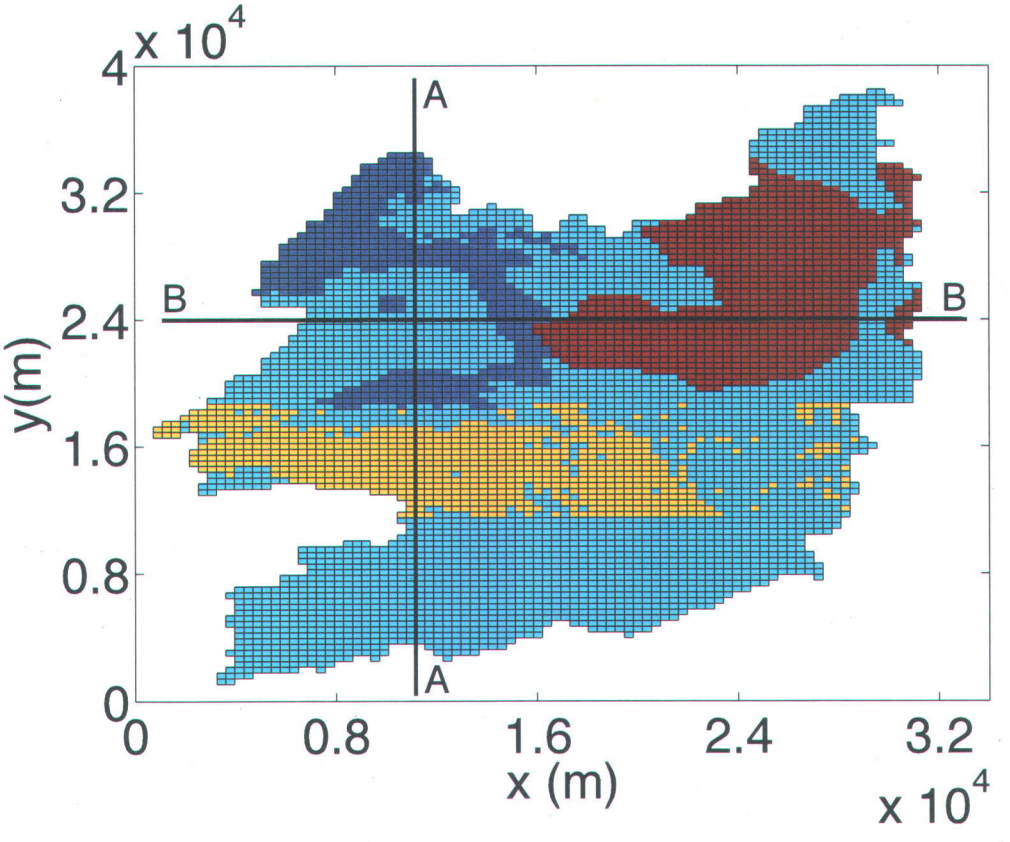

Figure F.1: Horizontal heterogeneity such as indicated in Table F.1: Zone 1 (blue), Zone 2 (cyan), Zone 3 (yellow), and Zone 4 (brown).

Two vertical profiles along a longitudinal and latitudinal transect are shown in Figure F.2. These two profiles illustrate the complex combination between topography and heterogeneity in the definition of the settings for the des Anglais catchment. In particular, the longitudinal

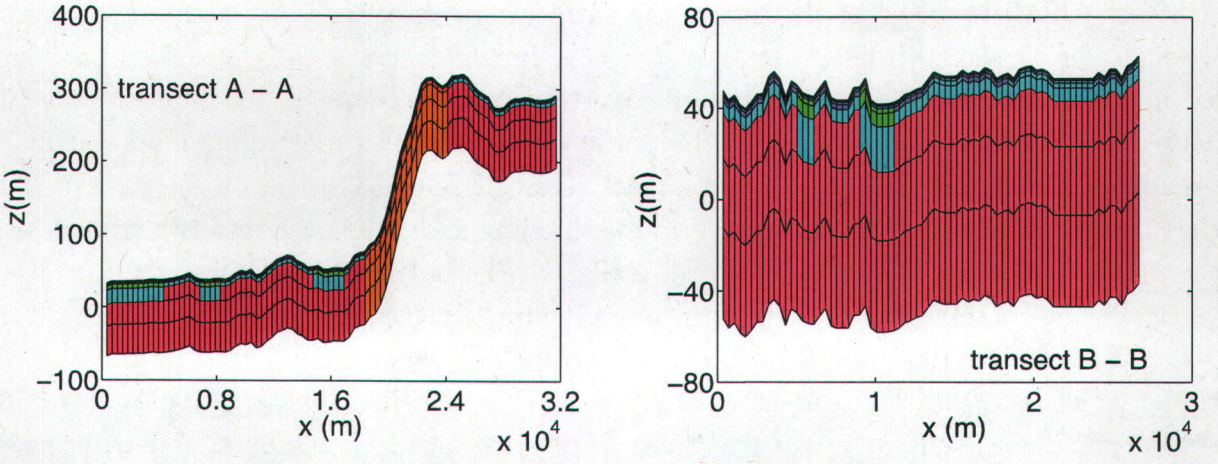

Figure F.2: Heterogeneity in the vertical cross section along the south-north (left graph) and west-east (right graph) transects depicted in Figure F.1. Colors along the vertical cross sections match those used in Table F.1.

cross section (transect A - A) clearly shows a strong topographic gradient in the presence of a high degree of anisotropy in the central part of the catchment.

G Data set (CD-ROM)